DYNAMICAL MODELLING OF AN IDEALIZED HEMISPHERICAL SKULL MODEL WITH FLUID PRESSURE INTERACTIONS USING MODAL ANALYSIS

A Dissertation
Submitted to the Graduate Faculty
of the
North Dakota State University
of Agriculture and Applied Science

By

Ashkan Eslaminejad

In Partial Fulfillment of the Requirements
for the Degree of
DOCTOR OF PHILOSOPHY

Major Department:
Mechanical Engineering

November 2018

Fargo, North Dakota

North Dakota State University
Graduate School

Title

Dynamical Modelling of an Idealized Hemispherical Skull Model with Fluid Pressure Interactions Using Modal Analysis

By

Ashkan Eslaminejad

The Supervisory Committee certifies that this ***disquisition*** complies with North Dakota State University's regulations and meets the accepted standards for the degree of

DOCTOR OF PHILOSOPHY

SUPERVISORY COMMITTEE:

Dr. Ghodrat Karami
Co-Chair

Dr. Mariusz Ziejewski
Co-Chair

Dr. Annie Tangpong

Dr. Kenneth Ruit

Dr. Kambiz Farahmand

Approved:

5/28/19 — Date

Dr. Alan Kallmeyer — Department Chair

ABSTRACT

In this dissertation, a non-invasive intracranial pressure (ICP) monitoring technique is introduced by developing a head dynamic model. The technique is based on modal frequency testing and vibration responses analysis of the skull. To examine and verify this methodology, we conducted vibration tests on a hemispherical shell to stand as a surrogate for human cranium to measure the effect of cerebrospinal fluid (CSF) pressure on human skull dynamic response; we utilized a hammer-impact modal testing methodology on the simulated hemispherical shell to extract its dynamic response characteristics.

To be able to examine the CSF-skull dynamics interactions, we measured the skull impulse responses using mechanical tensile tests at different strain rates. The modal analysis by finite elements eigenvalue analysis of the upper cranium skull model was conducted to find the material properties of the skull. Linear elastic, as well as, nonlinear hyperelastic material models were assumed for the skull to find its material parameters.

In the simulation of the human head, the cranium was modeled as a closed clamped hemispherical aluminum shell under internal fluid pressure. The interactions of CSF with the simulated cranium were studied and the frequency responses were obtained at different interior pressures. A numerical procedure for dynamic analysis of the systems was developed to measure the modal frequencies of the setup. We examined the changes to the peaks of frequency response under different fluid pressure. The results of modal analyses demonstrate changes in the frequency of bending-wave vibration modes, while longitudinal-wave modes are nominally altered under variable pressure conditions. A single-degree of freedom vibrational model was also developed to fit to the data for the sensitive modes. Linear regression analysis of the results reveals that the dynamic model's equivalent damping and stiffness parameters are sensitive to fluid pressure

variations while the equivalent mass parameter is relatively unaffected. As a result of this study we conclude that variance in CSF pressure has a measurable effect on the dynamic characteristics of the cranium and vice-versa. A calibrating system to connect the dynamic changes of the head can stand as a non-invasive system for ICP changes.

ACKNOWLEDGEMENTS

Firstly, I would like to express my sincere gratitude to my advisors Professor Ghodrat Karami and Professor Mariusz Ziejewski, for the continuous support of my Ph.D. study and related research, for their patience, motivation, and knowledge. Their guidance helped me in all the time of research and writing of this thesis.

In addition to my advisors, I would like to thank the members of my thesis committee: Professors Anne Tangpong, Kenneth Ruit, and Kambiz Farahmand, for their insightful comments and encouragement, and also for the hard questions which incented me to widen my research from various perspectives.

To my colleagues and friends of the Computational Lab in the Department of Mechanical Engineering, I thank them for their companionship for providing a pleasurable and friendly working atmosphere. In particular, I would like to thank Mr. Justin Hegstad, Dr. Sanaz Shojaei and Dr. Mohammad Hosseini-Farid for their friendship and help for the past three years.

Last but not the least, I would like to thank: my wife, my parents, my brother and sister for supporting me spiritually throughout my graduate study and my life in general.

DEDICATION

This thesis work is dedicated to my beautiful wife, Atena, who has been a constant source of support and encouragement during the challenges of graduate school and life. I am truly thankful for having you in my life. This work is also dedicated to my parents, Mahnaz and Farhang, who have always loved me unconditionally and whose good examples have taught me to work hard for the things that I aspire to achieve.

TABLE OF CONTENTS

LIST OF TABLES

LIST OF FIGURES

LIST OF ABBREVIATIONS

CAD .....Computer Aided Design

CMIF.....Complex Modal Indicator Function

CSF .....Cerebrospinal Fluid

CT .....Computed Tomography

DAQ.....Data Acquisition

DOF.....Degree of Freedom

ED .....Extraventricular Drain

EDM.....Engineering Data Management

FE.....Finite Element

FFT.....Fast Fourier Transform

FV .....Flow Velocity

FRF .....Frequency Response Function

FSI.....Fluid-Structure Interaction

ICP .....Intracranial Pressure

MAC .....Modal Assurance Criterion

MIF .....Modal Indicator Function

MMIF.....Multivariable Modal Indicator Function

MRI.....Magnetic Resonance Imaging

nICP .....Non-invasive Intracranial Pressure

nCPP .....Non-invasive Cerebral Perfusion Pressure

SDOF .....Single Degree of Freedom

TBI.....Traumatic Brain Injury

TCA.....Transcranial Acoustics

TCD.....Transcranial Doppler

LIST OF APPENDIX TABLES

LIST OF APPENDIX FIGURES

CHAPTER 1. INTRODUCTION

1.1. Motivation

Intracranial pressure (ICP) is the pressure inside the skull. This includes brain tissue enclosed by meninges membranes and perfused by cerebrospinal fluid (CSF). In a human head, the volume of intracranial contents is held in equilibrium between intracranial soft tissues and fluid inflows and outflows. Any changes in the volume of intracranial contents, such as changes in the volume of CSF or blood, can cause changes in ICP (Harary, Dolmans, & Gormley, 2018). This means that abnormal ICP can cause serious headaches, nausea, hemorrhaging, diplopia, tinnitus, or even traumatic brain injury (TBI). Therefore, an accurate determination of ICP is important for neurological health assessment.

Furthermore, even when these techniques are available, proper ICP monitoring must account for multiple considerations due to head biomechanical complications. The requisite considerations for safely performing such monitoring can be understood with knowledge of intracranial components and their participation in physiological processes, such as intracranial volume equilibration. We know that the human skull is an enclosed space fully filled with fluid and soft tissue. Within an adult human head (which includes the solid cranium, brain and cerebellum nerve tissue, CSF, and arterial and venous blood), the volumes of brain tissue, blood, and CSF are maintained in equilibrium. Changes in the volume of either soft-tissue (brain and blood vessels) or fluid (blood and CSF) can alter the ICP (Harary et al., 2018). Changes in volume affects pressure, which in turn, affects health. Thus, monitoring ICP is key to understanding the overall cranial health or injury of a patient For example, as shown in Figure 1-1, normal ICPs are typically observed in the range of 667-2000 Pa, intracranial hypertension occurs at pressures of over 3 kPa, and the threshold for adult brain death is 8 kPa.

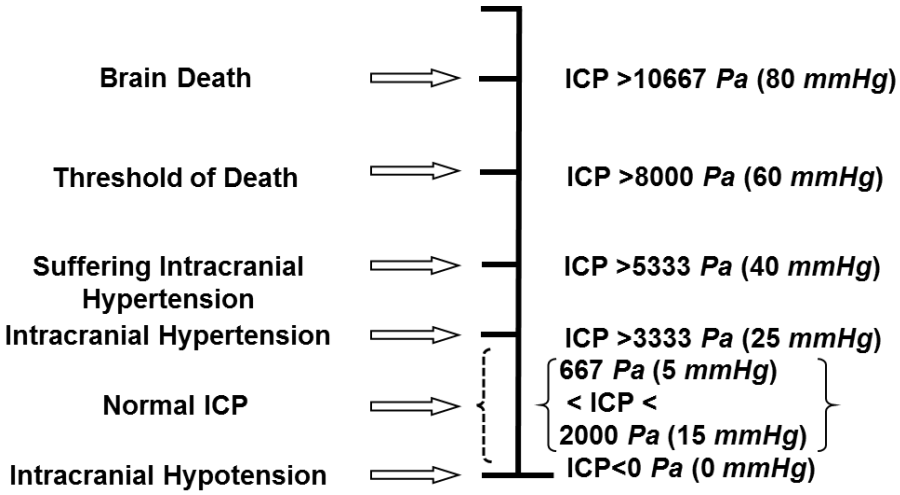

Figure 1-1. Neurological conditions associated with ranges of ICP (Liau, 2000), with the threshold for neurological death occurring at about 8 kPa or 80 cm of a column of water.

The ICP-intracranial volume curve in Figure 1-2 illustrates the relationship between volume and pressure within a human head. Under healthy conditions, ICP changes lead to alterations in the amount of one or more of the contents. In contrast, ICP changes can result from unhealthy conditions, including brain swelling, inflammation, tumors, cerebral aneurysm, bleeding in the brain, and meningitis (swelling and inflammation of pia mater, dura mater, and the arachnoid membrane caused by infections). These abnormalities can increase the volume of the brain and meninges which may trigger a decrease in CSF fluid and an increase in ICP. For example, hydrocephalus causes CSF to accumulate abnormally in the cerebral cavity, which increases ICP and squeezes arterial and venous blood vessels. On the other hand, because of intracranial volume equilibrium, ICP variation directly effects the volume of the intracranial contents. Although these volume alternations can be diagnosed by non-invasive imaging techniques, still there are the common issues in invasive and non-invasive methods which are expensive, time-consuming, and are not available in emergency situations such as combat fields.

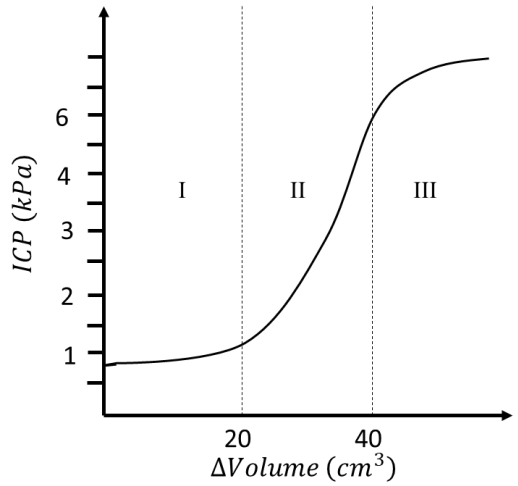

Figure 1-2. An ICP-Volume curve showing normal cerebrovascular responses delimited into three areas: good CSF compensatory reserve region (I), the rising area (II) depicting a poor compensatory reserve, and a flat curve area (III) seen at very high values of ICP (above the life-threatening ICP threshold) (Czosnyka & Pickard, 2004).

An alternative non-invasive technique can improve the current ICP monitoring health threatening drawbacks (high risks of infection and bleeding), even though the accuracy of these invasive techniques has been accepted. Recently, there are some studies conducted on non-invasive ICP (nICP) assessment such as the fluid-dynamics-based techniques. These nICP methods can diagnose ICP elevation (intracranial hypertension), however, these methods are not able to measure accurately the values of ICP and its variation range. These investigations of nICP assessment were carried out experimentally (clinical trial) on patients in clinical field which increase the investigation costs. The nICP monitoring trials with the personnel training are time-consuming along with high costs which are the common ICP monitoring issues and need to be improved. Because nICP techniques have not been sufficiently precise to be used in clinical situations, the nICP techniques are still being explored (Harary et al., 2018). Any study that can provide more information into our understanding of the head biomechanics and its corresponding intracranial interactions, can help us for developing an accurate and universal nICP monitoring technique.

From biomechanics points of view, ICP variation can change the mechanical and dynamic characteristics of head due to the CSF mass and stiffness at the interaction's boundaries on the brain tissue and skull interior surface. Therefore, we need a model that can simulate and predict these changes by ICP variation. By modelling of head with the head biomechanics information such as intracranial interactions and volume equilibrium, scholars might be leaded to understand better the unknowns and decrease uncertainties. Biomechanics models not only can provide opportunities for testing and simulating novel techniques using analytical and computational concepts, but also can decrease complications to decrease the testing and training costs.

Human head modelling that includes the intracranial contents is complex because of the geometrical complications, material nonlinearities, and internal and external component interactions. Although complex skull geometries can be modelled using imaging techniques such as 3D scanners, modelling of nonlinear material or interactions of internal contents still needs to be developed. Indeed, a physical and empirical technique that could mathematically map the intracranial materials with their interactions would improve head biomechanics models for nICP monitoring simulations. Furthermore, a dynamic model could more accurately represent the human head because the ICP varies with time, due to the heart pumping, breathing, head positioning, and CSF circulation. To be effective, the parameters of this dynamic model should be able to be measured noninvasively. Therefore, a dynamic head model including the CSF interactions for nICP monitoring should be developed.

1.2. Problem Statement

As it has been shown, still, we do not have a head dynamic model which simulates the human skull and how it interacts with interior contents such as CSF-skull interactions. Some studies have tried to model the CSF-skull interactions using classic mechanics, for example, CSF

was formulated as the solid linear elastic model with fluid bulk modules. However, still the behavior of CSF on skull dynamic modelling is poorly understood as a fluid-structure interaction (FSI) system. In addition, the accuracy of the assumptions in classical mechanics is under question and needs to be validated experimentally. In addition, there is currently no model that can simulate the interior fluid pressure variation effects on the dynamic model parameters. A dynamic model needs to predict the behavior of the skull with any variation in interior fluid pressure.

1.3. Aim and Objective of the Research

Developing a head dynamic model that includes the CSF-skull interactions has several advantages which leads to nICP monitoring improvements. For example, an accurate head dynamic model can be used not only for calibrating trial nICP monitoring methods but also for further studying of brain injury. In addition, a proper head dynamic model can provide the opportunity for better understanding of head biomechanical complexity. Other benefits of using a dynamic model include reducing costs, saving time, and eliminating risks to the patients.

It is very important to model the effects of CSF on the skull dynamic model parameters. Because, while the mass of CSF influences skull dynamic characteristics, the CSF stiffness also has a considerable effect on skull dynamic behavior. The fact that ICP uniformly pressurizes the skull during CSF loading suggests that it is worthwhile to investigate a novel nICP monitoring method based on the evaluation of interactions between the CSF and skull. Recent studies, however, tried to model the CSF and its effects on the skull dynamic characteristics (El Baroudi, Razafimahery, & Rakotomanana-Ravelonarivo, 2012a, 2012b; A. Engin & Y. K. Liu, 1970), the CSF fluid is too simplified as linear model and also these computational simulation were not validated experimentally. In addition, the effects of fluid pressure variation on the skull dynamic

model was not considered. Because of the CSF and skull interactions, the CSF and skull dynamic model can be considered as one dynamical system.

Dynamic model's parameters of any dynamical systems such as CSF-skull model can be obtained by vibration modal analysis technique. Vibration analysis is the techniques for evaluating the effects of CSF on the skull dynamic characteristics because of two reasons; First, vibration analysis can be conducted harmlessly based on excitation techniques such as acoustics pulse, hammer impulse, and shaker vibrator. Second, vibration analysis is a nondestructive method which can obtain the dynamic characteristics of head noninvasively. Skull can be vibrated in different frequency ranges with a hammer impactor that presents no injury risks. Head impulse responses will be captured by mechanical receivers such as sensitive accelerometers or noncontact vibration or acoustic sensors. Figure 1-3-(a) illustrates the vibration-based model scheme of head with the intracranial contents (and CSF loading).

The current study employs experimental and computational vibration analysis technique to develop a had dynamic model with CSF and skull interactions. This model includes the CSF interactions for detecting and evaluating the ICP variations. Therefore, the aim of this study is to evaluate the effects of interior fluid pressure variation on skull dynamic model and vibration responses. For reaching this aim, we need to reduce the human head complexities such as geometry, material nonlinearity, and intracranial contents effects such as brain tissue (since there is no contact between brain and skull interior surface). To concentrate on the CSF-skull interaction in head dynamic model, an idealized hemispherical head model introduces to simulate the upper cranium including frontal, parietal, and occipital bones. In addition, using the hemispherical head model can help to reduce the manufacturing complexities and costs for the current experimental vibration analysis. This head model is depicted in Figure 1-3-(b). This idealized hemispherical

head model is fully-filled with water as CSF. A flowchart of the overarching aim, specific objectives and corresponding hypotheses for the current manuscript are illustrated in Figure 1-4.

Before embarking upon CSF-skull vibration analysis, human skull impulse responses need to be investigated as linear elastic or nonlinear hyperelastic quantities. Therefore, the first contribution of this work is the human skull dynamic modelling. For the very first time, this will confirm whether the skull can be assumed and modeled as a homogenous, isotropic, with linear elastic material constitutive model for vibration simulation. These assumptions will be examined using experimental and numerical vibration modal analysis techniques on a human skull bone. This fulfills the first objective of this study.

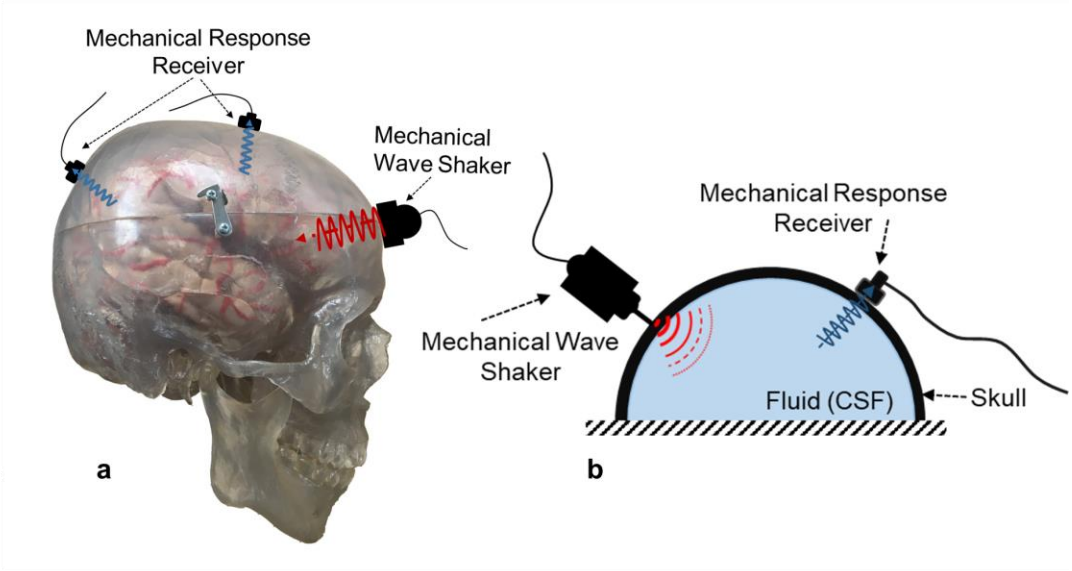

Figure 1-3. Current study scheme: prototype of skull vibration model with CSF pressure loading (a). Hemispherical model of upper cranium with CSF along with the experimental model setup (b).

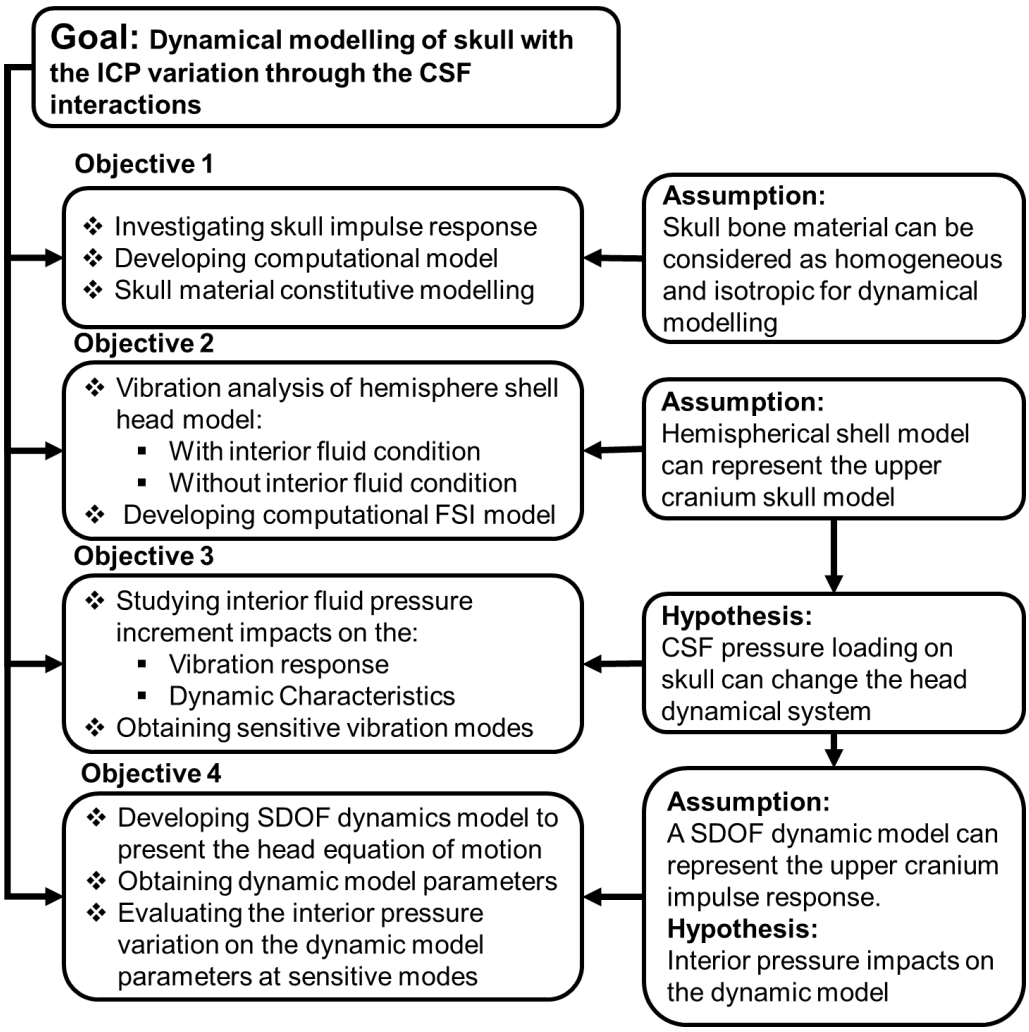

Figure 1-4. Summarized flowchart of the current manuscript goal, objectives, and corresponding hypotheses.

The second contribution of the current study is the CSF computational modelling with its interactions on skull dynamic model, which is considered as one CSF-skull dynamic model. This model can be validated by experimental modal analysis technique. However, due to the presence of cranium sutures, a human cadaver cranium cannot be filled with fluid (artificial CSF or water). In a simplified analytical form, vibrations of the idealized human skull in contact with CSF have been studied by several scholars (Baker, 1961; El Baroudi et al., 2012a; A. Engin & Y. K. Liu, 1970), however, no experimental studies have tried to validate these theoretical modelling. We choose an idealized hemispherical head model because it is a simplest form of head which help to

remove the influences from other parameters such as the head geometrical nonlinearity and brain tissue constitutive modeling. On the other hand, this idealization helps to control the influences of ICP on the dynamical system parameters through CSF interactions.

To model the idealized hemispherical head including CSF (CSF-skull system), a shell model is considered because the ratio of skull dimensions with respect to bone thickness is relatively high. Using examined simplifications (homogenous, isotropic, and linear elastic material model), an aluminum hemispherical shell will be used to simulate the three-dimensional linear elastic skull. In addition, using an aluminum hemispherical model decreases the manufacturing costs at this stage. Along with skull modelling, CSF are approximated as water with the compressible and non-viscous behavior and similar mechanical properties.

The third contribution of this work is the evaluation of the CSF pressure incremental increases consequences on the aluminum hemispherical head dynamic model in both vibration responses and dynamic characteristics. To experimentally examine this objective and simulate the CSF-skull vibration prototype model, we consider the vibration of a hemispherical aluminum shell fully filled with controlled pressurized water (with no free surface). In this experimental setup, the enclosed fluid pressure changed from 0 Pa to 15 kPa by step values of 2.5 kPa. These values are considered because, for nICP monitoring, (based on the statement from Association of Advancement of Medical Instrumentation), the deviation about 267 Pa (2 mmHg) is acceptable in the ICP intermediate from 0 to 2667 (20 mmHg) which is normal range of ICP variation (Popovic, Khoo, & Lee, 2009). Moreover, the differences less than 10 percent are acceptable from the ICP range from 2667 Pa (20mmHg) to 13332 Pa (100 mmHg). The main goal of this objective is to explain the impacts of CSF pressure variation on skull vibration characteristics (vibration frequency and mode shapes).

Finally, for the first time, after obtaining the sensitivity of cranium impulse responses with respect to CSF pressure incremental increases (which is equivalent to ICP increments), a single degree of freedom (SDOF) equivalent dynamical system model will be utilized to present the head model with two input invariants: 1) external impulse 2) internal fluid pressure changes. Using regression techniques, the impacts of ICP variations on cranium vibration responses might reveal sensitivity of the dynamical system governing equation to mass, damping, and stiffness behaviors. These simulations and modellings provide new insights into head dynamic modelling and our understanding from human head system and head injury health monitoring.

The current thesis includes six chapters, with one appendix to provide supplementary experimental measurements and analysis results. The dissertation flowchart is depicted in Figure 1-5.

Chapter 1: Introduction, motivation and research background of the current manuscript are provided in this chapter. The goal, research objectives with corresponding hypothesizes are explain in this chapter.

Chapter 2: The research background of biomechanics of human head, are provided along with dynamical systems modeling. The dynamical system modeling is explained to show the basis for the objectives of the current dissertation.

Chapter 3: In this chapter, the first objective is developed, which includes development of numerical skull models using a 3D scanner to incorporate accurate geometry, along with linear and nonlinear material constitutive modeling. This modelling is established to examine human skull behavior in nondestructive vibration analysis. Hammer-impact modal analysis is employed to extract the dynamic characteristics of the system. Experimental measurements inform numerical

modeling using FE. This study has been submitted for peer review to the Journal of Vibration and Acoustics-Transaction by ASME.

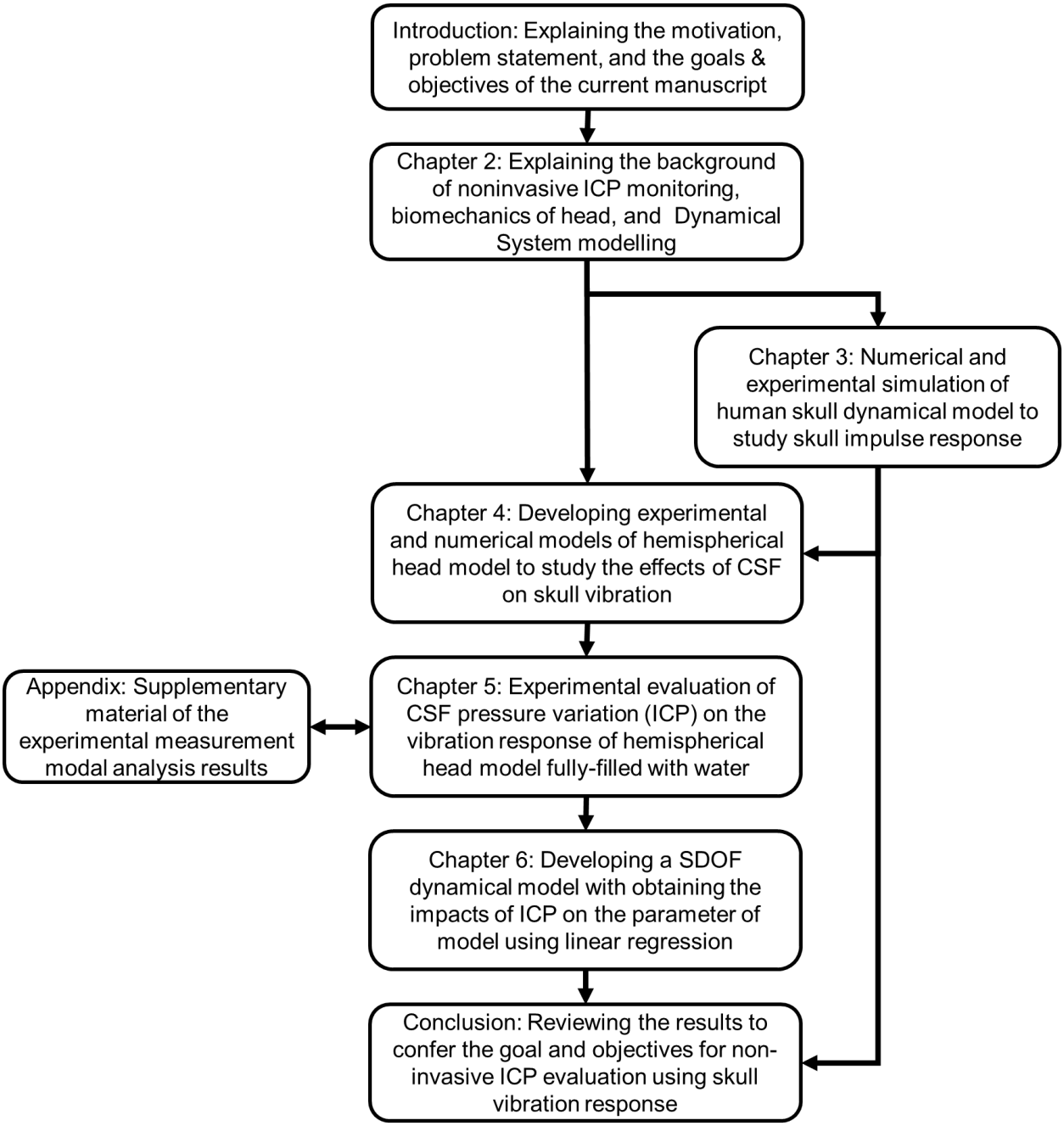

Figure 1-5. Flowchart of the current manuscript and the relation between chapters.

Chapter 4: In this chapter, based on the second objective of this manuscript, experimental and numerical vibration simulation of a hemispherical head model with and without CSF

interactions are established. First, the numerical dry hemispherical head model is validated by experimental modal analysis. Afterward, the CSF-skull (FSI problem) system is modeled numerically using a compressible acoustic fluid model for the CSF. The numerical modeling is validated using hammer-impact modal analysis of fully-filled hemispherical head models. The dynamic characteristics of these system are compared to show the effects of CSF-skull interaction. This study has been published in the Applied Acoustics Journal.

Chapter 5: ICP pressure variation effects on the hemispherical head model are investigated in conjunction with the third objective. First, the external frequency response of hemispherical head model is calculated experimentally. Sensitive FRF-summation peaks are obtained for study in modal analysis. Hammer-impact modal analysis techniques are used to obtain the modal frequencies, damping ratio, and mode shapes, which are termed as dynamic characteristics. Intracranial pressure variation effects on dynamic characteristics of the CSF-skull system are demonstrated. This study has been published in the Journal of Vibration and Acoustics-Transaction by ASME.

Chapter 6: Along with the fourth objective, this chapter introduces a SDOF dynamic model to present the modes of vibration which are sensitive to ICP increments. Linear regression is used to show the impacts of CSF pressure variation on dynamic motion parameters. The results present a SDOF model, which is a function of ICP, and which can be used to establish a novel nICP technique. This study has been submitted for peer review to the Journal of Vibration and Control.

Chapter 7: The final chapter represents a comprehensive review of all objectives and significant achievements. In addition, this chapter provides suggestions for further investigation.

CHAPTER 2. RESEARCH BACKGROUND

2.1. Biomechanics of the Human Head

The human head includes the skull, which holds the brain hemispheres, cerebellum, brain stem, CSF, dura matter, pia matter, and other components, such as facial features that are beyond the scope of this review. Based on the Monro-Kellie model (Greenberg, 2016) 80 % of the intracranial contents is brain tissue, 10 % is CSF, and 10 % is blood, which includes arterial and venous blood. The principal components of the cranium are exhibited in Figure 2-1. Inside the cranium, the pia membrane separates brain tissue (white and gray matter) from arachnoid and dura matter, and the space between them is filled with CSF. In addition, the two brain hemispheres are separated from each other by the Falx cerebri membrane.

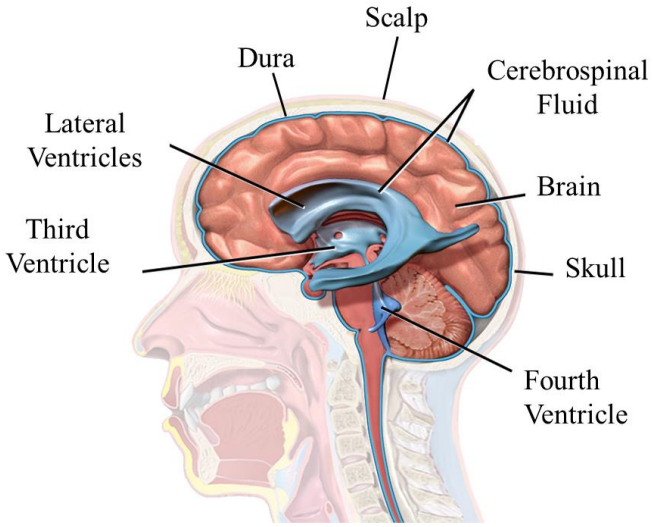

Figure 2-1. Schematic diagram of human head anatomy outlining the principal components of the cranium, including the CSF system and the ventricles in which CSF accumulates (Wikipedia, 2018).

The Falx membrane is attached to dura matter and prevents rotation of the brain inside the cranium. In addition to the Falx cerebri, meninges membranes, which are composed of dura matter, pia matter and the arachnoid mater, separate the brain and spinal cord tissue from CSF, the interior

surface of the cranium and the vertebral canal (Tse, Lim, Tan, & Lee, 2014). Pia matter is a thin, delicate, fibrous layer separating the brain tissue from surrounding CSF.

A main component of the human head is the brain, with a weight of three pounds. This is over one quarter of an adult human's total head weight of 11 pounds. The brain is comprised of the cerebrum, cerebellum, and spinal cord connection, called the brain stem. The cerebrum includes two hemispheres, each one having a frontal, temporal, parietal, and occipital lobe. A representation of a brain with corresponding names is depicted in Figure 2-2. The two cerebral hemispheres are connected to each other at the corpus callosum, which is mostly white matter and surrounded by the third and lateral ventricles filled with CSF.

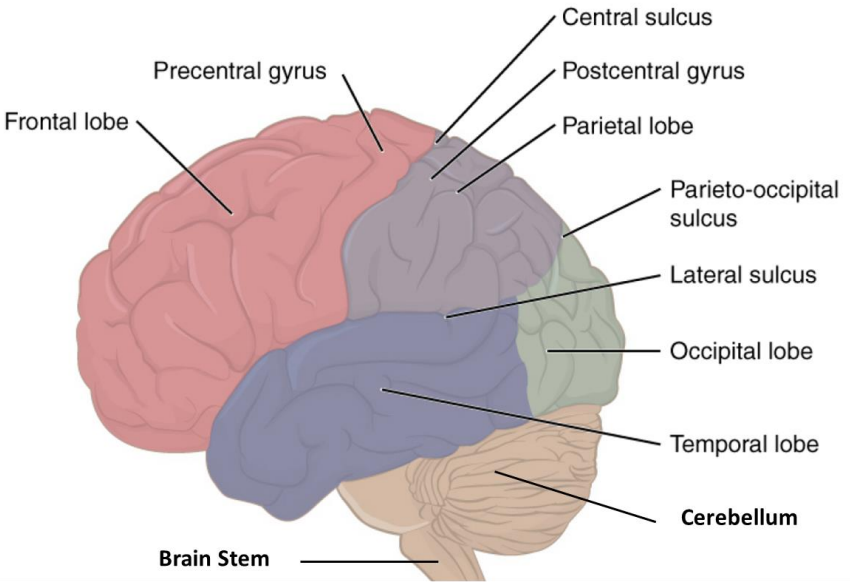

Figure 2-2. The human brain depicted with the cerebellum, brain stem and cerebrum colored and labelled with lobe names (Betts, 2017).

2.1.1. Skeletal Components of the Human Head

The bones of the human head can be separated into three regions: the base, facial bones, and the housing of the brain (Neurocranium) (Cheng & Reichert, 1998). More specifically, the human head consists of 22 connected bones, eight of which belong to the skull. The skull bones include the frontal, occipital, sphenoid, ethmoid, two parietal and two temporal bones. All skull

bones are joined together with ossified sutures. Figure 2-3 shows how these bones are situated in the head. On the whole, the adult skull can be considered as a single rigid body and not as juxtaposed bones.

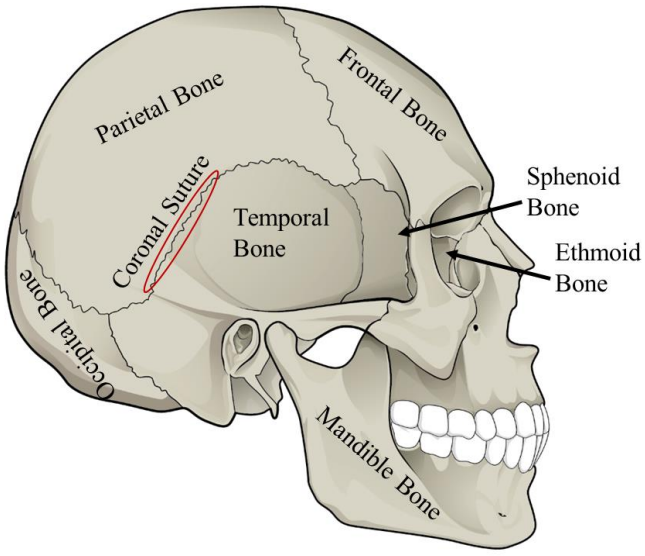

Figure 2-3. The skeletal components of the human head include face, base, and Neurocranium sections, with the latter containing the following constituents: Frontal, Occipital, Temporal and Parietal bones. These bones are locked together with sutures to form a single solid structure (Betts, 2017).

2.1.2. Cerebrospinal Fluid

Cerebrospinal fluid has properties similar to water (clear and colorless) and surrounds the brain and spinal cord. As depicted in Figure 2-1, CSF perfuses the space between the brain and dura matter, which is in contact with the skull. The CSF has an approximate volume of 150 ml in an adult. Moreover, CSF is secreted by the choroid plexuses three to four times a day, which results in a total volume of 450 to 600 ml being turned over each 24 hours (Sakka, Coll, & Chazal, 2011).

Cerebrospinal fluid governs the dynamic intracranial pressure system. Thus, it provides a medium for invasive ICP monitoring through the ventriculostomy method. Furthermore, in addition to hydromechanically protecting the intracranial nervous system, CSF supports neuronal

functionality. From a biomechanical point of view, ICP is uniformly distributed over the brain tissue and CSF, therefore, the ICP is uniformly applied over the skull.

2.2. Dynamical System Modelling

The human cranium and its interior components can be considered as a linear time-invariant dynamical system. A dynamic system can be referred to as a system in which the input and the response of the system to said input are time dependent. Mathematical models can describe dynamical systems precisely. For example, as depicted in Figure 2-4, the motion response of the cranium can be analyzed with a mathematical model of the head. In addition, by sending a mechanical impulse or even sinusoid signals, the head can be assessed for responses to defined stimuli. The receiver signal may include elements of the external excitation signals and the internal pulsatile signals. The internal pulsatile signal can be caused by breathing, blood pumping, and head posture effects that may be observable at a range of frequencies.

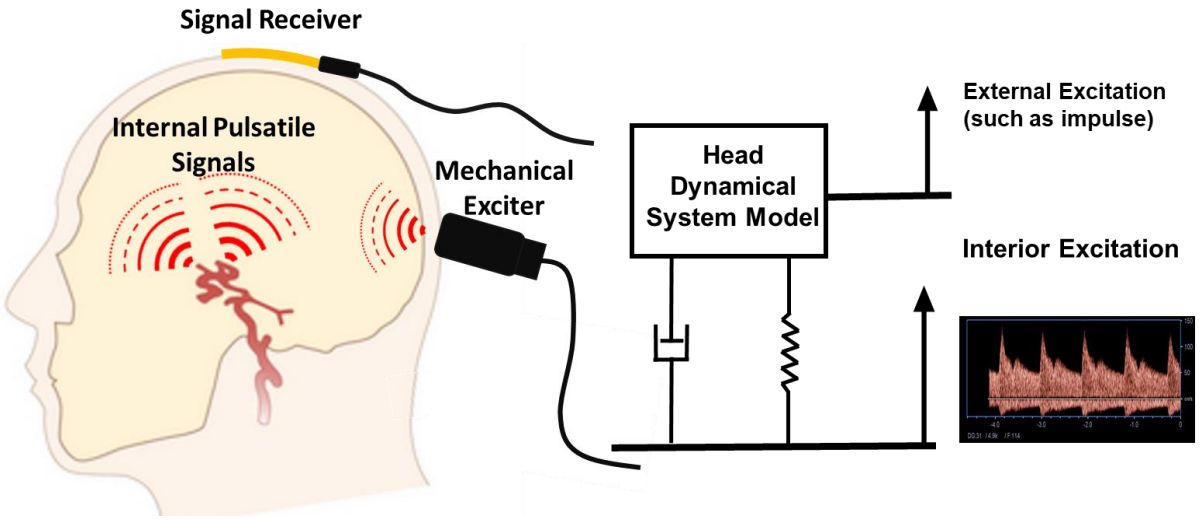

Figure 2-4. Dynamical Systems modeling of human head along with the input and output of the system.

In this example, a simple mathematical model can be defined using Newton's second law of motion, which is applied as the relationship between the rate of cranium elastic deformation changes in response to input forces for the given mass of system. An equation of motion in a SDOF

model can simulate systems of equivalent mass, damping, and stiffness parameters. Notably, environmental conditions and intrinsic factors, such as static ICP, can affect these parameters. Therefore, the state of these conditions needs to be considered in dynamical systems simulations. The state of a dynamical system is the numerical status of a variables that impact responses in the equation for head motion in. For this research, ICP is one of the variables that affects dynamical systems states.

A human head, with all of its complexity, is rarely a linear system in real life. However, understanding the role of ICP on the output of the system will help to estimate the state of the head dynamical system in a variety of situations. Figure 2-5 illustrates a linear time-invariant dynamical system model for the head with two inputs given as external impulse (or even sinusoidal waves) and ICP. The head dynamical state can be estimated experimentally and theoretically by ignoring ICP variation and using modal analysis techniques. Then, by modeling the dynamical state at different ICPs, it is possible to conduct sensitivity analysis. This in turn allows for determination of a frequency response function (Eslaminejad, Ziejewski, & Karami, 2019a, 2019b).

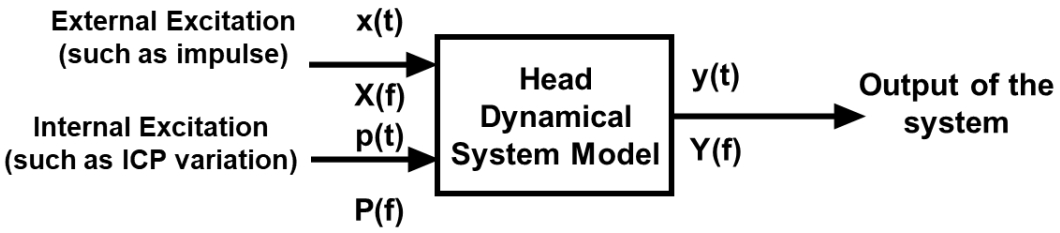

Figure 2-5. Multiple input, single output linear time-invariant model.

2.2.1. Frequency Response Determination

Under linear time-invariant assumptions with a constant ICP input, the output of the dynamical system can be obtained by convolution of the system and input as in equation (2.1)

$$y(t) = x(t) * h(t) = \int_{-\infty}^{+\infty} x(\tau)h(\mathrm{t}-\tau)d\tau \tag{2.1}$$

where h(t) is the system impulse response. Solving integral (1.1) can be problematic for estimating the system response h(t) experimentally. To produce a more feasible analysis, rather than solving the convolution integral, the system instead can be modeled as the product of the frequency spectrum of input in a dynamical system, as shown equation (2.2) in which H(f) is the frequency response function (FRF) of the system.

$$Y(f) = X(f) \times H(f) \tag{2.2}$$

The H(f) calculation is simple in theoretical approaches, yet, in experimental measurements, input noises and output measurement variability cannot be ignored. These noise and error factors in both input and output signals can lead incorrect conclusions concerning the state of the observed dynamical system. An experimental system with input and output signals incorporating uncertainty in conjunction with measured signals is depicted in Figure 2-6.

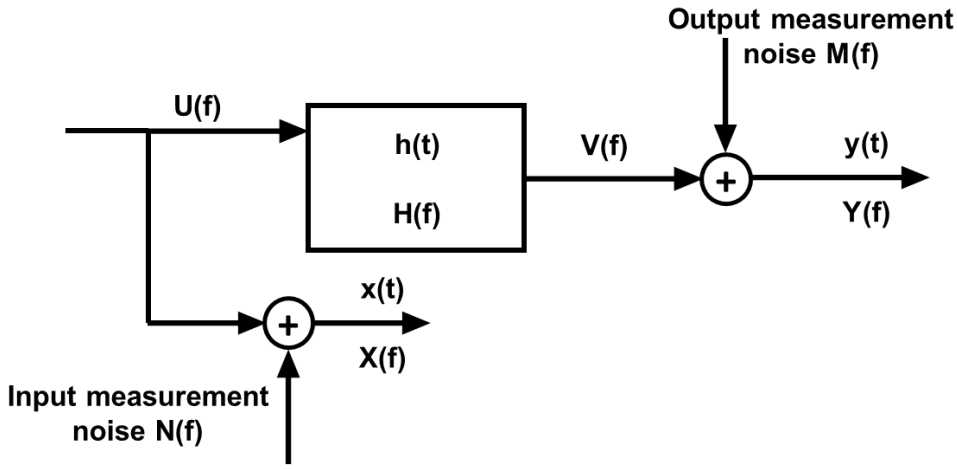

Figure 2-6. Experimental linear time invariant system which incorporates noises in input and output signals in a model with constant ICP.

To estimate a realistic FRF, H(f), it is necessary to calculate two FRFs, one considering input noise, N(f), and another one with noise in output measurements, M(f). For the case without input measurement noise (N(f)=0 and U(f)=X(f)), the output spectrum (frequency domain) can be

written as equation (2.3). In addition, in the case without output measurement noise (M(f)=0 and V(f)=Y(f)), the output spectrum can be presented as equation (2.4).

$$Y(f) = X(f) \times H_1(f) + M(f) \tag{2.3}$$

$$Y(f) = X(f) \times H_2(f) - N(f) \times H_2(f) \tag{2.4}$$

If the experimental setup is constructed precisely and hardware is chosen appropriately, the noises M(f), and N(f) can be ignored by increasing the noise exponents order and averaging of several measurements. The noise order is increased by multiplying X*(f), the complex conjugate of input signal X(f), into equation (2.3), and Y*(f), the complex conjugate of output measured signal Y(f), into equation (2.4). Therefore, we have high order noise factors that can approach zero by averaging results from several measurements observed under identical boundary conditions (Brandt, 2011).

$$X^*(f)Y(f) = X^*(f)X(f) \times H_1(f) + X^*(f)M(f) \tag{2.5}$$

$$Y^*(f)Y(f) = [Y^*(f)X(f) - Y^*(f)N(f)] \times H_2(f) \tag{2.6}$$

The term X*(f)Y(f) is known as the cross-power spectrum, while Y*(f)Y(f) and X*(f)X(f) are labelled as the power spectrum of input and output signals. Upon recording averages of several measurements, X*(f)M(f) and Y*(f)N(f) are approximately zero. Therefore, the FRF estimators H1 and H2 can be reasonably approximated as equations (2.7) and (2.8).

$$H_1 = \frac{X^*(f)Y(f)}{X^*(f)X(f)} \tag{2.7}$$

$$H_2 = \frac{Y^*(f)Y(f)}{Y^*(f)X(f)} \tag{2.8}$$

The true value of the FRF, H(f), is between the absolute magnitude of the complex $H_1(f)$ and $H_2(f)$ values. As a consequence, the coherence function γ, equation (2.9), which is defined as

the ratio of H_1 to H_2, delimits the accuracy of experimental measurements, with a coherence close to 1 being associated with the lowest measurement noises.

$$\gamma^2(f) = \frac{H_1(f)}{H_2(f)} = \frac{\left(X^*(f)Y(f)\right)^2}{\left(X^*(f)X(f)\right)\times\left(Y^*(f)Y(f)\right)} \tag{2.9}$$

$$0 \le \gamma^2 \le 1 \tag{2.10}$$

In the end, the FRF obtained from the observed system represents a linear, time-invariant dynamical system in the frequency domain. Dynamical characteristics (i.e. modal frequencies, damping ratios, and mode shapes) can be calculated using the FRF at each specific ICP. By changing the ICP and measuring the FRFs, the empirical impacts of ICP can be modeled.

2.3. Intracranial Pressure Monitoring Methods

Monitoring ICP changes can be categorized into two general groups based on the method: invasive or non-invasive. Invasive techniques are fluid-based measurements in which a probe penetrates the head to reach interior fluids, such as CSF or blood, either arterial or venous (Harary et al., 2018). These methods require surgical procedures, which are expensive, time consuming, and require professional personnel. In this section, current invasive methods are reviewed, and summaries of noninvasive studies are also provided.

2.3.1. Invasive Methods

Early utilization of ICP monitoring was implemented while reducing CSF volumes in hydrocephalus patients (Srinivasan, O'Neill, Jho, Whiting, & Oh, 2014). The extraventricular drain (ED) method drains abnormally accumulated CSF from brain ventricles. In the 20th century, ED methods became safer with the application of antiseptic methods to prevent hemorrhaging and iatrogenic infections (Aschoff, Kremer, Hashemi, & Kunze, 1999). In 1927, Adson and Lillie attempted to use the ED method to measure ICP (Adson & Lillie, 1927). Since then, ICP

monitoring has been incorporated into treatments for a variety of neurological pathologies, such as TBI, hydrocephalus and subarachnoid hemorrhaging. Currently, ICP monitoring based on ED methods is the standard for accuracy (Padayachy, Figaji, & Bullock, 2010).

Other invasive methods that have been successfully implemented for accurate monitoring of ICP are depicted in the Figure 2-7. The most of these are: ventriculostomy, intraparenchymal fiberoptic catheter, epidural transducer, subdural catheter, and subdural bolt. The tradeoff for the accurate measurement of ICP that these methods provide is that they can cause serious health problems such as cerebral hemorrhaging, spinal cord damage, or infection.

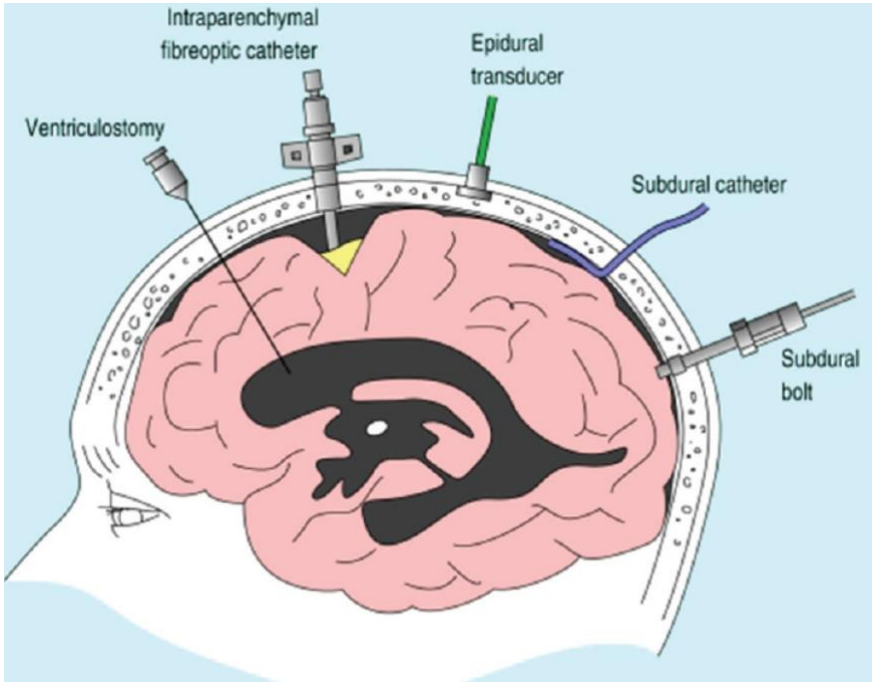

Figure 2-7. Invasive ICP monitoring methods (Ristic, Sutter, & Steiner, 2015)

Ventriculostomy accurately estimates the ICP from the CSF pressure in brain ventricles, though it is associated with the highest infection rates among the invasive methods. Plus, ventriculostomy has high costs and requires extra recovery time for the patient. In addition, there is up to a seven percent chance of intracranial bleeding caused by insertion of the needle in this methtod (Bauer, Razdan, Bartolucci, & Markert, 2011; Binz, Toussaint, & Friedman, 2009).

Overall, Ventriculostomy is not appropriate for long-standing ICP assessment and increases the risks of infection up to five percent after 5 days (Czosnyka & Pickard, 2004).

Another accurate invasive apparatus, the subdural bolt, inserts a probe into the subarachnoid space through a hole in the cranium and dura mater (Kawoos, McCarron, Auker, & Chavko, 2015). Although this method is accurate, it comes with a considerable risk of infection and does not allow CSF drainage, which, therefore, decreases the advantage of monitoring ICP using this technique (Bekar et al., 2009).

In addition to ED based ICP monitoring methods, ICP can also be monitored using transducer devices such as piezoelectric pressure transducers, a strain gauge-based diaphragm, or fiber optic sensors (Zhang et al., 2017). These devices and probes need to reach the CSF in ventricles similar to the aforementioned invasive techniques. Although low infection risks have been reported (Czosnyka & Pickard, 2004), their costs are high, and they cannot be calibrated in situ, which might impact their accuracy.

ICP monitoring is vital in certain clinical circumstances, although a number of studies have suggested that invasive ICP monitoring is not typically beneficial due to intricacies of the procedures and associated high risks of bleeding and infection. Suggested alternatives to invasive ICP monitoring include imaging techniques, such as Computed tomography (CT) scanning and Magnetic resonance imaging (MRI), along with neurological checkups (Aiolfi et al., 2017; Haddad et al., 2011; Shafi, Diaz-Arrastia, Madden, & Gentilello, 2008; Tang et al., 2015). In short, the aforementioned problems associated with invasive ICP monitoring techniques have encouraged researchers to develop novel nICP methods, as summarized in the following section.

2.3.2. Development of Non-invasive ICP Monitoring Methods

In recent publications, non-invasive methods have been categorized in accordance with the testing methods and procedures (Harary et al., 2018; Kristiansson et al., 2013; Padayachy, 2016; Robba et al., 2015; Zhang et al., 2017). As an example, Robba et al (Robba et al., 2015), have organized nICP monitoring methods into five main categories: brain imaging techniques, indirectly transmitted ICP measurements, cerebral blood flow change detection, monitoring of metabolic alternation, and neurophysiological registration of functional activity.

One useful, safe, and repeatable method for nICP evaluation, is classified under the cerebral blood flow change detection category. This technique is the transcranial Doppler (TCD) method, which utilizes the Doppler Effect to measure the flow velocity (FV) in cerebral arterial blood veins using ultrasonography probe devices. These devices use ultrasonic waves at frequencies below 2 MHz (Naqvi, Yap, Ahmad, & Ghosh, 2013). Cardim et al. (Cardim et al., 2016) have extensively studied nICP monitoring based on TCD methods. They have organized these methods into three semi-successful categories: (I) based on TCD and the pulsatility index (PI) (Bellner et al., 2004; de Riva et al., 2012), (II) based on TCD and non-invasive cerebral perfusion pressure (nCPP) measurements (Aaslid, Lundar, Lindegaard, & Nornes, 1986; Chan, Miller, Dearden, Andrews, & Midgley, 1992), and (III) methods based on TCD and mathematical models (F. Kashif, Heldt, & Verghese, 2008; F. M. Kashif, Verghese, Novak, Czosnyka, & Heldt, 2012; Kasuga, Nagai, Hasegawa, & Nitta, 1987).

Although implementation of TCD is relatively inexpensive, risk-free, easily repeatable, and suitable for emergency settings, its accuracy has been questioned. This method can detect changes in arterial blood volume with reasonable accuracy. However, as ICP depends on CSF circulation and brain parenchyma volume along with the inflow of arterial blood and venous blood

outflow, TCD cannot completely account for all contributors to ICP. Particularly low accuracies have been observed when changes in ICP are caused by alterations in CSF circulation or increases in parenchyma volume. This is due to the fact that changes in CSF and brain parenchyma are not be promptly transmitted to arterial beds like those of vasogenic origins (Cardim et al., 2016).

A recently introduced method of nICP monitoring based on the acoustic time-of-flight (TOF) technique evaluates the acoustic properties of intracranial contents through effects on ultrasound wave speed and attenuation factors (Petkus, Ragauskas, & Jurkonis, 2002). This technique relies on the fact that, because the cerebral volume is approximately constant, changes in the volume of the brain, dura mater, pia matter, arterial and venous blood vessels, or CSF are related to changes in the ICP. Changes in blood flow volume correspondingly alter acoustic properties and ultrasonic TOF. Petkus et al. (Petkus et al., 2002) described a mathematical model of intracranial media to obtain a relationship between intracranial acoustic properties and the characteristics of signal propagation inside the head. They evaluated the acoustic properties of intracranial contents by measuring ultrasonic signal TOF and the oscillation period. However, they were unable to construct a successful model due to limitations in material nonlinearities and interaction effects.

Levinsky et al. (Levinsky, Papyan, Weinberg, Stadheim, & Eide, 2016), examined a method based on mathematical modeling and optimization methods to estimate nICP by capturing and processing transcranial acoustic (TCA) signals and comparing them with invasive ICP (iICP) monitoring results. They obtained static and pulsatile ICP estimates that appeared to agree within acceptable limits with continuous iICP measurements. However, based on observed data for 24 patients, they concluded that the TCA method fails to estimate and evaluate ICP in clinical situations.

In short, for TCD-based methods, as well as, for TOF and TCA methods, the skull and its intracranial contents respond to a variety of extracranial and intracranial vibrations and signals over a range of frequencies, which, manifests as complex head dynamics, and, therefore, presents significant obstacles to development of accurate nICP monitoring methods that are robust over practical clinical circumstances. The non-invasive ICP monitoring studies to date have failed to identify an acceptable and accurate alternative to invasive methods. Failures to date have been attributed to limitations in measuring systems, inaccuracy of the methods, and the inherent nonlinearities. Nevertheless, there have been indications that accurate and robust nICP monitoring techniques are still possible. Encountered obstacles have not proven to be universally intractable. Therefore, further research with other nICP monitoring methods remains worth pursuing.

CHAPTER 3. CONSTITUTIVE PROPERTIES DETERMINATION OF HUMAN CRANIUM BY AN EXPERIMENTAL-COMPUTATIONAL MODAL ANALYSIS[1]

3.1. Abstract

In this paper, we identify the material constitutive property parameters of the human skull under tension. These parameters are strain-rate dependent and evaluated under dynamic loading. We examined and applied both linear-elastic and Mooney-Rivlin nonlinear hyperelastic constitutive models to experimental tensile data at different strain rates of 0.005, 0.1, 10, and 150 1/sec. A dried human skull including frontal, parietal, and occipital bones was modeled using a 3D laser scanner and discretized by HyperMesh software to carry out modal analysis using LS-Dyna finite element software. Using experimental roving hammer-impact modal tests, the first four natural frequencies of the skull were measured and validated by checking the Modal Assurance Criterion. The fitted results of nonlinear hyperelastic model observed shows more accuracy than those for linear elastic in terms of coefficient of determination. The first four experimental modal frequencies were extracted and validated as 496 Hz, 543.52 Hz, 1249.71 Hz, and 1286.88 Hz. These measured frequencies were compared with finite element computational simulations to obtain the constitutive model parameters under tensile loads with aforementioned strain rates. Lower relative errors between experimental and computational modal parameters were observed at strain rate of 0.1 1/sec. These results confer a better understanding of the human skull behavior under strain, which could increase the accuracy of nonlinearity dynamic simulations on the skull.

[1] The material in this chapter was co-authored by Ashkan Eslaminejad, Mohammad Hosseini-Farid, Mariusz Ziejewski, and Ghodrat Karami. Ashkan Eslaminejad conceived and carried out the experiments and analyzed the observed results. Ashkan Eslaminejad wrote this chapter in consultation with Mohammad Hosseini-Farid, Mariusz Ziejewski, and Ghodrat Karami. Ghodrat Karami supervised findings of this work.

3.2. Introduction

The examination of traumatic brain injury (TBI) is complicated, owing to its intricate mechanical mechanisms and biological properties. TBI can happen when the head is subjected to high acceleration motion such as ballistic impacts, or blast pressure shock waves, or when shear stress waves are induced into the brain tissue due to abrupt cranial motion, to name a few causes. To better understand TBI mechanisms, its affect is studied by numerous means toward the objective of improving protective devices and mitigating TBI occurrence. For instance, dummy heads such as Hybrid-III are used in vehicle crash studies in order to increase vehicle safety design regarding head injuries. Cadaver head models help researchers understand the mechanisms of human head kinematics and component interactions such as the skull, brain tissue, cerebrospinal fluid, etc. However, due to the high cost of experimental TBI analysis, the FE method has been widely used to investigate TBI under different case scenarios within past two decades. For example, the development of pads for combat helmets under blast or impact induced TBI were employed using FE simulations, and intracranial pressure (ICP) responses of the brain were measured to obtain brain injury thresholds with and without protective devices (Farid, Eslaminejad, Ziejewski, & Karami, 2017; Sarvghad-Moghaddam, Rezaei, Ziejewski, & Karami, 2015). Thus, the FE head model is an alternative to experimental TBI studies by which different injuries and the underlying causal mechanisms can be understood (Eslaminejad, Ramzanpour, Hosseini-Farid, Ziejewski, & Karami, 2018).

Developing a multi-material FE head model requires detailed geometry and accurate material constitutive models of each cranial component. The geometry model can be generated from head imaging techniques such as Magnetic Resonance Imaging or 3D scanning. In addition to accurate geometry models, the material of head components can be modeled using continuum

mechanics, whereby the mechanical material properties can be estimated using mechanical tests. Several studies have helped characterize the mechanical parameters of brain tissue, cerebellum, dura, falx, etc., and cranial mechanical parameters have been investigated by different methods. As regards cranial bone structure, the complex human head skeleton is separated into three parts: the head base, face bones, and the brain housing (Neurocranium) (Cheng & Reichert, 1998). The human skull includes 22 connected bones, of which eight bones belong to the cranium. The cranium bones are: one for each of the frontal, occipital, sphenoid, ethmoid bones, and two each for the parietal and temporal bones; all the bones collectively are jointed together with ossified sutures in adults.

Cranium material constitutive modelling is significantly important in FE TBI studies because kinematic motion directly influences brain tissue displacements. On one hand, the acceleration of the skull causes injury to brain tissue in coup and even contrecoup regions in impact or blast situations. On the other hand, the abrupt movement of the skull can produce shear stress waves which can oscillate the skull and brain tissue with lower modes of vibration. Shear stress waves can stretch brain tissue at nonhomogeneous borders such as the corpus callosum or the cerebellum (border of white matter and gray matter) (Laksari, Kurt, Babaee, Kleiven, & Camarillo, 2018). These injuries can occur without skull fracture.

The majority of skull bone material characterization studies have been employed in quasi-static strain rate conditions (Evans & Lissner, 1957; Margulies & Thibault, 2000; McElhaney et al., 1970). McElhaney *et al*. (McElhaney et al., 1970) tested the human cranium in compression, tensile, shear, and torsion tests quasi-statically, and obtained the linear elastic properties of the cranial regions. Several studies have been conducted to investigate dynamical responses of the cranium. Wood (Wood, 1971) studied the fracture, modulus of elasticity, and failure energy of the

cranium by employing tensile tests at different strain rates. Using the least square method, he fitted the observed results to a linear elastic model. It was observed that the Young's modulus parameter is dependent to strain rate; however, the failure energy of the skull bone is generally independent of strain rate variation. Motherway *et al.* (Motherway, Verschueren, Van der Perre, Vander Sloten, & Gilchrist, 2009) carried out the three-point bend tests at different dynamic speeds from 0.5 to 2.5 m/sec. They found that the testing speed, the strain rate, and the cranial sampling position all impose a significant effect on the computed mechanical parameters. These studies have attempted to involve the complex skull bone dynamic responses into the mechanical parameters by considering different test speeds and strain rates. However, the effect of dynamical parameters such as the modal frequencies, damping characteristics, and mode shapes are difficult to integrate into a conventional model.

The combination of experimental modal analysis and FE modal analysis can be utilized to determine material stiffness properties of the skull bone. The flowchart of the synthesized dynamical and FE modeling applied in this study is depicted in Figure 3-1. In this study, we utilize the roving hammer experimental modal analysis to obtain skull modal frequencies. The upper cranial part of the human skull including frontal, parietal, and occipital bones is considered (Figure 3-2-(a)). Using a 3D scanner, the geometric computer aided design (CAD) model of the skull is constructed for FE modal analysis of different bone properties (Figure 3-2-(b)). Published skull tensile test results are utilized to fit two different constitutive models (linear elastic and nonlinear hyperelastic) at different strain rates from 0.005 to 150 (sec^{-1}). The skull CAD model is meshed (Figure 3-2-(c)) and the obtained material properties are assigned to construct the governing equation of motion. Furthermore, the eigenvalue problem is solved to obtain the modal

frequencies. The modal frequencies are compared with the experimental measurements to find the material model and properties at different strain rates associated with the lowest error.

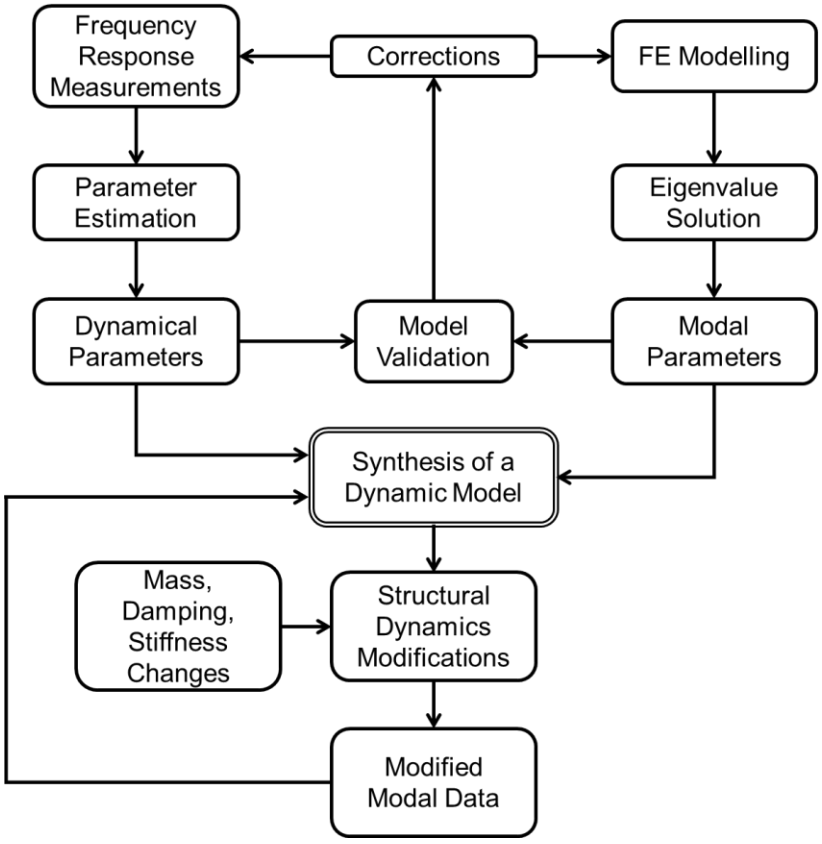

Figure 3-1. Dynamical Modelling process using the FE method (Avaitable, 2018).

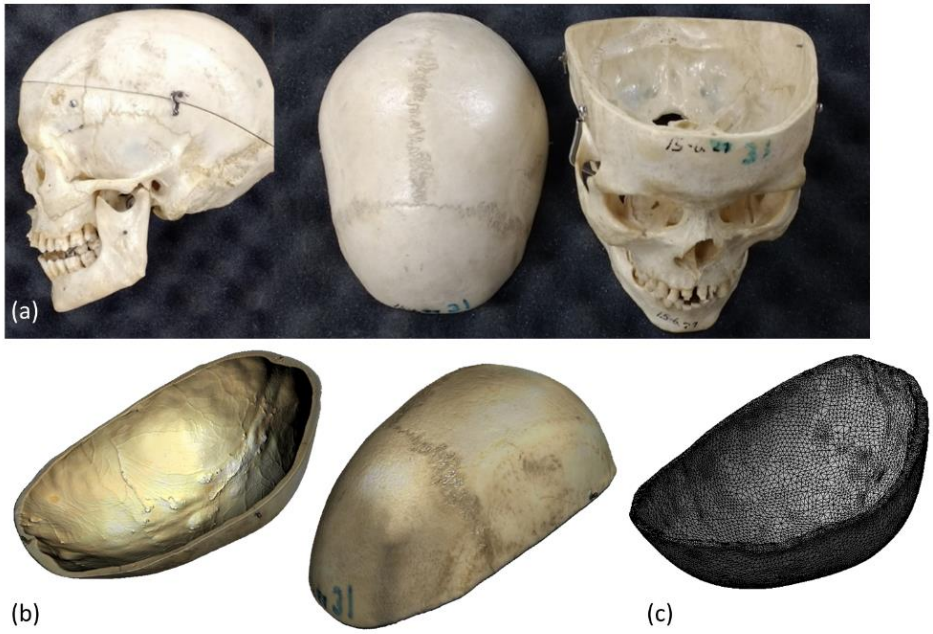

Figure 3-2. The upper cranium bone is cut and includes frontal, parietal, and occipital (a), the 3D scanned model of the upper cranium skull (b), and the discretized finite element model (c).

3.3. Materials and Methods

The upper cranium skull bone was cut and scanned to be discretized using HyperMesh software (HyperMesh, 2010) as it is depicted in Figure 3-2. The meshed model imported to the LS-Dyna for the implicit eigenproblem analysis (Hallquist, 2006). The general procedure of creating this eigenvalue problem is briefly presented in the following equations. The equation of motion is obtained based on a Lagrange equation in the form of

$$\frac{d}{dt}\left(\frac{\partial L}{\partial \dot{q}_i}\right)-\left(\frac{\partial L}{\partial q_i}\right)=Q_i^{nc} \tag{3.1}$$

where L is the Lagrange function and Q_i is the non-conservative forces system. The Lagrange function can be obtained based on the kinetic energy and potential energy functions of the continues structure. This equation of motion can be discretized into the form of

$$[\mathrm{M}]\{\ddot{q}\}+[\mathrm{K}]\{q\}=\{F\} \tag{3.2}$$

where [M], [K], and q are mass matrix, assembled stiffness matrix, and generalized coordinate vector, respectively. To obtain the homogeneous eigenvalues (natural frequencies), the general solution can be considered as

$$\{q\} = \{\varphi\} e^{i\omega t} \tag{3.3}$$

where the ω is natural frequencies and the φ is mode shape vector. Substituting equation (3.3) into equation (3.2) and considering the free vibration, F=0, the general eigenvalue problem can be written as

$$\left(-\omega^2 [\mathrm{M}] + [\mathrm{K}]\right)\{\varphi\} = 0 \tag{3.4}$$

By solving Eq. (3.4), the natural frequencies ω and corresponding mode shapes φ can be obtained for any of the two constitutive models at different strain rates. For constructing the assembled stiffness matrix, the material constitutive models should be defined, and the mechanical properties can be obtained based on the related mechanical tests. To this end, the tensile test results were considered to implement the linear elastic and nonlinear hyperplastic constitutive models.

3.4. Skull Constitutive Modelling

In order to obtain the skull material properties for the FE simulation, the uniaxial tensile test data from 120 specimens of 30 human adult skull subjects were used (Wood, 1971). The tested specimens were built from frontal, parietal, and occipital bones. These tensile tests were employed with the following strain rates: 0.005, 0.1, 10 and 150 (1/sec). The averaged stress-strain diagram is depicted in Figure 3-3 at each strain rate. The linear elastic and nonlinear hyperelastic model were considered to derive the stiffness constant coefficients at different rates.

In most of the FE head models, the cranium was considered linear elastic (Eslaminejad, Sarvghad-Moghaddam, Rezaei, Ziejewski, & Karami, 2016; Tse et al., 2014), however, the skull bone is actually complex material consisting of a three layered structure (Delille, Lesueur, Potier,

Drazetic, & Markiewicz, 2007; Motherway et al., 2009). The skull bone external and internal layers consist of compressed and dense bone, and the central layer can be considered a low-density, porous bone structure. Hereby, considering the isotropic linear elastic model can increase error in FE simulations. The nonlinear hyperelastic model provides a better fit to the nonlinear response of the cranium. These models are briefly explained in following.

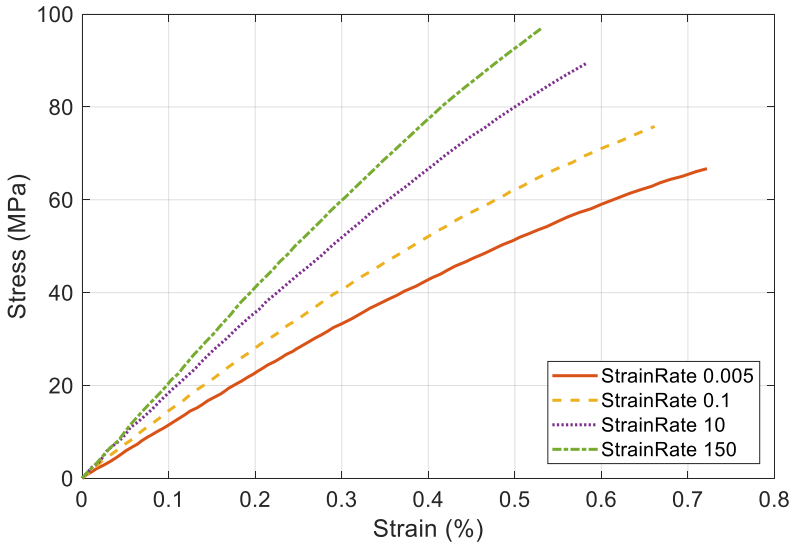

Figure 3-3. Stress-Strain tensile tests of uniaxial tensile tests of the cranium at different strain rates (Wood, 1971).

3.4.1. Linear Elastic

Using the Hook's law, equation (3.5), the linear elastic stress-strain relationship is fitted to each line applying the least square method.

$$\{\sigma\} = [E]\{\varepsilon\} \tag{3.5}$$

3.4.2. Nonlinear Hyperelastic

The strain energy function as Mooney-Rivlin (Hallquist, 2006) is modeled as a polynomial function of the principal strain invariant as:

$$W = \sum_{i+j=1}^{N} C_{ij} \left(J_1 - 3\right)^i \left(J_2 - 3\right)^j \tag{3.6}$$

where *C* are the stiffness constant related to distortion responses. In addition, J_1 and J_2 can be obtained using the left Cauchy-Green strain tensor for uniaxial tensile test as below

$$[\mathrm{B}] = \begin{bmatrix} \lambda_1^2 & 0 & 0 \\ 0 & \lambda_1^{-1} & 0 \\ 0 & 0 & \lambda_1^{-1} \end{bmatrix} \tag{3.7}$$

$$J_1 = Trace[B],\ J_2 = \frac{J_1 - Trace[B]^2}{2J_3}, and\ J_3 = \sqrt{\det[B]} = 1 \tag{3.8}$$

For the incompressible hyperelastic material the uniaxial Cauchy stress, σ_{11}, (Mendis, Stalnaker, & Advani, 1995) can be given by

$$\sigma_{11} = \lambda_1 \frac{\partial W}{\partial \lambda_1} \tag{3.9}$$

Therefore, the true uniaxial stress-stretch relation of Mooney-Rivlin can be given by

$$\sigma_{11} = 2C_{10}\left(\lambda_1^2 - \frac{1}{\lambda_1}\right) + 2C_{01}\left(\lambda_1 - \frac{1}{\lambda_1^2}\right) \tag{3.10}$$

Eventually, by fitting the equation (3.10) into the tensile test results, and by considering the stretch and engineering strain relationship: $\lambda = 1 + \varepsilon_{ENG}$, the stiffness constants Cs can be obtained.

3.5. Experimental Modal Analysis

To obtain the dynamical properties of cranium, the roving hammer-impact method was used. The schematics of this test are depicted in Figure 3-4, which shows the position of the skull on the foam which simulates the free-free boundary condition. To measure the frequency response function (FRF), 69 nodes were obtained on the skull and CAD geometry was composed for use in

post-processing software. These two models are illustrated in Figure 3-5. Engineering Data Management (EDM)-Modal software (Crystal-Instrument-Corporation, 2017) was utilized to implement the Modal Parameters Identification (MIF) techniques. A hard-plastic tip was used for the hammer-impactor, and a miniature accelerometer was embedded to the edges of the skull. Accelerometer locations was chosen based on the FE pre-study so that interested modes can be seen (Avaitable, 2018).

Using all the measured impact and response accelerations, the accelerance FRF sets were calculated. The maximum frequency range was considered less than 12 kHz which is the accelerometer frequency. In addition to hardware limitations, the maximum sampling rate and frequency range should be ten times higher than the interested frequency range which is up to 2 kHz. To increase measurement accuracy and decrease signal processing errors, each node was impacted five times and peak hold fast Fourier transform (FFT) averaged data was used to calculate the power and cross-power spectra. It should be noted that we did not use windowing to obtain the FRFs in capturing all modes with accurate damping ratios. The accuracy of each FRF set was checked using the Coherence diagram which is supposed to be close to one. Eventually, the dynamical parameters were obtained using the Multivariable MIF (MMIF) and the Stability diagram. Determinate modes were validated using the Modal Assurance Criterion (MAC) diagram based on the orthogonality of the mode shapes.

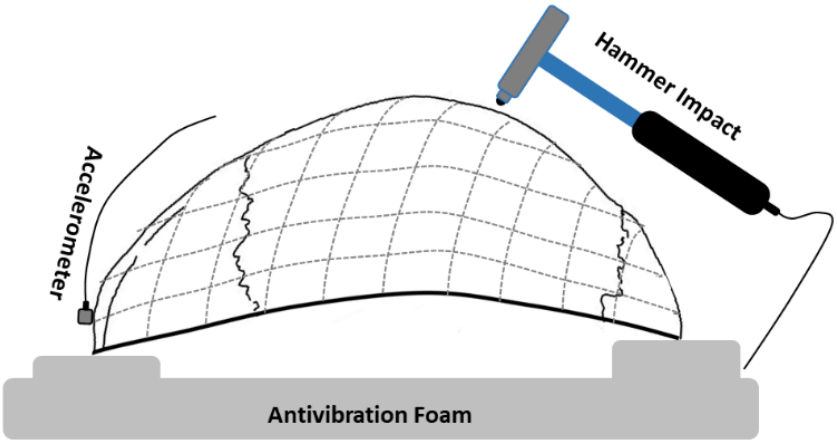

Figure 3-4. Schematic of experimental modal test.

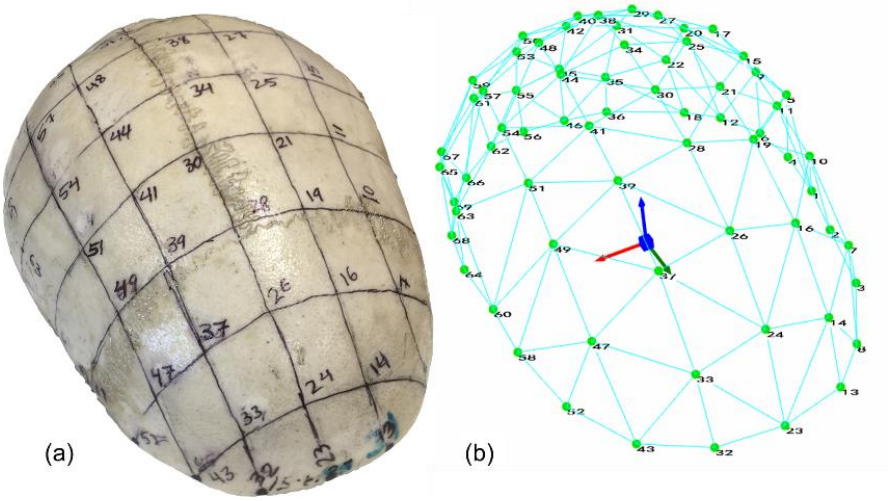

Figure 3-5. Skull grid nodes to be impacted (a), CAD model for the modal analysis post processing (b).

3.6. Results

In this section, the results of the linear and nonlinear elastic modeling of the skull for material constitutive modeling are presented. These results were utilized to compose the FE models for the eigen solutions. The experimental modal analysis results are presented for comparison with the numerical models' modes prior to the presentation of the FE results.

3.6.1. Skull Material Constitutive Modelling

The linear elastic and nonlinear hyperelastic models were fitted to the experimental uniaxial tensile tests using the general least square method with MATLAB (R2018a, Math Works, Inc., Natick, MA, USA). The constants of the linear model (Young's modulus) were obtained and tabulated in Table 3-1. Utilizing the obtained Young's modulus, the linear elastic models were depicted along with the tensile experimental results (Figure 3-6-(a)). In addition, the nonlinear hyperelastic model (Mooney-Rivlin with 2 parameter) was fitted to the uniaxial tensile test results by Wood (Wood, 1971), and the obtained stiffness constants are obtained and summarized in Table 3-2 in conjunction with the coefficient of determination (R^2) which presents accuracy of fitted results. Figure 3-6-(b) displays the relative agreement between the nonlinear skull bone response and obtained nonlinear model.

Table 3-1. The Young's modulus of skull fitted to the tensile test data at different strain rates along with the coefficient of determination R^2.

Strain Rate (sec^{-1})	Young's Modulus (Gpa)	R^2 (%)
0.005	10.10	98.44
0.1	12.52`	98.59
10	16.43	99.15
150	19.32	99.47

Table 3-2. The hyperelastic Mooney-Rivlin coefficient of skull tensile test fitted to the data at different strain rates along with the coefficient of determination R^2.

Strain Rate (sec^{-1})	C_{10} (Gpa)	C_{01} (Gpa)	R^2 (%)
0.005	-67.77	69.83	99.97
0.1	-91.79	94.33	99.98
10	-106.24	109.45	99.99
150	-100.67	104.29	99.97

Utilizing the obtained models at different strain rates, the FE skull models were analyzed in the eigenvalue problem. However, before proceeding with the numerical study, the experimental modal analysis is investigated.

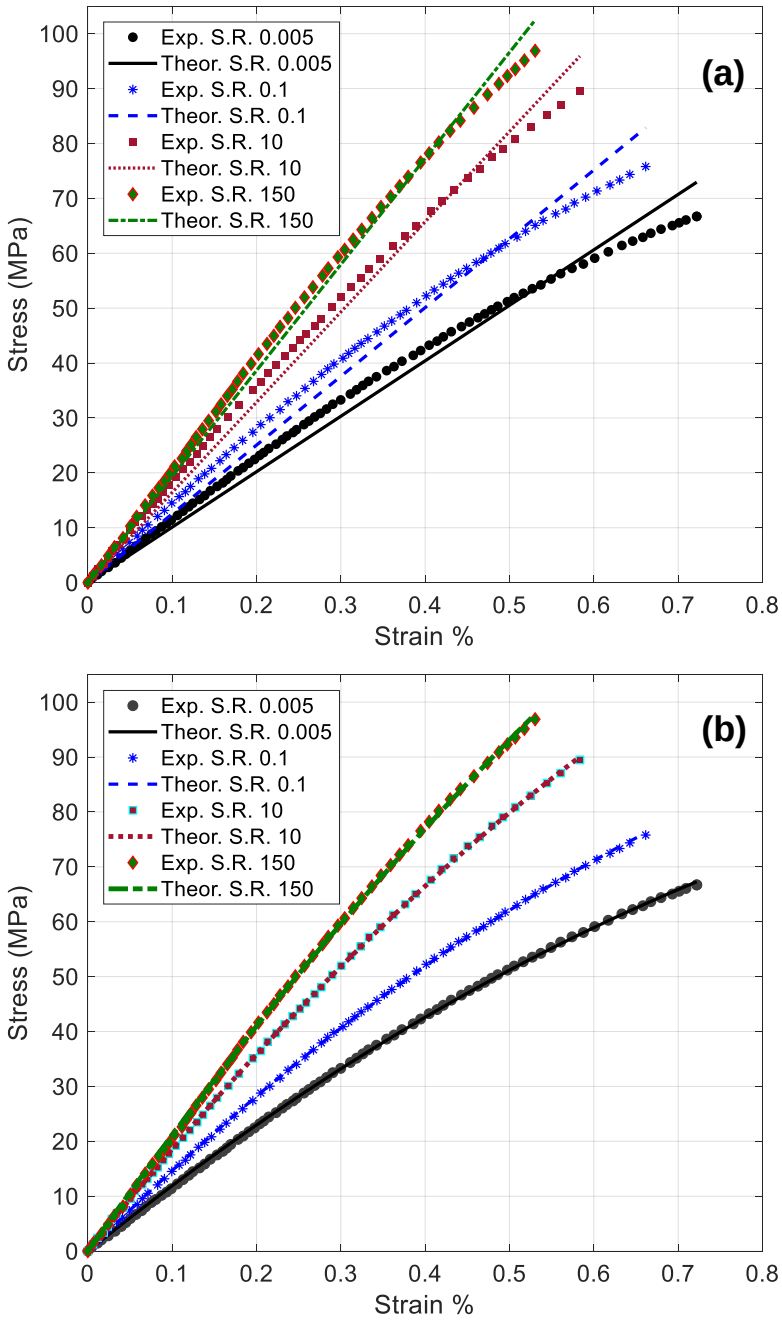

Figure 3-6. Fitted the linear elastic model to the results from uniaxial tensile tests (a), and the nonlinear hyperelastic Mooney-Rivlin model fitted well with the tensile results (b).

3.6.2. Experimental Modal Analysis

The 69 nodes were impacted and the FRFs sets were calculated. The overlaid FRFs sets are depicted in Figure 3-7-(a). The first two peaks demonstrate the first two modes observed in all

the FRF sets, however, modes three and four are not well separated due to the damping ratio and close spaced frequencies. To obtain modes three and four, the MMIF method was used to calculate the stability diagram with a maximum pole number of 25. The stability diagram of the MMIF is demonstrated in Figure 3-7-(b). Based on the green plus sign (stable poles) some modes were identified for validation with MAC. It should be told that the valley in MMIF can be the modal frequencies, therefore, the stable modes are picked from the digs and its regions.

The orthogonality of the nominated modes was checked based on the MAC diagram. The MAC bar chart was demonstrated in Figure 3-8. Although there is small interaction between mode one and mode four, these four modes are orthogonal. Therefore, these modal frequencies and the damping ratios were validated and tabulated in Table 3-3. After obtaining the modal frequencies along with their damping ratios, the modal shapes were elucidated using the complex least square curve fitting technique by the EDM-Modal. The mode shapes were elucidated for the CAD model of the experimental measurement using all obtained FRFs at each node. The mode shapes are plotted in Figure 3-9 and compared with FE results.

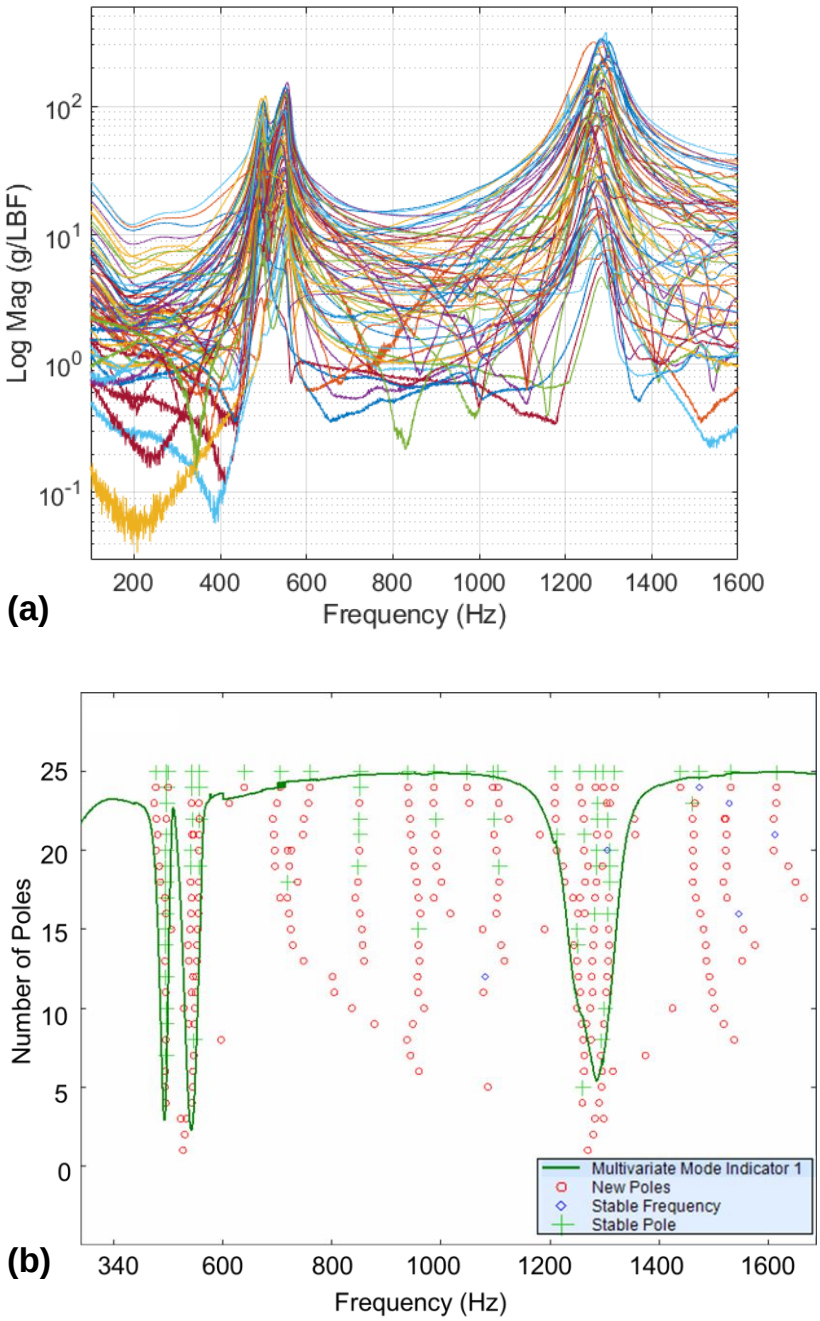

Figure 3-7. FRF set overlays of the 69 impacted grid points (a), and Stability diagram using the MMIF (b).

Table 3-3. Experimental modal frequencies along with the damping ratio

Modes Number	1	2	3	4
Modal Frequencies (Hz)	495.99	543.53	1249.71	1286.88
Damping Ratios (%)	1.84	3.11	2.73	1.63

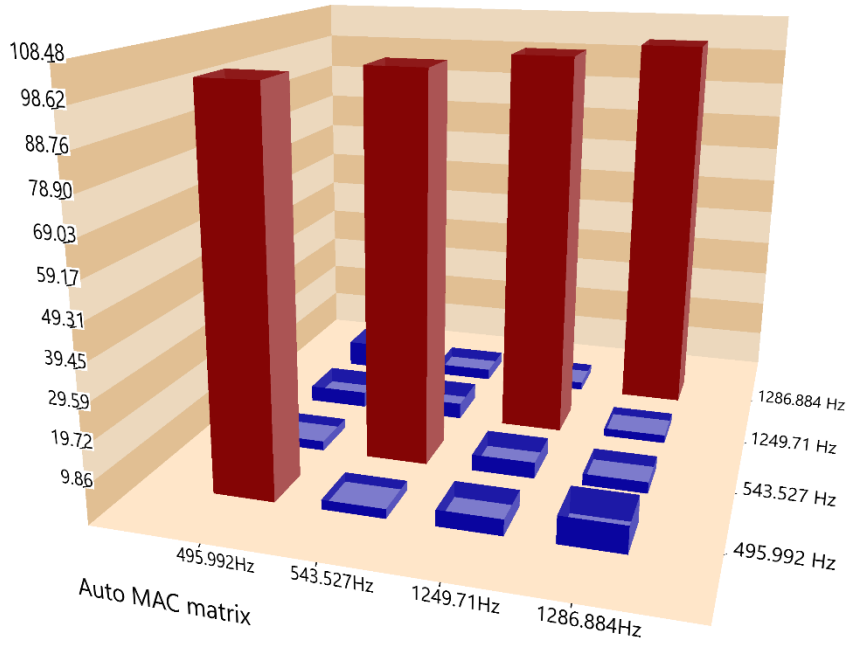

Figure 3-8. MAC diagram to compare the final nominated mode shapes.

3.6.3. FE Eigenvalue Solution

After obtaining the modal frequencies of the skull experimentally, we used the obtained material constitutive models at different strain rates in the LS-Dyna software, and the implicit eigenvalue problem was solved based on Lanczos method. The natural frequencies of the skull CAD model were extracted and summarized in Table 3-4 for the linear elastic model at different strain rates and tabulated in

Table 3-5 for the nonlinear hyperelastic model. The mass normalized mode shapes of these four modes are depicted in Figure 3-9 and compared with the experimental animated modes.

Table 3-4. Modal frequencies for the linear elastic model at different strain rates.

Strain Rate (sec^{-1})	Mode 1 (Hz)	Mode 2 (Hz)	Mode 3 (Hz)	Mode 4 (Hz)
0.005	446.19	489.14	1141.03	1167.19
0.1	496.78	544.60	1270.4	1299.52
10	569.08	623.87	1455.31	1488.67
150	617.109	675.52	1578.13	1614.3

Table 3-5. Modal frequencies for the hyperelastic model at different strain rates.

Strain Rate (sec^{-1})	Mode 1 (Hz)	Mode 2 (Hz)	Mode 3 (Hz)	Mode 4 (Hz)
0.005	443.32	485.99	1133.70	1152.67
0.1	492.26	539.65	1258.86	1287.71
10	553.40	606.67	1415.18	1447.62
150	587.67	644.25	1502.85	1537.30

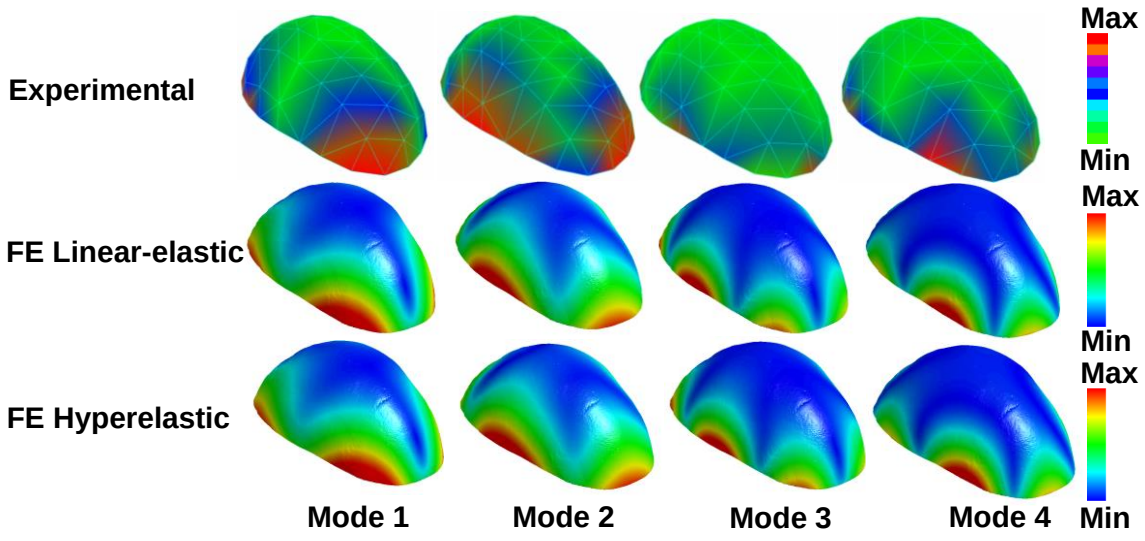

Figure 3-9. The plotted contour for the first four mass normalized mode shapes by FE method compared with experimental measured and animated mode shapes using EDM-Modal.

3.7. Discussion

The obtained modal frequencies, damping ratio, and modal shapes are the dynamical parameters of the skull model. In addition, a precise CAD model along with an appropriate material constitutive model are inferred to conduct the closest natural frequencies to the experimental obtained modal frequencies. The relative errors of the linear elastic and nonlinear hyperelastic models at different strain rates were calculated and plotted in Figure 3-10. The tensile test with the strain rates of 0.1 1/sec show lower relative errors for both linear and nonlinear constitutive models. Although the modal analysis includes the dynamical properties of the system, there are several limitations in the numerical modeling. On the other hand, it is a considerable approximation to use the low strain rate (quasi-static) mechanical tests to obtain the dynamical stiffness of the objects, which is why different responses based on the different strain rates are observed. Additionally, the linear elastic and hyperelastic material models have been widely utilized in the FE TBI analysis (Laksari et al., 2018; Tse et al., 2014) which can cause misleading results from the analysis.

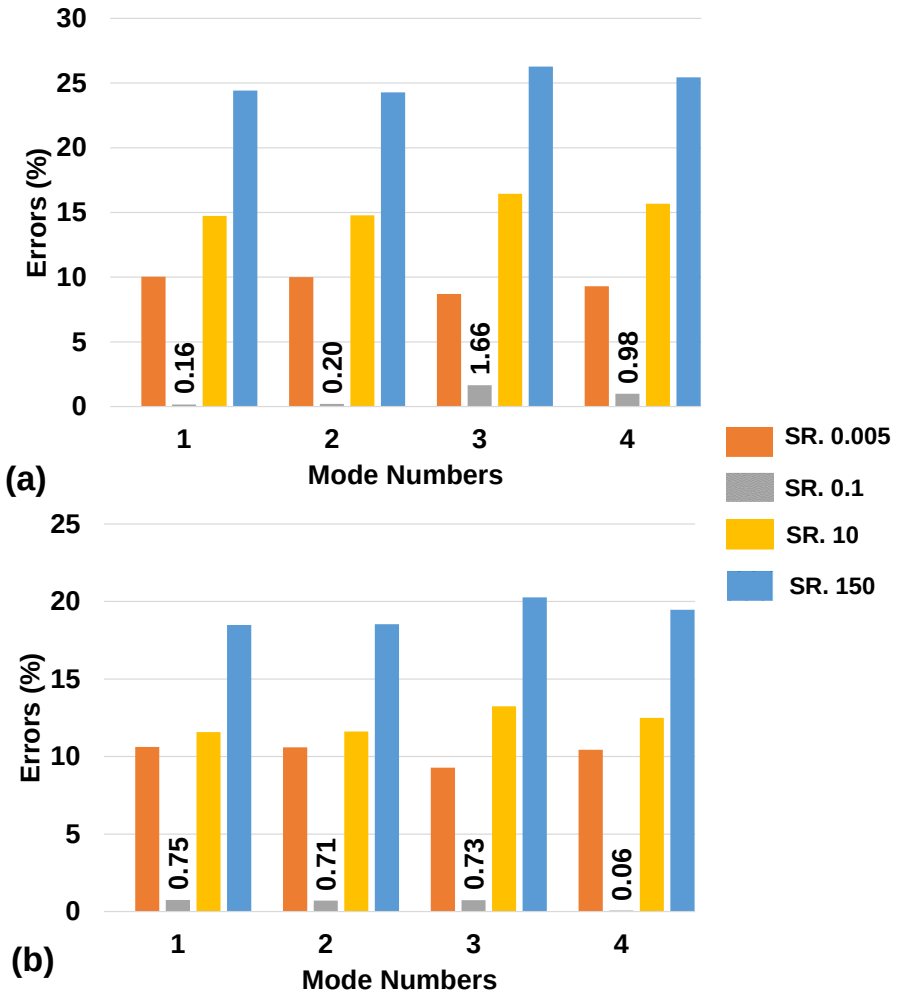

Figure 3-10. The relative errors with respect to the experimental modal analysis for the model with different rates. Linear elastic model (a) and nonlinear hyperelastic model. (b)

Mechanical properties of the skull such as Young's modulus are strain rate-dependent, except failure energy, based on the Wood investigation on dynamical properties of human skull (Wood, 1971). However, in Wood's theoretical modeling, the density of the models was not considered. Generally, the mass components of an object are one of the significant parameters of the dynamical properties of the equation of motion. Moreover, the nature of mechanical tests such as compression, tensile, shear, and torsion tests, do not include all mechanical system parameters of the specimen under loading. The mass and the mass proportion of the structural damping coefficient (as dynamical parameters), are not included in quasi-static tests. Furthermore, dynamic

tests such as modal analysis, which is based on the inherent mass, damping, and stiffness properties of a system, are independent from input and output of the system. Experimental modal analysis considers the dynamic parameters of mechanical systems, although the input and output data must be transfer to the frequency domain to obtain the mechanical system parameter. A linear mechanical system block diagram is depicted in Figure 3-11 (Schwarz & Richardson, 1999) which shows that in a frequency domain, the transfer function (H) can be easily determined by diving the output data from inputs. Although dynamic tests discern dynamic properties on the system, which could improve FE head models, they are difficult to utilize on multiphase systems.

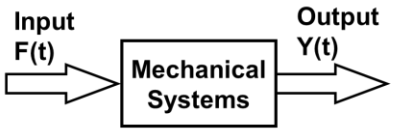

$$F(\omega) \times \left[H(\omega) \right] = Y(\omega)$$

Figure 3-11. Mechanical response block diagram in time and frequency domain (Schwarz & Richardson, 1999).

The linear elastic material model and the nonlinear hyperelastic material model with the strain rates of 0.1 1/sec resulted in lower relative errors. Although the nonlinear hyperelastic model confers a better fit compared to the linear elastic model in terms of stress-strain, the error of the linear elastic modal analysis is lower than nonlinear hyperelastic model (Figure 3-12). This likely is due to the complex geometry and the nonhomogeneous skull bones. Moreover, the linear elastic skull model has lower error for the first two modes of vibration. It should be noted that when the skull is considered as a continuous solid body deforming without failure, all dominant modes occur concurrently.

Although the nonlinear material model has higher relative error for the first two modes, the average errors for all modes is lower than observed in the linear elastic model. Therefore, considering the human skull FE model, the hyperelastic nonlinear model based on the Mooney-

Rivlin strain energy can be considered an appropriate material constitutive model along with high quality fitted stress-strain modeling.

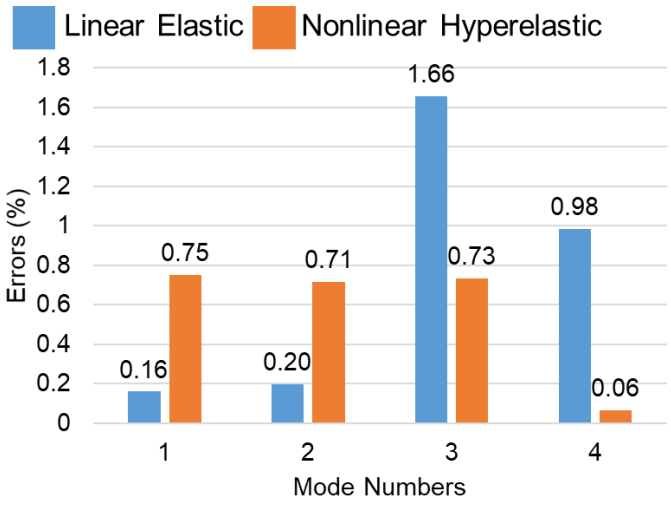

Figure 3-12. Comparison of the linear elastic and nonlinear hyperelastic models for the first four modes of vibration at the strain rate 0.1 (sec^{-1}).

3.8. Conclusion

This study examined the constitutive properties of the human skull by a computational-experimental modal analysis. A FE CAD model was constructed using the 3D scanner and the material constitutive properties were assumed as linear elastic and nonlinear hyperelastic (Mooney-Rivlin strain energy model). The material parameters were obtained at different strain rates. FE modal analysis was implemented to solve the eigenvalue problem based on all the material models with their parameters. In addition to computational modal analysis, experimental modal analysis was imposed on the skull and the FFT averaged FRF was extracted. The computed natural frequencies were compared with the experimental modal frequencies. Some other conclusions of this study are;

- The modal frequencies for the upper cranium skull bones (frontal, parietal, and occipital) were determined as 495.99 Hz, 543.53 Hz, 1249.71, and 1286.88 Hz. Although the FE modal analysis obtains the natural frequencies (eigenvalues of mass and stiffness matrices),

the experimental modal analysis confers modal frequencies include some structural hysteric damping.

- Based on coefficient of determination (R^2), the nonlinear hyperelastic material constitutive model can fit the skull bone tensile parameter better than the linear elastic model.
- Structural hysteric damping has an impact on the FE modal analysis solutions and cannot be obtained mathematically. Damping parameters can be obtained by using the experimental FRF Bode diagram. The structural damping obtained as 1.84%, 3.11%, 2.73%, and 1.63%. Therefore, the experimental modal analysis was needed before numerical dynamic simulation.

The strain rates of the mechanical parameter characterization tests (tensile, compression, shear, torsion, and bending) have significant impact on stiffness properties. In this study, the strain rate 0.1 1/sec was determined as the most appropriate tensile test strain rate for FE modeling on the human skull.

CHAPTER 4. AN EXPERIMENTAL-NUMERICAL MODAL ANALYSIS FOR THE STUDY OF SHELL-FLUID INTERACTIONS IN A CLAMPED HEMISPHERICAL SHELL[1]

4.1. Abstract

The vibration of an aluminum hemispherical shell filled with inviscid compressible fluid is considered. The modal frequencies, damping ratio and mode shapes of the shell are experimentally determined under both empty and fully-filled conditions. A numerical simulation based on the finite elements is conducted to be verified with the experimental modal analysis using a roving hammer-impact test. The finite element analysis of the fluid and the solid shell has been carried out implementing the fluid-solid interaction formulation analysis. The modal frequencies of modes are in good agreement with the numerical simulations. The modal frequencies decrement is observed in both numerical and experimental modal analysis as the impacts of the fluid-structure interaction on the hemisphere shell vibration. The simulated numerical mode shapes and the experimental ones are in close agreement and show that the fluid-solid interaction condition eventuates modal shape transformation.

4.2. Introduction

The interaction of free and forced vibration in fluid-filled spherical shells is an important aspect of numerous and varied engineering scenarios, from industrial applications such as liquid gas containers and explosive spherical chambers, to biomechanical computational simulations of

[1] The material in this chapter was co-authored by Ashkan Eslaminejad, Mariusz Ziejewski, and Ghodrat Karami. Content in this chapter was published in Journal of Applied Acoustics 152 (2019): 110-117. Ashkan Eslaminejad had primary responsibility for performing the manufacturing and performing the tests. Ashkan Eslaminejad also drafted and revised all version of this manuscript. Ghodrat Karami and Mariusz Ziejewski served as proofreader, and Ghodrat Karami supervised the project.

traumatic brain injury. Fluid interaction with a solid structure changes the dynamic characteristics of the structure, owing to the density and mass of the fluid, historic damping, and material stiffness characteristics. In computational modelling simulations of a multiphase structure, fluid-structure interaction (FSI) is a critically important consideration. In this study, spherical-shell vibration was used for computational modeling of a human head, which includes multiphase components such as solid skull in contact with cerebrospinal fluid (El Baroudi et al., 2012a; A. Engin & Y. K. Liu, 1970; Tse et al., 2014). Several simplifications were utilized in the computational modelling of the head. Specifically, the cerebrospinal fluid in a finite element (FE) head model is simulated as a linear elastic constitutive model, or membrane element formulation with fluid bulk properties (Eslaminejad, Hosseini Farid, Ziejewski, & Karami, 2018; Wu, Pan, Wimer, & Rosen, 2017). These simplifications are under question and needed to be validated and improved. From this model, experimental and numerical modal analysis is used to determine the structural dynamic characteristics, in terms of modal frequencies, damping ratios, and mode shapes of the system.

Numerous studies have used modal analysis to study fluid-filled cylindrical or spherical shell structures for different engineering applications conducted under different theoretical formulations (Baker, 1961; Lamb, 1882; Love, 1888; Naghdi & Kalnins, 1962). For example, Baker (1961) used the thin shell membrane theory to show the axisymmetric modes of vibration by ignoring the bending deformation effects. Kalnins (1964) included the bending effects in the spherical-shell model along with the axisymmetric modes. He found two branches of modes, termed flexural and membrane modes. To improve the shell formulation accuracy, JP Wilkinson (1965) considered shear deformation and rotary inertia effects in the spherical-shell equation of motion. He investigated the axisymmetric modes of vibration, and by including shear deformation, observed the tertiary branches of modes. These eigenvalue problems were solved based on the

axisymmetric simplifications; however, Silbiger (1962) showed that missing modes exist, termed non-axisymmetric modes of vibration. These modes are based on the azimuthal and meridional angles in the spherical coordinate system. In addition, it was argued although the sphere is symmetric, it can be vibrated with a similar frequency and specific set of axes. Duffey and Romero (2003) studied vibration of a spherical shell using the FE method to compare the analytical and numerical results in terms of axisymmetric and non-axisymmetric modes of vibration. They showed that FE modal analysis can elucidate all mode shapes including the real or even complex eigenvectors, as Silbiger (1962) mentioned. Although the analytical models of the sphere and hemisphere shells were developed based on different shell theories and thickness variation conditions, and the eigenvalue problems were solved using the axisymmetric and non-axisymmetric assumptions (Gautham & Ganesan, 1992; Hirai & Kuroda, 1989; Lee, 2009), there is not experimental validation included in any of these investigations.

Several theoretical models were developed using simplified thin shell theories to investigate the vibrational aspects of fluid filled spherical-shell fluid interactions (A. Engin & Y. K. Liu, 1970; Engin, 1969; Junger, 1952). Advani and Lee (1970) used the thick shell theory to obtain axisymmetric vibrational response of a fully filled sphere with inviscid and compressible fluid. However, based on the aforementioned Silbiger (1962) study, non-axisymmetric modes can be lost using the axisymmetric assumption. Chen and Ding (1999) investigated the non-axisymmetric free vibration of anisotropic linear elastic shell in contact with compressible fluid, which was modeled on the fluid velocity potential equation of motion. These studies investigated modal frequencies; however, other dynamic characteristics such as damping ratio and modal shapes, were not included. El Baroudi et al. (2012a) modeled a hemisphere shell in contact with fluid with using the analytical method and FE simulation. They used the Helmholtz decomposition

method to develop the equation of motion of the solid shell as deformation tensor. In addition, the acoustic fluid pressure equation of motion was considered to mathematically model the fluid. The analytical and numerical results were compared in terms of eigenfrequencies, and the modal shapes were depicted based the eigenvector solution using commercial FE software. However, no experimental verification was conducted.

Within the past two decades, experimental modal analysis techniques have been dramatically improved, with accurate modal postprocessing curve-fitting techniques (modal extraction) (Ewins, 2000). In this study, we investigate FSI on hemispherical shell vibration. Specifically, the vibration a clamped aluminum shell is studied under two cases; the empty shell, and the fluid-filled shell. Additionally, numerical FE models were developed using shell theory and the fluid acoustic formula. ANSYS Parametric Design Language (APDL) code was employed to model the aluminum shell under two-way coupling with inviscid compressible fluid. To validate the numerical model, experimental studies were conducted using the roving hammer-impact modal analysis test. The details of the theoretical formulation and experimental setup follow.

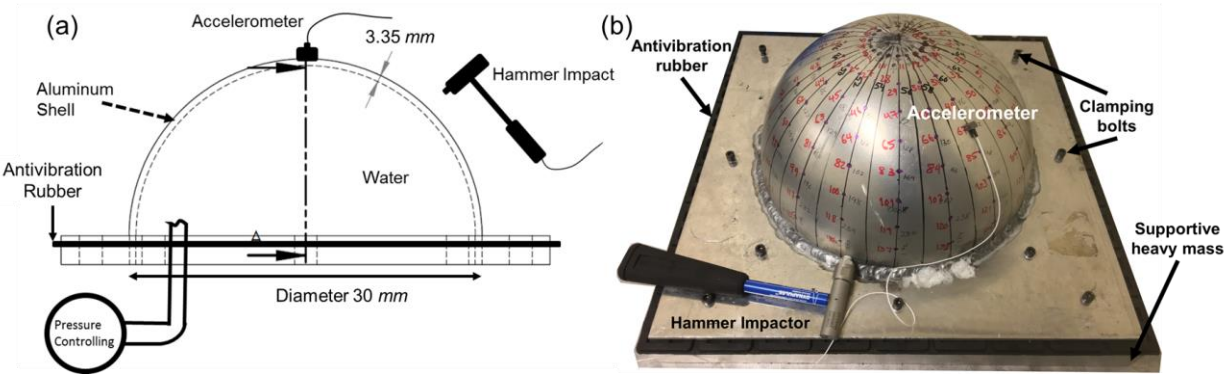

Figure 4-1. (a) schematic of the clamped aluminum hemisphere, (b) experimental setup of meshed hemisphere to be tested by roving hammer-impact modal analysis.

4.3. Experimental Modal Analysis

In this section, the experimental considerations of the modal analysis procedure are described. The clamped shell is three mm thick and has a 15.15 cm outer radius. The schematic of

the hemisphere is depicted in Figure 4-1-(a). The hemisphere was made of aluminum (Density 2700 kg/m^3, Young's modulus 6.9×10^{10} Pa, and Poisson's ratio 0.33) and was welded to six mm thick aluminum sheet. The base aluminum sheet was clamped to heavy mass support which was in turn clamped to an antivibration table. To remove the noise from the supportive mass and the table, an antivibration rubber sheet was placed between the hemisphere flange and the supportive heavy mass, as illustrated in Figure 4-1-(b). A square hole (ten cm sides) was made on the mass support and table to route pipes for the fluid pressure control inside the hemisphere.

Dynamic characteristics were extracted using the frequency response function (FRF). Experimental FRF data were obtained using Crystal Instrument Spider 80X data acquisition (DAQ) hardware. This DAQ is a 24-bit device with a maximum sampling frequency of 102.4 kHz. A Dytran hammer and the miniature accelerometer (Frequency Range up to 6000 Hz) were used for the fixed embedded accelerometer and roving hammer-impact method. The hemisphere was gridded, and 145 nodes were labeled for impact, as illustrated in Figure 4-1-(b). The location of the accelerometer was chosen based on the FE pre-study simulation such that the accelerometer is placed where modes can be detected with the highest possible deformation (Avaitable, 2018). each node was impacted five times, and resulting signals were averaged. The linear peak hold average of the fast Fourier transform (FFT) signals were calculated to increase the accuracy of FRF H1.

Modal frequencies, damping ratios, and mode shapes can be extracted experimentally using the measured FRF sets. The stability diagrams were calculated using the Multivariable/Complex mode indicator functions (MIF) to estimate the modes of vibration. Modal analysis postprocessing was conducted in Engineering Data Management (EDM) 7.1 software, developed by Crystal Instrument Inc. (Crystal-Instrument-Corporation, 2017). The software records the direction of impacted and captured signals. The hemisphere geometry was constructed in the EDM

environment (Figure 4-2-(a)). The selected possible modes were examined using the Auto Modal Assurance Criterion (MAC) method based on the modal orthogonality checking.

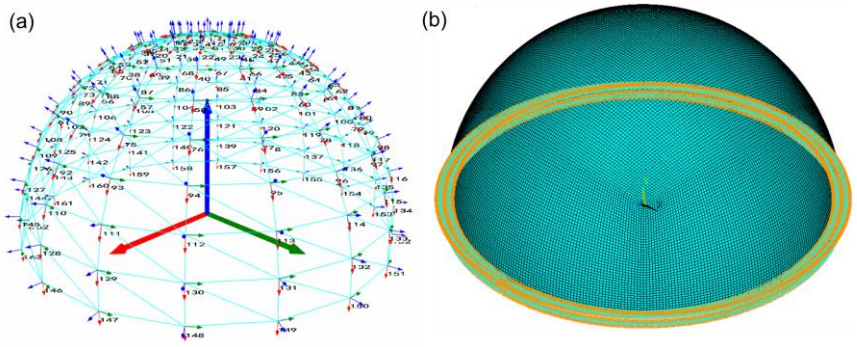

Figure 4-2. (a) The meshed geometry for the EDM experimental modal analysis. Each impact node is indicated in radial coordinate, (b) the meshed FE model in ANSYS with the fixed edge boundary conditions

4.4. Finite Element Formulation

The FE technique was used to formulate the fluid domain as acoustics fluid and quadratic shell elements as the aluminum hemispherical shell. The models were developed utilizing the ANSYS APDL codes. In this FE simulation, the aluminum hemisphere was considered as shell triangle element with six nodes, which each node has six degrees of freedom (DOF). The shell was clamped on the edges in all DOF. The FE model is illustrated in Figure 4-2-(b). In addition to solid shell modelling, the governing equation of fluid motion was derived based on the continuity equation of the fluid, equation(4.1).

$$\frac{\partial \rho}{\partial t} + \vec{V} \cdot \nabla \rho + \rho \nabla \cdot \vec{V} = 0 \tag{4.1}$$

where ρ is the fluid density and vector $\vec{v}$ is the velocity vector. Additionally, the fluid momentum equation (Navier-Stokes) was used to derive the fluid acoustics pressure equation of motion equation (4.2),

$$\rho \frac{\partial \vec{V}}{\partial t} + \rho\left(\vec{V} \cdot \nabla \vec{V}\right) - \frac{1}{3}\mu \nabla\left(\nabla . \vec{V}\right) = \rho \vec{g} - \nabla \vec{\mathrm{P}} + \mu \nabla^2 \vec{V} \tag{4.2}$$

where $\vec{\mathrm{P}}$, μ, $\vec{g}$ are the fluid acoustics pressure, the dynamic viscosity, and the gravity acceleration vector respectively. By taking the time derivative of the continuity and the spatial derivative of the Navier–Stokes equation, the acoustics pressure wave equation can be obtained as:

$$\nabla.\left(\frac{1}{\rho}\nabla\vec{\mathrm{P}}\right)-\frac{1}{\rho c^2}\frac{\partial^2\vec{\mathrm{P}}}{\partial t^2}+\nabla.\left(\frac{4\mu}{3\rho}\nabla\left(\frac{1}{\rho c^2}\frac{\partial\vec{\mathrm{P}}}{\partial t}\right)\right)=-\frac{\partial}{\partial t}\left(\frac{Q}{\rho}\right)+\nabla.\left(\frac{4\mu}{3\rho}\nabla\left(\frac{Q}{\rho}\right)\right) \tag{4.3}$$

where the c is the speed of sound in fluid media, and Q is mass source in continuity equation (ANSYS, 2017). The speed of sound constant (c) can be obtained by considering the fluid properties

$$c=\sqrt{\frac{K_s}{\rho}} \tag{4.4}$$

where the Ks is fluid the isentropic bulk modulus (Morse, 1936). The boundary condition for the fluid was considered as wall for the bottom plate and two ways FSI coupling for the interaction surface with solid shell.

Mass, damping and stiffness matrices were established and coupled with the acoustics fluid domain using the FE discretization method. The coupling FSI was defined as the equal normal direction displacement in fluid and solid at the interaction surfaces nods (ANSYS, 2017). By rewriting the fluid acoustics, solid shell equations of motion in the discrete matrix forms, and by employing the two ways FSI coupling condition, the governing equation of motion of this system was given as equation(4.5).

$$\begin{bmatrix}[\mathrm{M}_s] & 0\\ \rho_0[R]^T & [\mathrm{M}_F]\end{bmatrix}\begin{Bmatrix}\ddot{\vec{u}}\\ \ddot{\vec{\mathrm{P}}}\end{Bmatrix}+\begin{bmatrix}[C_s] & 0\\ 0 & [C_F]\end{bmatrix}\begin{Bmatrix}\dot{\vec{u}}\\ \dot{\vec{\mathrm{P}}}\end{Bmatrix}+\begin{bmatrix}[\mathrm{K}_s] & -[R]\\ 0 & [\mathrm{K}_F]\end{bmatrix}\begin{Bmatrix}\vec{u}\\ \vec{\mathrm{P}}\end{Bmatrix}=\begin{Bmatrix}F_s\\ F_f\end{Bmatrix} \tag{4.5}$$

where, the u, P, M, C, K, F, R is the displacement and rotation DOF vector, fluid acoustics pressure DOF, mass, damping, stiffness, force, and reaction impedance, respectively. It should be noted that the subscript S means solid properties and F means fluid properties.

For implementing FE damped modal analysis, a complex damping matrix was composed as equation(4.6),

$$\left[C^*\right] = j\left(\omega\left(\alpha\left[\mathrm{M}\right] + \beta\left[\mathrm{K}\right]\right) + g\left[\mathrm{K}\right]\right) \tag{4.6}$$

where j is the imaginary number. The α, β, g, and ω are Rayleigh mass coefficient, Rayleigh stiffness coefficient, constant structural damping coefficient (which was considered zero at this study) and the circular frequency, respectively.

The QR-factorization method is used to solve the eigenvalue problem in equation(4.5). This procedure extracts the complex eigenvalue along with the corresponding eigenvectors of the system. The real number of this eigenvalue shows the stability value and the imaginary number is the damped modal frequency. To use the QR damping method, the stiffness matrix should be divided into symmetric and unsymmetrical matrices. First, using the symmetrical method, and removing the damping and external forces, the eigenvalues and eigenvectors are obtained to transform the eigenvalue problem into the modal subspace, equation(4.7), in which phi is the mass normalized eigenvector and X is the modal coordinates.

$$\{u\} = \left[\phi\right]\{X\} \tag{4.7}$$

Now, we can rewrite the governing equation (4.5) in the form of equation (4.8) in which the Λ is the diagonal eigenfrequencies. It should be noted that the mass, stiffness, and damping matrices in equation (4.5) written in general simple form normalized to mass.

$$\left[I\right]\left\{\ddot{X}\right\} + \left[\phi\right]^T\left[C_{total}\right]\left[\phi\right]\left\{\dot{X}\right\} + \left(\left[\Lambda^2\right] + \left[\phi\right]^T\left[K_{Unsymetry}\right]\left[\phi\right]\right)\{X\} = \{0\} \tag{4.8}$$

By defining the state variable vector $\boldsymbol{w}$, equation(4.9), the equation(4.8), can be rewritten in the form of equation(4.10).

$$\{w\}^T = \left\{\{X\}^T, \left\{\dot{X}\right\}^T\right\}^T \tag{4.9}$$

$$[I]\{\dot{w}\} = [\mathrm{A}]\{w\} \tag{4.10}$$

where the **A** is given by

$$[\mathrm{A}] = \begin{bmatrix} [0] & [I] \\ -[\Lambda^2] - [\phi]^T [K_{Unsymetry}][\phi] & -[\phi]^T [C_{Total}][\phi] \end{bmatrix} \tag{4.11}$$

Using the QR factorization method on the general eigenvalue problem, equation (4.10), the complex eigenvalues can be obtained (JH Wilkinson & Reinsch, 1971). Hereby, the corresponding complex eigenvectors are given by inverse method. These computations were carried out using the ANSYS APDL code.

4.5. Results and Discussions

The experimental results of the aluminum hemisphere with and without FSI condition are provided for comparison with the computational simulation under identical boundary conditions. Based on the FE modal pre-analysis, it was expected to observe the first five modes of vibration in frequency range from 3000 to 6000, without considering the FSI condition. The first six modes selected were based on the accelerometer frequency range (6000 Hz). In addition, for the case with the FSI condition, the first six modes appeared in the frequency range from 500 to 4000 Hz. The experimental and numerical results are presented in terms of the modal frequencies, damping ratios, and modal shapes.

4.5.1. Experimental Modal Analysis

The accelerance FRF sets were calculated using all the peak-hold averaged FFT data from the impacted force and the acceleration responses signals. The overlaid FRF plot are illustrated in Figure 4-3 for both cases under study. The peaks of the FRF generally show the modal frequencies for systems with low damping and large spaced modal frequency (Avaitable, 2018). The FRF peaks for the case with FSI are shifted to the lower frequency range. As shown in Figure 4-3-(a),

the first dominant peaks appeared around 4000 Hz, which is the first mode of vibration. However, the first FRFs peak in the second case (which involved FSI condition), Figure 4-3-(b), emerged around 1600 Hz.

Analysis of symmetrical systems with repeated poles often confer peaks associated with closely spaced modes with high damping ration. These modes merge into each other and cannot be recognized as peaks of FRF. Therefore, additional other analysis techniques are needed to disambiguate the data. Mode indicator techniques can be utilized to extract modal vibration data from the FRF sets. Mode indicator functions (MIF) such as Complex (CMIF) and Multivariable (MMIF) methods within EDM-Modal software were utilized to distinguish closely spaced or repeated modal frequencies.

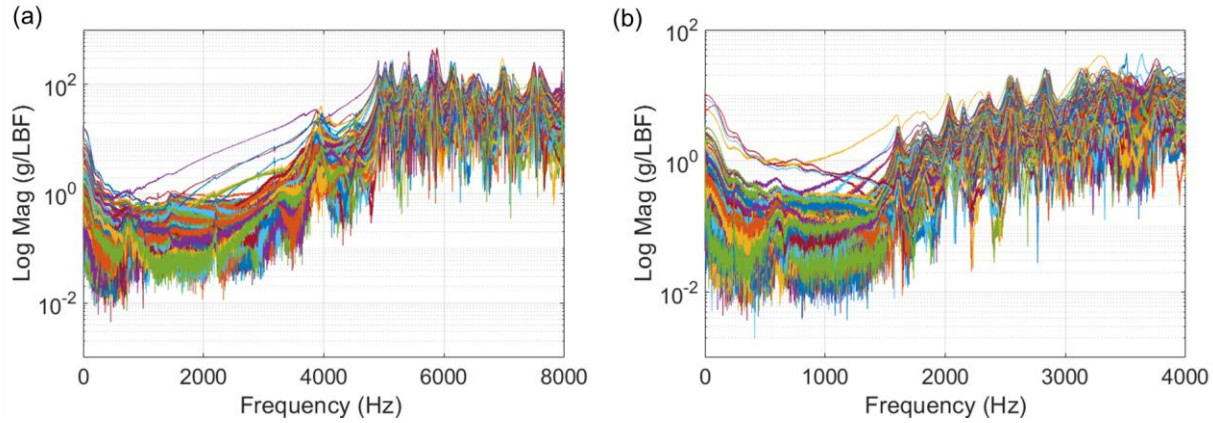

Figure 4-3. FRF overlaid plot, (a) for the case without FSI, (b) the case with FSI condition.

4.5.1 1. The empty hemispherical shell

The first lower modes appeared as peaks in the CMIF plot depicted in Figure 4-4-(a). The frequency range between 3670 Hz to 5275 Hz was selected to calculate the Stability CMIF curve fitting plot. The stability diagram was calculated and plotted over the stated frequency range to identify stable poles in frequency and damping ratios. The Least Square Complex Exponential curve fitting technique was used to identify stability poles. The stability diagram for the selected rang is depicted in Figure 4-4-(b). Based on the most stable poles, modes 4911 Hz, 4936 Hz and

5115 Hz were evaluated as possible modes of vibration. However, the first peak in FRF sets which occur around 4000 Hz, appeared as an overdamped mode, and cannot be selected as possible stable pole. In addition to the modal frequencies, the damping ratio of each mode was calculated based on single degree of freedom Q factor method (Crystal-Instrument-Corporation, 2017). Eventually, the extracted modal parameters need to be checked by auto MAC matric (Allemang, 2003). The MAC matrix was calculated and tabulated in Table 4-1.

Checking the MAC matrix table shows that the selected modes one (4911 Hz) and two (4936 Hz) had some contribution in each other which cannot be avoided in the experimental measurements. Furthermore, mode one also affects Mode three (5115 Hz). These modal contributions decrease the vibration measurement accuracy. Increasing the number of measurements at regions with high mode shapes deformation could improve the experimental measurement quality. In our case, although the number of measurements was increased from 32 to 145 nodes of impacts the modes did not become distinguishable. This can be justified because of the high damped modes and close space peaks.

Conclusively, the first three modes of vibration of this hemisphere can be reported as 4911 Hz, 4936 Hz and 5115 Hz. In addition, the averaged damping ratios for these three modes are 0.101 %, 0.848 %, and 0.373 %, respectively. The animations of experimental mode shapes are depicted and reported along with the numerical solution results in following, Figure 4-6-(a-c).

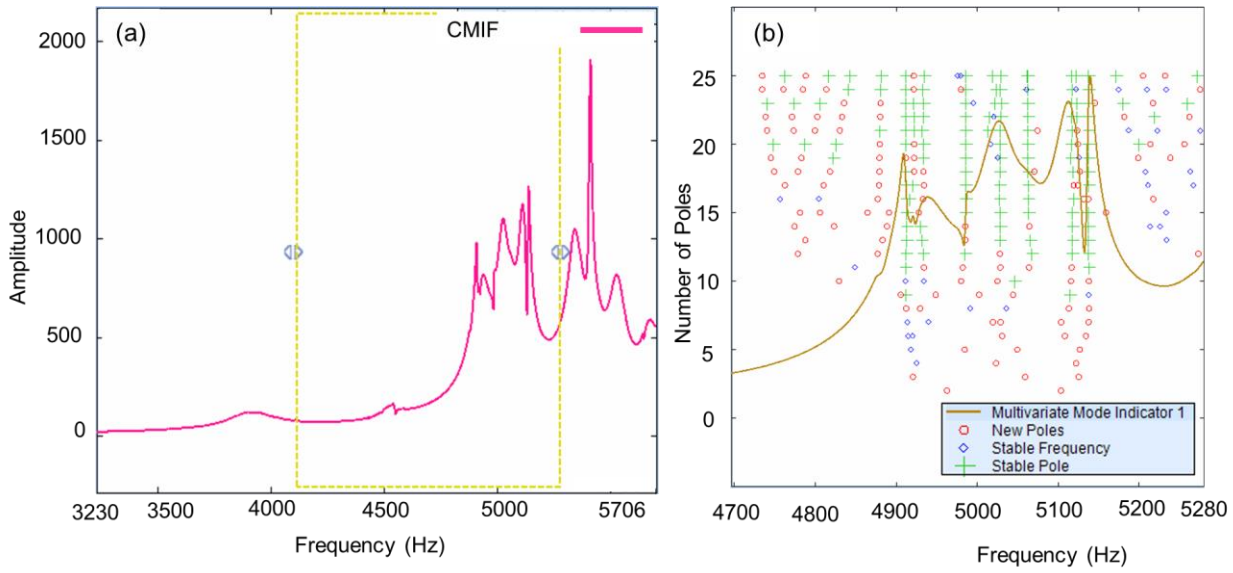

Figure 4-4. (a) Complex Modal Indicator Function of the FRF data to select the interested range, (b) Stability diagram with 25 poles curve fitting.

Table 4-1. Auto MAC matrix of the extracted modal frequecnies for the empty aluminum shell

Frequency (Hz)	Mode 1, 4911.178 Hz	Mode 2, 4936.428 Hz	Mode 3, 5115.041 Hz
Mode 1, 4911.178	100	33.537	18.213
Mode 2, 4936.428	33.537	100	4.53
Mode 3, 5115.041	18.213	4.53	100

4.5.1 2. The fully-filled hemispherical shell with FSI condition

The same procedure carried out on the second case, in which the hemisphere was fully fluid-filled. Using the FRFs overlaid sets, Figure 4-3-(b), the MMIF and stability diagram were calculated and plotted in Figure 4-5. The digs in MMIF are identified as the possible modes and can be selected for the stability analysis. The selected frequency range was from 1480 to 2100 Hz, where most of the lower modes were observed. The stability diagram of the selected frequency range of MMIF data was plotted, and the stable poles were identified for verification using the modal validation tools, Figure 4-5-(b). After checking the modes of vibration validation, mode

orthogonality was investigated using the auto MAC matrix. The auto MAC matrix is summarized in Table 4-2. As shown in the MAC matrix, the mode one contributes nominally to the second mode with low value. The frequency modes of vibration concluded as 1651.39 Hz, 1865.51 Hz, and 2067.04 Hz and the damping ratios of these mode obtained of 1.135 %, 1.591 %, and 0.746 %, respectively. Mode shapes animation corresponding to these frequency modes are depicted in Figure 4-7-(a-c).

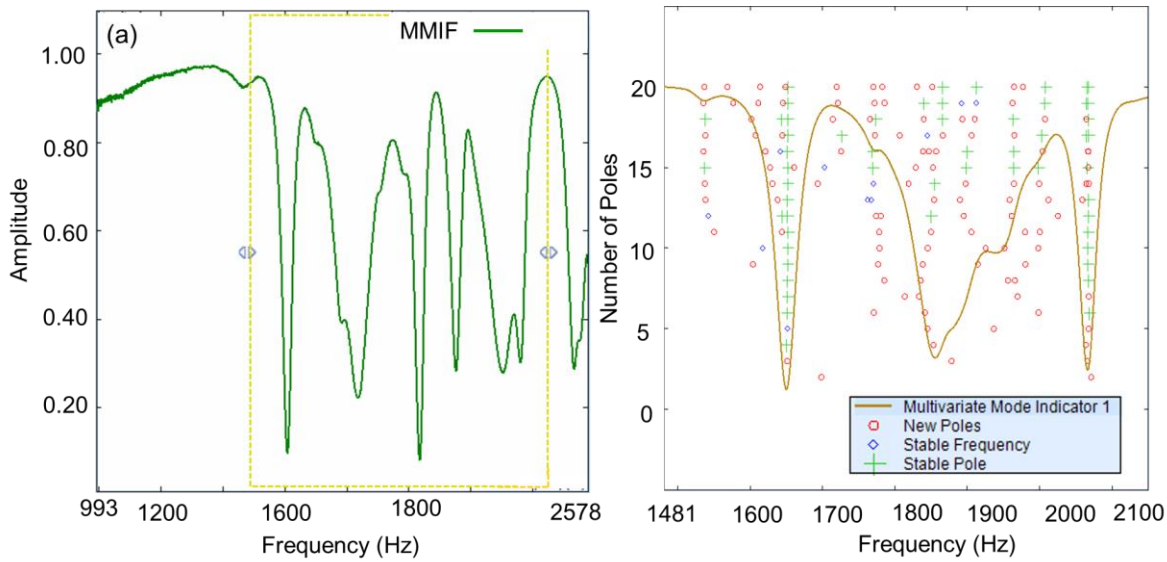

Figure 4-5. (a) Multivariable Modal Indicator Function of the FRFs data to select the interested range, (b) Stability diagram with 20 poles curve fitting.

Table 4-2. Auto MAC Matrix of the extracted modal frequecnies for the fully-filled aluminum shell

Frequency (Hz)	Mode 1, 1651.393 Hz	Mode 2, 1865.506 Hz	Mode 3, 2067.043 Hz
Mode 1, 1651.393	100	1.299	0.039
Mode 2, 1865.506	1.299	100	0.896
Mode 3, 2067.043	0.039	0.896	100

4.5.2. Finite Element Simulation

Rayleigh proportional damping of mass and stiffness factors (α and β) were obtained using the damping ratios (ξ) from the experimental measurements. For the frequency range from the ω_1 to ω_2, the α and β are given by equations(4.12).

$$\alpha = 2\xi \frac{\omega_1 \omega_2}{\omega_1 + \omega_2}, \ \beta = \frac{2\xi}{\omega_1 + \omega_2} \tag{4.12}$$

Using the QR-Damped eigenvalue solving method, the complex eigenvalues of the damped and undamped clamped aluminum hemisphere were calculated and summarized in Table 4-3. The real number of the complex eigenvalue shows exponential amplitude damping that is negative value. In addition, the imaginary part of the complex frequency is the vibration wave frequency. The undamped FE mode shapes are depicted in Figure 4-6-(d-h).

Table 4-3. Experimental modal frequencies vs. FE damped, and undamped eigenfrequencies for the case without FSI condition

Mode Number	**Experimental (Hz)**	**Damping Ratio (%)**	**FE Results**		**Mode Shapes**
			Damped (Hz)	Undamped (Hz)	
1	N.A.	N.A.	-43.52+j3122	3122.7	N.A.
2	N.A.	N.A.	-74.74+j4150.1	4150.8	N.A.
3	4911	0.101	-99.94+j4821.3	4822.4	Matched
4	4936	0.848	100.27+j4829.5	4830.5	Matched
5	5115	0.373	111.30+j5095.0	5096.2	Matched

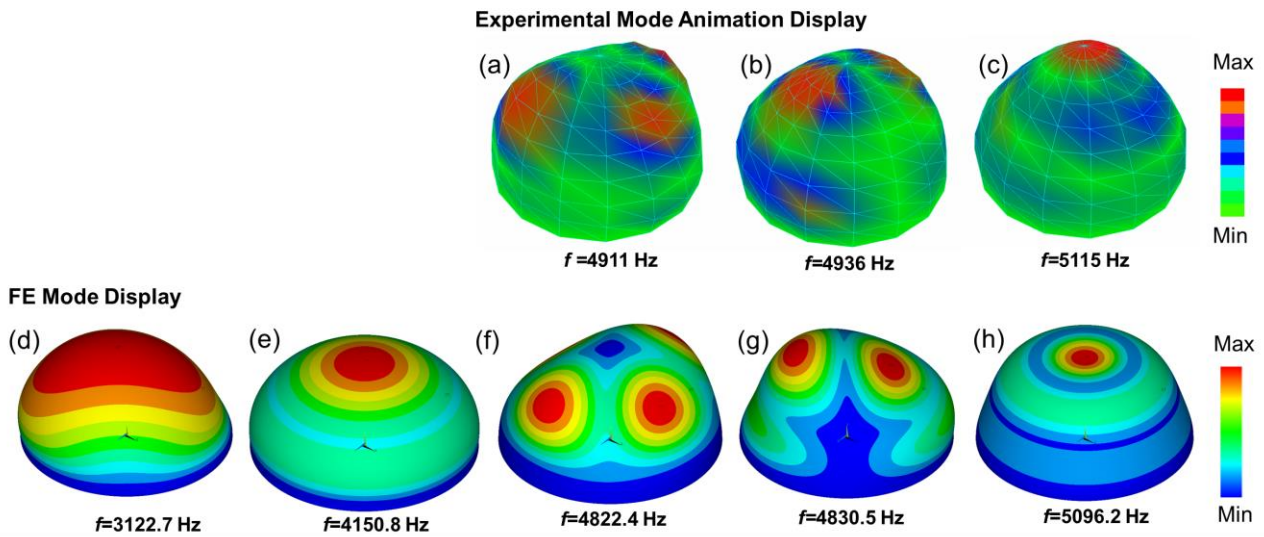

Figure 4-6. (a-c) Vibration mode shapes of the experimental modal analysis, (d-h) the undamped FE simulation for the shell without the FSI condition.

For the case of the fully fluid-filled aluminum hemisphere, the eigenfrequencies of the equation (4.5) were obtained using the QR-Damped eigenvalue problem solver. The modal frequencies of the damped and undamped case are summarized in Table 4-4. In addition to eigenfrequencies, the corresponding eigenvectors are plotted in Figure 4-7-(d-h). The first two modes of vibration were not activated in experimental modal analysis, although 145 nodes were impacted.

Solving the case with FSI condition which includes the unsymmetrical mass, and stiffness matrices, give two solution systems. First the deformation eigenvectors which showed the pattern of the hemispherical shell vibration. Second, the fluid acoustic pressure distribution pattern as the eigenvector of the fluid domain. These mode shapes are demonstrated for the first five modes of vibration in Figure 4-8.

Table 4-4. Experimental modal frequencies vs. FE damped, and undamped eigenfrequencies for the case with FSI condition.

Mode Number	Experimental (Hz)	Damping Ratio (%)	FE Results		Mode Shapes
			Damped (Hz)	Undamped (Hz)	
1	N.A.	N.A.	-4.52+j1051.9	1051.9	N.A.
2	N.A.	N.A.	-8.97+j1479.9	1479.9	N.A.
3	1651.39	1.135	-12.26+j1755.5	1755.6	Matched
4	1865.51	1.591	-15.23+j1932.7	1932.7	Matched
5	2067.04	0.746	-18.49+j2132.2	2132.2	Matched

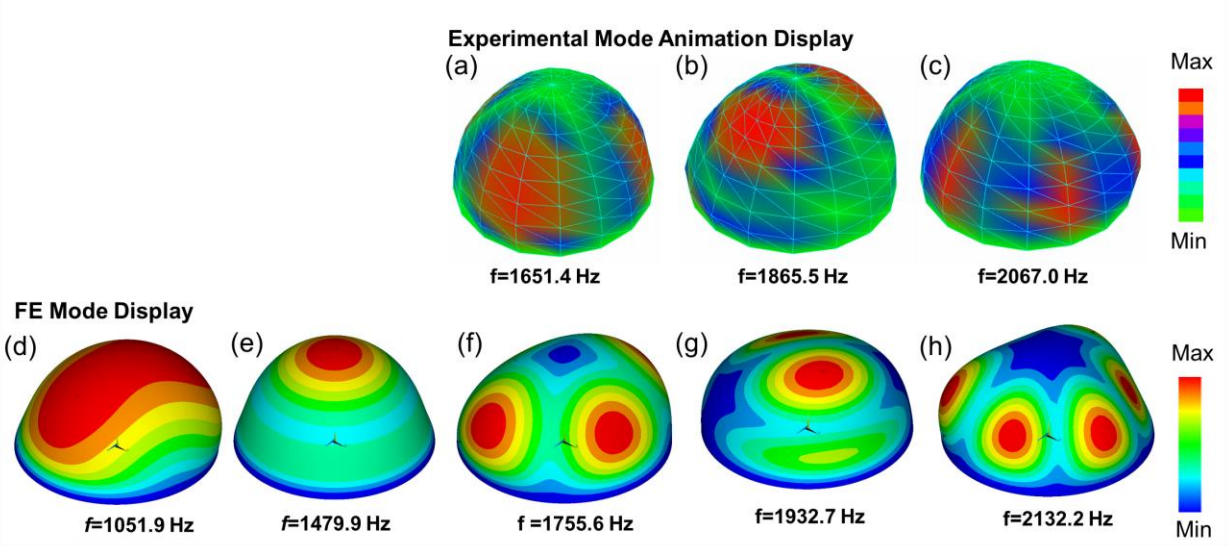

Figure 4-7. (a-c) Vibration mode shapes of the experimental modal analysis, (d-h) the undamped FE simulation for the shell with the FSI condition.

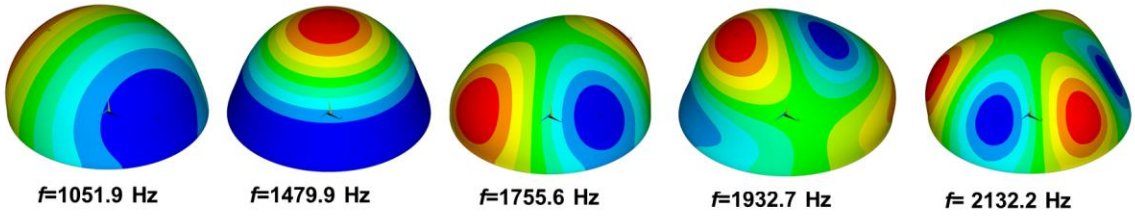

Figure 4-8. The first five modes of vibration of the fluid media in the case with FSI condition.

The vibration modes of the clamped hemisphere were conducted as close spaced twin modes for mode one, three and five. However, the modes number three and five, in the case without FSI and the mode three of the fully fluid-filled shell are single mode shape. The comparison of the FE results and experimental measured modes showed that the modes one and two could not be activated practically in both cases under study, because of the high damping ratios and low spaced frequency peaks intrinsic to the system. This phenomenon observed in the CMIF and MMIF plots above. Furthermore, modes three, four and five are the dominant lower modes of vibration.

The experimental mode shapes are depicted in Figure 4-6 and Figure 4-7. In the both cases under study, experimental modes one and two were matched with the FE modes three and four. However, for the case without FSI condition, the experimental mode number three was replaced by the bending wave vibration mode as it is demonstrated in the FSI conditioned case. These modes are demonstrated in Figure 4-6-(c), (h) and Figure 4-7 -(c), (h). Although modes one and two were not observed in the experimental study to verify the FE results, modes three, four and five of FE solution were verified with good agreement with experimental measurements.

While this FSI dynamic study verified the accurate numerical modeling, there are limitations that might be considered in the experimental procedure and numerical modeling. For instance, the shaker test might be utilized in addition to the roving hammer-impact test, although the first two overdamped modes still be difficult to elucidate. Additionally, damping numerical modeling can be improve by considering the FSI interaction impedance damping in FE numerical which make the system of the equation nonlinear and unsymmetrical semipositive definite.

4.6. Conclusion

In this study, experimental vibration measurements were carried out on an aluminum hemisphere shell. Two case scenarios were considered to show the effects of fluid interacting on

the structural dynamic characteristics. In addition to the experimental modal analysis, the numerical formulation was developed using FE methods. Dynamic characteristic results were obtained in terms of modal frequencies, damping ratios, and vibration mode shapes.

The technical specifications of the experimental equipment limited the ability to extract modes higher than 6000 Hz at the 95 % confidence threshold. However, three vibrational modes were successfully extracted for empty hemisphere. The experimental results from modes up to number 5 showed good agreement with the numerical modeling. Comparing the experimental modes with the numerical simulation confirms high FE modeling accuracy. The experimentally mode shapes were conferred the mode shapes depicted by numerical eigenvectors.

Under FSI condition, the lower three modes were obtained and were compared with FE modeling results. Although some modes of the structure are observed as overdamped may not be elucidated in the experimentally measured FRFs, the extracted modal frequencies are in good agreement with numerical simulation. It was observed in all modes that FSI could decrees the modal frequencies along with modal shape transformation. The first three experimental mode shapes were found in good agreement with numerically undamped frequency mode shapes. It can be concluded that using the acoustics inviscid compressible fluid element is acceptable for the cases of FSI instead of linear elastic element with fluid bulk properties. It should be noted that the two-way coupling method needs to be considered for the FSI dynamic analysis.

CHAPTER 5. VIBRATIONAL PROPERTIES OF A HEMISPHERICAL SHELL WITH ITS INNER FLUID PRESSURE: AN INVERSE METHOD FOR NON-INVASIVE INTRACRANIAL PRESSURE MONITORING[1]

5.1. Abstract

Vibration due to a hammer-impact on an aluminum hemisphere fully-filled with water is determined to study the frequency response of the structure at different inner fluid pressures. Modal analysis techniques are utilized on the frequency response functions to extract the modal frequencies and the damping ratios at each pressure level. As fluid pressure increases, changes to the peaks of frequency response are observed. Due to this the modal frequencies will also undergo some shifts with changes in the repeated poles of frequency response. Changes can also be observed in singular bending wave modes. An inverse analysis of such changes due to inner pressure in modal frequencies of the structure can make a possible method for using vibrational stimulus and response in a non-invasive intracranial pressure monitoring system.

5.2. Introduction

The human head includes the cranium and intracranial components such as brain, cerebellum, and cerebrospinal fluid (CSF). Moreover, an adult cranium is a semi-porous elastic shell with limited volume to maintain brain tissue, blood, and CSF. The pressure inside the head is called intracranial pressure (ICP) distributed uniformly on brain tissue by the CSF. Monitoring ICP is vital in many clinical situations, such as neurosurgical postoperative care or other head

[1] The material in this chapter was co-authored by Ashkan Eslaminejad, Mariusz Ziejewski, and Ghodrat Karami. Content in this chapter was published in Journal of Vibration and Acoustics (2019) 141 (4), 041002. Ashkan Eslaminejad had primary responsibility for performing the manufacturing and performing the tests. Ashkan Eslaminejad also drafted and revised all version of this manuscript. Ghodrat Karami and Mariusz Ziejewski served as proofreader, and Ghodrat Karami supervised the project.

trauma events. All conventional monitoring techniques are invasive, and increase the risk of infection and bleeding, with high procedure cost. These drawbacks provide incentive to investigate and develop non-invasive techniques for ICP monitoring.

Although many studies have been carried out to study non-invasive ICP monitoring techniques (Cardim et al., 2016; Khan, Shallwani, Khan, & Shamim, 2017; Popovic et al., 2009; Raboel, Bartek, Andresen, Bellander, & Romner, 2012; Robba et al., 2015; Zhang et al., 2017), no reliable non-invasive method has been established that is suitably accurate and transferrable to clinical applications. Non-invasive ICP monitoring techniques can be categorized into five main categories based on the physiopathological mechanism exploited: using imaging techniques, transmitted ICP, cerebral blood flow monitoring, metabolic alternation monitoring, and neurophysiological functional activity (Robba et al., 2015). ICP variation which uniformly pressurizes brain tissue can be indirectly transmitted through elastic deformation of the skull. Owing to this fact, ICP variation may be estimated by monitoring dynamic properties of the skull which can be measured non-invasively. Because ICP is uniformly loaded on the interior surface of the skull, cranial vibration characteristics can be affected by CSF mass, stiffness and damping.

Investigating the impacts of CSF on skull dynamics, several numerical and analytical studies have utilized spherical head models fully-filled with fluid (A. E. Engin & Y. K. Liu, 1970). Spherical shell modeling without initial stresses is based on linear shell theories considering the skull membrane and bending deformation, along with axisymmetric assumptions (Engin, 1969; Rand & DiMaggio, 1967). Fluid-governing equations were modeled using the velocity potential wave equation. Spherical shell modelling was improved by considering the transverse shear deformation and rotary inertia as thick shell theory in conjunction with the inviscid and compressible fluid potential function (Advani & Lee, 1970). In these studies, the axisymmetric

assumption was considered to obtain modal frequencies and mode shapes. However, Silbiger (Silbiger, 1962) showed that the axisymmetric assumption caused the loss of some vibrational modes, called non-axisymmetric modes. This claim later was verified using finite elements (FE) modeling (Duffey & Romero, 2003).

Bai and Wu (Bai & Wu, 1994) used the Love-Kirchhoff shell theory to derive the governing equation of motion of the spherical shell. They used a hybrid numerical technique in which the spherical shell was modeled using the FE method and the linear fluid-acoustics was modeled using the boundary element method. Moreover, Baroudi et al (El Baroudi et al., 2012a) developed a spherical head model considering the material properties of the skull and CSF. They used an elasto-acoutics coupled model using the Helmholtz decomposition of linear elastic displacement to simulate the fluid-structure interaction (FSI) problem. They compared the results with FE simulation in terms of natural frequencies for two cases of study as both a deformable and rigid skull model. Although these investigations provided substantial analytical and numerical basis, experimental measurement was needed to check and verify the assumptions. Additionally, the effects of ICP variation was not examined in their studies. Piacsek et al. (Piacsek, Abdul-Wahid, & Taylor, 2012) experimentally measured the frequency response function (FRF) of an air-filled aluminum shell subjected to internal pressurization for potential toward non-invasive ICP monitoring. However, the pressure increment range considered was much higher than the human ICP threshold, which is less than eight kPa. In addition to resonance frequency analysis, that study did not consider modal curve fitting analysis, or the closed-space or repeated roots of the FRF.

In this study, an aluminum hemisphere shell fully filled with water is utilized as a model for the human skull to show the impacts of CSF pressure variation on skull vibration. Theoretically, the frequency response of the human head can be measured by sending the harmless wave signals

and capturing the responses by receiver sensors, as depicted Figure 5-1-(a). Therefore, the upper cranial part of the skull, which includes the frontal parietal, and occipital bones, can be modeled as a hemisphere, in Figure 5-1-(b). As such, we experimentally measured the FRF of a clamped hemisphere fully-filled with water at different pressures. Dynamical properties such as modal frequencies, damping ratio and mode shapes of the system will be extracted from the data to obtain the sensitivity of lower band modes of vibration with respect to fluid pressure increments.

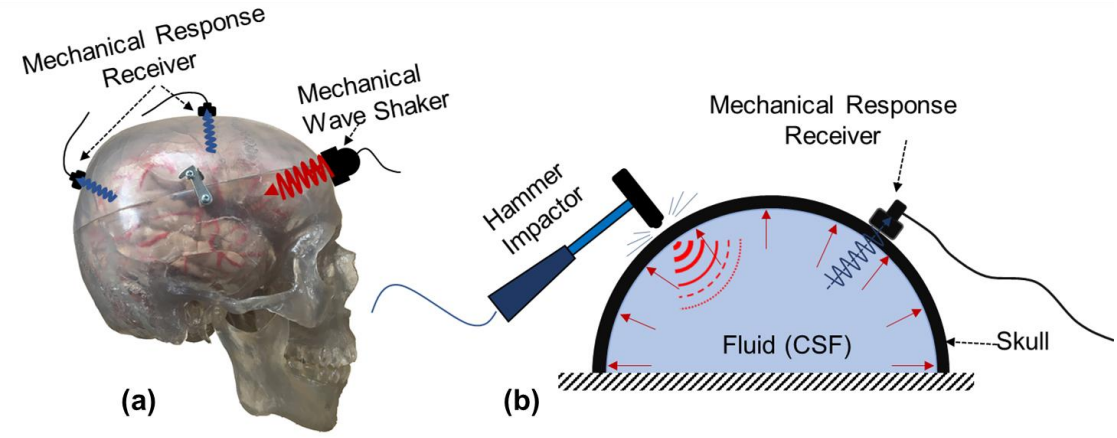

Figure 5-1. Human skull schematic model for monitoring ICP non-invasively (a), the hemisphere alternative model as upper cranium part of the skull includes the frontal, parietal, and occipital bones.

5.3. Materials and Methods

An aluminum hemisphere was welded to an aluminum plate which was in turn clamped to a heavy supportive mass. This supportive mass was clamped to antivibration table. The hemisphere dimensions include an outer radius of 15.15 cm, and thickness of 3 mm. A layer of antivibration rubber was placed between model and table to suppress the noise from the table structure. This model is illustrated in Figure 5-2. The hemisphere was fully-filled with water and purged of all air, as the CSF free surface and sloshing modes do not exist in human head. In this system, the pressure could be increased up to 15 kPa using the column of water.

The model was gridded, and 145 loci (nodes) were mapped for a roving hammer impact modal analysis test. An accelerometer was embedded on node 67. This location was obtained based on the FE pre-study to observe the interested vibration modes in the corresponding location; as such, the accelerometer location should not be at the antivibration node (Avaitable, 2018). Figure 5-3 illustrates the pre-study FE mode shapes of the aluminum hemispherical shell with elastic material properties of; Young's modulus 70 GPa, Poisson ratio of 0.33, and density of 2700 kg/m^-3. These mode shapes presented the patterns of normalized displacements. Three locations were selected to embed the accelerometer, one on top, one in mid-lateral, and one in low-lateral places. The location on top, at some modes is under maximum displacement (red color region), and in some other modes (modes three, four, six, seven and eight) is under antivibration (blue color). The location at mid-lateral is not under antivibration in these low branch vibration modes. The location of mid-lateral is the node number 67 on the mapped hemispherical shell. In this study, the frequency range of interest is the lower range up to 5 000 Hz, per the limitation of hardware and instrumentation.

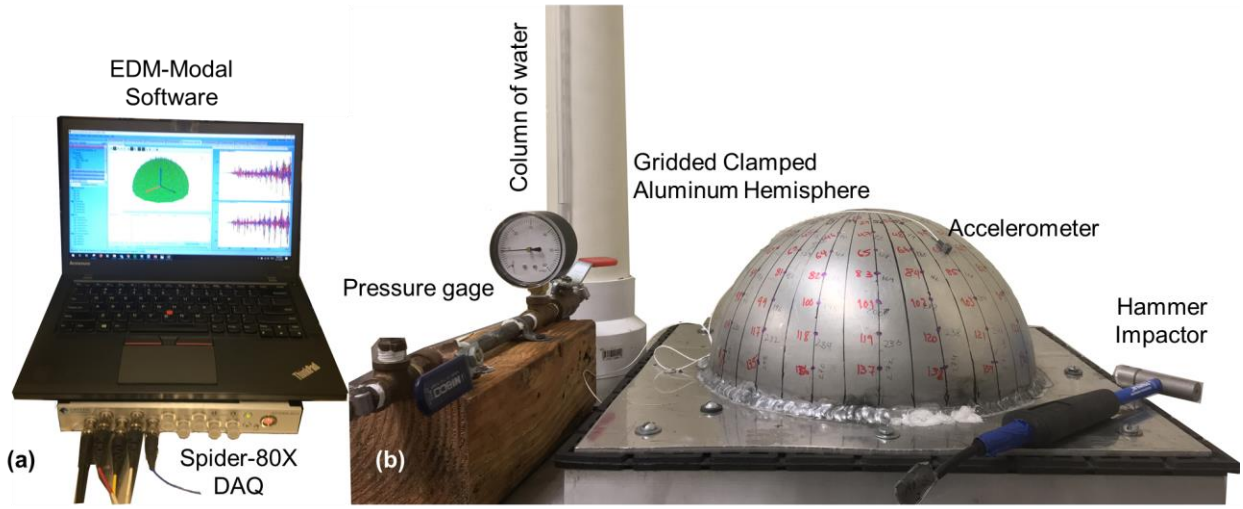

Figure 5-2. Spider-80X DAQ and the EDM FFT analyzer software (a), experimental setup of the aluminum hemisphere along with the fluid pressure controlling system (b).

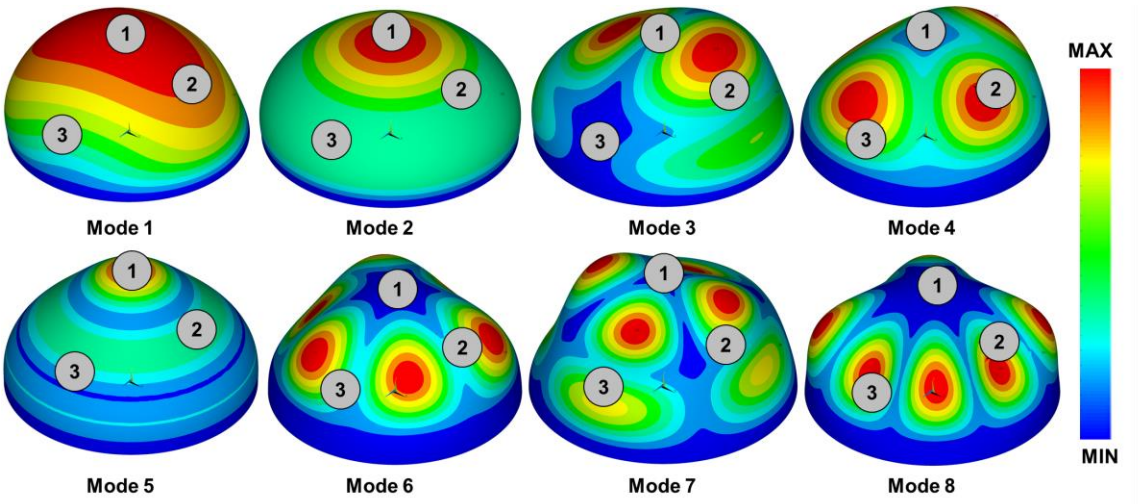

Figure 5-3. FE pre-study to show the best location for accelerometer embedding. The location two is considered as the appropriate place which is node number 67 on the hemisphere.

A roving hammer-impact test was utilized to experimentally measure the dynamic aspects of an aluminum hemispherical model fully filled with water at different pressure loads. The hammer-impact test is not only accurate, with low cost, but also confers mode shapes experimentally. A Dytran 3133A1 accelerometer weighing 800 mg was utilized to minimize the mass effect of the accelerometer on experimental measurements. A Dytran 5800B2 hammer impactor was chosen to create measured impulses. A metal hammer tip was utilized, because the estimated frequency range of interest is high, from 1 000 Hz to 5 000 Hz (Avaitable, 2018). The signal processing of the fast Fourier transform (FFT) setting was determined based on the frequency range of interest so that the minimum sampling rate was at least 10 times the maximum frequency. To study the high frequency range, the sampling rate was 81.92 kHz. The Block size was 65 536, so as to increase the resolution of both frequency and time domain data analysis. To prevent unwanted high frequency noise, a 36 864 Hz low pass filter was used in all signal measurements. Peak-hold FFT averaging was implemented, with n=3. An eight-channel Spider 80X 24-bit data acquisition device recorded the impact and response acceleration signals.

Exponential windowing was utilized on the captured acceleration signals with a damping factor of 13 %. The exponential window removes noise in the FFT analyzer by suppressing latent acceleration signals at bandwidth end. A triggering delay was used in the FFT analyzer to isolate the initial post-impulse signals. Additionally, the coherence diagram was checked for each measurement to accept or reject the captured signal (Avaitable, 2018). The EDM-Modal software package created by Crystal Instrument Inc. (Crystal-Instrument-Corporation, 2017) was used to capture the signals, employ the FFT analysis, and using the modal postposing techniques such as modal curve fitting.

After setting up the signal processing analyzer, the pressure of the fluid was increased from 0 Pa to 15 kPa. For each FRFs set, the FRF-summation was calculated relative to the aforementioned internal loading pressure. The FRF summation is calculated based on the real and imaginary part of the FRF values as the equation (5.1) in which N is the number of FRF data sets.

$$\mathbf{Re}(FRF_{SUM}) = \frac{\sum_{i=1}^{N} \mathbf{Re}(FRF_i)}{N}$$
$$\mathbf{Im}(FRF_{SUM}) = \frac{\sum_{i=1}^{N} \mathbf{Im}(FRF_i)}{N} \tag{5.1}$$

Additionally, the Multivariable Modal Indicator Function (MMIF) and Complex Modal Indicator Function (CMIF) were utilized to determine the modal frequencies along with damping ratios. The obtained modal frequencies were validated using the Modal Assurance Criteria (MAC) diagram to check the orthogonality of modes.

5.4. Results

Using the power spectrum and cross-power spectrums, the H1 estimator transfer function was calculated for the 145 impacted measurements, and their accuracy was checked by the

coherence diagram. These measurements were carried out at different fluid static start pressures, from 0 kPa to 15 kPa. The 3D contour of the FRF-summation sets with respect to the internal pressure increment are depicted in Figure 5-4-(a). As can be observed, pressure increments made small changes in FRF peak shifting and amplitude decrement. The FRF-summation variations are depicted in the Figure 5-4-(b), where the thickness of the line illustrates the distinction caused by internal pressure increment.

In addition to the investigation of the fluid pressure impressions on the FRF-summation deviations, the FRF-summation of several pressures are selected and plotted in Figure 5-5. As shown, the fluid pressure can shift some peaks to lower values. The FRF-summation peaks value variation is severe in some peaks and small in others. To better understand these effects, modal analysis was employed on the FRF data sets. The dynamic parameters were determined relative to modal frequencies and damping ratios using rational polynomial function curve fitting.

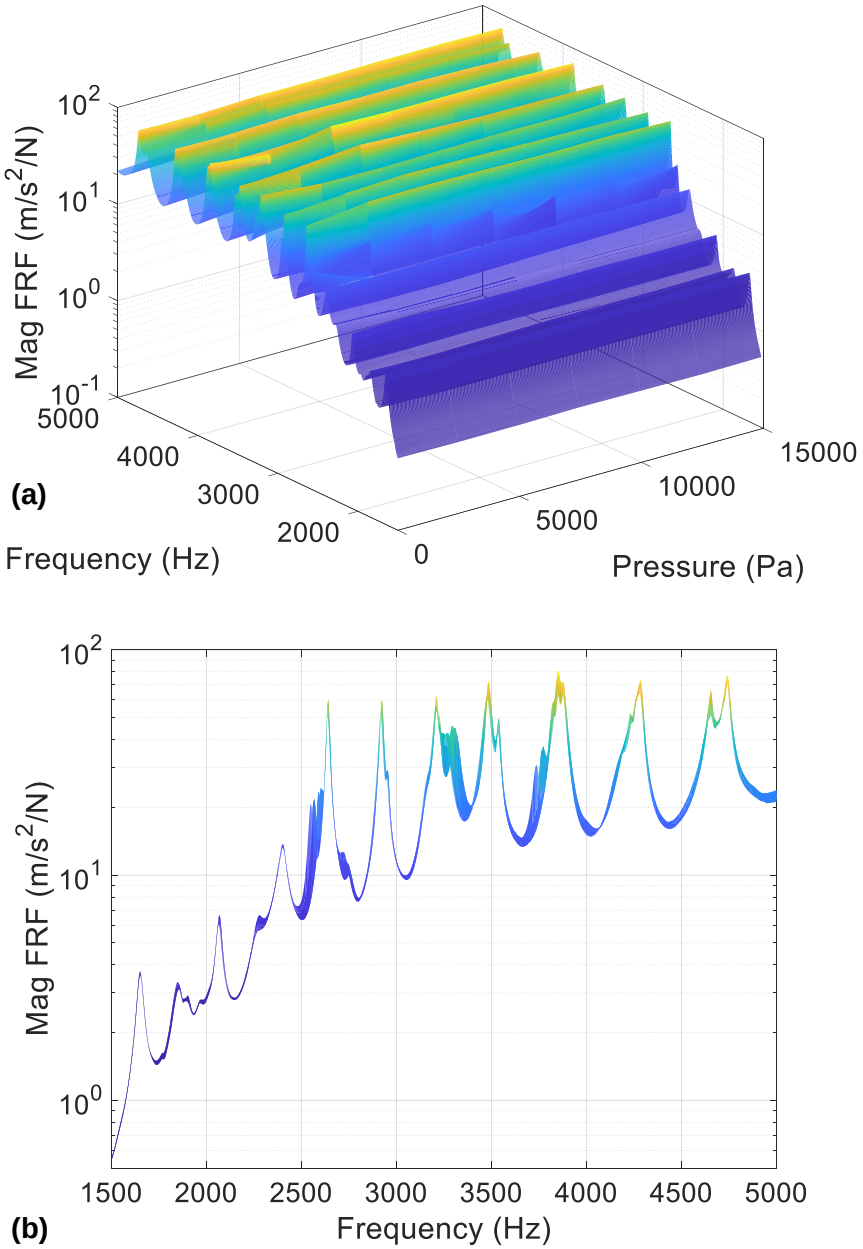

Figure 5-4. FRF-summation of the hemisphere with respect to the fluid static pressure increment up to 15 kPa (a). The FRF diagram of the model: the thickness shows the deviation by the pressure variation.

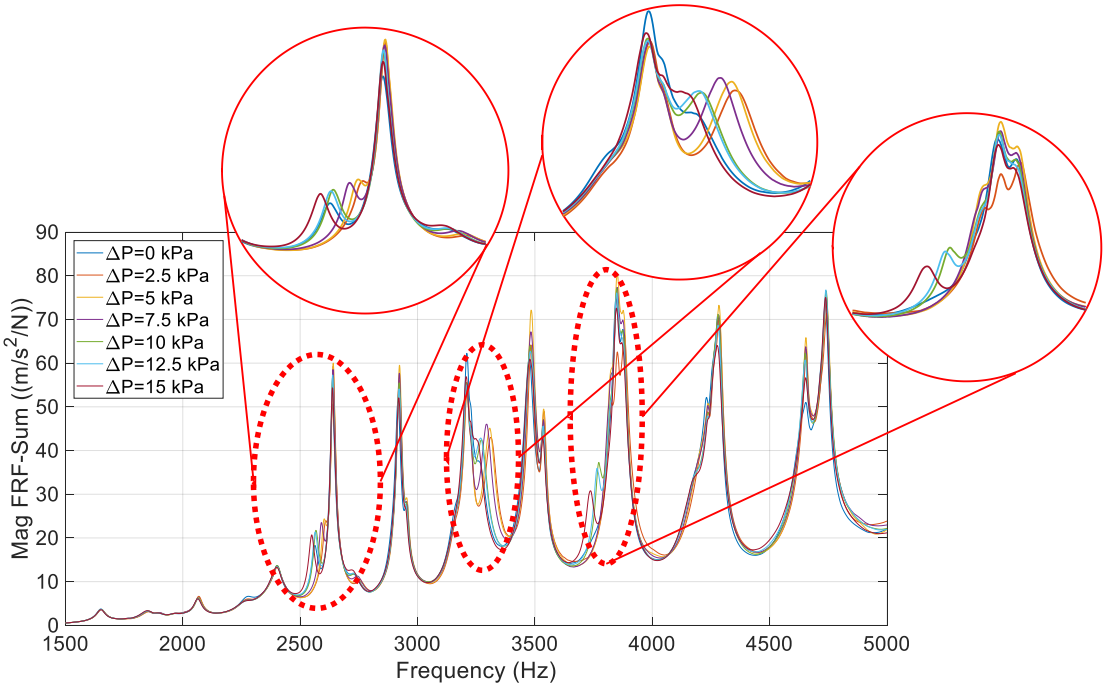

Figure 5-5. The FRF-summation of the fluid fully filled aluminum hemisphere at different fluid pressure increments from zero to 15 kPa.

The MMIF and CMIF were used on to determine modal frequencies from the FRF data sets. The bandwidth of the FRF sets were divided into three zones: 1.) a low frequency zone from 1500 to 2710 Hz that includes the low amplitude modes of vibration; 2.) a medium frequency zone from 2 490 to 4 030 Hz which include the light damping modes, and 3.) a high frequency ranges from 3 640 to 5 000 Hz. Since the rational polynomial fraction method is used for curve fitting, overlap was considered at the beginning of the second and third zones. These overlaps help to indicate the modal parameters accurately so that overlapped modes should be obtained with same stable poles in the stability analysis. Using the selected bandwidth, the modal frequencies and damping ratios were nominated using the stability diagram based on CMIF method. The orthogonality of the stable modal frequencies was checked by the Auto MAC diagram so that each mode of vibration should be orthogonal to other modes. The modal frequencies of the first 24

modes of vibration were extracted and tabulated in Table 5-1 for different internal fluid pressure loads. All postprocessing analysis was carried out in the EDM-Modal postprocessing modulus.

In addition to the modal frequencies and the corresponding damping ratios, the modal shapes were calculated for the first six modes of vibration. These normalized mode shapes are depicted in Figure 5-6. In this figure, the frequencies and damping ratios were obtained in the case of a standard pressure (15 kPa).

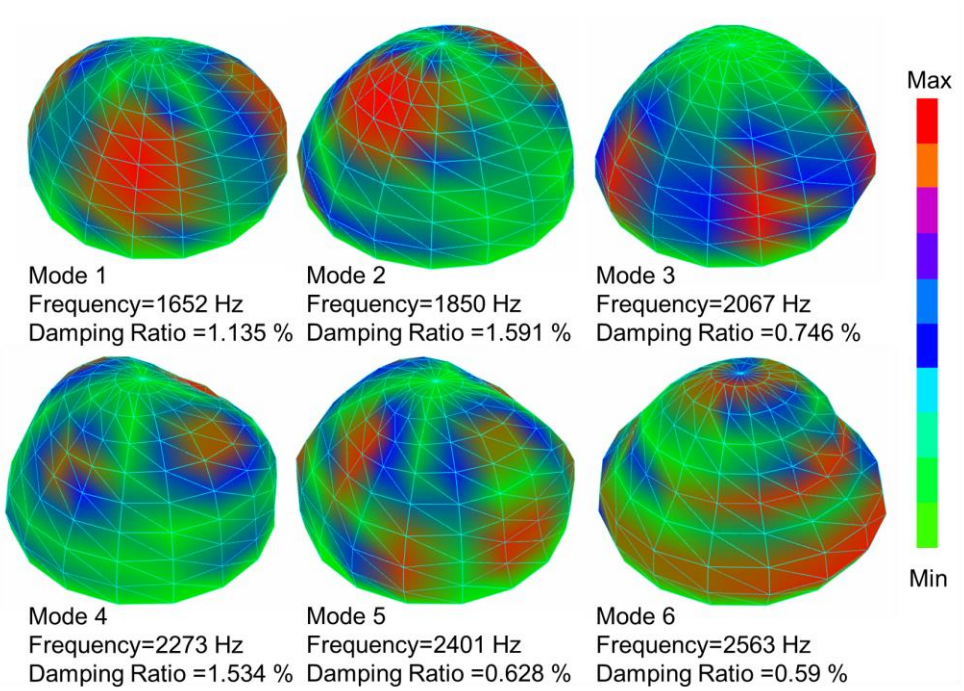

Figure 5-6. Experimental mode shapes along with the modal frequency and damping ratio for the fully filled aluminum hemisphere at zero static pressure increment. The color contours show the normalized modal displacements indicating the pattern of motions at modal frequencies.

Table 5-1. Modal frequencies of the aluminum hemisphere fully-filled with water at different internal pressure

Mode	**ΔP=0 kPa**		**ΔP=2.5 kPa**		**ΔP=5 kPa**		**ΔP=7.5 kPa**		**ΔP=10 kPa**		**ΔP=12.5 kPa**		**ΔP= 15 kPa**	
Number	f(Hz)	ξ (%)	f(Hz)	ξ (%)	f(Hz)	ξ (%)	f(Hz)	ξ (%)	f(Hz)	ξ (%)	f(Hz)	ξ (%)	f(Hz)	ξ (%)
1	1651.975	1.135	1653.121	1.099	1653.911	1.117	1652.924	1.148	1652.214	1.138	1652.224	1.143	1651.752	1.154
2	1850.832	1.591	1858.837	1.677	1859.546	1.513	1859.983	1.635	1856.707	1.641	1855.211	1.695	1853.287	1.709
3	2067.067	0.746	2068.2	0.742	2067.282	0.802	2065.393	0.805	2065.516	0.773	2064.535	0.79	2063.967	0.788
4	2273.188	1.534	2269.905	1.739	2270.608	1.718	2267.965	1.779	2266.736	1.808	2264.84	1.862	2262.57	1.841
5	2401.825	0.628	2402.289	0.604	2402.479	0.623	2401.108	0.625	2401.044	0.614	2401.459	0.636	2399.109	0.675
6	2563.091	0.59	2606.102	0.562	2602.133	0.468	2590.937	0.459	2567.412	0.503	2564.161	0.512	2548.868	0.548
7	2637.653	0.368	2641.324	0.311	2640.572	0.326	2640.152	0.31	2638.981	0.324	2638.717	0.326	2638.263	0.344
8	2738.874	1.166	2761.29	1.107	2758.384	1.008	2751.481	0.985	2741.135	1.035	2737.973	1.016	2728.654	1.021
9	2917.858	0.391	2922.356	0.364	2923.635	0.337	2922.832	0.348	2922.199	0.354	2921.761	0.359	2920.835	0.378
10	2955.251	0.249	2954.535	0.254	2954.428	0.254	2953.236	0.266	2952.333	0.268	2951.301	0.283	2950.274	0.292
11	3159.756	0.934	3163.678	1.018	3165.273	0.992	3163.405	1.087	3162.516	1.163	3162.962	1.206	3166.399	1.443
12	3210.928	0.407	3211.069	0.44	3211.045	0.427	3210.075	0.467	3210.07	0.445	3207.568	0.45	3206.817	0.496
13	3269.523	0.78	3311.176	0.775	3306.453	0.713	3293.804	0.718	3275.258	0.744	3271.525	0.771	3258.011	0.796
14	3477.822	0.705	3483.2	0.384	3483.961	0.433	3482.123	0.502	3476.982	0.64	3476.417	0.632	3472.296	0.72
15	3535.63	0.299	3538.465	0.289	3538.026	0.283	3536.972	0.299	3536.303	0.305	3535.471	0.312	3534.698	0.339
16	3813.824	0.745	3824.308	0.479	3822.803	0.401	3817.541	0.373	3773.695	0.44	3766.381	0.433	3734.284	0.522
17	3845.596	0.437	3852.436	0.487	3850.668	0.335	3847.093	0.37	3847.619	0.429	3848.886	0.375	3846.526	0.419
18	3876.269	0.414	3880.601	0.45	3880.235	0.367	3877.734	0.388	3877.912	0.364	3877.198	0.381	3875.122	0.393
19	4181.062	1.099	4199.5	1.19	4194.56	1.098	4188.314	1.049	4175.901	1.068	4175.338	1.1	4169.272	1.096
20	4228.995	0.415	4233.932	0.374	4236.478	0.269	4232.796	0.346	4231.072	0.358	4233.302	0.329	4229.947	0.434
21	4253.162	0.392	4265.227	0.378	4264.305	0.342	4261.47	0.432	4262.582	0.391	4263.037	0.389	4262.858	0.401
22	4282.195	0.337	4286.454	0.345	4285.514	0.348	4284.246	0.362	4282.094	0.371	4282.19	0.371	4280.839	0.402
23	4659.097	0.357	4658.418	0.253	4657.314	0.254	4656.866	0.274	4655.617	1.041	4654.135	0.327	4656.45	0.29
24	4737.575	0.326	4742.849	0.366	4742.458	0.354	4739.933	0.348	4739.411	0.35	4738.766	0.351	4737.399	0.35

5.5. Discussion

The first 24 modal frequencies of the aluminum hemisphere were determined at pressures ranging from 0 to 15 kPa at 2.5 kPa increments. The observed modal results showed that the modal frequencies shifted from the internal fluid pressure variation. The changes of FRF peak by fluid pressure have been observed experimentally in other studies on symmetrical curvature geometries such as cylindrical (DIGiovanii & Dugundji, 1965; Fung, 1957; Miserentino & Vosteen, 1965) and spherical (Piacsek et al., 2012). In the FSI study on the spherical by Piacsek et al. (Piacsek et al., 2012), the shifts of frequency response peaks could be predicted from the indirect relationship for the lower branch modes. However, our experimental modal analysis results showed unpredictable difference values in hemisphere model with increasing pressure. The maximum changes for each modal frequency are depicted in Figure 5-7, where the horizontal axis denotes the hemisphere modes. In addition to the modal frequencies, the damping ratios of each mode was calculated based on the half power method. The changes of the damping ratios are illustrated in Figure 5-8.

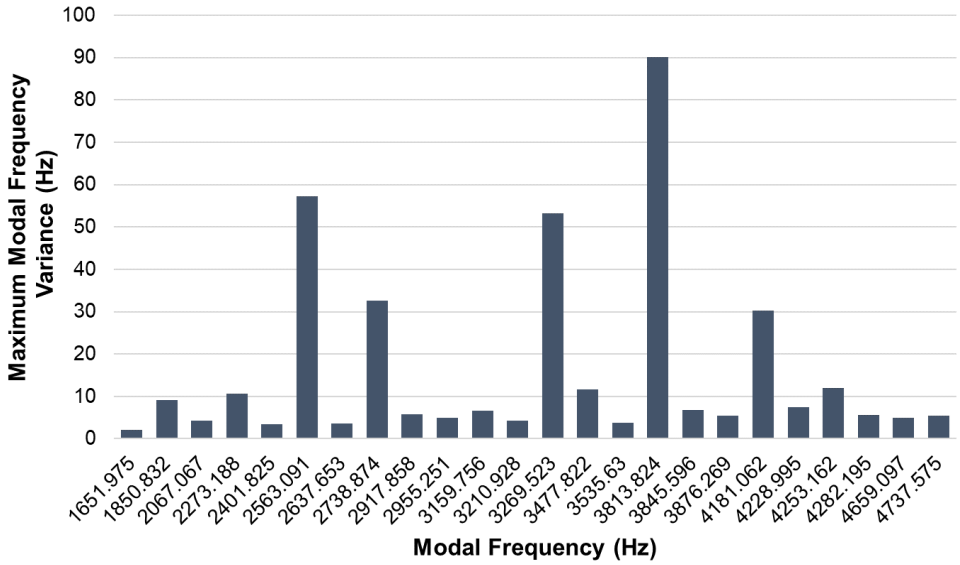

Figure 5-7. Measured frequency response and the maximum differences of each mode under static fluid pressure changes.

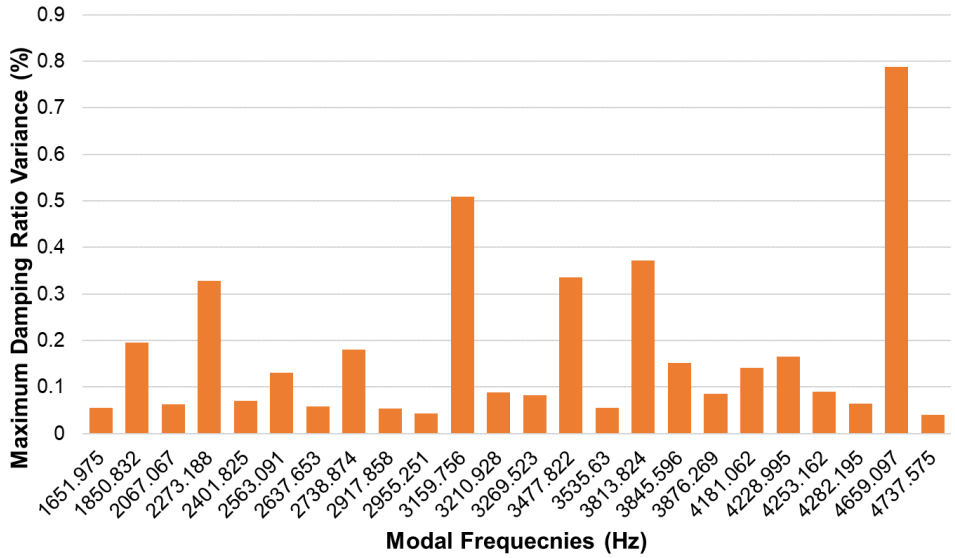

Figure 5-8. Measured damping ratios of each mode and the corresponding differences with increasing static fluid pressure.

Our results show a major difference between the type of modes. It should be noted that some of the modes decreased with increasing pressure; however, the value shift is small in some modes. This suggests that these modes are approximately independent from fluid loading in the current pressure range. On the other hand, the axisymmetric shells have different types of mode shapes at repeated poles. The repeated poles are the modes that have same (or close) frequency values and different mode shapes. These modes can be recognized using the stability diagram along with orthogonality checking. The repeated poles are not orthogonal. Nevertheless, some modes are proximally close, and because of the high damping ratio (width of the FRF peaks) cannot be recognized using only the modal indicator functions. Stability analysis can determine these proximal modes as stable poles which need to be orthogonal (Avaitable, 2018).

The sensitivity of each mode was calculated with respect to incremental fluid pressure loading, which showed that the modes 6, 8, 13, and 16 are the most sensitive to internal pressure variation (Figure 5-9). Linear regression was employed on these modal frequencies with interior pressure increments and the sensitives were calculated as the slope of the trend line. The absolute

values for the sensitivities of modes 6, 8, 13, and 16 are 5.76 (Hz/kPa), 3.38 (Hz/kPa), 5.18 (Hz/kPa), and 14.41 (Hz/kPa), respectively. Depicting the corresponding mode shape of 6, Figure 5-6, declared that bending modal waves are sensitive to fluid pressure interactions; however, other longitudinal modal waves are not changed considerably. This observation was reported by (Piacsek et al., 2012) as well, although the fluid pressure was increased to 1.1 MPa which is much higher than the ICP variance. In this study, the range of pressure variation was taken within the intermediate range of normal ICP for an adult which is from 667 Pa (5 mmHg) to 2 000 Pa (15 mmHg) (Raboel et al., 2012). It is noted that the ICP threshold for human brain death is 8-10 kPa (Liau, 2000). . The sensitivity analysis shows that some frequency modes are considerably dependent to the internal fluid pressure (such as ICP). By identifying these modes and monitoring them, the internal pressure variation can be recognized.

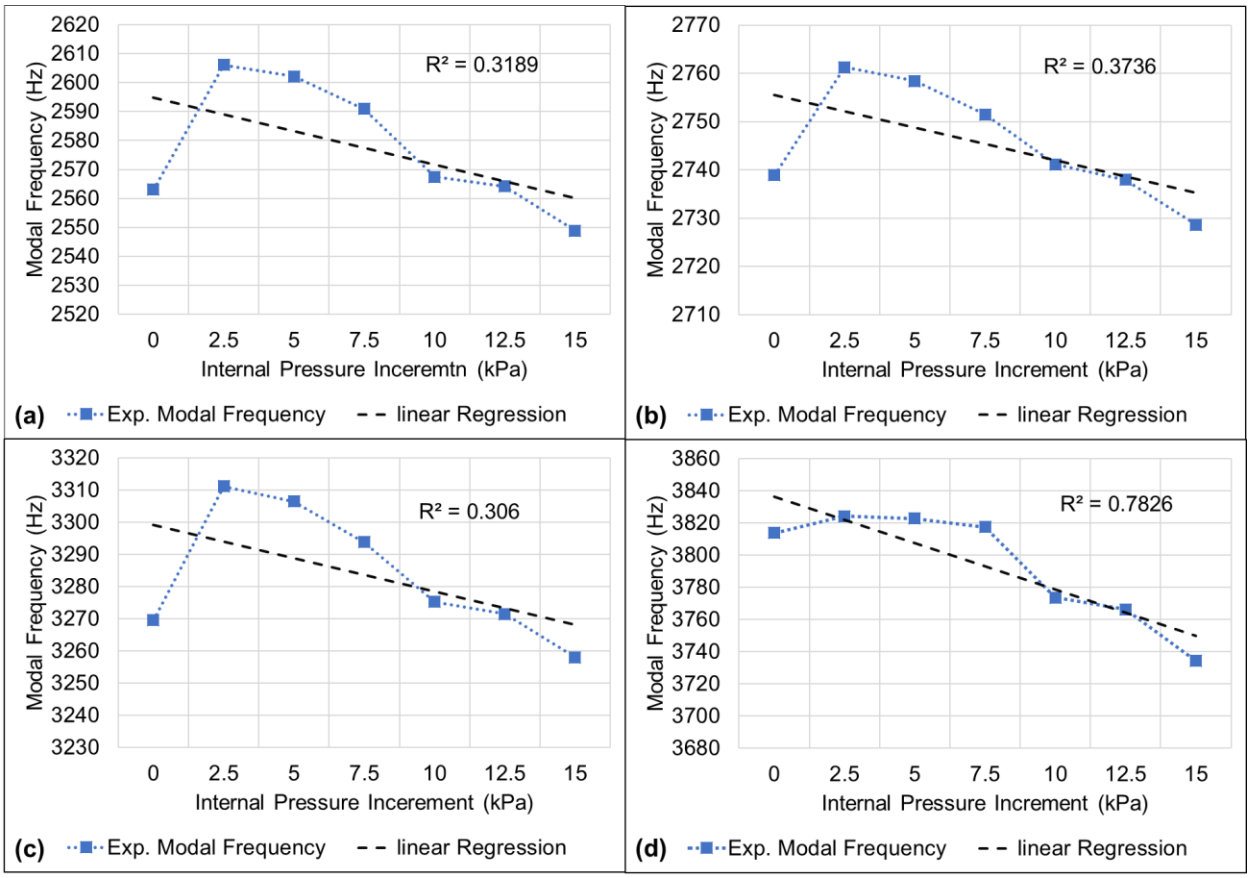

Figure 5-9. Modal frequency variation with pressure increment up to 15 kPa for the sensitive mode numbers 6 (a), 8 (b), 13 (c), and 16 (d).

There are factors in the experimental design that were not factored into the current experimental model, and warrant discussion. The stress distribution in the shell conferred by the weight of the water inside the hemisphere is non-uniform. This effect is negligible, however, since all measurements were conducted under identical conditions and the aforementioned stress distribution was equal at all observed pressures. Additionally, the accurate range of hardware and equipment constrained us to study FRF up to 5 000 Hz. The miniature accelerometer used has 5 % tolerance error at 6 000 Hz, which becomes non-negligible. However, with this hammer-impact method, the modal shape variation observed in some cases shows modal shift or distortion at certain frequencies which clearly exceeds the error tolerances.

The system of hammer-impact modal analysis may be replaced by alternative excitation techniques in clinical situation; however, this method was utilized to establish a basis to study the effects of CSF pressure on skull vibration characteristics. The results of the current study confer a better understanding from which to investigate other techniques that might be suitable to studying the ICP frequency response, such as using ultrasonic acoustic excitation actuator and a high-speed camera to capture high frequency resolution motion, or other methodologies.

5.6. Conclusion

The frequency responses of an aluminum hemisphere shell fully-filled with water were measured using the roving hammer-impact method with the internal fluid static pressure increased from 0 kPa up to 15 kPa. The FRF-summations were calculated to study the effects of fluid pressure on the frequency peaks, amplitudes and the damping ratios. On the average, the peaks of FRF-summation decreased about 2 Hz by each pressure increment of 2.5kPa; however, some peaks were changed more drastically in terms of frequencies and amplitude power.

Modal analysis techniques were utilized to investigate the effect of internal fluid pressure on the shell vibrational properties. As the hemispherical shell is symmetric, some modes were identified as repeat-poles and needed to be distinguished from the proximal modes with high damping ratios. Therefore, stability analysis was employed on the FRF sets. The obtained modal frequencies and corresponding damping ratios were smoothly changed in longitudinal wave modes. Some of the observed bending wave mode shifts were highly affected by fluid pressure changes.

The modal analysis of the FRF sets shows that some modes are sensitive to internal pressure variation. The observation of dynamically sensitive modes affirms their potential as a

theoretical basis for non-invasive ICP monitoring, despite the obvious challenges of methodological development and implementation.

CHAPTER 6. VIBRATION CHARACTERISTICS OF A FULLY-FILLED SHELL WITH FLUID TO MEASURE INTRACRANIAL PRESSURES[1]

6.1. Abstract

Intracranial pressure increments can be monitored noninvasively through cranium vibration because of the pressure by cerebrospinal fluid on the interior surface of the cranium. We study the interaction of this fluid with the cranium structure and obtain the frequency response at different interior pressures for a clamped hemispherical aluminum shell fully-filled with water. It is observed that the peaks of frequency responses are changed by increasing the fluid pressure; however, the change in one of the peaks is identified to be considerable. Consequently, we employ modal testing techniques to obtain resonance frequency, damping ratio and mode shapes. The modal analysis results demonstrate that the changes in frequency of the bending-wave vibration modes are exceedingly bigger than the longitudinal-wave modes. A single degree freedom dynamic model is introduced and fitted to the experimental observation of the sensitive modes. The equivalent mass, damping, and stiffness are obtained at each internal fluid pressure level. Linear regression reveals that the equivalent damping and stiffness of dynamic model are more sensitive to fluid pressure variation than the equivalent mass. Finally, the intracranial pressure through the cerebrospinal fluid on the solid cranium is investigated to develop a non-invasive assessment method.

[1] The material in this chapter was co-authored by Ashkan Eslaminejad, Mohammad Hosseini-Farid, Mariusz Ziejewski, and Ghodrat Karami. Ashkan Eslaminejad conceived and carried out the experiments and analyzed the observed results. Ashkan Eslaminejad wrote this chapter in consultation with Mariusz Ziejewski and Ghodrat Karami. Ghodrat Karami supervised findings of this work.

6.2. Introduction

Intracranial hypertension (IH) is the increment of pressure inside the cranium which is termed as intracranial pressure (ICP). IH occurs via volume changes of intracranial contents such as brain, cerebrospinal fluid (CSF), and blood vessels. This volume variation can occur because of medical conditions such as hemorrhage, strokes, meningitis, and hydrocephalus. Due to this, the ICP assessment becomes extremely important in brain health monitoring. Although the accuracy of ICP monitoring techniques have been examined and accepted, the invasive character of these methods increases the risks of infection and bleeding. Because invasive methods need clinical environments and professional personnel to administer, there is a high cost associated. These complications create the need for non-invasive techniques for ICP monitoring. A future alternative technique to the common invasive methods needs to be accurate, transferable and have low implementation costs.

To develop a non-invasive ICP monitoring technique, numerous investigations have been employed (Cardim et al., 2016; Khan et al., 2017; Kristiansson et al., 2013; Popovic et al., 2009; Raboel et al., 2012; Zhang et al., 2017); however, a consistent non-invasive method has not been recognized. Robba et al. categorized all the studies on non-invasive ICP assessment into seven categories based on their physio-pathological mechanisms (Robba et al., 2015). For instance, visualization of ICP effects on the Optic disk swelling are categorized as indirect pressure transmission. In other words, ICP is uniformly loaded on the Optic nerve and internal surface of the dura membrane, and could be monitored non-invasively. ICP increments alter the measurable properties of the outer components of the head through intracranial contents such as the optic nerve and CSF. Another measurable property is the elastic-dynamic deformation of the cranium interacting with CSF. Indeed, dynamic characteristics of the cranium can be varied by ICP

increments. It is because of the fluid pressure loads on the interior of cranium through CSF mass, stiffness and impedance damping.

Obtaining the CSF-cranium dynamical parameters, several experimental and computational investigations were carried out. Stevanovic et al. (1995) experimentally determined the relationship between the ICP increment and skull vibration responses to shaker actuator using one ovine animal. They elevated the ICP and measured the vibration response of the ovine skull using four accelerometers. Using the same techniques, Håkansson, Brandt, Carlsson, and Tjellström (1994) measured the dynamical properties (modal frequencies and damping ratio) of human cranium *in vivo*; however, the impacts of CSF pressure variation were not considered in the measurements. The modal frequencies were compared with the human cranium (without CSF and brain tissue) modal analysis results by Khalil and Viano (Khalil, Viano, & Smith, 1979). This comparison showed the influences of CSF and the intracranial contents on the skull modal frequencies are considerable. Moreover, Piacsek et al. (2012) modeled the human head as a fully-filled aluminum sphere with water as CSF. The frequency response function (FRF) of the model were measured experimentally to show the impacts of ICP increments, however, the pressure increment range was much higher than human ICP ranges. Furthermore, the peaks of FRF were not necessarily the modal frequency and needs modal analysis techniques.

In addition to experimental measurement, numerous analytical and numerical modelling studies have utilized spherical head models interacting with CSF (A. Engin & Y. K. Liu, 1970). To model the CSF, fluid acoustics and potential flow velocity equations of motion were considered along with linear elastic constitutive model for brain tissue. Different shell theories with linear elastic behavior were utilized to model a spherical cranium model (Advani & Lee, 1970; Bai & Wu, 1994; A. Engin & Y. K. Liu, 1970; Rand & DiMaggio, 1967). In addition to cranium shell

modeling, El Baroudi et al. (2012a) determined the spherical skull equation of motion based on linear elastic displacement relation using the Helmholtz decomposition. Although these modeling and simulations developed advanced governing dynamical equations of human spherical head model interacting with CSF, the experimental validation was desired to examine the approximation and uncertainties. In addition, most of these studies neglected the impacts of ICP increments on the skull dynamical properties.

The current study describes an experimental method based on modal testing techniques to disclose the effects of CSF pressure increments on cranium dynamical properties in terms of modal frequency, damping ratio, and mode shapes. However, there is a fluid-structure interaction (FSI) problem. The upper cranium of the human head includes the frontal, parietal, and occipital bones, which was demonstrated as a fully-filled hemisphere with water as CSF. This model is depicted in Figure 6-1-(a). To find a non-invasive ICP assessment technique, the FRF of cranium can be measured by applying an unharmful impulse and capturing the embedded receiver signals, Figure 6-1-(b). Moreover, we examined the impacts CSF pressure on the receiver signals. Eventually, by obtaining the sensitivity of the dynamical properties with respect to internal pressure variation, an equivalent single degree freedom (SDOF) dynamic model was employed to study the pressure influences on the equivalent mass, damping, and stiffness of motion.

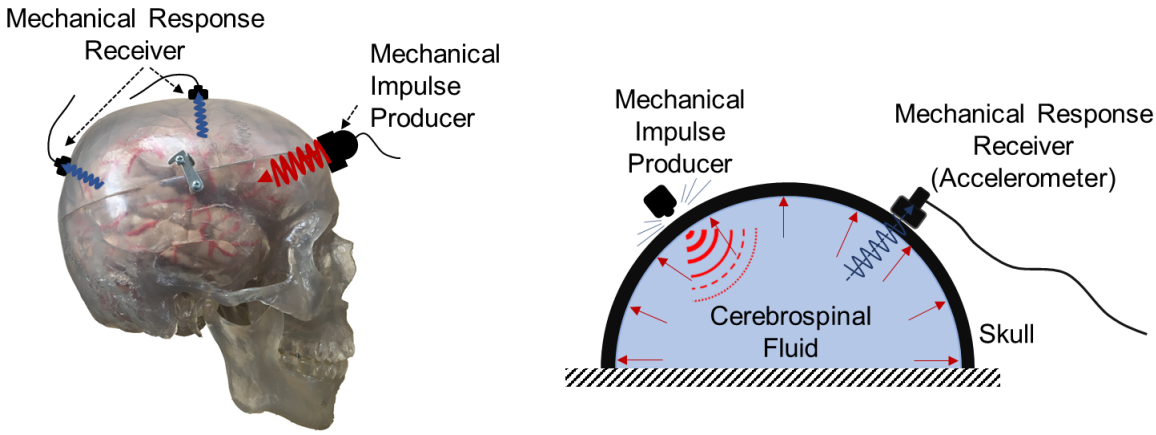

Figure 6-1. Human cranium model for non-invasive ICP monitoring using the frequency response to unharmful impulse (a) and the schematic of the aluminum hemisphere head model includes frontal, parietal and occipital bones fully-filled with water as CSF.

6.3. Experimental Measurements

To experimentally measure the FRF of hemisphere head model fully-filled with water, the aluminum hemisphere was welded to a flange plate. The flange plate was bolted to the supportive heavy mass. The device is demonstrated in Figure 6-2. The aluminum (alloy 3003) hemisphere, which has a radius of 15.15 cm and thickness of 0.3 cm, was fully filled with water. The water pressure could be controlled by the column of water and checked by the pressure gage in middle of the hemisphere. It should be noted that the trapped air inside the hemisphere involves the free surface wave sloshing mode which must be avoided because the CSF free surface does not exist in the human head. The pressure increments were considered up to 15 kPa, which is 50 percent higher than the ICP threshold of brain tissue death on average (Liau, 2000). The pressure was increased by a step value of 2.5 kPa.

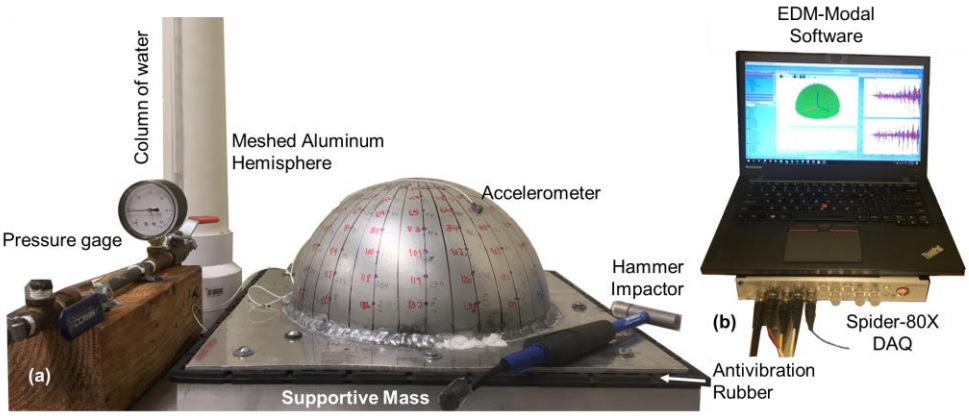

Figure 6-2**.** Experimental apparatus setup of the clamped aluminum hemisphere and the fluid pressure control column of water (a), the data acquisition Spider-80X hardware and EDM-Modal Software for recording the input-output signals (b).

Roving hammer-impact modal testing was used to measure the FRF sets at each fluid pressure level. One layer of antivibration rubber was placed between the hemisphere and supportive mass to suppress the noises from the lab floor and table structure. The outer surface of the hemisphere was gridded, and 145 locations were obtained for hammer impacting using the Hammer Dytran 5800B2. A miniature accelerometer (Dytran 3133A1) was embedded on node 67. The location of the response receiver was obtained based on the FE pre-modal testing of the aluminum hemisphere shell. Indeed, the vibration modes of interest should be seen in the location (Avaitable, 2018). In other words, the accelerometer embedding location should not be an antivibration area. In this study the frequency range of interest is the lower range up to 2800 Hz because the first 10 modes of vibrations can be observed. In addition, the metal tip of the hammer was used after several measurements and analysis was completed because the frequency range of interest was considered up to 2800 Hz and force power spectrum is close smooth curve line (Avitabile, 2001).

The signal processing of the fast Fourier transform (FFT) setting was obtained based on the frequency range of interest. The sampling rate needed to be higher than ten times of the determined frequency ranges. Therefore, a sampling rate of 81.92 kHz and Block size of 65536

was considered to increase the resolution of both frequency and time domain data analysis. To prevent the unwanted high frequency noises, the low pass filter of 36864 Hz was employed in all measurement's signals. The peak-hold FFT averaging was implemented with number of averages of 3 to decrease the measurement errors. The 8 channels Crystal Instrument Spider 80X 24-bit data acquisition device recorded all the impulses and the acceleration responses, Figure 6-2-(b).

The exponential windowing was employed on each captured acceleration signal with the damping ratio of 13 %. This window eliminates the high frequency noises in FFT analyzer by suppressing the acceleration signals which become zero at the termination of the bandwidth. The triggering delay was employed to focus on the signals exactly after the impact applied in the FFT analyzer. The coherence diagram was checked for each measurement to accept or reject the captured force and accelerometer signal. The software Engineering-Data-Management (EDM) Modal package created by Crystal Instrument Inc. (Crystal-Instrument-Corporation, 2017) was used to capture the dynamic signals, employ the FFT analysis, and calculate the averaged FRF. After obtaining the FRF sets, the EDM Modal package was utilized for modal post-processing methods such as modal curve fitting, animation of the mode shapes, stability calculations etc.

For each FRFs set, the FRF-summation was calculated to be compared at the aforementioned internal pressure loading. The FRF-summation is calculated based on the real and imaginary part of the FRF values which is given by equation (6.1)

$$\begin{aligned} \mathbf{Re}(FRF_{SUM}) &= \frac{1}{N}\sum_{i=1}^{N}\mathbf{Re}(FRF_i) \\ \mathbf{Im}(FRF_{SUM}) &= \frac{1}{N}\sum_{i=1}^{N}\mathbf{Im}(FRF_i) \end{aligned} \tag{6.1}$$

where N is the number of FRF experimental data sets. It should be noted that the peaks of FRFs or FRF-summation does not mean modal frequency and needed to be examined by modal testing

techniques. Modal extraction methods such as Complex Modal Indicator Function (CMIF) were studied to conduct the modal frequencies in conjunction with damping ratios. The obtained modal frequencies were confirmed using the auto Modal Assurance Criteria (MAC) based on the modal orthogonality (Avaitable, 2018).

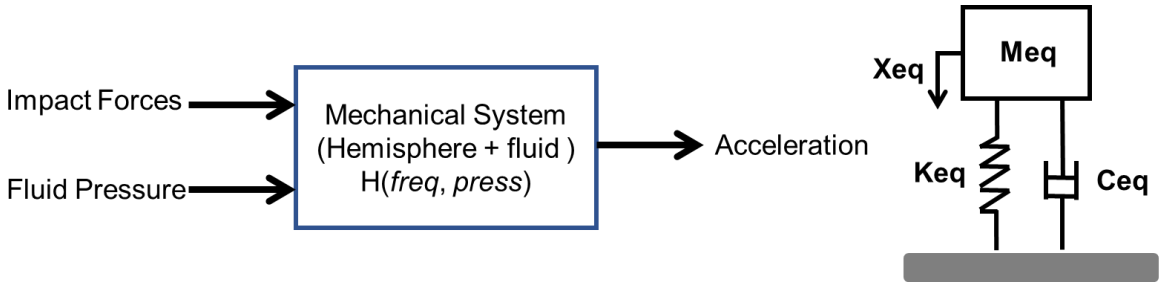

Figure 6-3. SDOF dynamical modeling as equivalent mass, damping, and spring system by considering multi-input one-output linear system.

6.4. Dynamical Modelling Method

After obtaining the modes of vibration with respect to internal fluid pressure increments, sensitivity analysis was considered to obtain the sensitive vibration modes. The most sensitive mode was selected to be modeled as SDOF dynamic system. This equivalent SDOF model is depicted in Figure 6-3 as a linear system with multi-input and single-output (MISO). The equation of motion of the SDOF is given by equation (6.2)

$$M_{eq}\ddot{X}(t)+C_{eq}\dot{X}(t)+K_{eq}X(t)=F(t) \tag{6.2}$$

where M, C, K, and X represent the equivalent mass, damping, stiffness, and displacement, respectively. These parameters are unknown and can be obtained by fitting to the experimental FRF data. In addition, F is the external force as input of this linear system, Figure 6-3. To obtain these parameters, the dynamic compliance transfer function is obtained using Laplace transformation

$$H(s)=\frac{X}{F}=\frac{1}{M_{eq}S^2+C_{eq}S+K_{eq}} \tag{6.3}$$

$$K(\omega) = \frac{F}{X} = K_{eq} - M_{eq}\omega^2 + jC_{eq}\omega \tag{6.4}$$

where $S=j\omega$ in which j is the complex number and ω is radian frequency ($2\pi f$). Because fitting this rational fraction transfer function is unstable, the dynamic stiffness was used (Steele et al., 1988). By substituting the S, the imaginary and real parts of the dynamic stiffness were obtained as equation (6.4). The experimental FRFs are Inertance (acceleration per force) and required to be transferred as dynamic stiffness FRFs by considering the relationship of $FRF_{Inertance} = -\omega^2 K(\omega)$ (Ewins, 2000). Since the experimental and theoretical dynamic stiffnesses are complex, the real and imaginary parts can be fitted respectively using

$$K_n^{\mathrm{Re}} + jK_n^{\mathrm{Im}} = K_{eq} - M_{eq}\omega^2 + j\left(C_{eq}\omega\right) = a_n + jb_n \tag{6.5}$$

where a and b show the real and imaginary parts of the observation dynamic stiffness FRF and n is the nth data. To obtain the equivalent mass, damping and stiffness, the n system of equation needs to be solved as

$$\mathbf{Ax} = \mathbf{b} \tag{6.6}$$

where

$$\begin{aligned} \mathbf{x}^T &= \begin{bmatrix} M_{eq} & C_{eq} & K_{eq} \end{bmatrix} \\ \mathbf{b}^T &= \begin{bmatrix} a_1 & b_1 & a_2 & b_2 & \cdots & a_n & b_n \end{bmatrix} \\ \mathbf{A} &= \begin{bmatrix} -\omega_n^2 & 0 & 1 \\ 0 & \omega_n & 0 \end{bmatrix} \end{aligned} \tag{6.7}$$

The linear system of equation (6.6) is ill-conditioned (high condition number) (Soysal & Semlyen, 1993). To obtain an accurate solution, we implemented the column scaling, therefore, the equation (6.6) is scaled as

$$\mathbf{ADD^{-1}x} = \mathbf{b} \tag{6.8}$$

and the linear system can be rewritten as

$$\hat{\mathbf{A}}\hat{\mathbf{x}} = \mathbf{b} \tag{6.9}$$

where $\hat{\mathbf{A}} = \mathbf{AD}$ and $\hat{\mathbf{x}} = \mathbf{D}^{-1}\mathbf{x}$. Therefore, the final solution can be obtained $\hat{\mathbf{x}} = \mathbf{Dx}$. To solve the scaled equation system, equation (6.9), a direct method was considered using singular value decomposition (SVD) techniques (Lawson & Hanson, 1995). Using the SVD method, the rectangular *n* by 3 matrix $\hat{\mathbf{A}}$ can be written as

$$\hat{\mathbf{A}} = \mathbf{USV}^T \tag{6.10}$$

where U and V are orthogonal matrices by dimension of *n* by *n* and 3 by 3, respectively. Because matrix $\hat{\mathbf{A}}$ is rectangular, the singular value matrix **S** can be written as

$$\mathbf{S} = \begin{bmatrix} \mathbf{S}_1 \\ 0 \end{bmatrix} \qquad \mathbf{S}_1 = diag\{\lambda_i\} \quad i = 1,2,3 \tag{6.11}$$

where λ represents the singular values of matrix $\hat{\mathbf{A}}$. The solution can be obtained by solving the decomposed system of equations of

$$\begin{aligned} &\mathbf{Sy} = \mathbf{g} \\ &\mathbf{y} = \mathbf{V}^T\hat{\mathbf{x}} \\ &\mathbf{g} = \mathbf{U}^T\mathbf{b} = \begin{bmatrix} \mathbf{g}_1 \\ \mathbf{g}_2 \end{bmatrix} \end{aligned} \tag{6.12}$$

where $\mathbf{g}_1$ is a one by three nonzero vector. The final solution can be given by

$$\mathbf{y} = \mathbf{S}_1^{-1}\mathbf{g}_1 \tag{6.13}$$

Eventually, the equivalent mass, damping, and stiffness cab be obtained by fitting the SDOF rational fraction FRF for each pressure set. The regression study was utilized to extract the impact of internal fluid pressure variation on these equivalent parameters.

6.5. Results

The 145 hammer-impacted locations FRFs were measured. Figure 6-4-(a) demonstrates the FRF overlaid with the experimental apparatus at atmospheric internal fluid pressure. To compare

the frequency response at different internal fluid pressures, the FRF-summations were calculated and depicted in Figure 6-4-(b). As can be observed, one of the peaks of FRF-summation, in the frequency range of 2550 Hz, was changed by increasing the interior fluid pressure.

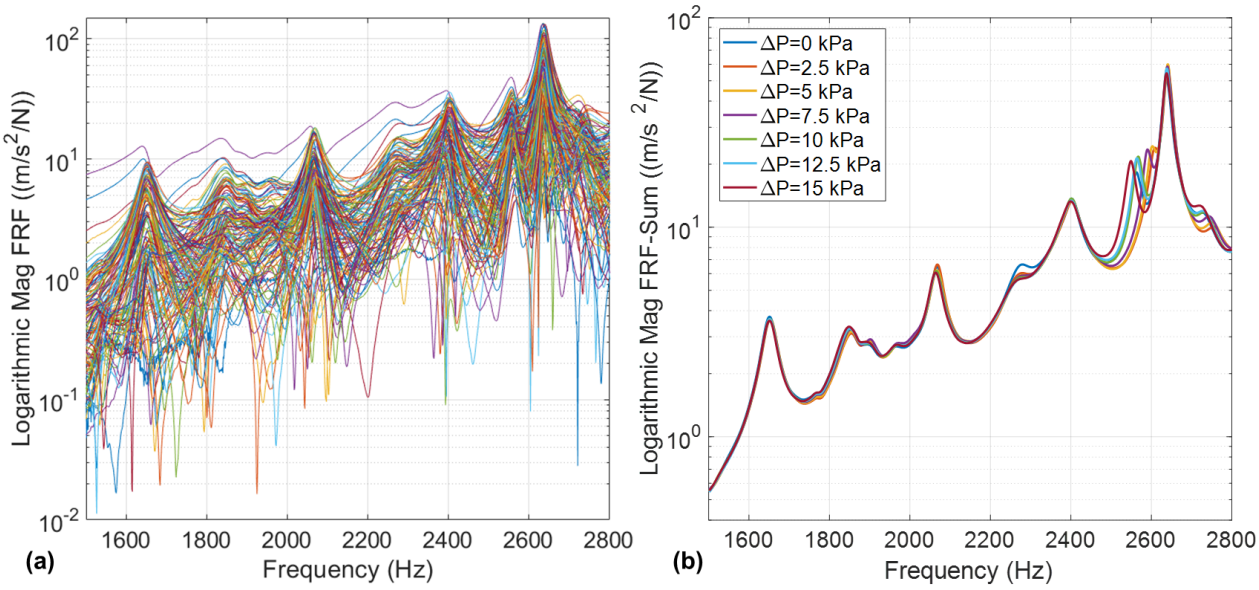

Figure 6-4. FRF overlaid of the 145 averaged measurements at atmospheric internal pressure loading (a). The FRF-summation of measurement sets by internal pressure increment from.0 kPa to 15 kPa (b).

The peak frequency of FRF-summation does not certainly mean modal frequencies. To obtain the modal properties the aforementioned modal indicator techniques are needed. Using CMIF, the stability diagram up to 25 poles was calculated and is illustrated in Figure 6-5-(a). The green plus signs represent the stable modal frequencies and damping ratios via fitting the rational fraction polynomial transfer function with different pole orders from 1 to 25. As can be seen in the stability diagram, some modes such as 1653 Hz, 2068 HZ, and 2402 Hz have another stable pole in their neighborhood. These modes are termed as repeated poles which means the system vibrates with different mode shapes at the same modal frequencies. This can occur because of the symmetric nature of the model and pattern of mode shapes.

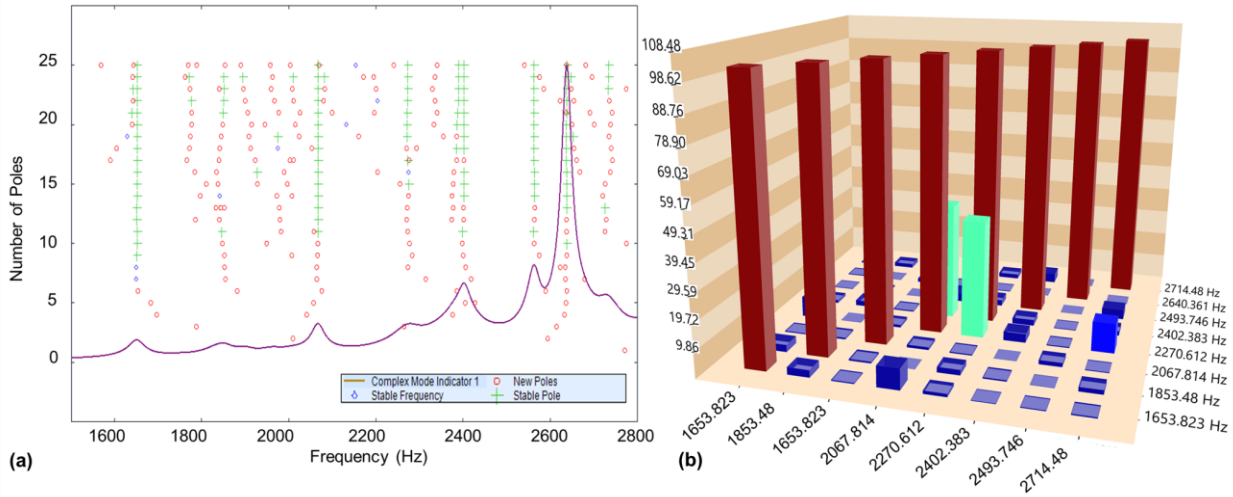

Figure 6-5. Stability diagram by 25 poles (a). Auto MAC diagram to check the obtained modal orthogonality (b).

To examine the selected stable modal frequencies, auto MAC analysis was considered to check the modal orthogonality. The auto MAC diagram is illustrated in Figure 6-5-(b). Although the mode frequency of 2270 Hz has contributed in the mode frequency of 2067 Hz, this contribution can be neglected since the contribution value is low, and the mode shapes have a similar pattern of motion.

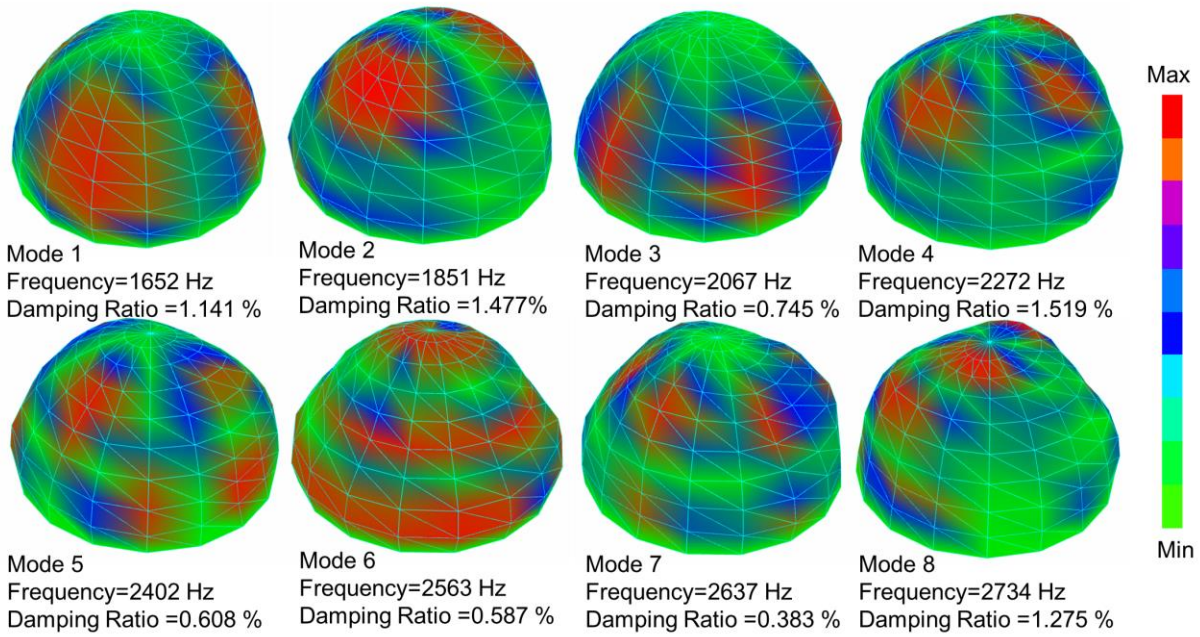

Figure 6-6. Experimental obtained modes shapes corresponding to the modal frequencies and damping ration for the aluminum hemisphere fully-filled with water.

Using the CMIF, stability, and auto MAC diagrams, the modal parameters along with mode shapes were calculated. These dynamical properties are provided in Figure 6-6. In addition, these first eight modes of vibration extracted from the FRF sets at atmospheric internal fluid pressure. By implementing the same procedure, the modal parameters were obtained and tabulated in Table 6-1 at different internal fluid pressures. As was observed from the FRF-summation comparison, Figure 6-4-(b), the sensitive modes occurred at frequency ranges of mode number 6. The frequency shifting occurred in all modal frequencies, significantly mode number 6.

Table 6-1. Modal parameter table a different internal fluid pressure loading for the first 8 modes of vibration using the modal testing techniques.

Mode Number		1	2	3	4	5	6	7	8
ΔP=0 kPa	f (Hz)	1651.975	1850.832	2067.067	2273.188	2401.825	2563.091	2637.653	2734.874
	ξ (%)	1.135	1.591	0.746	1.534	0.628	0.590	0.368	1.166
ΔP=2.5 kPa	f(Hz)	1653.121	1858.837	2068.200	2269.905	2402.289	2606.102	2641.324	2761.290
	ξ (%)	1.099	1.677	0.742	1.739	0.604	0.562	0.311	1.107
ΔP=5 kPa	f(Hz)	1653.911	1859.546	2067.282	2270.608	2402.479	2602.133	2640.572	2758.384
	ξ (%)	1.117	1.513	0.802	1.718	0.623	0.468	0.326	1.008
ΔP=7.5 kPa	f(Hz)	1652.924	1859.983	2065.393	2267.965	2401.108	2590.937	2640.152	2751.481
	ξ (%)	1.148	1.635	0.805	1.779	0.625	0.459	0.31	0.985
ΔP=10 kPa	f(Hz)	1652.214	1856.707	2065.516	2266.736	2401.044	2567.412	2638.981	2741.135
	ξ (%)	1.138	1.641	0.773	1.808	0.614	0.503	0.324	1.035
ΔP=12.5 kPa	f(Hz)	1652.224	1855.211	2064.535	2264.840	2401.459	2564.161	2638.717	2737.973
	ξ (%)	1.143	1.695	0.79	1.862	0.636	0.512	0.326	1.016
ΔP= 15 kPa	f(Hz)	1651.752	1853.287	2063.967	2262.57	2399.109	2548.868	2638.263	2728.654
	ξ (%)	1.154	1.709	0.788	1.841	0.675	0.548	0.344	1.021

Mode number 6 with a frequency of 2563 Hz varies by interior pressure. However, this mode is not active in all 145 impacted FRF sets, and in some local measurements it demonstrates an antiresonance behavior. Therefore, it is the most active FRF of this mode collected based on the maximum magnitude FRF. The location of suitable FRF collection from impact in top and response at maximum deformation is shown in Figure 6-7. By collecting the FRF real and imaginary FRF data, the SDOF model can be fitted to obtain the equation of motion parameters. The real and imaginary frequency responses are depicted in Figure 6-8-(a) and (b). The peak frequency in the imaginary shows the modal frequency.

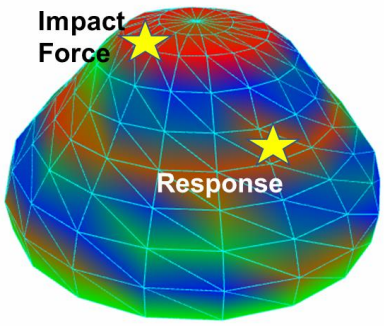

Figure 6-7. The sensitive mode shape and the location of input impulse and response acceleration for SDOF modeling

After obtaining the most sensitive mode of the internal fluid pressure increment, the SDOF model was fitted to the FRF set. As mentioned above, the real and imaginary parts of dynamic stiffnesses were calculated to solve the linear system expression (6.6). Therefore, the equivalent mass, damping, and stiffnesses were obtained. Using the obtained parameters, the fitted model is depicted in terms of real and imaginary dynamic stiffness, Figure 6-8. It should be noted that the imaginary part of the dynamic stiffness is a C_{eq} constant in the SDOF model, which is a straight line in the imaginary diagram. All equivalent mass, damping and stiffness parameters were obtained from the FRF peak. The best fitted data was collected based on the coefficient of determination (R^2) which should be more than at least 90 %. The equivalent mass, damping and stiffnesses were obtained and tabulated in Table 6-2.

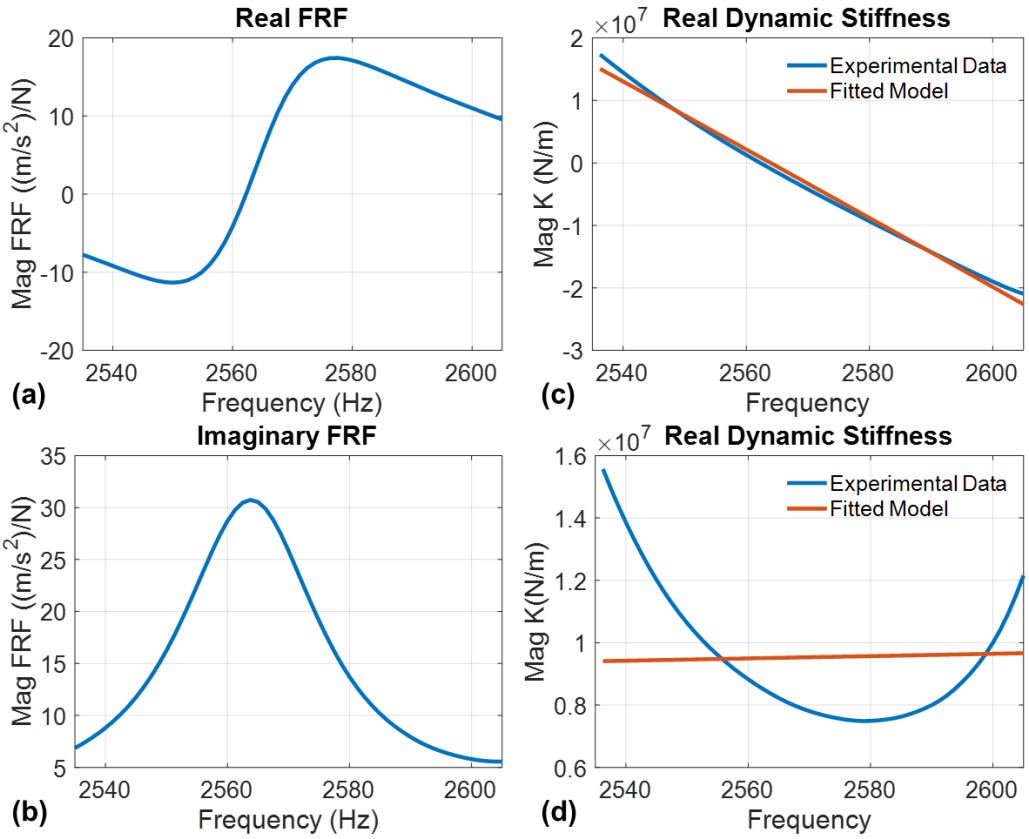

Figure 6-8. The FRF coincident (a) and quadrature (b) plot for the sensitive mode at atmospheric pressure loading. Corresponding real and imaginary dynamic stiffness (c), and (d) along with the fitted SDOF dynamic stiffness.

Table 6-2. Equivalent mass, damping, and stiffness of SDOF dynamic model, at different interior pressure levels.

ΔP (kPa)	0	2.5	5	7.5	10	12.5	15
Meq (kg)	2.7	2.8493	2.6593	2.7859	2.606589	2.56603	2.46033
Ceq (kg/s)	590.37	482.25	439.76	475.40	485.31	461.03	463.30
Keq (N/m)	7.01E+08	7.65E+08	7.12E+08	7.39E+08	6.78E+08	6.66E+08	6.3E+08

6.6. Discussion

FRF-summation of 145 impacted locations at different interior fluid pressures (from atmospheric to 15 kPa) show shifting in the peak frequencies, which is distinct in one peak frequency. The changes of FRF peak by fluid pressure have been observed experimentally in other studies on symmetrical curvature geometries such as cylindrical (DIGiovanii & Dugundji, 1965; Fung, 1957; Miserentino & Vosteen, 1965) and spherical (Piacsek et al., 2012). The frequency peak shifting, owing to fluid pressure impacts on the aluminum spherical shell, was examined by Piacsek et al. (2012) which is in consistent by the current observation. However, the fluid pressure variation ranges were much higher than ICP ranges in their research. Although high fluid pressure loading on the spherical shell caused linear increases in certain peak frequencies, lower ranges of frequency responses were not studied. In the current study, the lower range of FRF declared that fluid pressure can significantly change certain modes. Therefore, experimental modal analysis was employed using hammer-impact.

Based on the modal analysis of the FRF sets at different pressure levels, the first eight mode shapes showed that the frequency shifting phenomenon of the bending wave modes are significantly higher than other longitudinal wave modes. This observation confers with the conclusion of the study by Piacsek et al. (2012). However, no specific trend of shifting was observed by internal fluid pressure increments. One of the advantages of the hammer-impact modal analysis, with several measurements, is to depict the mode shapes experimentally. These

results can be used to validate the numerical and analytical spherical head models interacting with CSF, which were formulated based on the continuum linear elastic assumptions (El Baroudi et al., 2012a).

After discovering the bending vibration mode which is sensitive to interior fluid pressure, Figure 6-7, the location of impact testing was obtained for modelling a SDOF dynamic model to an active FRF. This frequency response observation showed the importance of selecting the right measurement location on skull for developing non-invasive ICP monitoring method. On the other hand, to monitor the effects of CSF pressure on the vibration of the skull, not only the sensitive modal frequency is needed to be obtained. The locations of sending the impulse and capturing the response signals are important for high resolution frequency response analysis as well. After obtaining the FRF based on the collected ICP sensitive signals, a simplified mathematical model can simulate the impacts of fluid pressure on the system parameters.

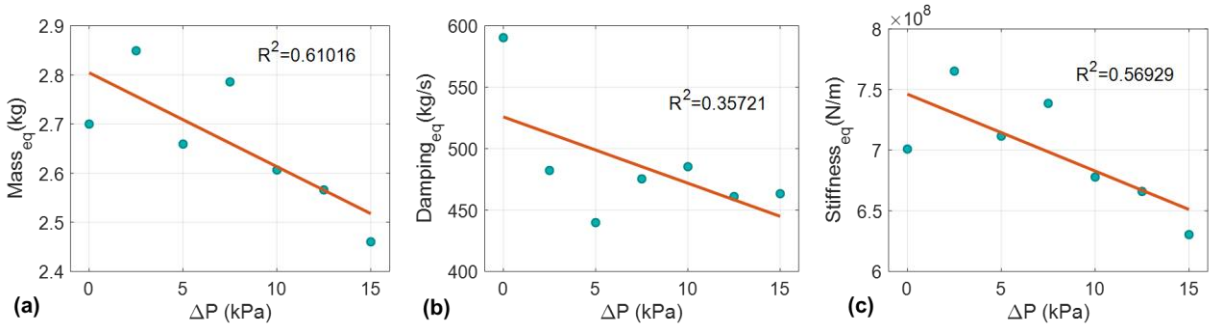

Figure 6-9. Regression analysis of equivalent mass, damping, and stiffness of the model with fluid pressure increment

The equivalent mass, damping, and stiffness at each interior fluid pressure were obtained by solving the aforementioned linear system. The SDOF equation of motion parameters is illustrated in Figure 6-9 with respect to fluid pressure. In addition to SDOF modelling, linear regressions were employed to show the possible impacts of fluid pressure on the shell structure. As can be observed, mass, damping and stiffness of this linear dynamical system are decreased by

increasing the pressure. Normalized sensitivity analysis showed that equivalent stiffness sensitivity is 9 % and damping sensitivity is 9.1 %, which are higher than the equivalent mass sensitivity of 7 %. These values were normalized using the mass, damping, stiffness values at atmospheric pressure and the brain death ICP threshold of 10 kPa.

Although the linear regression showed the equivalent mass, damping and stiffness are a function of fluid pressure, more measurements are needed with a wide range of fluid pressure loading in the FSI problem modelling. The interior fluid pressure range was chosen based on the intermediate range of brain ICP threshold; however, smaller pressure step values can increase the accuracy of linear and nonlinear regressions. In addition to measurement setups, using the other modal testing method, based on shaker excitation, can prove the whole of vibration analysis of the current FSI problem.

6.7. Conclusion

The experimental vibration analysis carried out on the aluminum shell hemisphere fully-filled with water demonstrated that the frequency response is shifting with interior fluid pressure increment. The peaks at the FRF-summation were changed slightly, but one specific frequency peak of 2563 Hz was identified as exceedingly sensitive to the internal fluid pressure increment. As the peak frequency of FRF is not very much correlated to the resonance frequency, a modal testing technique was employed to obtain the dynamic characteristics of the setup. The first eight modes of vibration were extracted using the hammer-impact modal testing technique. These modes were validated using the MAC orthogonality examination technique. By calculating the mode shapes of vibration, the impact of internal fluid pressure was found to be smaller in longitudinal-wave modes than those of bending-wave ones.

In addition to modal analysis, a regional study was implemented to obtain the best location for applying the impulse and to embed the receiver (accelerometer). Based on these signals, active FRF was computed to show the FRF sensitive peak. This observation led us to develop a SDOF dynamic model to study the effect of fluid pressure loading on the dynamic system's parameters in terms of mass, damping, and stiffness. Employing linear regression demonstrated that lower sensitivity of mass to pressure increments than those of damping and stiffness. These observations helped us to develop a linear system model with two input (force on the structure and its pressure loading) and one output in modeling of this FSI problem.

The observations in this study can provide an empirical-physical dynamic model of human cranium interacting with CSF to develop a non-invasive ICP monitoring system. The current results not only can provide a better cranium-CSF model for biomedical applications, but also can be utilized in other engineering applications which involve the FSI conditions. In addition to develop ICP monitoring method, a human skull 3D printed model can be composed and fully-filled with water to employ the current dynamic modelling procedure.

CHAPTER 7. CONCLUSION AND SUGGESTIONS FOR FUTURE WORKS

7.1. Discussions and Conclusions

For non-invasive ICP monitoring and evaluation, the vibration response of skull, along with CSF interactions, was introduced. To study the CSF interactions effects on the skull dynamic model, vibration response and dynamic characteristics of human skull were examined. Before embarking on CSF interaction and ICP variation impacts, the behavior and constitutive properties of the human skull were obtained by a computational-experimental modal analysis. A FE CAD model was constructed using a 3D scanner and the material constitutive properties were assumed as linear elastic and nonlinear hyperelastic (Mooney-Rivlin strain energy model). The material parameters were obtained at different strain rates. FE modal analysis was implemented to solve the eigenvalue problem based on all the material models with their parameters. In addition to computational modal analysis, experimental modal analysis was imposed on the skull and the FFT averaged FRF was extracted. The computed natural frequencies were compared with the experimental modal frequencies.

The following are some conclusions of the study of human cranium dynamic modeling and measurement:

- The modal frequencies for the upper cranium skull bones (frontal, parietal, and occipital) were determined as 495.99 Hz, 543.53 Hz, 1249.71, and 1286.88 Hz. Although the FE modal analysis obtains the natural frequencies (eigenvalues of mass and stiffness matrices), the experimental modal analysis confers modal frequencies and include some structural hysteric damping.
- Based on coefficient of determination (R^2), the nonlinear hyperelastic material constitutive model can fit the skull bone tensile parameter better than the linear elastic model.

- Structural hysteric damping has an impact on the FE modal analysis solutions and cannot be obtained mathematically. Damping parameters can be obtained by using the experimental FRF Bode diagram. The structural damping was obtained as 1.84%, 3.11%, 2.73%, and 1.63%. Therefore, experimental modal analysis was needed before numerical dynamic simulation.
- The strain rates of the mechanical parameter characterization tests (tensile, compression, shear, torsion, and bending) have significant impact on stiffness properties. In this study, the strain rate 0.1 1/sec was determined as the most appropriate tensile test strain rate for FE modeling on the human skull.

Because of cranial sutures, the human skull could not be fully filled with artificial CSF (water in this study), therefore, a linear elastic aluminum hemispherical shell was considered as head model to be filled with CSF. The experimental vibration measurements were carried out on an aluminum hemisphere shell. Two case scenarios were considered to show the effects of fluid interaction on the structural dynamic characteristics. In addition to the experimental modal analysis, the numerical formulation was developed using FE methods. Dynamic characteristic results were obtained in terms of modal frequencies, damping ratios, and vibration mode shapes.

The following are some conclusions of the study of hemispherical head model with and without CSF interaction:

- Three vibrational modes were successfully extracted for the empty hemisphere. The experimental results from modes up to number five showed good agreement with the numerical modeling.

- Comparing the experimental modes with the numerical simulation confirms high FE modeling accuracy. The experimental mode shapes were conferred with the mode shapes depicted by numerical eigenvectors.
- The lower three modes were obtained and compared with FE simulation results under FSI condition. Although some modes of the structure are observed as overdamped, these may not be elucidated in the experimentally measured FRFs. The extracted modal frequencies are in good agreement with numerical simulation.
- FSI could decrease the modal frequencies along with modal shape transformation. The first three experimental mode shapes were found to be in good agreement with numerically undamped frequency mode shapes.
- It can be concluded that using the acoustics inviscid compressible fluid element is acceptable for the cases of FSI instead of a linear elastic element with fluid bulk properties. It should be noted that the two-way coupling method needs to be considered for the FSI dynamic analysis.

The frequency responses of an aluminum hemisphere shell fully-filled with water were measured using the roving hammer-impact method with the internal fluid static pressure increased from 0 kPa up to 15 kPa. The FRF-summations were calculated to study the effects of fluid pressure on the frequency peaks, amplitudes and the damping ratios. Modal analysis techniques were utilized to investigate the effect of internal fluid pressure on the shell's vibrational properties.

The modal analysis of the FRF sets showed that some modes are sensitive to internal pressure variation. These modes were validated using the MAC orthogonality examination technique. This observation led us to develop a SDOF dynamic model to study the effect of fluid pressure loading on the dynamic system's parameters in terms of mass, damping, and stiffness. In

addition to modal analysis, a regional study was implemented to obtain the best location for applying the impulse and to embed the receiver (accelerometer). Based on these signals, active FRF was computed to show the FRF sensitive peak.

In experimental measurement and dynamical system modelling of the sensitive bending mode of vibration, the subsequent observations were extracted:

- On average, the peaks of FRF-summation decreased about 2 Hz by each pressure increment of 2.5kPa; however, some peaks were changed more drastically in terms of frequencies and amplitude power.
- As the hemispherical shell is symmetric, some modes were identified as repeat-poles and needed to be distinguished from the proximal modes with high damping ratios.
- The obtained modal frequencies and corresponding damping ratios were smoothly changed in longitudinal wave modes. Some of the observed bending wave mode shifts were highly affected by fluid pressure changes.
- The peaks at the FRF-summation were changed slightly, but one specific frequency peak of 2563 Hz was identified as exceedingly sensitive to the internal fluid pressure increment.
- Employing linear regression demonstrated that sensitivity of mass to pressure increments was lower than those of damping and stiffness.
- These observations helped us develop a linear system model with two input (force on the structure and its pressure loading) and one output in modeling of this FSI problem.
- The observations in this study provided an empirical-physical dynamic model of human cranium interaction with CSF to develop a non-invasive ICP monitoring system.

The current results not only provide a better cranium-CSF model for biomedical applications but can also be utilized in other engineering applications which involve the FSI conditions.

7.2. Suggestion for Future Work

Below are several suggested tasks and case studies for future consideration:

- To improve the geometry accuracy, a 3D printed human skull model can be composed and fully-filled with water to employ the current developed dynamic modelling procedure. Modal analysis on an enclosed 3D printed cranium model provides the sensitive mode shapes related to skull vibration and the effects of FSI condition.
- In the current study, the hammer-impact modal analysis technique was implemented using one reference accelerometer and roving hammer. For the future, one could consider the related multi reference hardware and software modal hammer-impact modal analysis technique to reduce measurement time. In multireference modal analysis, we suggest using two or three triaxle accelerometers as multireference and more impacts to depict the higher mode shapes.
- In this study, the numerical model was developed using FE technique. It is suggested to try other numerical/analytical techniques such as boundary element numerical method.

The SDOF dynamic model was used to show the impacts of interior fluid pressure on the dynamic characteristics along with dynamical system parameters. It is suggested to used multi-degree-of-freedom (MDOF) model to simulate the hemispherical solid shell with fluid interaction. A MDOF model can separate the dynamic parameters for solid and fluid parts. The impacts of fluid pressure variation can be modelled on the sensitive modes using linear and nonlinear regression.

REFERENCES

Aaslid, R., Lundar, T., Lindegaard, K., & Nornes, H. (1986). Estimation of cerebral perfusion pressure from arterial blood pressure and transcranial Doppler recordings *Intracranial pressure VI* (pp. 226-229): Springer.

Adson, A., & Lillie, W. (1927). The relationship of intracranial pressure, choked disc, and intraocular tension. *Trans Am Acad Opthalmol, 30*, 138-154.

Advani, S., & Lee, Y.-C. (1970). Free vibrations of fluid-filled spherical shells. *Nasa Technical Resports Server*.

Aiolfi, A., Benjamin, E., Khor, D., Inaba, K., Lam, L., & Demetriades, D. (2017). Brain trauma foundation guidelines for intracranial pressure monitoring: Compliance and effect on outcome. *World journal of surgery, 41*(6), 1543-1549.

Allemang, R. J. (2003). The modal assurance criterion–twenty years of use and abuse. *Sound and vibration, 37*(8), 14-23.

ANSYS, A. (2017). Theory Manual. Release 18.2: Ansys, Canonsburg, Pa, USA.

Aschoff, A., Kremer, P., Hashemi, B., & Kunze, S. (1999). The scientific history of hydrocephalus and its treatment. *Neurosurgical review, 22*(2-3), 67-93.

Avaitable, P. (2018). *Modal Testing a Practitioner's Guide*. Hoboken, New Jersey, USA: Wiley.

Avitabile, P. (2001). Experimental modal analysis. *Sound and vibration, 35*(1), 20-31.

Bai, M. R., & Wu, K. (1994). Free vibration of a thin spherical shell containing a compressible fluid. *The journal of the Acoustical society of America, 95*(6), 3300-3310.

Baker, W. E. (1961). Axisymmetric modes of vibration of thin spherical shell. *The journal of the Acoustical society of America, 33*(12), 1749-1758.

Bauer, D. F., Razdan, S. N., Bartolucci, A. A., & Markert, J. M. (2011). Meta-analysis of hemorrhagic complications from ventriculostomy placement by neurosurgeons. *Neurosurgery, 69*(2), 255-260.

Bekar, A., Doğan, Ş., Abaş, F., Caner, B., Korfalı, G., Kocaeli, H., . . . Korfalı, E. (2009). Risk factors and complications of intracranial pressure monitoring with a fiberoptic device. *Journal of Clinical Neuroscience, 16*(2), 236-240.

Bellner, J., Romner, B., Reinstrup, P., Kristiansson, K.-A., Ryding, E., & Brandt, L. (2004). Transcranial Doppler sonography pulsatility index (PI) reflects intracranial pressure (ICP). *Surgical neurology, 62*(1), 45-51.

Betts, J. (2017). *Anatomy & Physiology-Rice University OpenStax CNX pp 787-846*. Retrieved from

Binz, D. D., Toussaint, L. G., & Friedman, J. A. (2009). Hemorrhagic complications of ventriculostomy placement: a meta-analysis. *Neurocritical care, 10*(2), 253.

Brandt, A. (2011). *Noise and vibration analysis: signal analysis and experimental procedures*: John Wiley & Sons.

Cardim, D., Robba, C., Bohdanowicz, M., Donnelly, J., Cabella, B., Liu, X., . . . Czosnyka, M. (2016). Non-invasive Monitoring of Intracranial Pressure Using Transcranial Doppler Ultrasonography: Is It Possible? *Neurocritical care*, 1-19.

Chan, K.-H., Miller, J. D., Dearden, N. M., Andrews, P. J., & Midgley, S. (1992). The effect of changes in cerebral perfusion pressure upon middle cerebral artery blood flow velocity and jugular bulb venous oxygen saturation after severe brain injury. *Journal of neurosurgery, 77*(1), 55-61.

Chen, W., & Ding, H. (1999). Natural frequencies of a fluid-filled anisotropic spherical shell. *The journal of the Acoustical society of America, 105*(1), 174-182.

Cheng, J., & Reichert, K. (1998). Adult and Child—Head Anatomy *Frontiers in Head and Neck Injury* (pp. 3-17): IOS Press, Washington, DC.

Crystal-Instrument-Corporation. (2017). EDM Modal Unser's Manual: Complete Modal Testing and Analysis Suite (Version 7.0). Santa Clara, California, USA.

Czosnyka, M., & Pickard, J. D. (2004). Monitoring and interpretation of intracranial pressure. *Journal of Neurology, Neurosurgery & Psychiatry, 75*(6), 813-821. doi:10.1136/jnnp.2003.033126

de Riva, N., Budohoski, K. P., Smielewski, P., Kasprowicz, M., Zweifel, C., Steiner, L. A., . . . Czosnyka, M. (2012). Transcranial Doppler pulsatility index: what it is and what it isn't. *Neurocritical care, 17*(1), 58-66.

Delille, R., Lesueur, D., Potier, P., Drazetic, P., & Markiewicz, E. (2007). Experimental study of the bone behaviour of the human skull bone for the development of a physical head model. *International Journal of Crashworthiness, 12*(2), 101-108.

DIGiovanii, P. R., & Dugundji, J. (1965). *Vibrations of freely-supported orthotropic cylindrical shells under internal pressure*. Retrieved from

Duffey, T. A., & Romero, C. (2003). Strain growth in spherical explosive chambers subjected to internal blast loading. *International Journal of Impact Engineering, 28*(9), 967-983.

El Baroudi, A., Razafimahery, F., & Rakotomanana-Ravelonarivo, L. (2012a). Study of a spherical head model. Analytical and numerical solutions in fluid–structure interaction approach. *International Journal of Engineering Science, 51*, 1-13.

El Baroudi, A., Razafimahery, F., & Rakotomanana-Ravelonarivo, L. (2012b). Three-dimensional modal analysis of an idealized human head including fluid–structure interaction effects. *Acta Mechanica, 223*(9), 1899-1915.

Engin, A., & Liu, Y. K. (1970). Axisymmetric response of a fluid-filled spherical shell in free vibrations. *Journal of biomechanics, 3*(1), 11-22.

Engin, A. E. (1969). Vibrations of Fluid-Filled Spherical Shells. *The journal of the Acoustical society of America, 46*(1B), 186-190.

Engin, A. E., & Liu, Y. K. (1970). Axisymmetric response of a fluid-filled spherical shell in free vibrations. *Journal of biomechanics, 3*(1), 11-16.

Eslaminejad, A., Hosseini Farid, M., Ziejewski, M., & Karami, G. (2018). Brain Tissue Constitutive Material Models and the Finite Element Analysis of Blast-Induced Traumatic Brain Injury. *Scientia Iranica*, -. doi:10.24200/sci.2018.20888

Eslaminejad, A., Ramzanpour, M., Hosseini-Farid, M., Ziejewski, M., & Karami, G. (2018). CEREBROSPINAL FLUID-SKULL INTERACTION ANALYSIS FOR A NON-INVASIVE INTRACRANIAL MONITORING TECHNIQUE.

Eslaminejad, A., Sarvghad-Moghaddam, H., Rezaei, A., Ziejewski, M., & Karami, G. (2016). *Comparison of Brain Tissue Material Finite Element Models Based on Threshold for Traumatic Brain Injury.* Paper presented at the ASME 2016 International Mechanical Engineering Congress and Exposition.

Eslaminejad, A., Ziejewski, M., & Karami, G. (2019a). An experimental–numerical modal analysis for the study of shell-fluid interactions in a clamped hemispherical shell. *Applied Acoustics, 152*, 110-117.

Eslaminejad, A., Ziejewski, M., & Karami, G. (2019b). Vibrational Properties of a Hemispherical Shell With Its Inner Fluid Pressure: An Inverse Method for Noninvasive Intracranial

Pressure Monitoring. *Journal of Vibration and Acoustics, 141*(4), 041002-041002-041007. doi:10.1115/1.4042928

Evans, F. G., & Lissner, H. R. (1957). Tensile and compressive strength of human parietal bone. *Journal of Applied Physiology, 10*(3), 493-497.

Ewins, D. (2000). *Modal Testing: Theory, Practice, and Application* (2nd ed.). Baldock, Hertfordshire, England Research Studies Press.

Farid, M. H., Eslaminejad, A., Ziejewski, M., & Karami, G. (2017). *A Study on the Effects of Strain Rates on Characteristics of Brain Tissue.* Paper presented at the ASME 2017 International Mechanical Engineering Congress and Exposition.

Fung, Y. (1957). On the vibration of thin cylindrical shells under internal pressure. *Journal of the Aeronautical Sciences, 24*(9), 650-660.

Gautham, B., & Ganesan, N. (1992). Free vibration analysis of thick spherical shells. *Computers & structures, 45*(2), 307-313.

Greenberg, M. S. (2016). Treatment of hydrocephalus. *Handbook of neurosurgery. 8th ed. New York: Thieme*, 414-437.

Haddad, S., Aldawood, A., Alferayan, A., Russell, N., Tamim, H., & Arabi, Y. (2011). Relationship between intracranial pressure monitoring and outcomes in severe traumatic brain injury patients. *Anaesthesia and intensive care, 39*(6), 1043.

Håkansson, B., Brandt, A., Carlsson, P., & Tjellström, A. (1994). Resonance frequencies of the human skull in vivo. *The journal of the Acoustical society of America, 95*(3), 1474-1481.

Hallquist, J. O. (2006). LS-DYNA theory manual. *Livermore software Technology corporation, 3*, 25-31.

Harary, M., Dolmans, R. G., & Gormley, W. B. (2018). Intracranial Pressure Monitoring—Review and Avenues for Development. *Sensors, 18*(2), 465.

Hirai, T., & Kuroda, M. (1989). Analysis of natural vibrations of a spherical shell with variable thickness. *The journal of the Acoustical society of America, 86*(5), 1864-1875.

HyperMesh, A. (2010). 11.0. Altair Engineering. *Inc., Troy, MI, USA*.

Junger, M. C. (1952). Vibrations of Elastic Shell in a Fluid Medium and the Associated Radiation of Sound. *Journal of Applied Mechanics, Vol. 19, Trans. ASME, 74*, 439-445.

Kalnins, A. (1964). Effect of bending on vibrations of spherical shells. *The journal of the Acoustical society of America, 36*(1), 74-81.

Kashif, F., Heldt, T., & Verghese, G. (2008). *Model-based estimation of intracranial pressure and cerebrovascular autoregulation.* Paper presented at the Computers in Cardiology, 2008.

Kashif, F. M., Verghese, G. C., Novak, V., Czosnyka, M., & Heldt, T. (2012). Model-based noninvasive estimation of intracranial pressure from cerebral blood flow velocity and arterial pressure. *Science translational medicine, 4*(129), 129ra144-129ra144.

Kasuga, Y., Nagai, H., Hasegawa, Y., & Nitta, M. (1987). Transmission characteristics of pulse waves in the intracranial cavity of dogs. *Journal of neurosurgery, 66*(6), 907-914.

Kawoos, U., McCarron, R. M., Auker, C. R., & Chavko, M. (2015). Advances in intracranial pressure monitoring and its significance in managing traumatic brain injury. *International journal of molecular sciences, 16*(12), 28979-28997.

Khalil, T. B., Viano, D., & Smith, D. (1979). Experimental analysis of the vibrational characteristics of the human skull. *Journal of Sound and Vibration, 63*(3), 351-376.

Khan, M. N., Shallwani, H., Khan, M. U., & Shamim, M. S. (2017). Noninvasive monitoring intracranial pressure–A review of available modalities. *Surgical neurology international, 8*.

Kristiansson, H., Nissborg, E., Bartek Jr, J., Andresen, M., Reinstrup, P., & Romner, B. (2013). Measuring elevated intracranial pressure through noninvasive methods: a review of the literature. *Journal of neurosurgical anesthesiology, 25*(4), 372-385.

Laksari, K., Kurt, M., Babaee, H., Kleiven, S., & Camarillo, D. (2018). Mechanistic Insights into Human Brain Impact Dynamics through Modal Analysis. *Physical Review Letters, 120*(13), 138101.

Lamb, H. (1882). On the vibrations of a spherical shell. *Proceedings of the London Mathematical Society, 1*(1), 50-56.

Lawson, C. L., & Hanson, R. J. (1995). *Solving least squares problems* (Vol. 15): Siam.

Lee, J. (2009). Free vibration analysis of spherical caps by the pseudospectral method. *Journal of Mechanical Science and Technology, 23*(1), 221-228.

Levinsky, A., Papyan, S., Weinberg, G., Stadheim, T., & Eide, P. K. (2016). Non-invasive estimation of static and pulsatile intracranial pressure from transcranial acoustic signals. *Medical engineering & physics, 38*(5), 477-484.

Liau, J. (2000). *Noninvasive methods to monitor intracranial pressure: An exploratory study. Dissertation.* (Ph.D. Dissertation), Stanford University.

Love, A. E. H. (1888). The small free vibrations and deformation of a thin elastic shell. *Philosophical Transactions of the Royal Society of London. A, 179*, 491-546.

Margulies, S. S., & Thibault, K. L. (2000). Infant skull and suture properties: measurements and implications for mechanisms of pediatric brain injury. *Journal of biomechanical engineering, 122*(4), 364-371.

McElhaney, J. H., Fogle, J. L., Melvin, J. W., Haynes, R. R., Roberts, V. L., & Alem, N. M. (1970). Mechanical properties of cranial bone. *Journal of biomechanics, 3*(5), 495-511.

Mendis, K., Stalnaker, R., & Advani, S. (1995). A constitutive relationship for large deformation finite element modeling of brain tissue. *Journal of biomechanical engineering, 117*(3), 279-285.

Miserentino, R., & Vosteen, L. F. (1965). *Vibration tests of pressurized thin-walled cylindrical shells*. Retrieved from

Morse, P. M. (1936). *Vibration and sound* (Vol. 3): McGraw-Hill New York.

Motherway, J. A., Verschueren, P., Van der Perre, G., Vander Sloten, J., & Gilchrist, M. D. (2009). The mechanical properties of cranial bone: the effect of loading rate and cranial sampling position. *Journal of biomechanics, 42*(13), 2129-2135.

Naghdi, P. M., & Kalnins, A. (1962). On vibrations of elastic spherical shells. *Journal of Applied Mechanics, 29*(1), 65-72.

Naqvi, J., Yap, K. H., Ahmad, G., & Ghosh, J. (2013). Transcranial Doppler ultrasound: a review of the physical principles and major applications in critical care. *International journal of vascular medicine, 2013*.

Padayachy, L. C. (2016). Non-invasive intracranial pressure assessment. *Child's Nervous System*, 1-11.

Padayachy, L. C., Figaji, A. A., & Bullock, M. (2010). Intracranial pressure monitoring for traumatic brain injury in the modern era. *Child's Nervous System, 26*(4), 441-452.

Petkus, V., Ragauskas, A., & Jurkonis, R. (2002). Investigation of intracranial media ultrasonic monitoring model. *Ultrasonics, 40*(1), 829-833.

Piacsek, A. A., Abdul-Wahid, S., & Taylor, R. (2012). Resonance frequencies of a spherical aluminum shell subject to static internal pressure. *The journal of the Acoustical society of America, 131*(6), EL506-EL512.

Popovic, D., Khoo, M., & Lee, S. (2009). Noninvasive monitoring of intracranial pressure. *Recent patents on biomedical engineering, 2*(3), 165-179.

Raboel, P., Bartek, J., Andresen, M., Bellander, B., & Romner, B. (2012). Intracranial pressure monitoring: invasive versus non-invasive methods—a review. *Critical care research and practice, 2012*.

Rand, R., & DiMaggio, F. (1967). Vibrations of Fluid-Filled Spherical and Spheroidal Shells. *The journal of the Acoustical society of America, 42*(6), 1278-1286.

Ristic, A., Sutter, R., & Steiner, L. A. (2015). Current neuromonitoring techniques in critical care. *Journal of Neuroanaesthesiology and Critical Care, 2*(2), 97.

Robba, C., Bacigaluppi, S., Cardim, D., Donnelly, J., Bertuccio, A., & Czosnyka, M. (2015). Non-invasive assessment of intracranial pressure. *Acta Neurologica Scandinavica*.

Sakka, L., Coll, G., & Chazal, J. (2011). Anatomy and physiology of cerebrospinal fluid. *European annals of otorhinolaryngology, head and neck diseases, 128*(6), 309-316.

Sarvghad-Moghaddam, H., Rezaei, A., Ziejewski, M., & Karami, G. (2015). A comparative study on the protection efficiency of combat helmets against ballistic impacts and blast waves. *Journal of Head Trauma Rehabiliation*, E66-E66.

Schwarz, B. J., & Richardson, M. H. (1999). Experimental modal analysis. *CSI Reliability week, 35*(1), 1-12.

Shafi, S., Diaz-Arrastia, R., Madden, C., & Gentilello, L. (2008). Intracranial pressure monitoring in brain-injured patients is associated with worsening of survival. *Journal of Trauma and Acute Care Surgery, 64*(2), 335-340.

Silbiger, A. (1962). Nonaxisymmetric modes of vibration of thin spherical shells. *The journal of the Acoustical society of America, 34*(6), 862-862.

Soysal, A. O., & Semlyen, A. (1993). Practical transfer function estimation and its application to wide frequency range representation of transformers. *IEEE Transactions on Power Delivery, 8*(3), 1627-1637.

Srinivasan, V. M., O'Neill, B. R., Jho, D., Whiting, D. M., & Oh, M. Y. (2014). The history of external ventricular drainage: Historical vignette. *Journal of neurosurgery, 120*(1), 228-236.

Steele, C., Zhou, L.-J., Guido, D., Marcus, R., Heinrichs, W., & Cheema, C. (1988). Noninvasive determination of ulnar stiffness from mechanical response—in vivo comparison of stiffness and bone mineral content in humans. *Journal of biomechanical engineering, 110*(2), 87-96.

Stevanovic, M., Wodicka, G. R., Bourland, J. D., Graber, G. P., Foster, K. S., Lantz, G. C., . . . Cymerman, A. (1995). The effect of elevated intracranial pressure on the vibrational response of the ovine head. *Annals of biomedical engineering, 23*(6), 720-727.

Tang, A., Pandit, V., Fennell, V., Jones, T., Joseph, B., O'Keeffe, T., . . . Rhee, P. (2015). Intracranial pressure monitor in patients with traumatic brain injury. *journal of surgical research, 194*(2), 565-570.

Tse, K. M., Lim, S. P., Tan, V. B. C., & Lee, H. P. (2014). A review of head injury and finite element head models. *American Journal of Engineering, Technology and Society, 1*(5), 28-52.

Wikipedia, C. (2018). Cerebrospinal Fuid --- Wikipedia,The Free Encyclopedia. Retrieved from https://en.wikipedia.org/w/index.php?title=Cerebrospinal_fluid&oldid=826520030

Wilkinson, J. (1965). Natural frequencies of closed spherical shells. *The journal of the Acoustical society of America, 38*(2), 367-368.

Wilkinson, J., & Reinsch, C. (1971). Linear Algebra: Handbook for Automatic Computation, vol. 11. *Grundlehren der mathematischen Wissenschaften in Einzeldarstellungen, Bd, 186*.

Wood, J. L. (1971). Dynamic response of human cranial bone. *Journal of biomechanics, 4*(1), IN1-IN3.

Wu, J. Z., Pan, C. S., Wimer, B. M., & Rosen, C. L. (2017). An improved finite element modeling of the cerebrospinal fluid layer in the head impact analysis. *Bio-medical materials and engineering, 28*(2), 187-199.

Zhang, X., Medow, J. E., Iskandar, B. J., Wang, F., Shokoueinejad, M., Koueik, J., & Webster, J. G. (2017). Invasive and noninvasive means of measuring intracranial pressure: a review. *Physiological measurement, 38*(8), R143.

APPENDIX. EXPERIMENTAL MODAL ANALYSIS OF HEMISPHERICAL ALUMINUM SHELL FULLY-FILLED WITH WATER AT DIFFERENT PRESSURE LEVELS

In this section, the experimental results were analyzed using modal extraction techniques are provided. All the results can be categorized into three main frequency domains. All the FRF-summation, CMIF and MMIF stability diagram, and mode shape tables along with the Auto MAC diagram validation, are obtained for the hemisphere fully-filled by water at different pressure level.

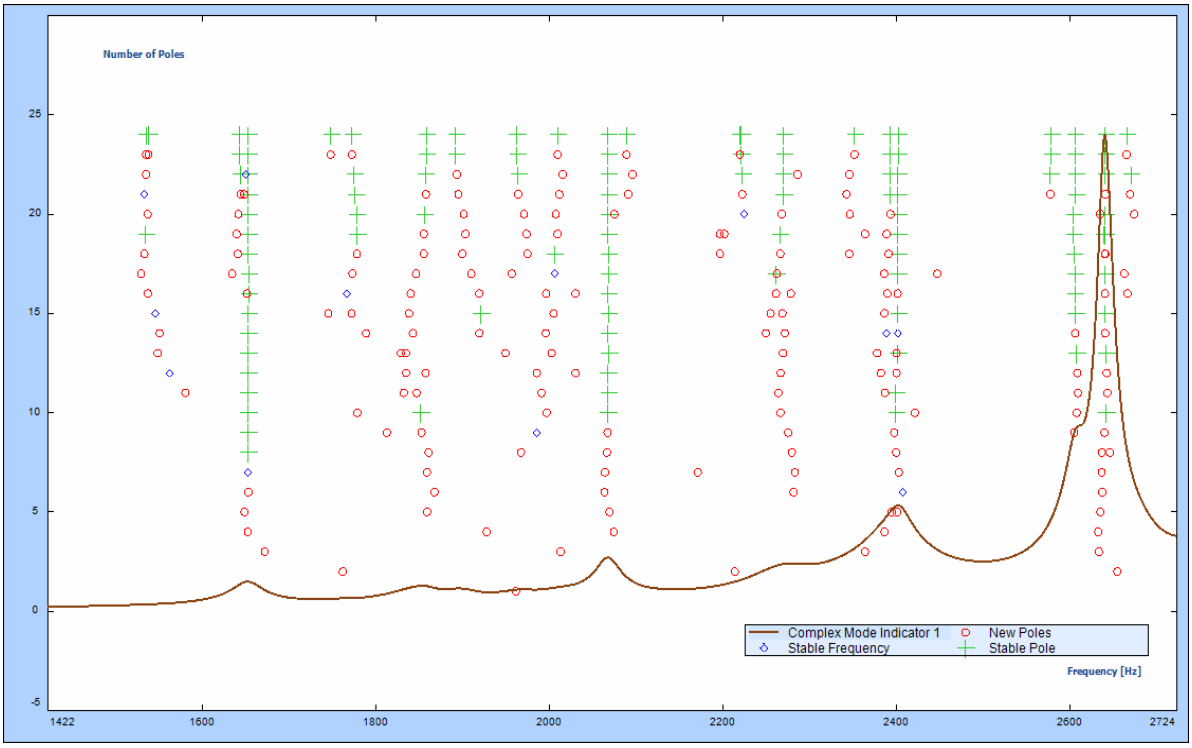

Figure A-1. Stability diagram of the hemispherical head model fully filled with water with internal pressure of 0 kPa within the frequency range from 1500 to 2710 Hz.

Table A-1. Auto MAC Matrix of the extracted modal frequencies for the fully-filled aluminum shell with internal pressure of 0 kPa within the frequency range from 1500 to 2710 Hz.

Mode No.	Frequency (Hz)	Mode 1 1653.121 Hz	Mode 2 1858.837 Hz	Mode 3 2068.20 Hz	Mode 4 2269.905 Hz	Mode 5 2402.289 Hz	Mode 6 2606.102 Hz	Mode 7 2641.324 Hz
Mode 1	1653.121	100	1.973	0.343	3.29	0.293	0.113	0.72
Mode 2	1858.837	1.973	100	0.659	0.93	4.273	0.901	0.992
Mode 3	2068.2	0.343	0.659	100	2.331	1.168	0.249	0.478
Mode 4	2269.905	3.29	0.93	2.331	100	42.18	0.063	0.356
Mode 5	2402.289	0.293	4.273	1.168	42.18	100	0.125	0.173
Mode 6	2606.102	0.113	0.901	0.249	0.063	0.125	100	0.788
Mode 7	2641.324	0.72	0.992	0.478	0.356	0.173	0.788	100

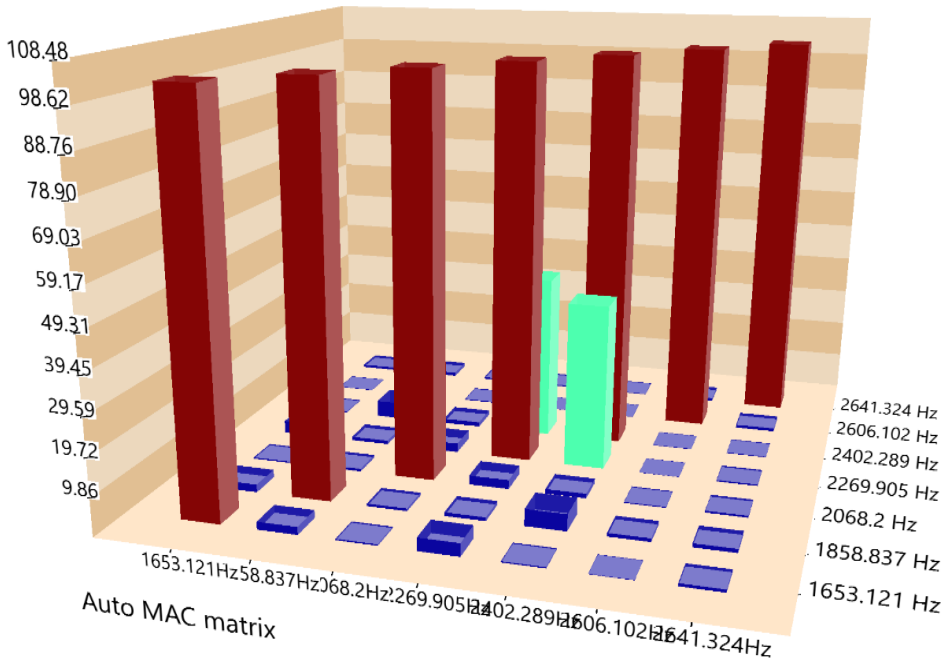

Figure A-2. Display Auto Modal Assurance Criterion (%) of the case with hemispherical with internal pressure of 0 kPa within the frequency range from1500 to 2710 Hz.

Table A-2. Modal Parameter of the case with hemispherical with internal pressure of 0 kPa within the frequency range from 1500 to 2710 Hz.

Mode	Frequency (Hz)	Damping (%)
F#1	1653.121	1.099
F#2	1858.837	1.677
F#3	2068.2	0.742
F#4	2269.905	1.739
F#5	2402.289	0.604
F#6	2606.102	0.562
F#7	2641.324	0.311

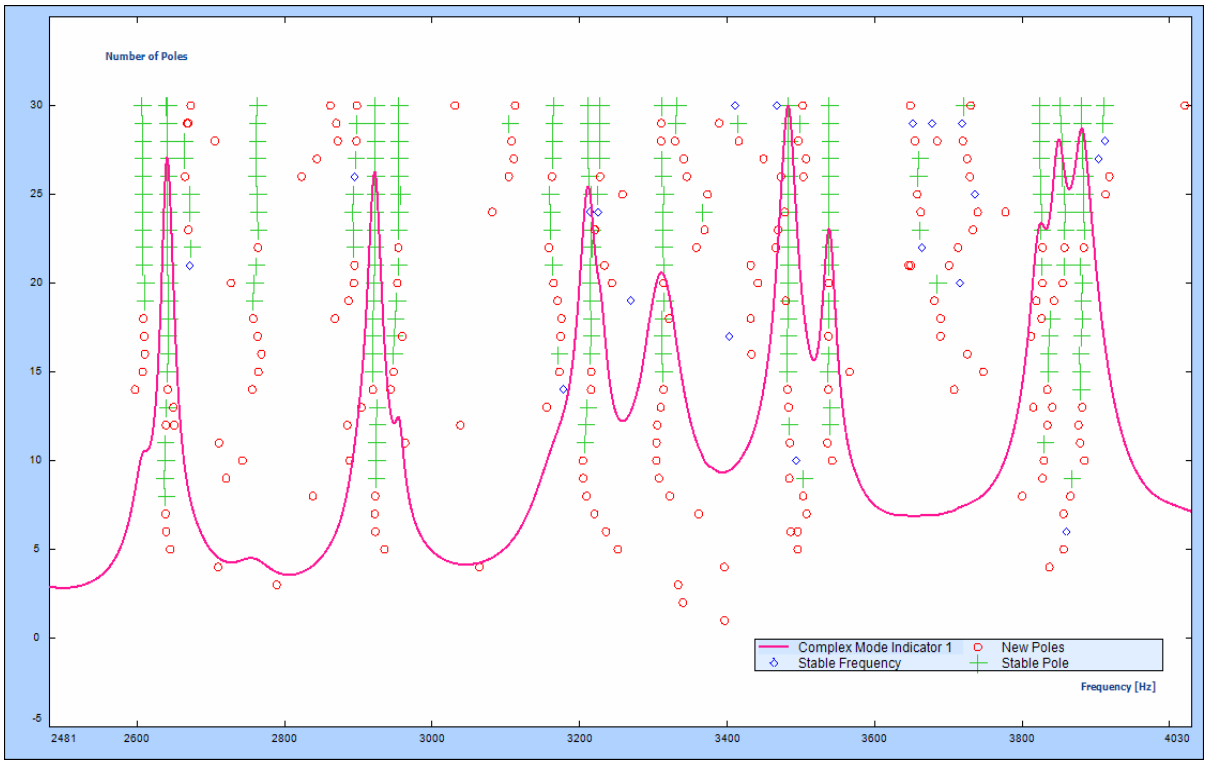

Figure A-3. Stability diagram of the hemispherical head model fully filled with water with internal pressure of 0 kPa within the frequency range from 2490 to 4030 Hz.

Table A-3. Auto MAC Matrix of the extracted modal frequencies for the fully-filled aluminum shell with internal pressure of 0 kPa within the frequency range 2490 to 4030 Hz.

Mode No	Frequency (Hz)	Mode 1 2607.38	Mode 2 2641.69	Mode 3 2761.29	Mode4 2922.36	Mode 5 2954.53	Mode 6 3163.68	Mode 7 3211.09	Mode 8 3311.16	Mode 9 3483.2	Mode 10 3538.46	Mode 11 3824.30	Mode 12 3852.43	Mode 13 3880.60
Mode 1	2607.31	100	2.905	6.063	0.539	1.216	3.717	0.279	1.304	0.144	0.355	1.759	0.05	0.451
Mode 2	2641.69	2.905	100	2.136	0.394	0.13	5.523	0.525	0.701	0.749	0.426	0.243	0.003	0.151
Mode 3	2761.29	6.063	2.136	100	1.539	2.149	19.589	0.265	2.255	4.355	2.222	0.976	0.099	2.506
Mode 4	2922.36	0.539	0.394	1.539	100	1.399	0.775	0.243	0.382	0.209	0.01	0.071	0.033	0.305
Mode 5	2954.54	1.216	0.13	2.149	1.399	100	5.808	0.208	0.098	1.207	0.797	0.13	0.021	0.505
Mode 6	3163.68	3.717	5.523	19.589	0.775	5.808	100	1.857	1.156	3.938	3.038	0.259	0.172	1.077
Mode 7	3211.07	0.279	0.525	0.265	0.243	0.208	1.857	100	2.209	1.15	0.413	0.183	0.913	0.738
Mode 8	3311.18	1.304	0.701	2.255	0.382	0.098	1.156	2.209	100	1.616	0.907	0.871	1.293	2.905
Mode 9	3483.2	0.144	0.749	4.355	0.209	1.207	3.938	1.15	1.616	100	0.758	0.507	0.299	0.12
Mode 10	3538.45	0.355	0.426	2.222	0.01	0.797	3.038	0.413	0.907	0.758	100	0.664	1.104	0.086
Mode 11	3824.31	1.759	0.243	0.976	0.071	0.13	0.259	0.183	0.871	0.507	0.664	100	14.233	0.702
Mode 12	3852.43	0.05	0.003	0.099	0.033	0.021	0.172	0.913	1.293	0.299	1.104	14.233	100	13.335
Mode 13	3880.60	0.451	0.151	2.506	0.305	0.505	1.077	0.738	2.905	0.12	0.086	0.702	13.335	100

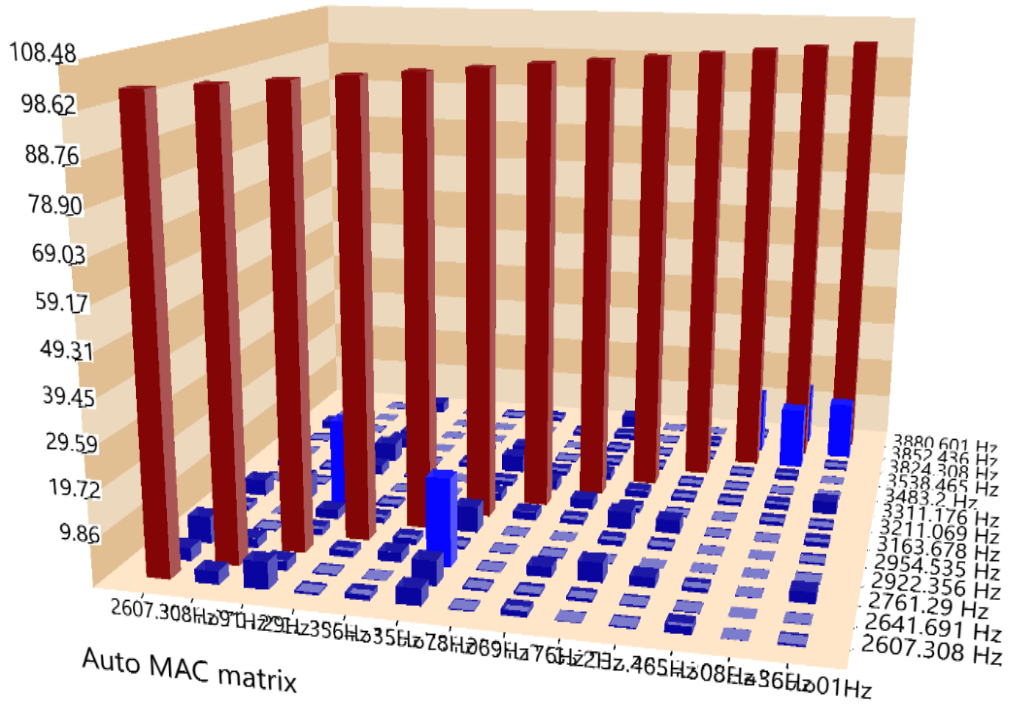

Figure A-4. Display Auto Modal Assurance Criterion (%) of the case with hemispherical with internal pressure of 0 kPa within the frequency range from 2490 to 4030 Hz

Table A-4. Modal Parameter of the case with hemispherical with internal pressure of 0 kPa within the frequency range from 1500 to 2710 Hz.

Mode	Frequency (Hz)	Damping (%)
F#1	2607.308	0.516
F#2	2641.691	0.346
F#3	2761.29	1.107
F#4	2922.356	0.364
F#5	2954.535	0.254
F#6	3163.678	1.018
F#7	3211.069	0.44
F#8	3311.176	0.775
F#9	3483.2	0.384
F#10	3538.465	0.289
F#11	3824.308	0.479
F#12	3852.436	0.487
F#13	3880.601	0.45

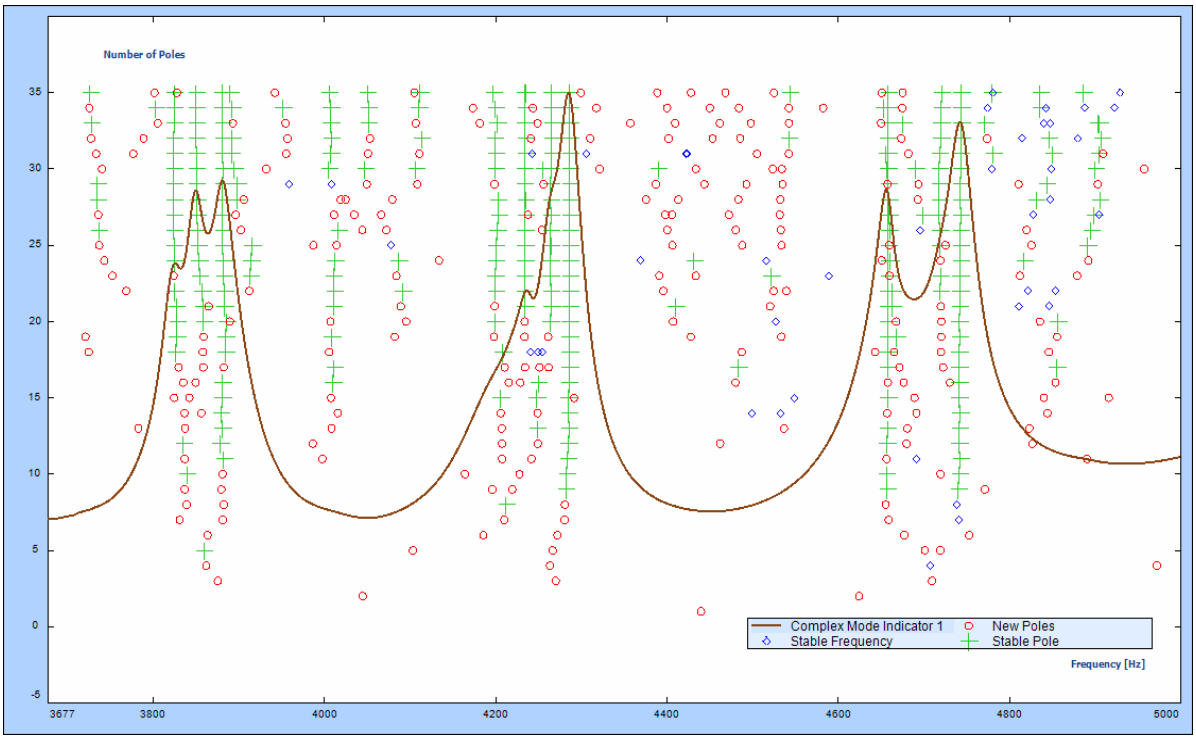

Figure A-5. Stability diagram of the hemispherical head model fully filled with water with internal pressure of 0 kPa within the frequency range 3640 to 5000 Hz

Table A-5. Auto MAC Matrix of the extracted modal frequencies for the fully-filled aluminum shell with internal pressure of 0 kPa within the frequency range 3640 to 5000 Hz

Mode No.	Frequency (Hz)	M 1 3824.188 Hz	M 2 3850.196 Hz	M 3 3882.412 Hz	M 4 4199.500 Hz	M 5 4233.932 Hz	M 6 4265.227 Hz	M 7 4286.454 Hz	M 8 4658.418 Hz	M 9 4718.014 Hz	M 10 4742.849 Hz
M 1	3824.188	100	3.902	2.354	0.179	1.515	0.246	0.141	2.508	2.149	1.976
M 2	3850.196	3.902	100	11.915	1.507	0.448	0.815	0.089	1.122	3.542	2.002
M 3	3882.412	2.354	11.915	100	1.149	0.439	0.002	0.218	3.384	2.884	4.371
M 4	4199.5	0.179	1.507	1.149	100	4.267	2.816	0.38	0.261	0.259	0.682
M 5	4233.932	1.515	0.448	0.439	4.267	100	4.435	0.845	1.04	1.323	0.031
M 6	4265.227	0.246	0.815	0.002	2.816	4.435	100	3.521	0.074	0.09	1.682
M 7	4286.454	0.141	0.089	0.218	0.38	0.845	3.521	100	0.054	0.005	0.601
M 8	4658.418	2.508	1.122	3.384	0.261	1.04	0.074	0.054	100	14.817	4.051
M 9	4718.014	2.149	3.542	2.884	0.259	1.323	0.09	0.005	14.817	100	17.168
M 10	4742.849	1.976	2.002	4.371	0.682	0.031	1.682	0.601	4.051	17.168	100

121

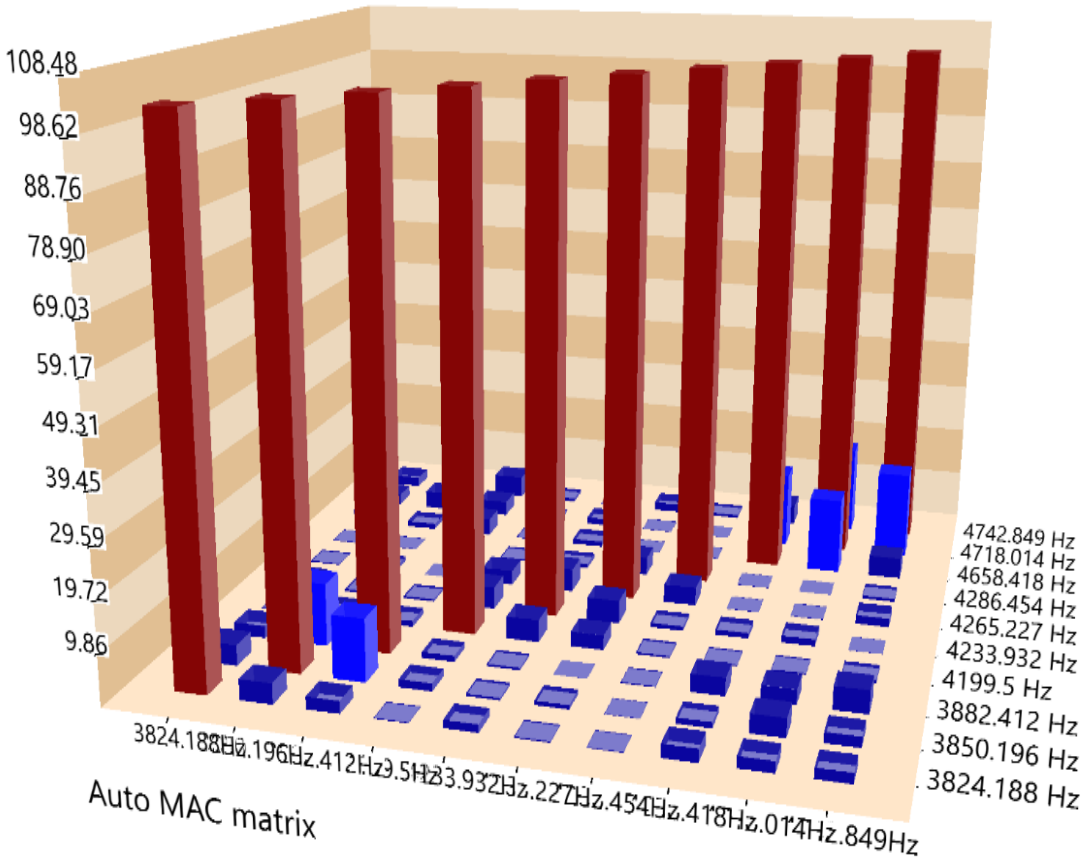

Figure A-6. Display Auto Modal Assurance Criterion (%) of the case with hemispherical with internal pressure of 0 kPa within the frequency range from 3640 to 5000 Hz.

Table A-6. Modal Parameter of the case with hemispherical with internal pressure of 0 kPa within the frequency range from 3640 to 5000 Hz

Mode	Frequency (Hz)	Damping (%)
F#1	3824.188	0.39
F#2	3850.196	0.367
F#3	3882.412	0.46
F#4	4199.5	1.19
F#5	4233.932	0.374
F#6	4265.227	0.378
F#7	4286.454	0.345
F#8	4658.418	0.253
F#9	4718.014	0.444
F#10	4742.849	0.366

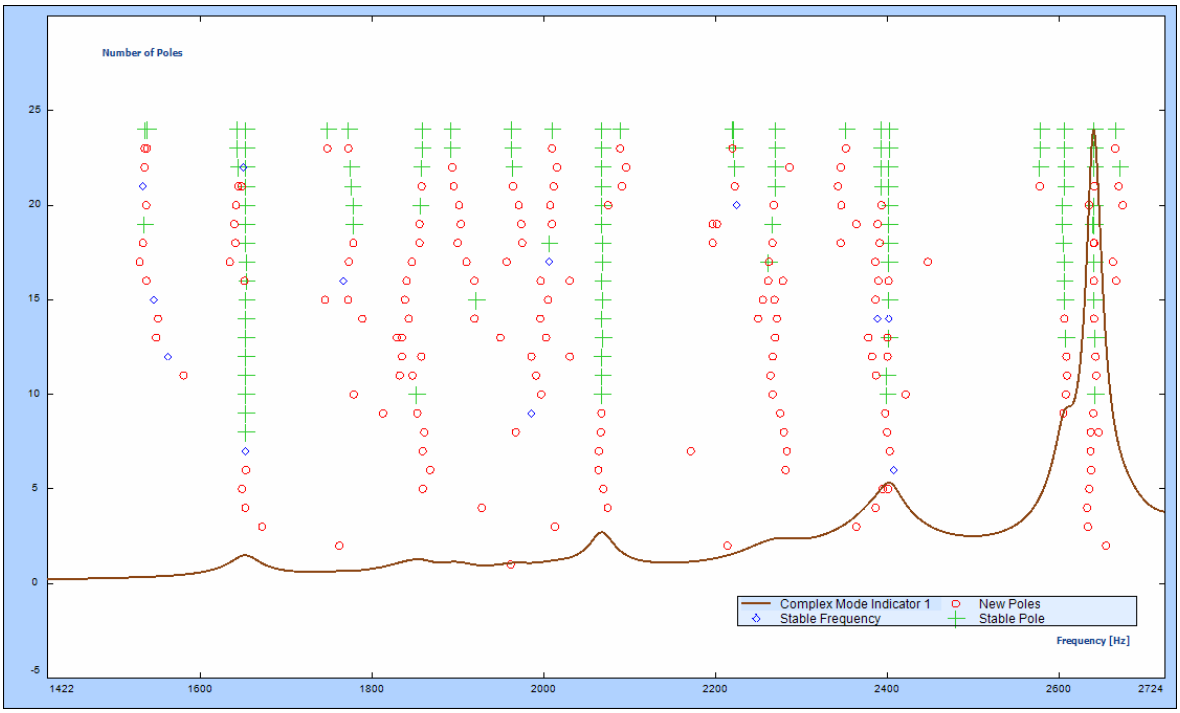

Figure A-7. Stability diagram of the hemispherical head model fully filled with water with internal pressure of 2.5 kPa within the frequency range from 1500 to 2710 Hz.

Table A-7. Auto MAC Matrix of the extracted modal frequencies for the fully-filled aluminum shell with internal pressure of 2.5 kPa within the frequency range from 1500 to 2710 Hz.

Mode No.	Frequency (Hz)	Mode 1 1653.121 Hz	Mode 2 1858.837 Hz	Mode 3 2068.2 Hz	Mode 4 2269.905 Hz	Mode 5 2402.289 Hz	Mode 6 2606.102 Hz	Mode 7 2641.324 Hz
Mode 1	1653.121	100	1.973	0.343	3.29	0.293	0.113	0.72
Mode 2	1858.837	1.973	100	0.659	0.93	4.273	0.901	0.992
Mode 3	2068.2	0.343	0.659	100	2.331	1.168	0.249	0.478
Mode 4	2269.905	3.29	0.93	2.331	100	42.18	0.063	0.356
Mode 5	2402.289	0.293	4.273	1.168	42.18	100	0.125	0.173
Mode 6	2606.102	0.113	0.901	0.249	0.063	0.125	100	0.788
Mode 7	2641.324	0.72	0.992	0.478	0.356	0.173	0.788	100

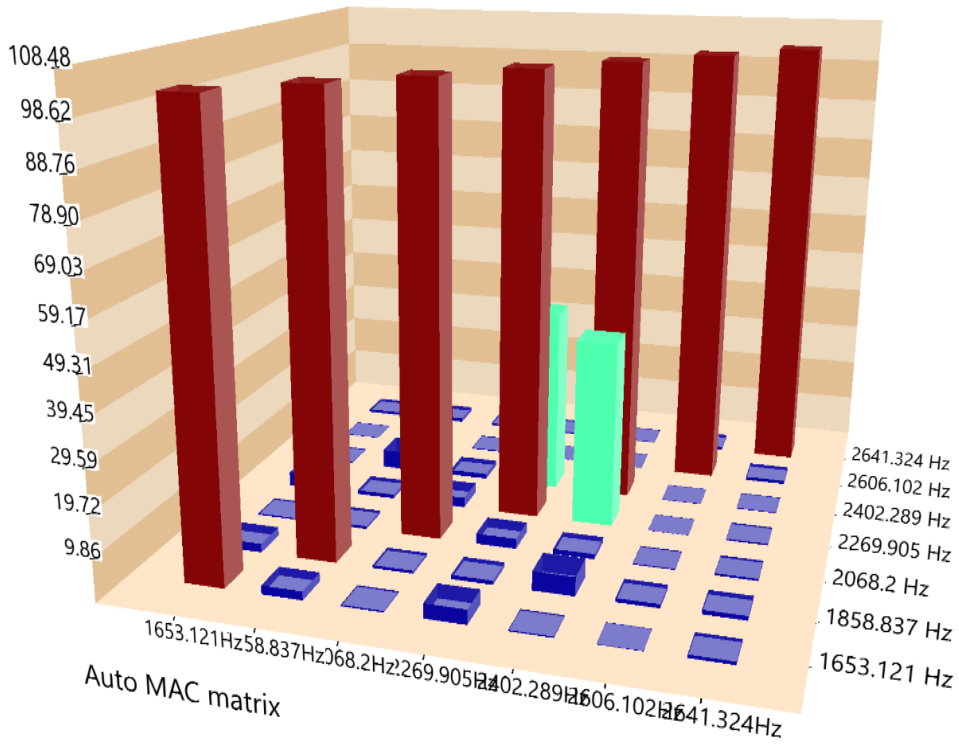

Figure A-8. Display Auto Modal Assurance Criterion (%) of the case with hemispherical with internal pressure of 2.5 kPa within the frequency range from1500 to 2710 Hz.

Table A-8. Modal Parameter of the case with hemispherical with internal pressure of 2.5 kPa within the frequency range from 1500 to 2710 Hz.

Mode	Frequency (Hz)	Damping (%)
F#1	1653.121	1.099
F#2	1858.837	1.677
F#3	2068.2	0.742
F#4	2269.905	1.739
F#5	2402.289	0.604
F#6	2606.102	0.562
F#7	2641.324	0.311

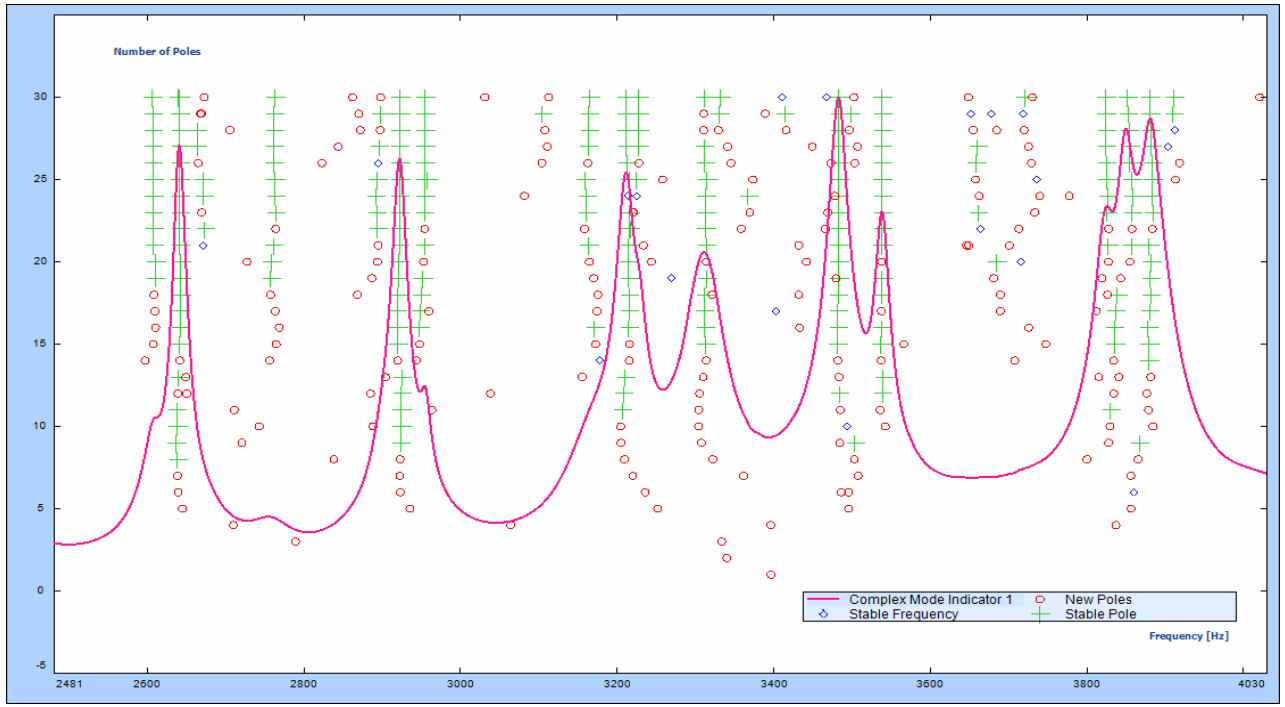

Figure A-9. Stability diagram of the hemispherical head model fully filled with water with internal pressure of 2.5 kPa within the frequency range from 2490 to 4030 Hz.

Table A-9. Auto MAC Matrix of the extracted modal frequencies for the fully-filled aluminum shell with internal pressure of 2.5 kPa within the frequency range 2490 to 4030 Hz.

Mode No.	Frequency (Hz)	Mode 1 2607.308 Hz	Mode 2 2641.691 Hz	Mode 3 2761.29 Hz	Mode 4 2922.356 Hz	Mode 5 2954.535 Hz	Mode 6 3163.678 Hz	Mode 7 3211.069 Hz	Mode 8 3311.176 Hz	Mode 9 3483.200 Hz	Mode 10 3538.465 Hz	Mode 11 3824.308 Hz	Mode 12 3852.436 Hz	Mode 13 3880.601 Hz
Mode 1	2607.308	100	2.905	6.063	0.539	1.216	3.717	0.279	1.304	0.144	0.355	1.759	0.05	0.451
Mode 2	2641.691	2.905	100	2.136	0.394	0.13	5.523	0.525	0.701	0.749	0.426	0.243	0.003	0.151
Mode 3	2761.29	6.063	2.136	100	1.539	2.149	19.58	0.265	2.255	4.355	2.222	0.976	0.099	2.506
Mode 4	2922.356	0.539	0.394	1.539	100	1.399	0.775	0.243	0.382	0.209	0.01	0.071	0.033	0.305
Mode 5	2954.535	1.216	0.13	2.149	1.399	100	5.808	0.208	0.098	1.207	0.797	0.13	0.021	0.505
Mode 6	3163.678	3.717	5.523	19.58	0.775	5.808	100	1.857	1.156	3.938	3.038	0.259	0.172	1.077
Mode 7	3211.069	0.279	0.525	0.265	0.243	0.208	1.857	100	2.209	1.15	0.413	0.183	0.913	0.738
Mode 8	3311.176	1.304	0.701	2.255	0.382	0.098	1.156	2.209	100	1.616	0.907	0.871	1.293	2.905
Mode 9	3483.200	0.144	0.749	4.355	0.209	1.207	3.938	1.15	1.616	100	0.758	0.507	0.299	0.12
Mode 10	3538.465	0.355	0.426	2.222	0.01	0.797	3.038	0.413	0.907	0.758	100	0.664	1.104	0.086
Mode 11	3824.308	1.759	0.243	0.976	0.071	0.13	0.259	0.183	0.871	0.507	0.664	100	14.23	0.702
Mode 12	3852.436	0.05	0.003	0.099	0.033	0.021	0.172	0.913	1.293	0.299	1.104	14.23	100	13.33
Mode 13	3880.601	0.451	0.151	2.506	0.305	0.505	1.077	0.738	2.905	0.12	0.086	0.702	13.33	100

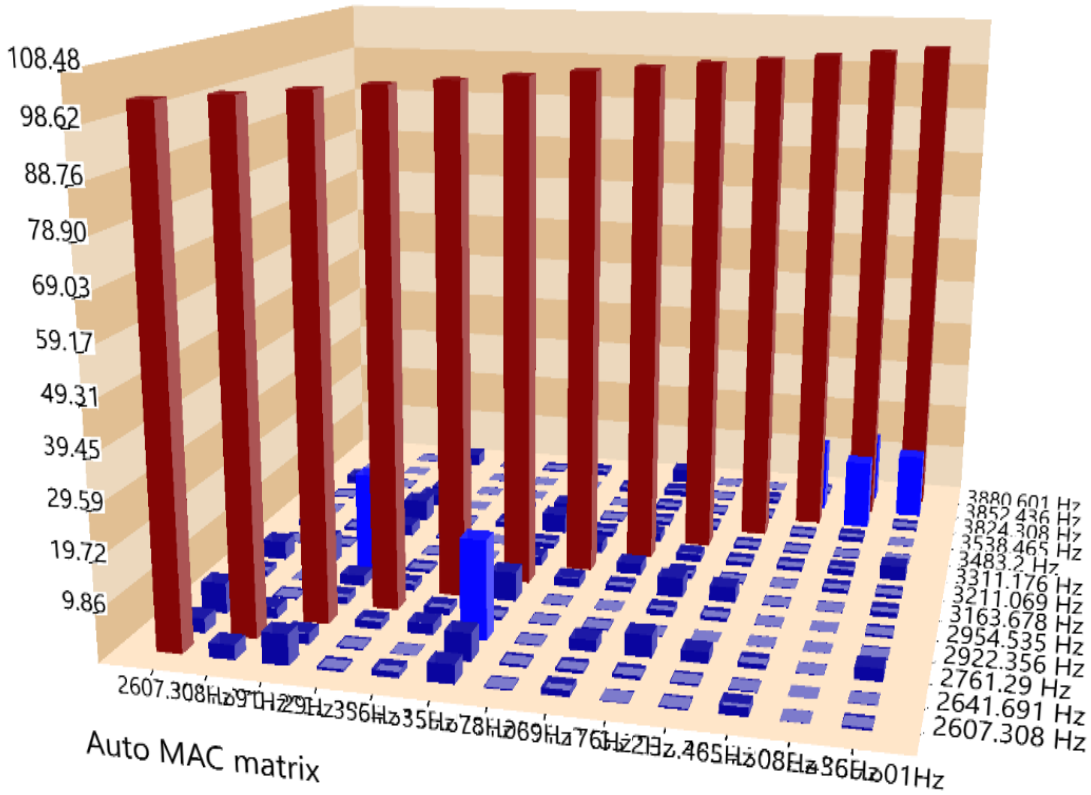

Figure A-10. Display Auto Modal Assurance Criterion (%) of the case with hemispherical with internal pressure of 2.5 kPa within the frequency range from 2490 to 4030 Hz.

Table A-10. Modal Parameter of the case with hemispherical with internal pressure of 2.5 kPa within the frequency range from 2490 to 4030Hz.

Mode	Frequency (Hz)	Damping (%)
F#1	2607.308	0.516
F#2	2641.691	0.346
F#3	2761.29	1.107
F#4	2922.356	0.364
F#5	2954.535	0.254
F#6	3163.678	1.018
F#7	3211.069	0.44
F#8	3311.176	0.775
F#9	3483.2	0.384
F#10	3538.465	0.289
F#11	3824.308	0.479
F#12	3852.436	0.487
F#13	3880.601	0.45

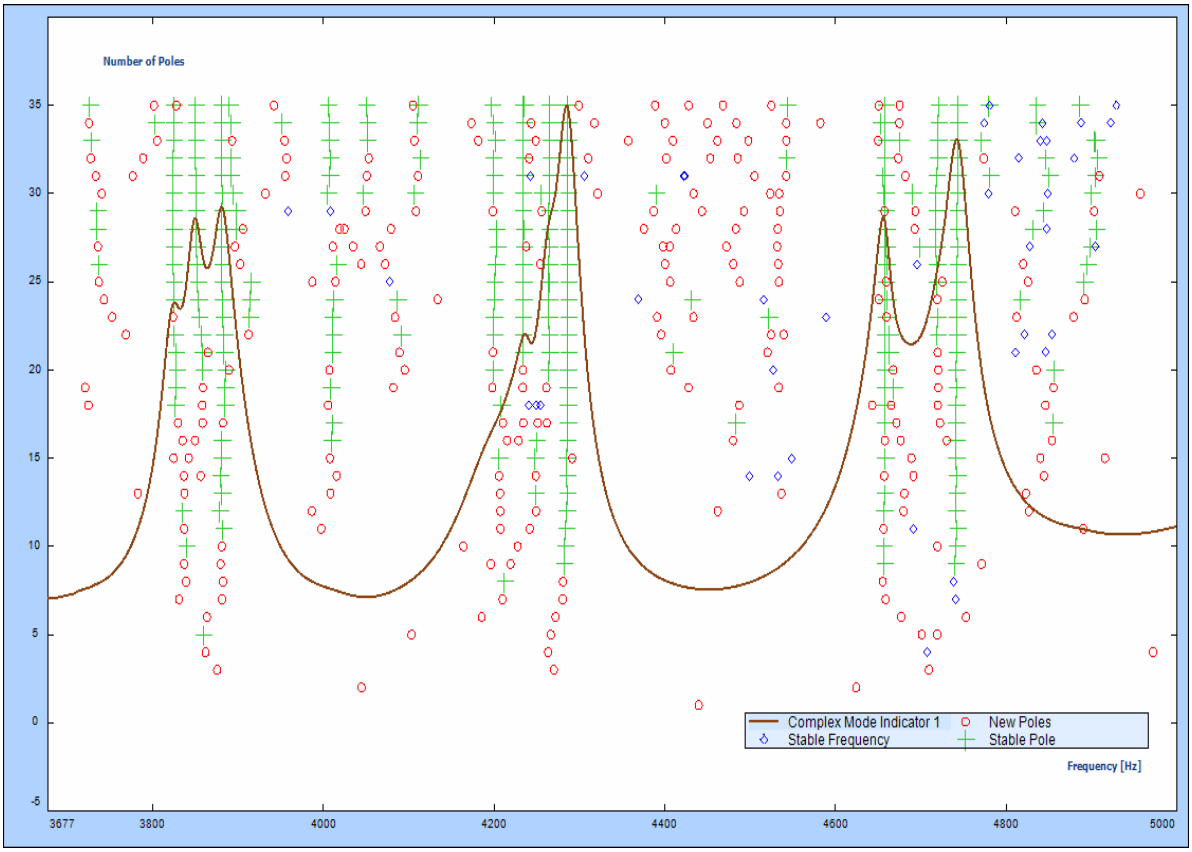

Figure A-11. Stability diagram of the hemispherical head model fully filled with water with internal pressure of 2.5 kPa within the frequency range from 3640 to 5000 Hz.

Table A-11. Auto MAC Matrix of the extracted modal frequencies for the fully-filled aluminum shell with internal pressure of 2.5 kPa within the frequency range 3640 to 5000 Hz.

Mode No.	Frequency (Hz)	Mode 1 3824.188 Hz	Mode 2 3850.196 Hz	Mode 3 3882.412 Hz	Mode 4 4199.5 Hz	Mode 5 4233.932 Hz	Mode 6 4265.227 Hz	Mode 7 4286.454 Hz	Mode 8 4658.418 Hz	Mode 9 4718.014 Hz	Mode 10 4742.849 Hz
Mode 1	3824.18	100	3.902	2.354	0.179	1.515	0.246	0.141	2.508	2.149	1.976
Mode 2	3850.19	3.902	100	11.915	1.507	0.448	0.815	0.089	1.122	3.542	2.002
Mode 3	3882.41	2.354	11.915	100	1.149	0.439	0.002	0.218	3.384	2.884	4.371
Mode 4	4199.5	0.179	1.507	1.149	100	4.267	2.816	0.38	0.261	0.259	0.682
Mode 5	4233.93	1.515	0.448	0.439	4.267	100	4.435	0.845	1.04	1.323	0.031
Mode 6	4265.22	0.246	0.815	0.002	2.816	4.435	100	3.521	0.074	0.09	1.682
Mode 7	4286.45	0.141	0.089	0.218	0.38	0.845	3.521	100	0.054	0.005	0.601
Mode 8	4658.41	2.508	1.122	3.384	0.261	1.04	0.074	0.054	100	14.817	4.051
Mode 9	4718.04	2.149	3.542	2.884	0.259	1.323	0.09	0.005	14.817	100	17.168
Mode 10	4742.84	1.976	2.002	4.371	0.682	0.031	1.682	0.601	4.051	17.168	100

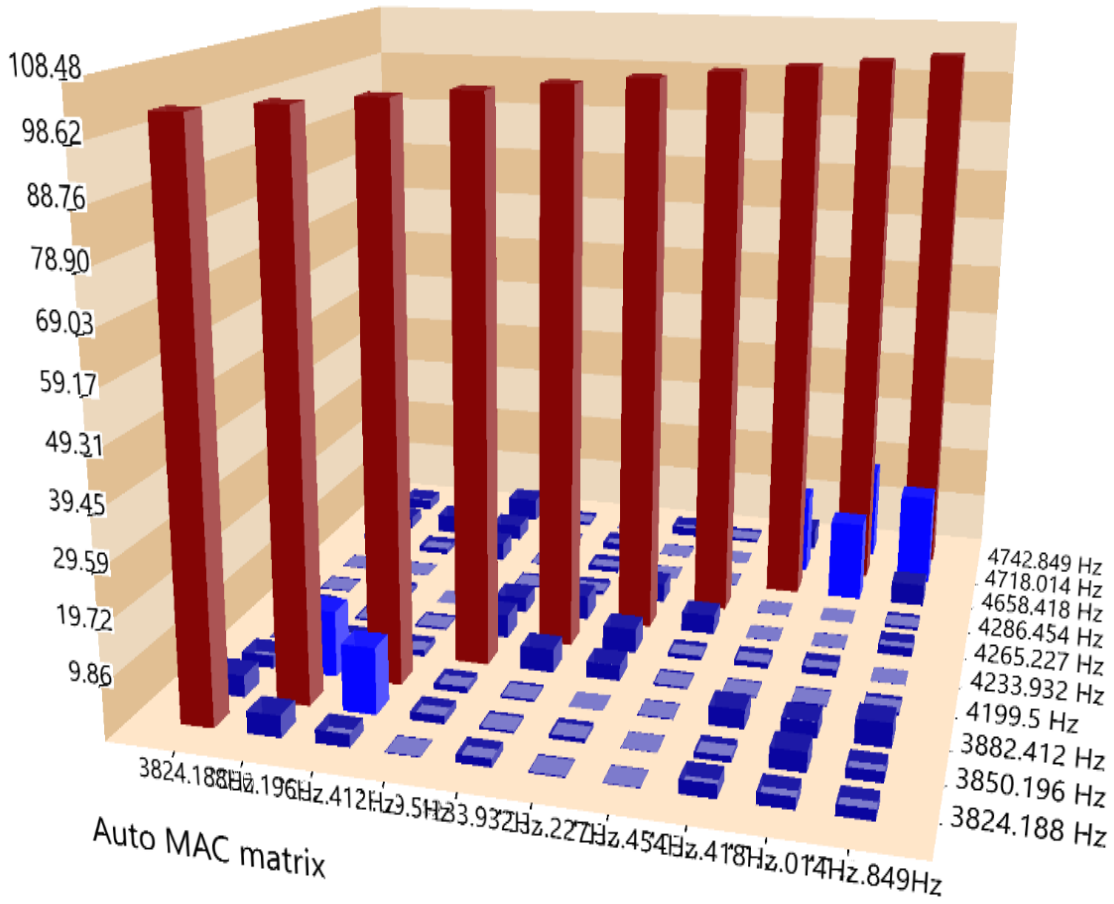

Figure A-12. Display Auto Modal Assurance Criterion (%) of the case with hemispherical with internal pressure of 2.5 kPa within the frequency range from 3640 Hz to 5000 Hz.

Table A-12. Modal Parameter of the case with hemispherical with internal pressure of 2.5 kPa within the frequency range from 3640 to 5000Hz.

Mode	Frequency (Hz)	Damping (%)
F#1	3824.188	0.39
F#2	3850.196	0.367
F#3	3882.412	0.46
F#4	4199.5	1.19
F#5	4233.932	0.374
F#6	4265.227	0.378
F#7	4286.454	0.345
F#8	4658.418	0.253
F#9	4718.014	0.444
F#10	4742.849	0.366

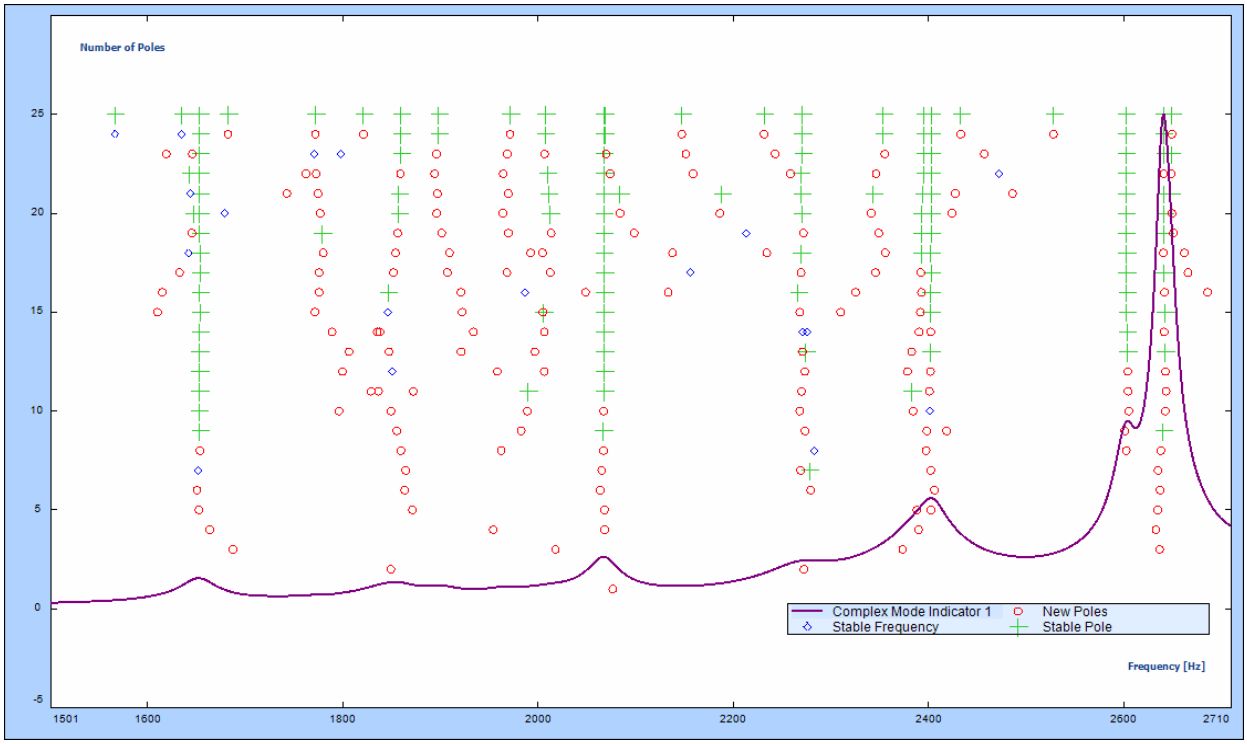

Figure A-13. Stability diagram of the hemispherical head model fully filled with water with internal pressure of 5 kPa within the frequency range from 1500 to 2710 Hz.

Table A-13. Auto MAC Matrix of the extracted modal frequencies for the fully-filled aluminum shell with internal pressure of 5 kPa within the frequency range from 1500 to 2710 Hz.

Mode No.	Frequency (Hz)	Mode 1 1653.911 Hz	Mode 2 1859.546 Hz	Mode 3 2067.282 Hz	Mode 4 2270.608 Hz	Mode 5 2395.526 Hz	Mode 6 2402.479 Hz	Mode 7 2602.133 Hz	Mode 8 2640.572 Hz
Mode 1	1653.911	100	0.255	0.007	8.238	2.02	0.375	0.553	0.464
Mode 2	1859.546	0.255	100	0.413	5.172	1.898	1.268	0.934	0.469
Mode 3	2067.282	0.007	0.413	100	0.301	1.131	1.324	0.52	1.91
Mode 4	2270.608	8.238	5.172	0.301	100	54.264	7.244	0.346	0.316
Mode 5	2395.526	2.02	1.898	1.131	54.264	100	19.414	0.589	2.606
Mode 6	2402.479	0.375	1.268	1.324	7.244	19.414	100	0.891	3.975
Mode 7	2602.133	0.553	0.934	0.52	0.346	0.589	0.891	100	0.837
Mode 8	2640.572	0.464	0.469	1.91	0.316	2.606	3.975	0.837	100

Table A-14. Modal Parameter of the case with hemispherical with internal pressure of 5 kPa within the frequency range from 1500 to 2710Hz.

Mode	Frequency (Hz)	Damping (%)
F#1	1653.911	1.117
F#2	1859.546	1.513
F#3	2067.282	0.802
F#4	2270.608	1.718
F#5	2395.526	1.351
F#6	2402.479	0.623
F#7	2602.133	0.468
F#8	2640.572	0.326

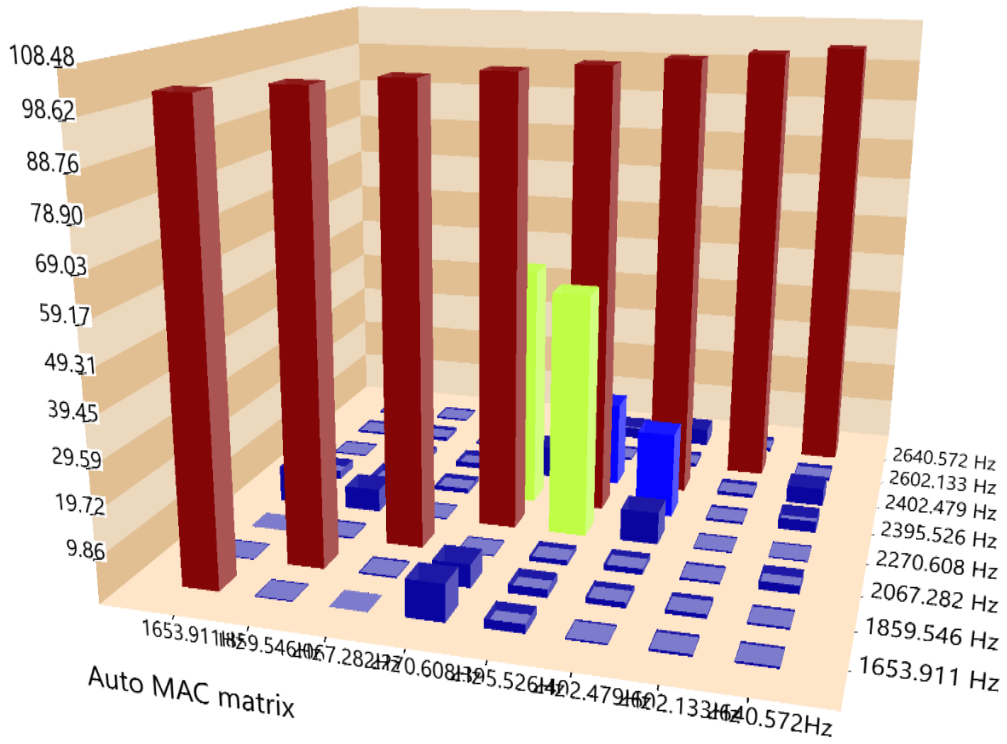

Figure A-14. Display Auto Modal Assurance Criterion (%) of the case with hemispherical with internal pressure of 5 kPa within the frequency range from1500 to 2710 Hz.

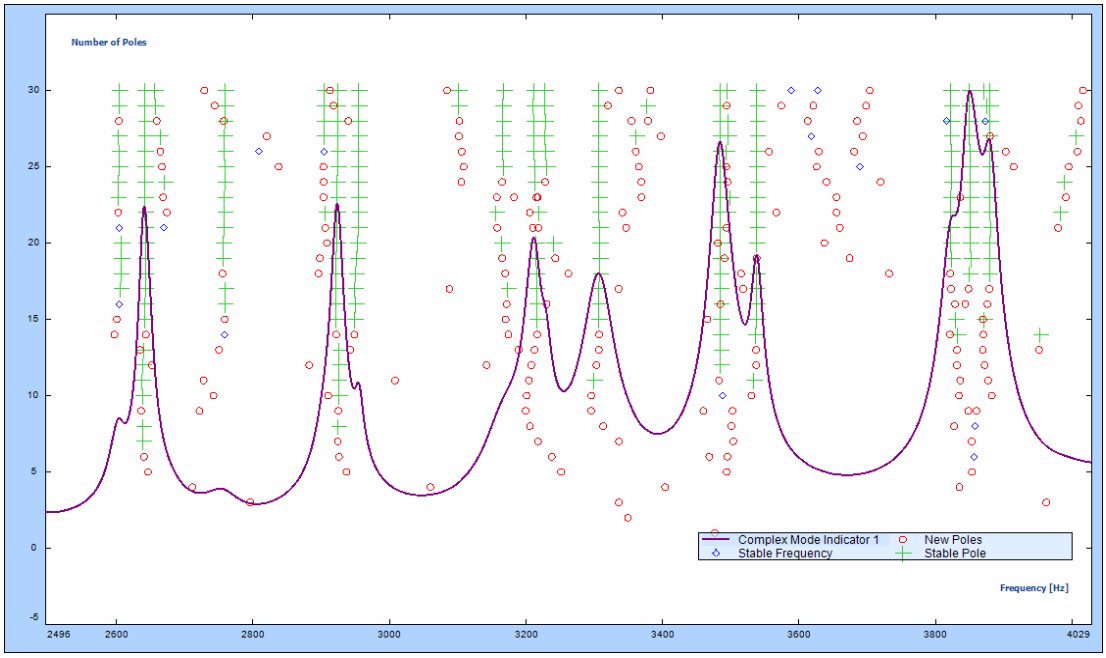

Figure A-15. Stability diagram of the hemispherical head model fully filled with water with internal pressure of 5 kPa within the frequency range from 2490 to 4030 Hz.

Table A-15. Auto MAC Matrix of the extracted modal frequencies for the fully-filled aluminum shell with internal pressure of 5 kPa within the frequency range from 2490 to 4030 Hz.

Mode No.	Frequency (Hz)	Mode 1 2603.212 Hz	Mode 2 2641.56 Hz	Mode 3 2758.384 Hz	Mode 4 2904.037 Hz	Mode 5 2923.635 Hz	Mode 6 2954.428 Hz	Mode 7 3165.273 Hz	Mode 8 3211.045 Hz	Mode 9 3228.117 Hz	Mode 10 3306.453 Hz	Mode 11 3483.961 Hz	Mode 12 3538.026 Hz	Mode 13 3822.803 Hz	Mode 14 3850.668 Hz	Mode 15 3880.235 Hz
M 1	2603.212	100	0.09	8.68	7.41	0.92	0.46	1.03	0.34	0.70	3.72	1.80	0.05	1.27	0.77	0.24
M 2	2641.56	0.01	100	1.11	0.61	0.44	0.11	3.44	0.88	0.39	0.31	0.08	0.16	0.17	0.26	0.01
M 3	2758.384	8.68	1.14	100	10.7	1.80	0.83	2.59	0.35	0.47	1.29	6.56	0.36	0.56	1.21	2.27
M 4	2904.037	7.41	0.61	10.7	100	2.86	1.17	2.02	0.32	0.92	3.13	6.67	0.05	0.64	0.25	1.12
M 5	2923.635	0.92	0.44	1.80	2.86	100	0.23	1.03	0.16	0.07	0.08	0.96	0.15	0.01	0.10	0.03
M 6	2954.428	0.46	0.11	0.83	1.11	0.23	100	0.52	0.22	0.48	0.78	1.30	0.10	0.17	0.01	0.37
M 7	3165.273	1.01	3.42	2.59	2.05	1.03	0.52	100	3.35	0.25	4.29	2.47	0.58	4.28	2.00	1.21
M 8	3211.045	0.34	0.86	0.35	0.32	0.12	0.22	3.34	100	5.80	0.06	0.16	0.82	0.66	1.53	0.28
M 9	3228.117	0.70	0.39	0.47	0.96	0.07	0.48	0.25	5.80	100	0.71	0.65	0.65	0.05	0.31	1.23
M10	3306.453	3.72	0.31	1.29	3.15	0.08	0.78	4.29	0.09	0.17	100	0.05	0.40	0.09	0.06	0.05
M11	3483.961	1.80	0.08	6.56	6.69	0.96	1.30	2.47	0.11	0.65	0.05	100	0.12	0.39	0.06	0.07
M12	3538.026	0.05	0.16	0.36	0.09	0.15	0.10	0.58	0.82	0.65	0.40	0.12	100	0.01	1.09	0.21
M13	3822.803	1.27	0.17	0.56	0.68	0.01	0.17	4.28	0.69	0.05	0.09	0.39	0.01	100	1.65	0.67
M14	3850.668	0.77	0.26	1.21	0.26	0.10	0.01	2.00	1.53	0.31	0.06	0.06	1.09	1.65	100	4.27
M15	3880.235	0.24	0.01	2.27	1.12	0.00	0.37	1.21	0.28	1.23	0.05	0.07	0.21	0.67	4.27	100

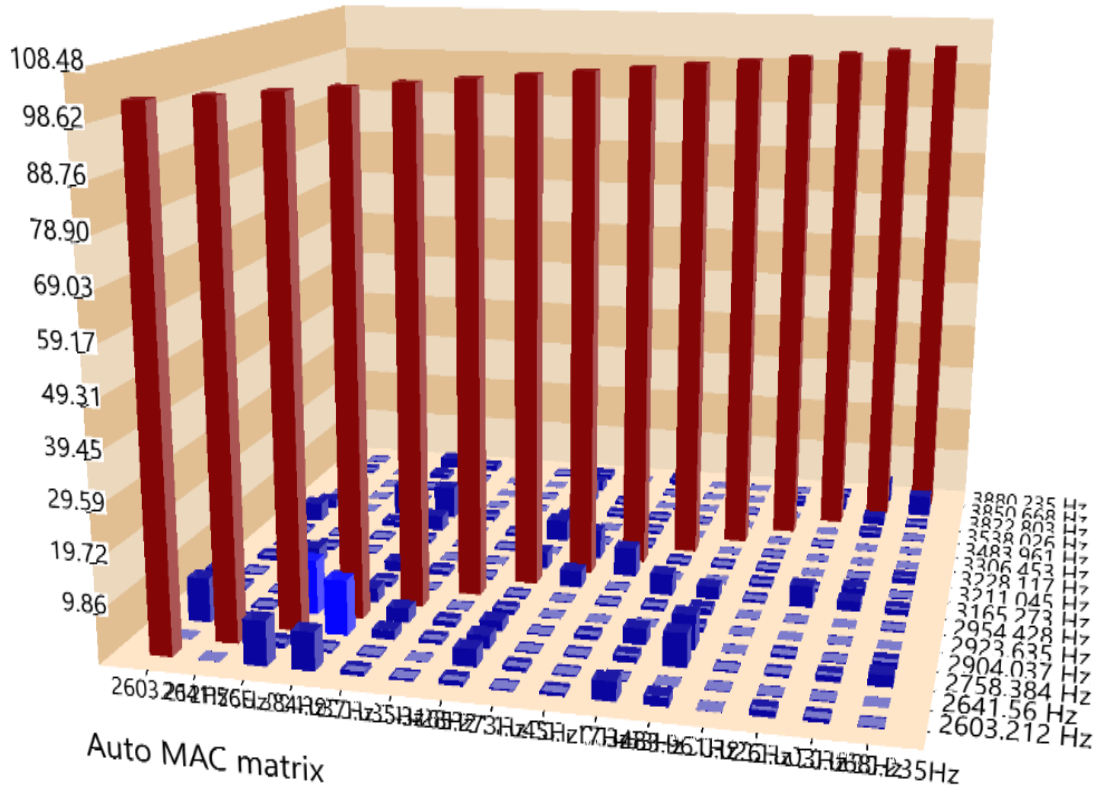

Figure A-16. Display Auto Modal Assurance Criterion (%) of the case with hemispherical with internal pressure of 5 kPa within the frequency range from 2490 to 4030 Hz.

Table A-16. Modal Parameter of the case with hemispherical with internal pressure of 5 kPa within the frequency range from 2490 to 4030 Hz..

Mode	Frequency (Hz)	Damping (%)
F#1	2603.212	0.506
F#2	2641.56	0.313
F#3	2758.384	1.008
F#4	2904.037	0.541
F#5	2923.635	0.337
F#6	2954.428	0.254
F#7	3165.273	0.992
F#8	3211.045	0.427
F#9	3228.117	0.309
F#10	3306.453	0.713
F#11	3483.961	0.433
F#12	3538.026	0.283
F#13	3822.803	0.401
F#14	3850.668	0.335
F#15	3880.235	0.367

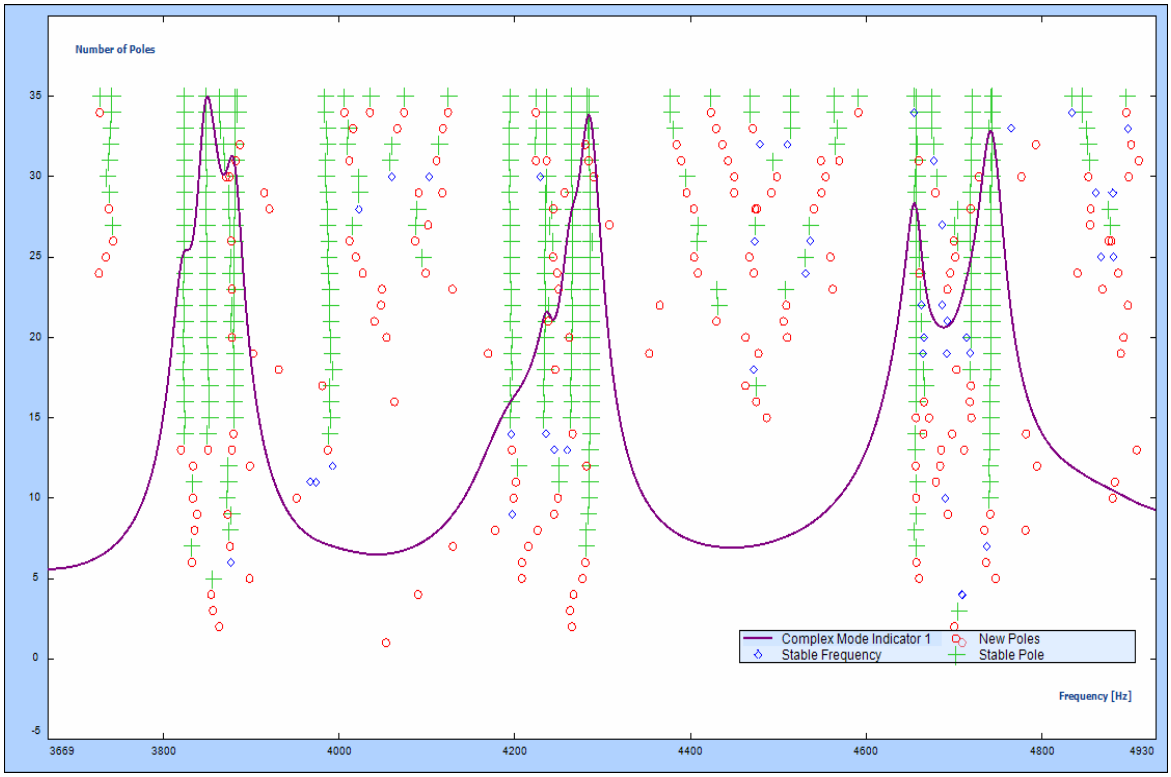

Figure A-17. Stability diagram of the hemispherical head model fully filled with water with internal pressure of 5 kPa within the frequency range from 3640 to 5000 Hz.

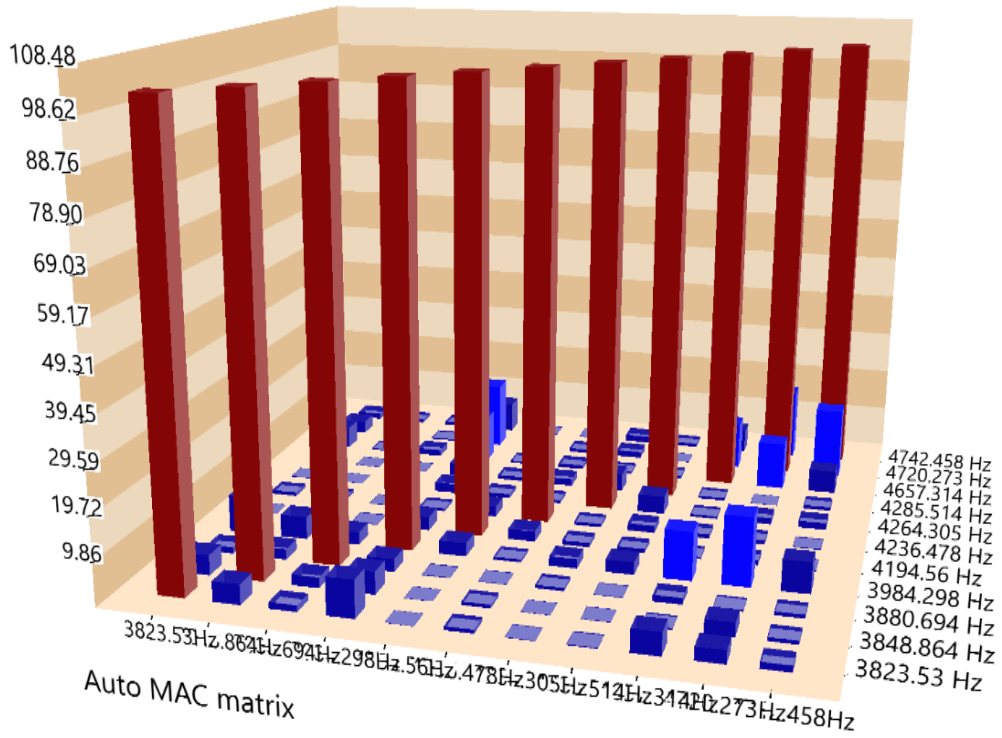

Figure A-18. Display Auto Modal Assurance Criterion (%) of the case with hemispherical with internal pressure of 5 kPa within the frequency range from 3640 to 5000 Hz.

Table A-17. Auto MAC Matrix of the extracted modal frequencies for the fully-filled aluminum shell with internal pressure of 5 kPa within the frequency range from 3640 to 5000 Hz.

Mode No.	Frequency (Hz)	Mode 1 3823.53 Hz	Mode 2 3848.864 Hz	Mode 3 3880.694 Hz	Mode 4 3984.298 Hz	Mode 5 4194.56 Hz	Mode 6 4236.478 Hz	Mode 7 4264.305 Hz	Mode 8 4285.514 Hz	Mode 9 4657.314 Hz	Mode 10 4720.273 Hz	Mode 11 4742.458 Hz
M 1	3823.53	100	4.42	1.434	8.226	0.062	0.836	0.12	0.216	4.946	2.869	1.398
M 2	3848.864	4.42	100	2.326	4.982	0.076	0.771	0.066	0.104	0.318	2.989	0.817
M 3	3880.694	1.434	2.326	100	2.814	0.176	0.135	0.709	0.13	1.431	0.349	0.824
M 4	3984.298	8.226	4.982	2.814	100	2.991	0.635	2.088	2.768	10.716	15.204	6.896
M 5	4194.56	0.062	0.076	0.176	2.991	100	2.334	0.975	0.933	0.522	1.077	0.255
M 6	4236.478	0.836	0.771	0.135	0.635	2.334	100	0.759	1.609	0.936	0.817	0.176
M 7	4264.305	0.12	0.066	0.709	2.088	0.975	0.759	100	4.005	0.576	1.45	1.521
M 8	4285.514	0.216	0.104	0.13	2.768	0.933	1.609	4.005	100	0.577	0.085	0.801
M 9	4657.314	4.946	0.318	1.431	10.716	0.522	0.936	0.576	0.577	100	10.727	5.15
M 10	4720.273	2.869	2.989	0.349	15.204	1.077	0.817	1.45	0.085	10.727	100	15.932
M 11	4742.458	1.398	0.817	0.824	6.896	0.255	0.176	1.521	0.801	5.15	15.932	100

Table A-18. Modal Parameter of the case with hemispherical with internal pressure of 5 kPa within the frequency range from 3640 to 5000 Hz.

Mode	Frequency (Hz)	Damping (%)
F#1	3823.53	0.388
F#2	3848.864	0.338
F#3	3880.694	0.321
F#4	3984.298	1.035
F#5	4194.56	1.098
F#6	4236.478	0.269
F#7	4264.305	0.342
F#8	4285.514	0.348
F#9	4657.314	0.254
F#10	4720.273	0.398
F#11	4742.458	0.354

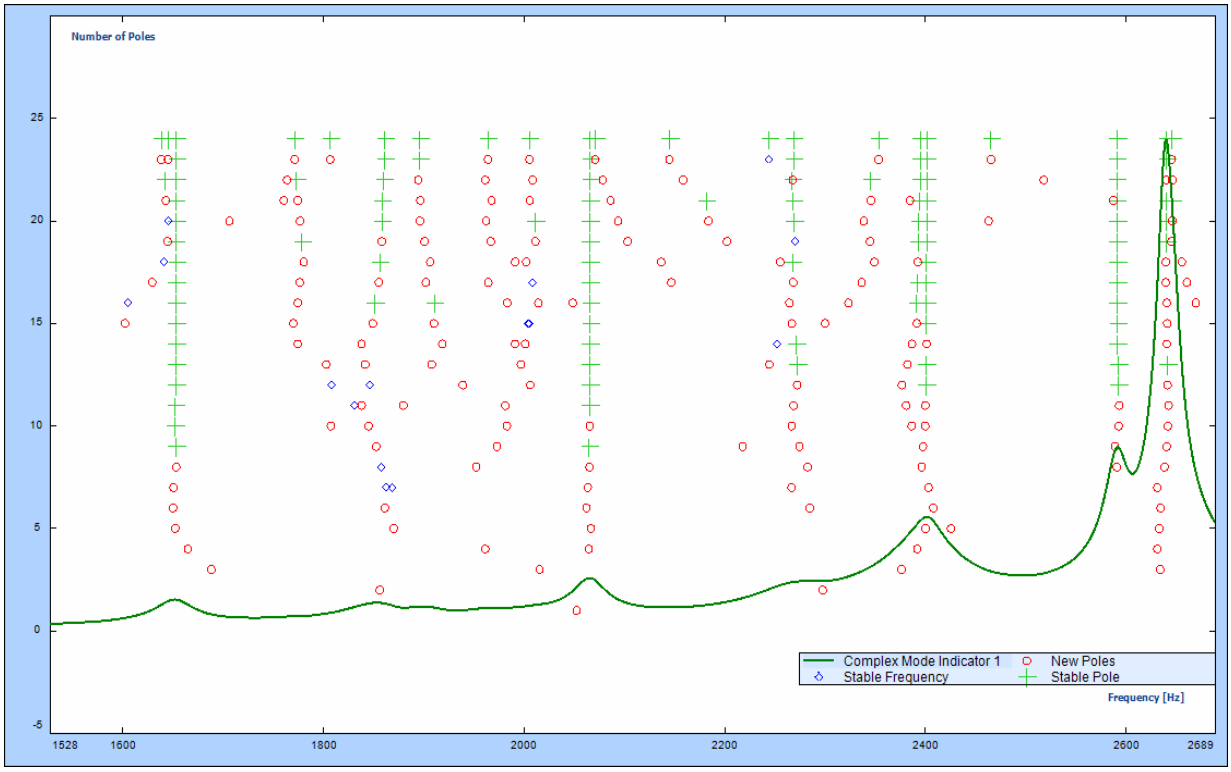

Figure A-19. Stability diagram of the hemispherical head model fully filled with water with internal pressure of 7.5 kPa within the frequency range from 1500 to 2710 Hz.

Table A-19. Auto MAC Matrix of the extracted modal frequencies for the fully-filled aluminum shell with internal pressure of 7.5 kPa within the frequency range from 1500 to 2710 Hz.

Mode No.	Frequency (Hz)	Mode 1 1652.924 Hz	Mode 2 1859.983 Hz	Mode 3 2065.393 Hz	Mode 4 2267.965 Hz	Mode 5 2401.108 Hz	Mode 6 2590.937 Hz	Mode 7 2640.152 Hz
Mode 1	1652.924	100	1.217	0.186	8.988	1.849	0.172	0.04
Mode 2	1859.983	1.217	100	0.008	3.587	1.777	1.744	2.357
Mode 3	2065.393	0.186	0.008	100	0.832	0.659	0.85	1.983
Mode (4	2267.965	8.988	3.587	0.832	100	46.124	0.043	0.105
Mode 5	2401.108	1.849	1.777	0.659	46.124	100	0.137	0.379
Mode 6	2590.937	0.172	1.744	0.85	0.043	0.137	100	0.083
Mode 7	2640.152	0.04	2.357	1.983	0.105	0.379	0.083	100

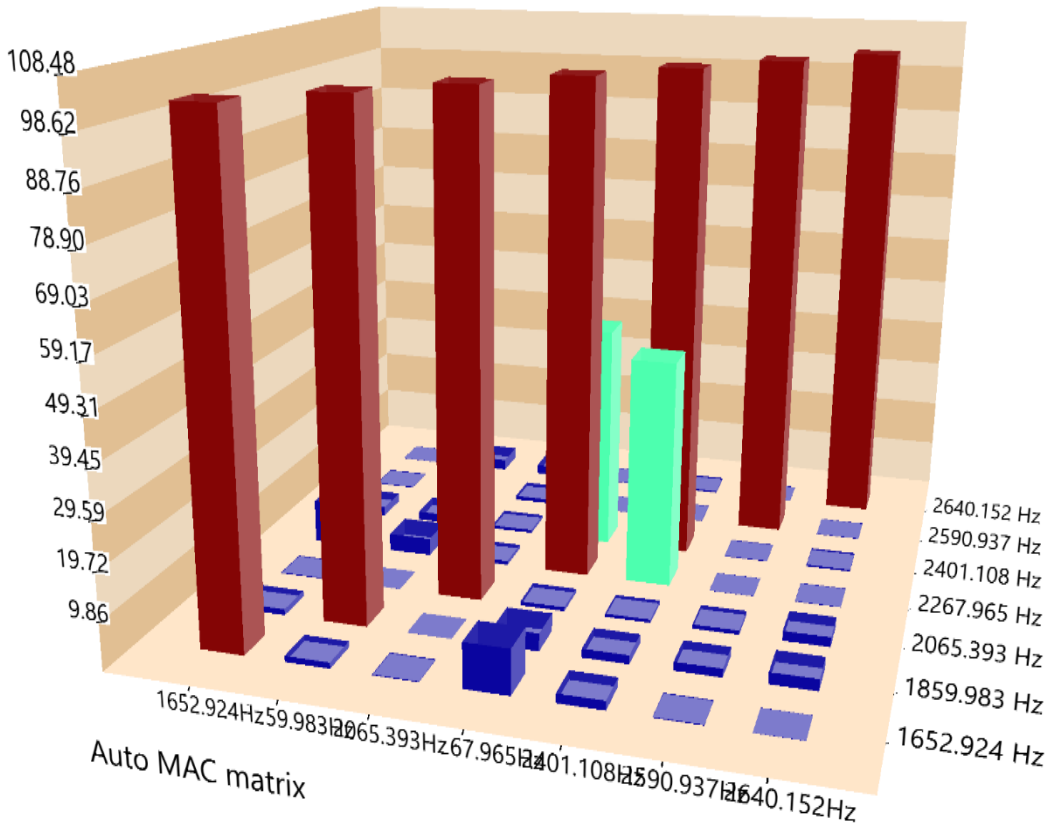

Figure A-20. Display Auto Modal Assurance Criterion (%) of the case with hemispherical with internal pressure of 7.5 kPa within the frequency range from1500 to 2710 Hz.

Table A-20. Modal Parameter of the case with hemispherical with internal pressure of 7.5 kPa within the frequency range from 1500 to 2710Hz.

Mode	Frequency (Hz)	Damping (%)
F#1	1652.924	1.148
F#2	1859.983	1.635
F#3	2065.393	0.805
F#4	2267.965	1.779
F#5	2401.108	0.625
F#6	2590.937	0.459
F#7	2640.152	0.31

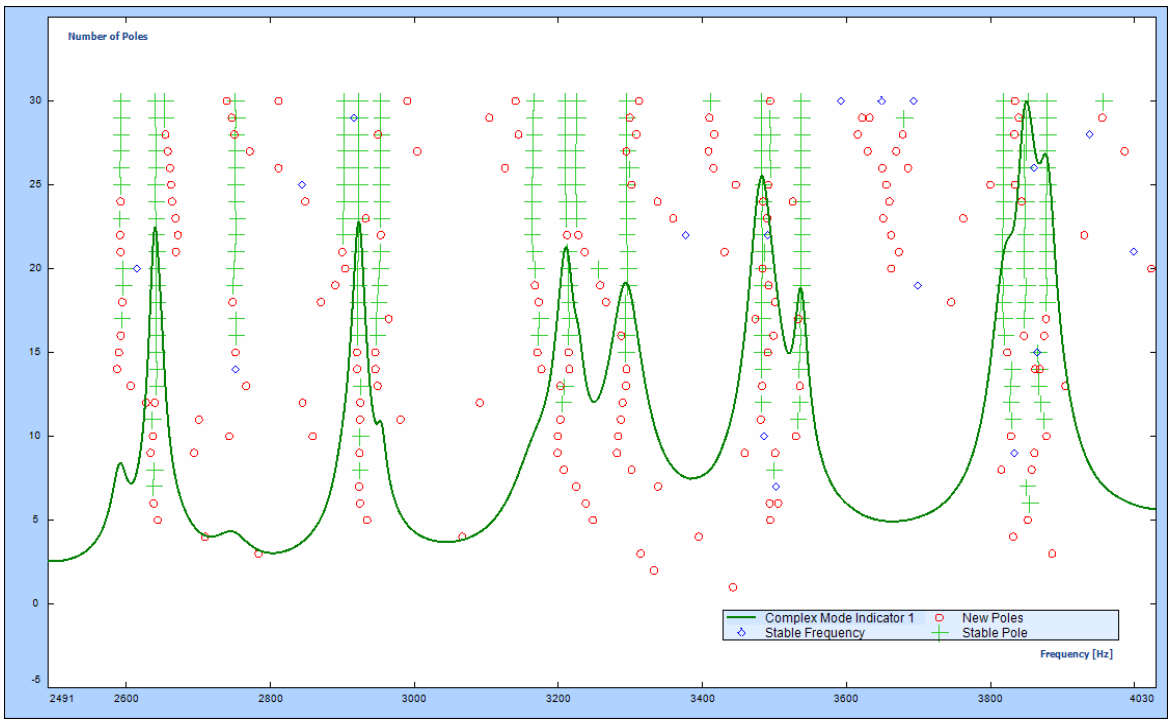

Figure A-21. Stability diagram of the hemispherical head model fully filled with water with internal pressure of 7.5 kPa within the frequency range from 2490 to 4030 Hz.

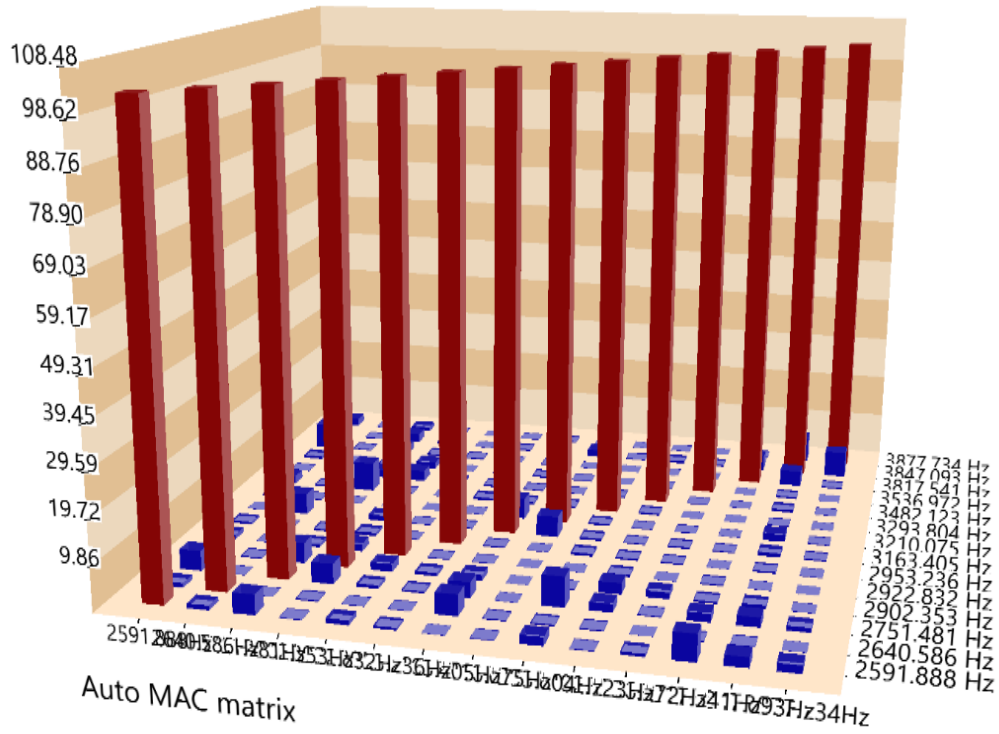

Figure A-22. Display Auto Modal Assurance Criterion (%) of the case with hemispherical with internal pressure of 7.5 kPa within the frequency range from 2490 to 4030 Hz.

Table A-21. Auto MAC Matrix of the extracted modal frequencies for the fully-filled aluminum shell with internal pressure of 7.5 kPa within the frequency range from 2490 to 4030 Hz.

Mode No.	Frequency (Hz)	Mode 1 2591.888 Hz	Mode 2 2640.586 Hz	Mode 3 2751.481 Hz	Mode 4 2902.353 Hz	Mode 5 2922.832 Hz	Mode 6 2953.236 Hz	Mode 7 3163.405 Hz	Mode 8 3210.075 Hz	Mode 9 3293.804 Hz	Mode 10 3482.123 Hz	Mode 11 3536.972 Hz	Mode 12 3817.541 Hz	Mode 13 3847.093 Hz	Mode 14 3877.734 Hz
M 1	2591.888	100	1.012	4.321	0.15	1.016	0.532	0.055	0.142	1.852	0.18	0.65	5.662	2.159	1.698
M 2	2640.586	1.012	100	0.116	0.296	0.155	0.155	4.555	0.249	0.371	0.257	0.02	0.244	0.187	0.047
M 3	2751.481	4.321	0.116	100	4.363	0.723	0.43	3.374	0.079	6.504	1.83	0.224	1.804	2.042	0.993
M 4	2902.353	0.15	0.296	4.363	100	1.657	0.71	1.22	0.02	0.158	2.392	1.419	0.442	0.712	0.099
M 5	2922.832	1.016	0.155	0.723	1.657	100	0.206	0.174	0.003	0.027	0.52	0.03	0.294	0.073	0.001
M 6	2953.236	0.532	0.155	0.43	0.71	0.206	100	0.306	0.112	0.591	0.39	0.289	0.037	0.385	0.134
M 7	3163.405	0.055	4.555	3.374	1.22	0.174	0.306	100	4.512	0.492	0.241	0.388	0.236	0.862	0.303
M 8	3210.075	0.142	0.249	0.079	0.02	0.003	0.112	4.512	100	0.448	0.182	0.179	0.071	1.589	0.202
M 9	3293.804	1.852	0.371	6.504	0.158	0.027	0.591	0.492	0.448	100	0.42	0.013	0.012	0.194	0.068
M 10	3482.123	0.18	0.257	1.83	2.392	0.52	0.39	0.241	0.182	0.42	100	0.163	0.091	0.571	0.094
M 11	3536.972	0.65	0.02	0.224	1.419	0.03	0.289	0.388	0.179	0.013	0.163	100	0.013	0.398	0.01
M 12	3817.541	5.662	0.244	1.804	0.442	0.294	0.037	0.236	0.071	0.012	0.091	0.013	100	3.456	0.33
M 13	3847.093	2.159	0.187	2.042	0.712	0.073	0.385	0.862	1.589	0.194	0.571	0.398	3.456	100	5.806
M 14	3877.734	1.698	0.047	0.993	0.099	0.001	0.134	0.303	0.202	0.068	0.094	0.01	0.33	5.806	100

Table A-22. Modal Parameter of the case with hemispherical with internal pressure of 7.5 kPa within the frequency range from 2490 to 4030 Hz.

Mode	Frequency (Hz)	Damping (%)
F#1	2591.888	0.467
F#2	2640.586	0.333
F#3	2751.481	0.985
F#4	2902.353	0.538
F#5	2922.832	0.348
F#6	2953.236	0.266
F#7	3163.405	1.087
F#8	3210.075	0.467
F#9	3293.804	0.718
F#10	3482.123	0.502
F#11	3536.972	0.299
F#12	3817.541	0.373
F#13	3847.093	0.37
F#14	3877.734	0.388

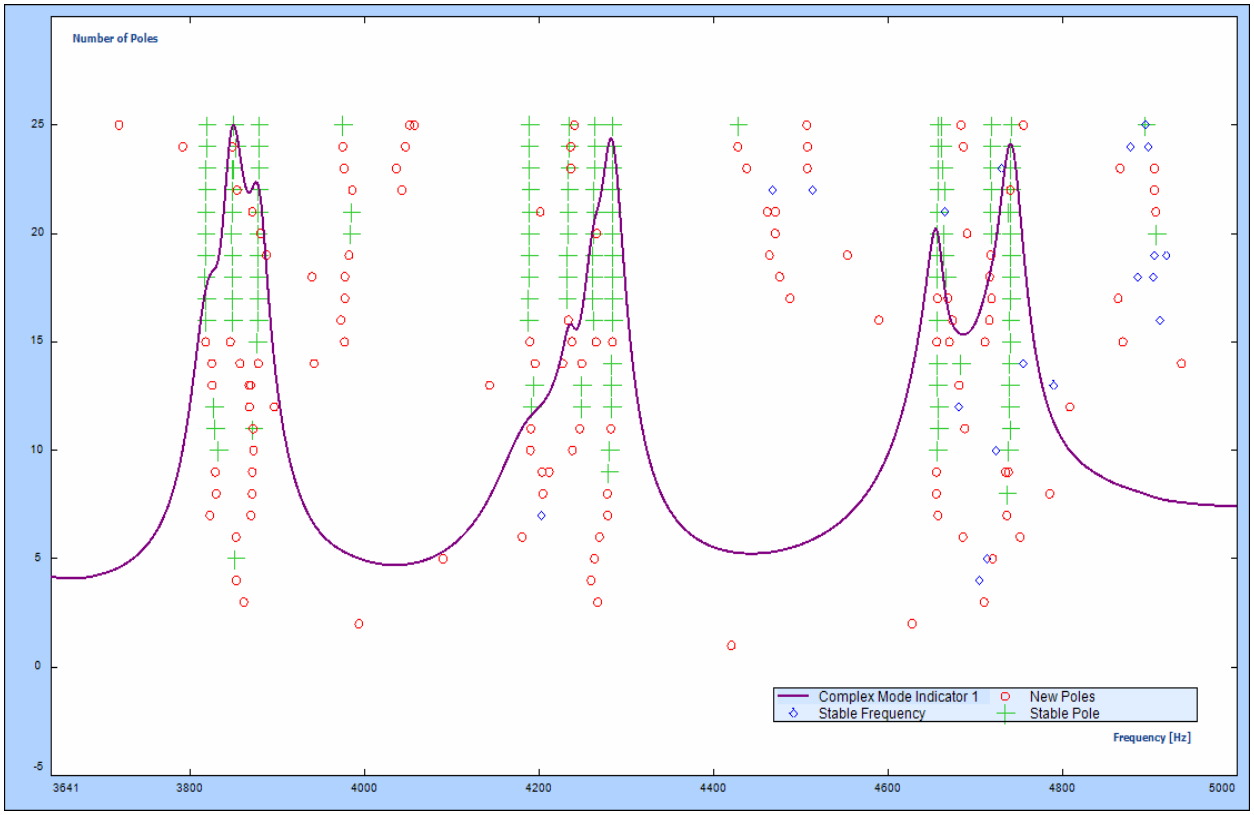

Figure A-23. Stability diagram of the hemispherical head model fully filled with water with internal pressure of 7.5 kPa within the frequency range from 3640 to 5000 Hz.

Table A-23. Auto MAC Matrix of the extracted modal frequencies for the fully-filled aluminum shell with internal pressure of 7.5 kPa within the frequency range from 3640 to 5000 Hz.

Mode No.	Frequency (Hz)	Mode 1 3817.98 Hz	Mode 2 3848.59 Hz	Mode 3 3878.09 Hz	Mode 4 4188.34 Hz	Mode 5 4232.79 Hz	Mode 6 4261.47 Hz	Mode 7 4284.26 Hz	Mode 8 4656.86 Hz	Mode 9 4739.93 Hz
M 1	3817.988	100	2.805	0.626	0.041	0.028	0.746	0.199	2.054	0.074
M 2	3848.559	2.805	100	5.86	0.479	0.371	0.11	0.186	1.24	0.056
M 3	3878.09	0.626	5.86	100	1.078	0.204	0.725	0.07	0.783	0.457
M4	4188.314	0.041	0.479	1.078	100	4.998	10.609	3.681	5.693	1.106
M 5	4232.796	0.028	0.371	0.204	4.998	100	12.05	0.174	2.155	0.278
M 6	4261.47	0.746	0.11	0.725	10.609	12.05	100	11.571	5.636	2.272
M 7	4284.246	0.199	0.186	0.07	3.681	0.174	11.571	100	0.978	1.655
M 8	4656.866	2.054	1.24	0.783	5.693	2.155	5.636	0.978	100	1.034
M9	4739.933	0.074	0.056	0.457	1.106	0.278	2.272	1.655	1.034	100

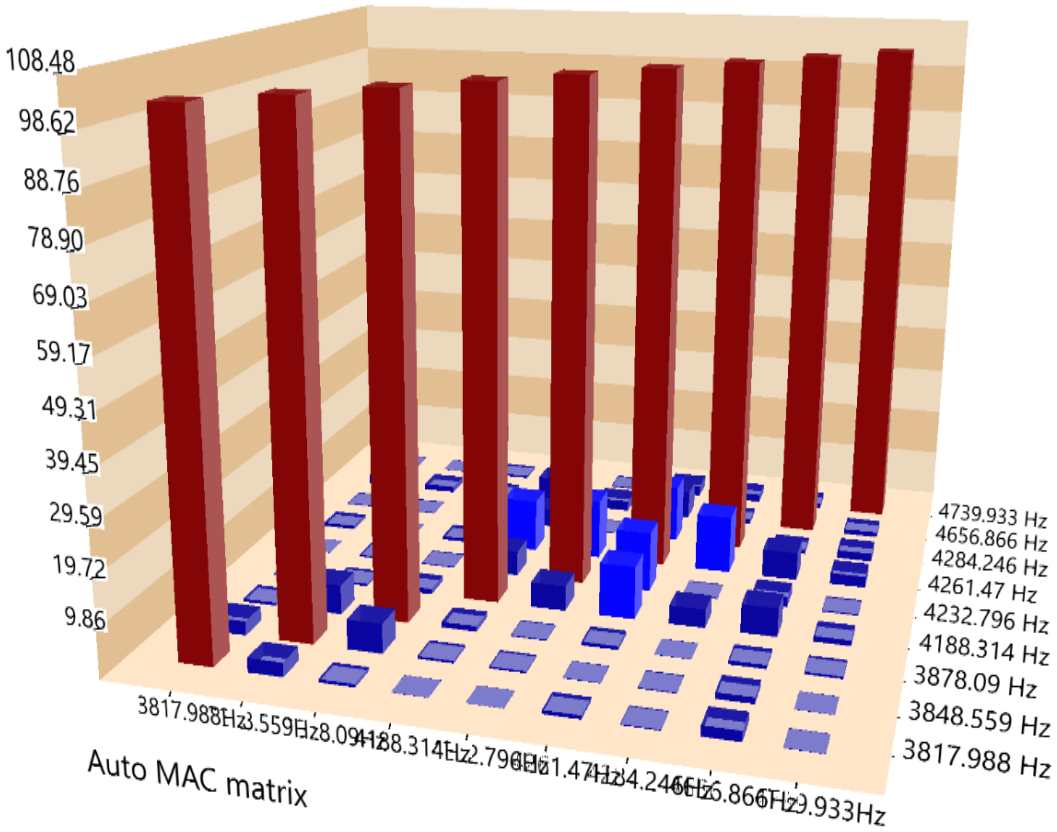

Figure A-24. Display Auto Modal Assurance Criterion (%) of the case with hemispherical with internal pressure of 7.5 kPa within the frequency range from 3640 to 5000 Hz.

Table A-24. Modal Parameter of the case with hemispherical with internal pressure of 7.5 kPa within the frequency range from 3640 to 5000 Hz.

Mode	Frequency (Hz)	Damping (%)
F#1	3817.988	0.394
F#2	3848.559	0.372
F#3	3878.09	0.382
F#4	4188.314	1.049
F#5	4232.796	0.346
F#6	4261.47	0.432
F#7	4284.246	0.362
F#8	4656.866	0.274
F#9	4739.933	0.348

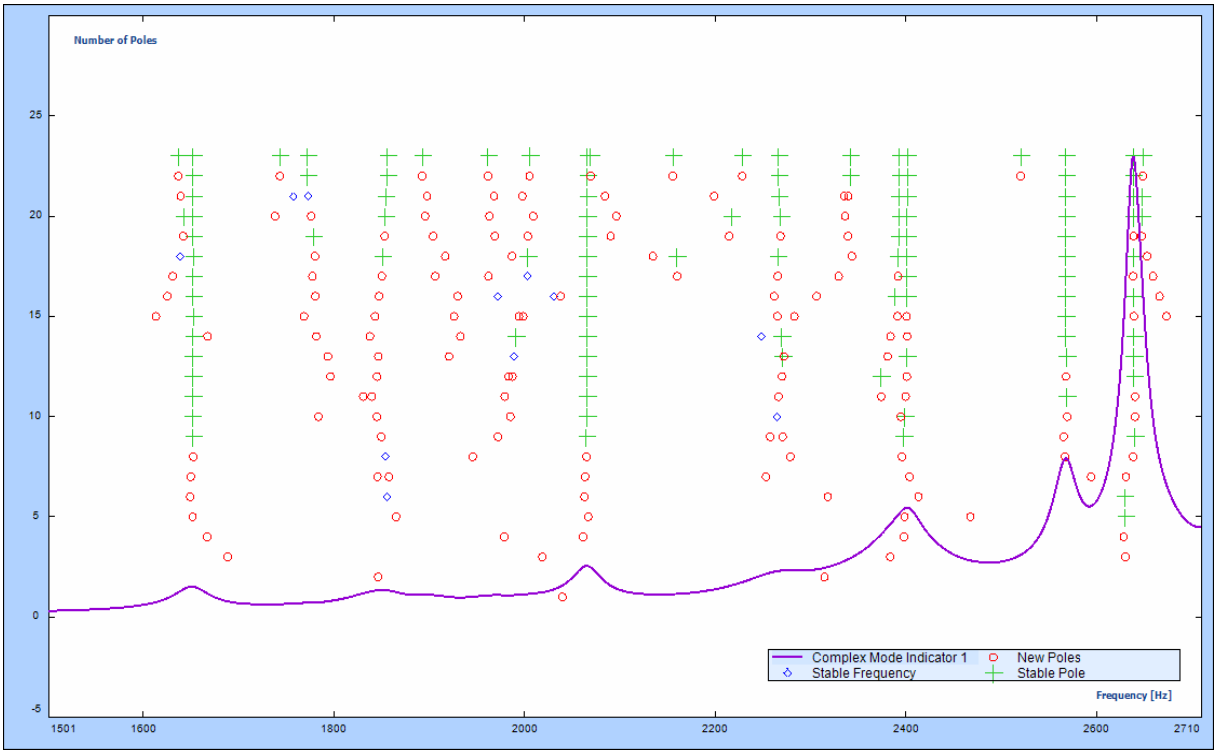

Figure A-25. Stability diagram of the hemispherical head model fully filled with water with internal pressure of 10 kPa within the frequency range from 1500 to 2710 Hz.

Table A-25. Auto MAC Matrix of the extracted modal frequencies for the fully-filled aluminum shell with internal pressure of 10 kPa within the frequency range from 1500 to 2710 Hz.

Mode No.	Frequency (Hz)	Mode 1 1652.214 Hz	Mode 2 2065.516 Hz	Mode 3 2266.736 Hz	Mode 4 2401.044 Hz	Mode 5 2567.412 Hz	Mode 6 2638.981 Hz
Mode 1	1652.214	100	0.055	5.84	2.193	0.124	0.505
Mode 2	2065.516	0.055	100	3.346	0.636	0.276	1.272
Mode 3	2266.736	5.84	3.346	100	42.058	0.046	0.053
Mode 4	2401.044	2.193	0.636	42.058	100	0.048	0.227
Mode 5	2567.412	0.124	0.276	0.046	0.048	100	0.065
Mode 6	2638.981	0.505	1.272	0.053	0.227	0.065	100

Table A-26. Modal Parameter of the case with hemispherical with internal pressure of 10 kPa within the frequency range from 1500 to 2710 Hz.

Mode	Frequency (Hz)	Damping (%)
F#1	1652.214	1.138
F#2	2065.516	0.773
F#3	2266.736	1.808
F#4	2401.044	0.614
F#5	2567.412	0.503
F#6	2638.981	0.324

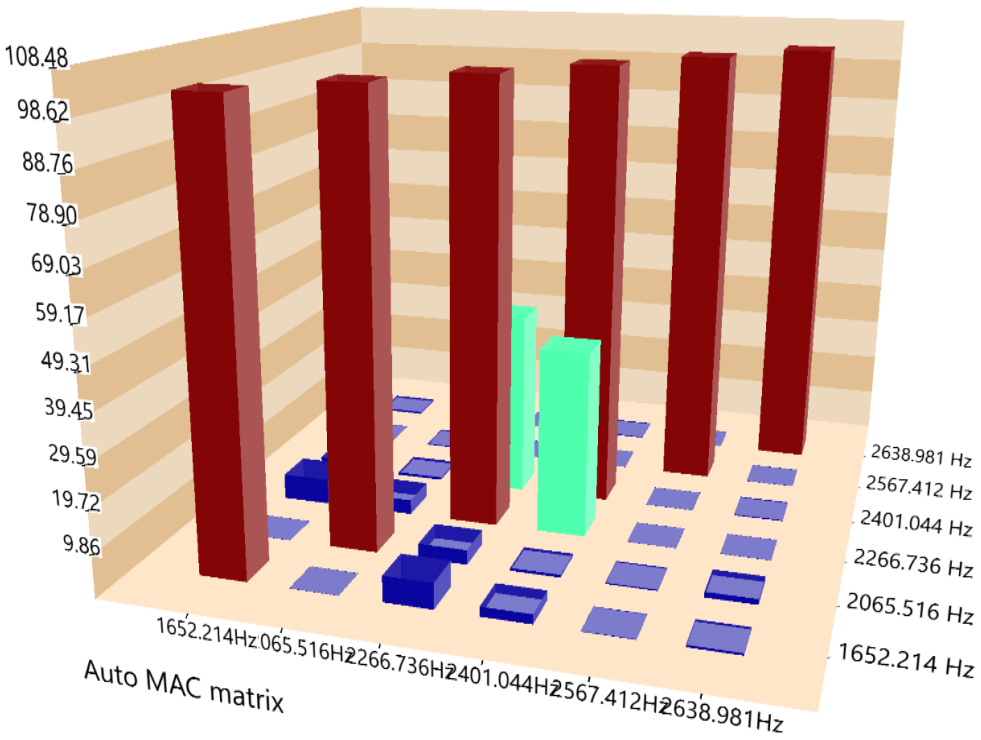

Figure A-26. Display Auto Modal Assurance Criterion (%) of the case with hemispherical with internal pressure of 10 kPa within the frequency range from 1500 to 2710 Hz.

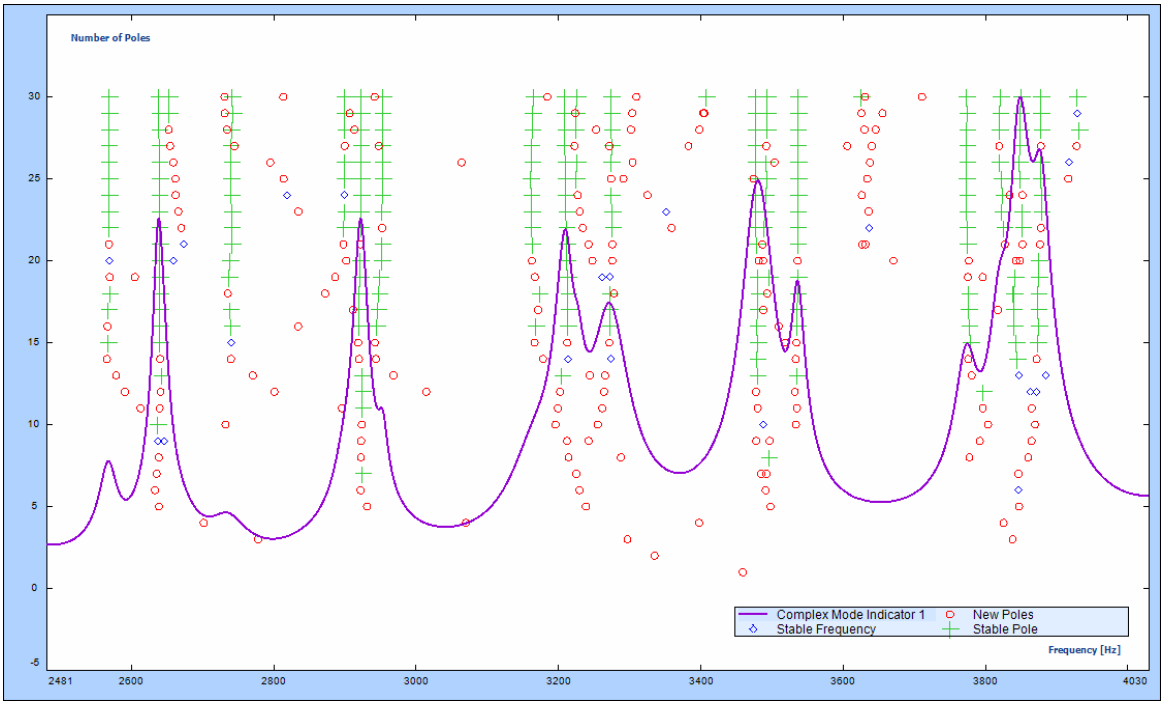

Figure A-27. Stability diagram of the hemispherical head model fully filled with water with internal pressure of 10 kPa within the frequency range from 2490 to 4030 Hz.

Table A-27. Auto MAC Matrix of the extracted modal frequencies for the fully-filled aluminum shell with internal pressure of 10 kPa within the frequency range from 2940 to 4030Hz.

Mode No.	Frequency (Hz)	Mode 1 2568.401 Hz	Mode 2 2639.025 Hz	Mode 3 2741.135 Hz	Mode 4 2922.199 Hz	Mode 5 2952.333 Hz	Mode 6 3162.516 Hz	Mode 7 3210.07 Hz	Mode 8 3275.258 Hz	Mode 9 3476.982 Hz	Mode 10 3536.303 Hz	Mode 11 3773.695 Hz	Mode 12 3820.714 Hz	Mode 13 3847.619 Hz	Mode 14 3877.912 Hz
M 1	2568.401	100	3.05	4.49	4.24	2.40	5.15	0.36	5.44	5.13	1.68	6.38	8.3	5.67	0.38
M 2	2639.025	3.05	100	5.46	0.21	0.72	10.0	1.89	1.74	0.78	0.18	1.18	5.18	1.63	0.16
M 3	2741.135	4.49	5.46	100	6.04	2.01	10.3	0.25	0.52	6.14	2.68	9.56	20.5	11.6	0.39
M 4	2922.199	4.24	0.21	6.04	100	3.40	1.36	1.40	2.04	0.98	0.29	2.91	5.13	3.89	1.08
M 5	2952.333	2.40	0.72	2.01	3.40	100	2.32	0.16	0.62	2.46	0.09	0.93	1.21	1.11	0.35
M 6	3162.516	5.15	10.0	10.3	1.36	2.32	100	5.60	10.1	1.17	0.44	3.3	11.2	3.13	0.17
M 7	3210.07	0.36	1.89	0.28	1.40	0.16	5.60	100	3.28	0.19	0.89	0.48	0.30	0.1	0.09
M 8	3275.258	5.44	1.74	0.52	2.04	0.62	10.1	3.28	100	0.00	0.44	3.39	7.78	4.61	0.11
M 9	3476.982	5.13	0.78	6.01	0.98	2.46	1.17	0.19	0.00	100	0.84	0.86	2.82	4.25	0.72
M 10	3536.303	1.68	0.18	2.06	0.29	0.09	0.44	0.89	0.44	0.84	100	1.56	3.13	0.90	0.27
M 11	3773.695	6.38	1.18	9.59	2.91	0.93	3.3	0.48	3.39	0.86	1.56	100	9.41	8.82	0.31
M 12	3820.714	8.3	5.18	20.5	5.13	1.21	11.2	0.30	7.78	2.82	3.13	9.41	100	25.7	2.83
M 13	3847.619	5.67	1.63	11.6	3.89	1.11	3.13	0.1	4.61	4.25	0.90	8.82	25.7	100	7.69
M 14	3877.912	0.38	0.16	0.39	1.02	0.35	0.17	0.09	0.11	0.72	0.27	0.31	2.83	7.69	100

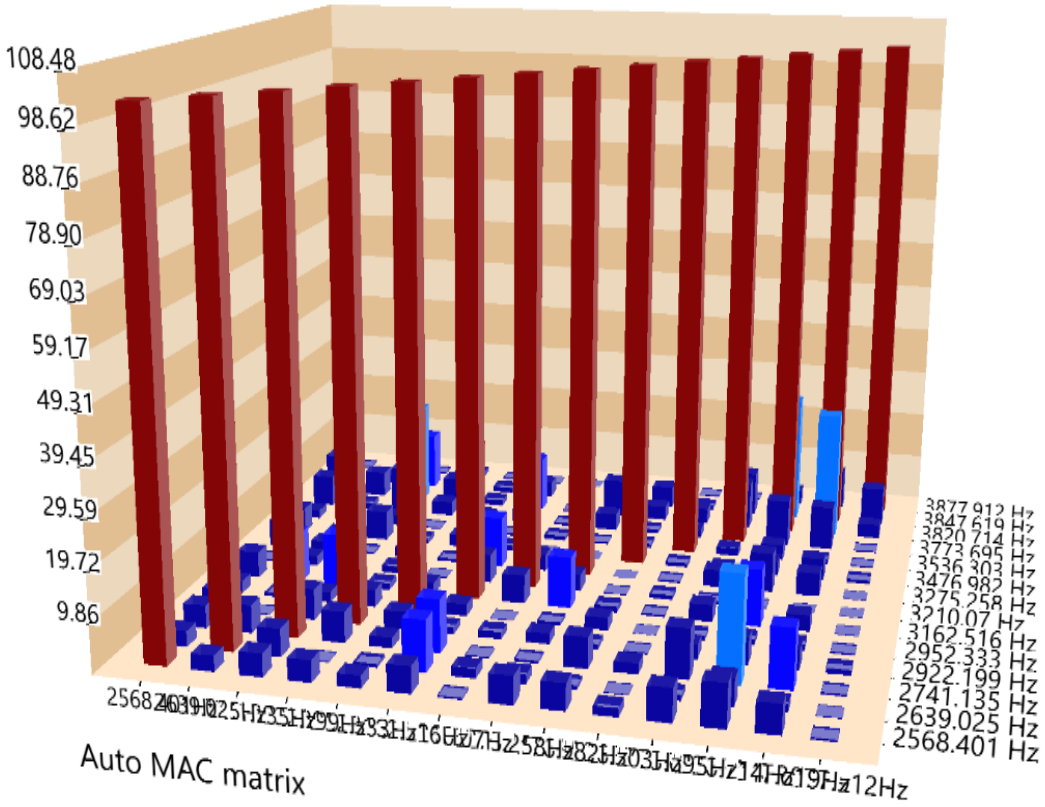

Figure A-28. Display Auto Modal Assurance Criterion (%) of the case with hemispherical with internal pressure of 10 kPa within the frequency range from 2490 to 4030 Hz.

Table A-28. Modal Parameter of the case with hemispherical with internal pressure of 10 kPa within the frequency range from 2490 to 4030 Hz.

Mode	Frequency (Hz)	Damping (%)
F#1	2568.401	0.513
F#2	2639.025	0.324
F#3	2741.135	1.035
F#4	2922.199	0.354
F#5	2952.333	0.268
F#6	3162.516	1.163
F#7	3210.07	0.445
F#8	3275.258	0.744
F#9	3476.982	0.64
F#10	3536.303	0.305
F#11	3773.695	0.44
F#12	3820.714	0.435
F#13	3847.619	0.429
F#14	3877.912	0.364

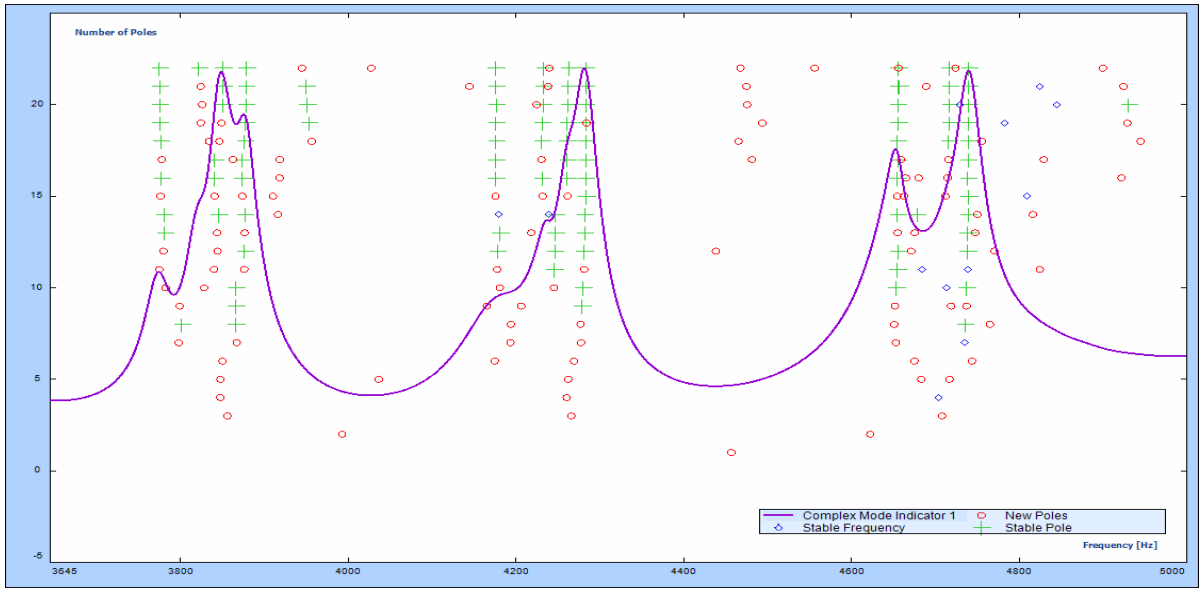

Figure A-29. Stability diagram of the hemispherical head model fully filled with water with internal pressure of 10 kPa within the frequency range from 3640 to 5000 Hz.

Table A-29. Auto MAC Matrix of the extracted modal frequencies for the fully-filled aluminum shell with internal pressure of 10 kPa within the frequency range from 3640 to 5000 Hz.

Mode No.	Frequency (Hz)	Mode 1 3775.418 Hz	Mode 2 3850.496 Hz	Mode 3 3878.397 Hz	Mode 4 4175.901 Hz	Mode 5 4231.072 Hz	Mode 6 4262.582 Hz	Mode 7 4282.094 Hz	Mode 8 4655.617 Hz	Mode 9 4717.087 Hz	Mode 10 4739.411 Hz
M 1	3775.418	100	4.635	2.38	0.118	0.183	0.067	0.251	2.53	2.773	0.236
M 2	3850.496	4.635	100	7.97	1.601	0.265	1.408	0.416	1.107	0.122	0.282
M 3	3878.397	2.38	7.97	100	1.461	0.95	0.874	0.137	0.33	0.58	0.505
M 4	4175.901	0.118	1.601	1.461	100	1.273	1.018	1.646	0.332	0.216	0.054
M 5	4231.072	0.183	0.265	0.95	1.273	100	3.309	1.809	1.55	1.678	0.106
M 6	4262.582	0.067	1.408	0.874	1.018	3.309	100	10.041	1.312	1.13	0.431
M 7	4282.094	0.251	0.416	0.137	1.646	1.809	10.041	100	0.535	0.019	0.876
M 8	4655.617	2.53	1.107	0.33	0.332	1.55	1.312	0.535	100	26.588	2.33
M 9	4717.087	2.773	0.122	0.58	0.216	1.678	1.13	0.019	26.588	100	14.411
M 10	4739.411	0.236	0.282	0.505	0.054	0.106	0.431	0.876	2.33	14.411	100

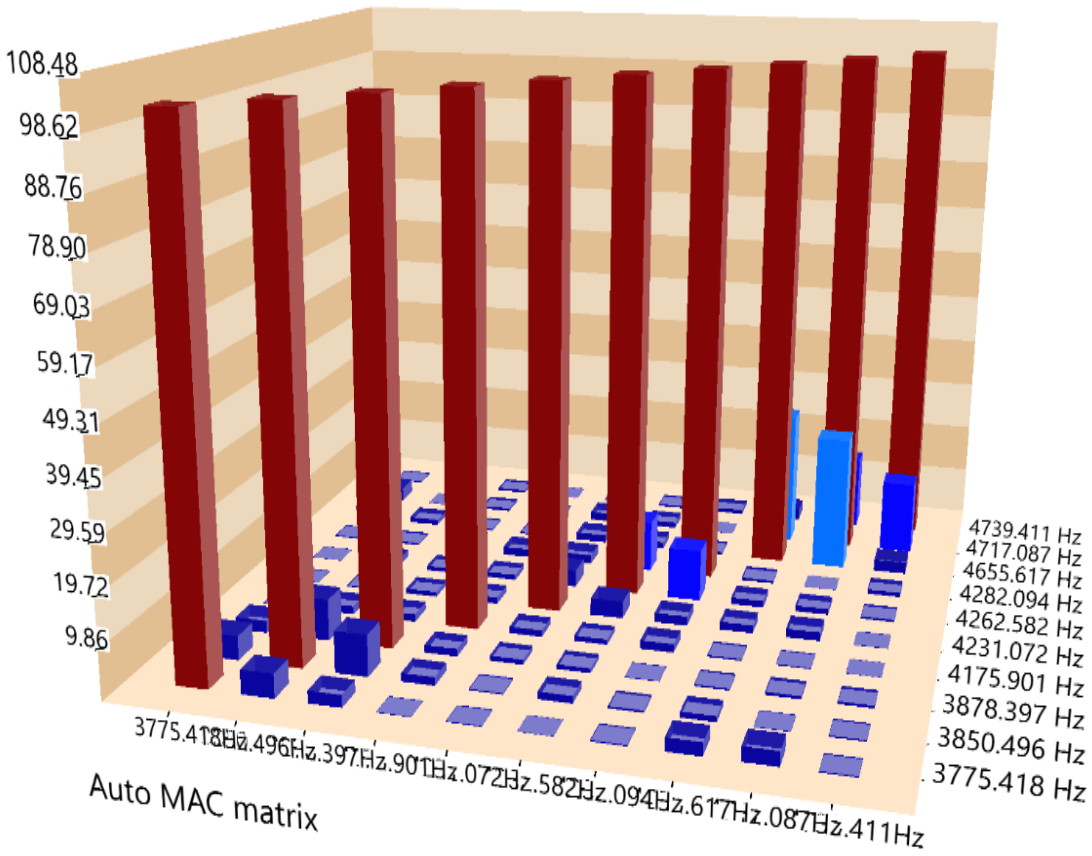

Figure A-30. Display Auto Modal Assurance Criterion (%) of the case with hemispherical with internal pressure of 10 kPa within the frequency range from 3640 to 5000 Hz.

Table A-30. Modal Parameter of the case with hemispherical with internal pressure of 10 kPa within the frequency range from 3640 to 5000 Hz.

Mode	Frequency (Hz)	Damping (%)
F#1	3775.418	0.467
F#2	3850.496	0.375
F#3	3878.397	0.404
F#4	4175.901	1.068
F#5	4231.072	0.358
F#6	4262.582	0.391
F#7	4282.094	0.371
F#8	4655.617	1.041
F#9	4717.087	0.45
F#10	4739.411	0.35

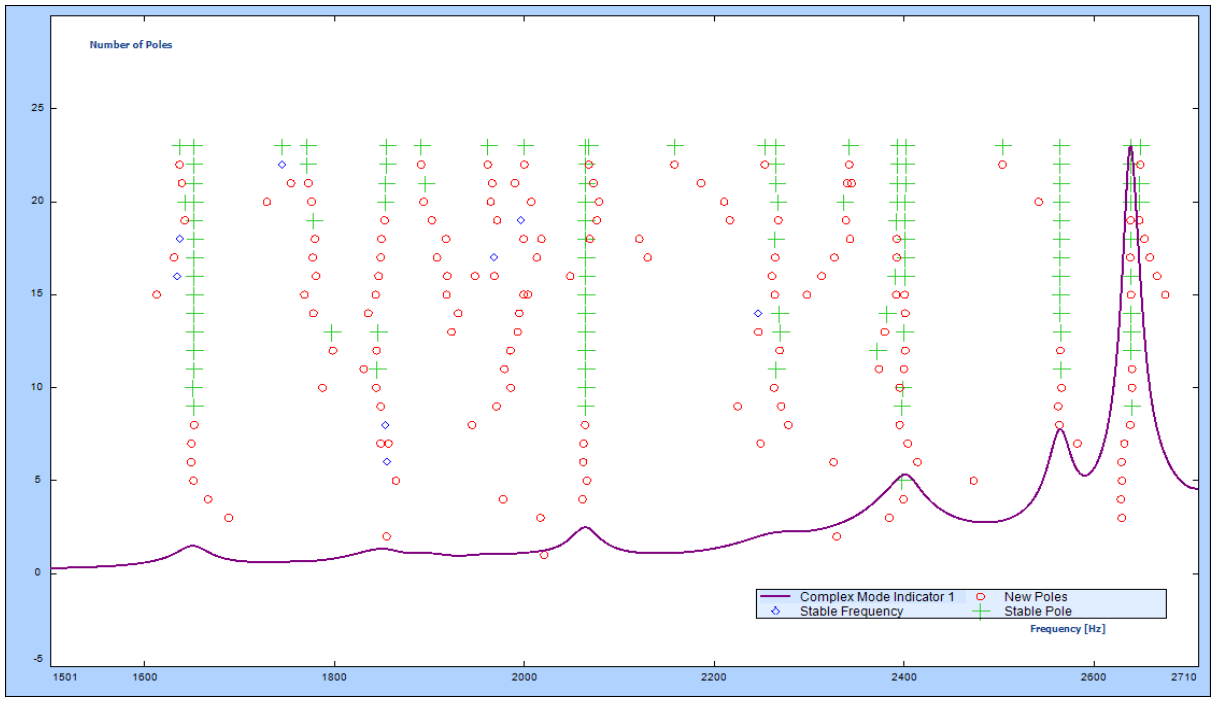

Figure A-31. Stability diagram of the hemispherical head model fully filled with water with internal pressure of 12.5 kPa within the frequency range from 1500 to 2710 Hz.

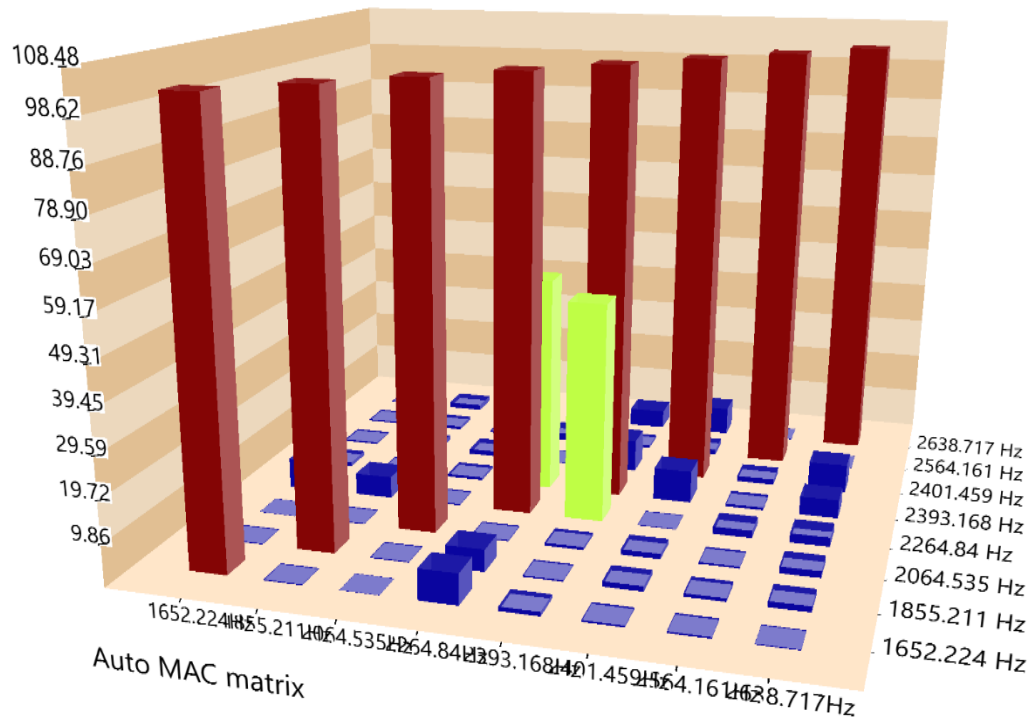

Figure A-32. Display Auto Modal Assurance Criterion (%) of the case with hemispherical with internal pressure of 12.5 kPa within the frequency range from 1500 to 2710 Hz

Table A-31. Auto MAC Matrix of the extracted modal frequencies for the fully-filled aluminum shell with internal pressure of 12.5 kPa within the frequency range from 1500 to 2710 Hz.

Mode No.	Frequency (Hz)	Mode 1 1652.224 Hz	Mode 2 1855.211 Hz	Mode 3 2064.535 Hz	Mode 4 2264.84 Hz	Mode 5 2393.168 Hz	Mode 6 2401.459 Hz	Mode 7 2564.161 Hz	Mode 8 2638.717 Hz
M 1	1652.224	100	0.226	0.079	7.048	0.978	0.399	0.362	0.207
M 2	1855.211	0.226	100	0.242	5.076	0.334	1.211	0.783	1.331
M 3	2064.535	0.079	0.242	100	0.306	0.684	1.221	0.419	1.541
M 4	2264.84	7.048	5.076	0.306	100	50.645	0.17	1.73	2.168
M 5	2393.168	0.978	0.334	0.684	50.645	100	7.589	0.641	4.33
M 6	2401.459	0.399	1.211	1.221	0.17	7.589	100	1.308	6.628
M 7	2564.161	0.362	0.783	0.419	1.73	0.641	1.308	100	0.06
M 8	2638.717	0.207	1.331	1.541	2.168	4.33	6.628	0.06	100

Table A-32. Modal Parameter of the case with hemispherical with internal pressure of 12.5 kPa within the frequency range from 1500 to 2710 Hz.

Mode	Frequency (Hz)	Damping (%)
F#1	1652.224	1.143
F#2	1855.211	1.695
F#3	2064.535	0.79
F#4	2264.84	1.862
F#5	2393.168	1.41
F#6	2401.459	0.636
F#7	2564.161	0.512
F#8	2638.717	0.326

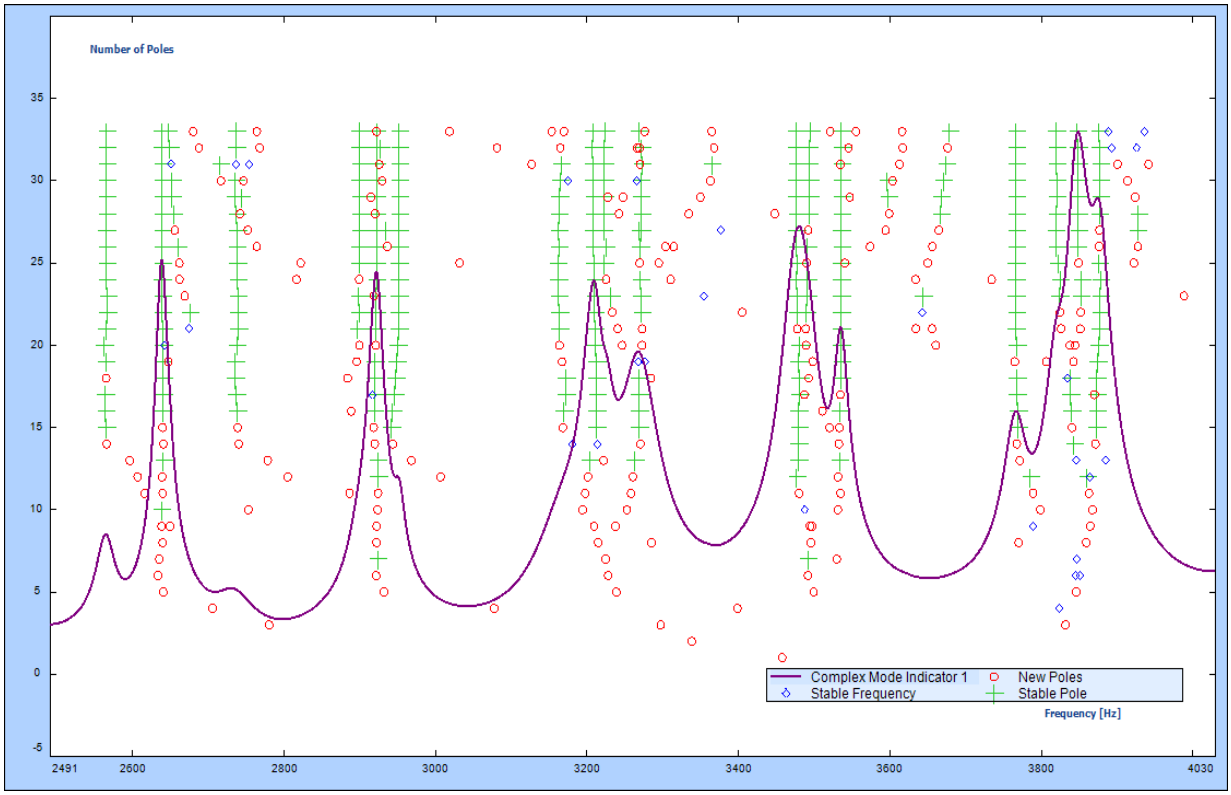

Figure A-33. Stability diagram of the hemispherical head model fully filled with water with internal pressure of 12.5 kPa within the frequency range from 2940 to 4030 Hz.

Table A-33. Auto MAC Matrix of the extracted modal frequencies for the fully-filled aluminum shell with internal pressure of 12.5 kPa within the frequency range from 2940 to 4030 Hz.

Mode No.	Frequency (Hz)	Mode 1 2564.928 Hz	Mode 2 2638.675 Hz	Mode 3 2737.973 Hz	Mode 4 2899.672 Hz	Mode 5 2921.761 Hz	Mode 6 2951.301 Hz	Mode 7 3162.962 Hz	Mode 8 3207.568 Hz	Mode 9 3271.525 Hz	Mode 10 3476.417 Hz	Mode 11 3535.471 Hz	Mode 12 3766.381 Hz	Mode 13 3848.886 Hz	Mode 14 3877.198 Hz
M 1	2564.928	100	0.066	0.869	0.19	0.067	0.011	0.788	0.276	0.133	1.14	0.104	5.532	0.247	0.031
M 2	2638.675	0.066	100	11.15	7.622	4.006	0.562	6.076	1.319	0.386	0.406	0.22	1.63	1.519	0.808
M 3	2737.973	0.869	11.15	100	67.48	9.329	4.986	32.09	3.774	4.317	3.57	1.506	16.68	0.459	5.274
M 4	2899.672	0.19	7.622	67.48	100	8.207	6.032	28.60	2.333	0.727	4.039	2.057	10.29	0.068	2.861
M 5	2921.761	0.067	4.006	9.329	8.207	100	0.282	5.249	0.587	2.498	1.783	0.036	1.321	0.459	0.716
M 6	2951.301	0.011	0.562	4.986	6.032	0.282	100	3.293	0.022	0.157	1.633	0.283	0.767	0.016	0.382
M 7	3162.962	0.788	6.076	32.09	28.60	5.249	3.293	100	4.575	5.334	0.879	2.198	6.173	1.881	4.686
M 8	3207.568	0.276	1.319	3.774	2.333	0.587	0.022	4.575	100	4.241	0.053	0.105	0.567	0.994	0.307
M 9	3271.525	0.133	0.386	4.317	0.727	2.498	0.157	5.334	4.241	100	3.351	0.203	0.915	0.474	0.445
M 10	3476.417	1.14	0.406	3.57	4.039	1.783	1.633	0.879	0.053	3.351	100	2.511	0.114	0.52	0.53
M 11	3535.471	0.104	0.22	1.506	2.057	0.036	0.283	2.198	0.105	0.203	2.511	100	0.541	0.822	0.215
M 12	3766.381	5.532	1.63	16.68	10.29	1.321	0.767	6.173	0.567	0.915	0.114	0.541	100	2.437	2.943
M 13	3848.886	0.247	1.519	0.459	0.068	0.459	0.016	1.881	0.994	0.474	0.52	0.822	2.437	100	6.701
M 14	3877.198	0.031	0.808	5.274	2.861	0.716	0.382	4.686	0.307	0.445	0.53	0.215	2.943	6.701	100

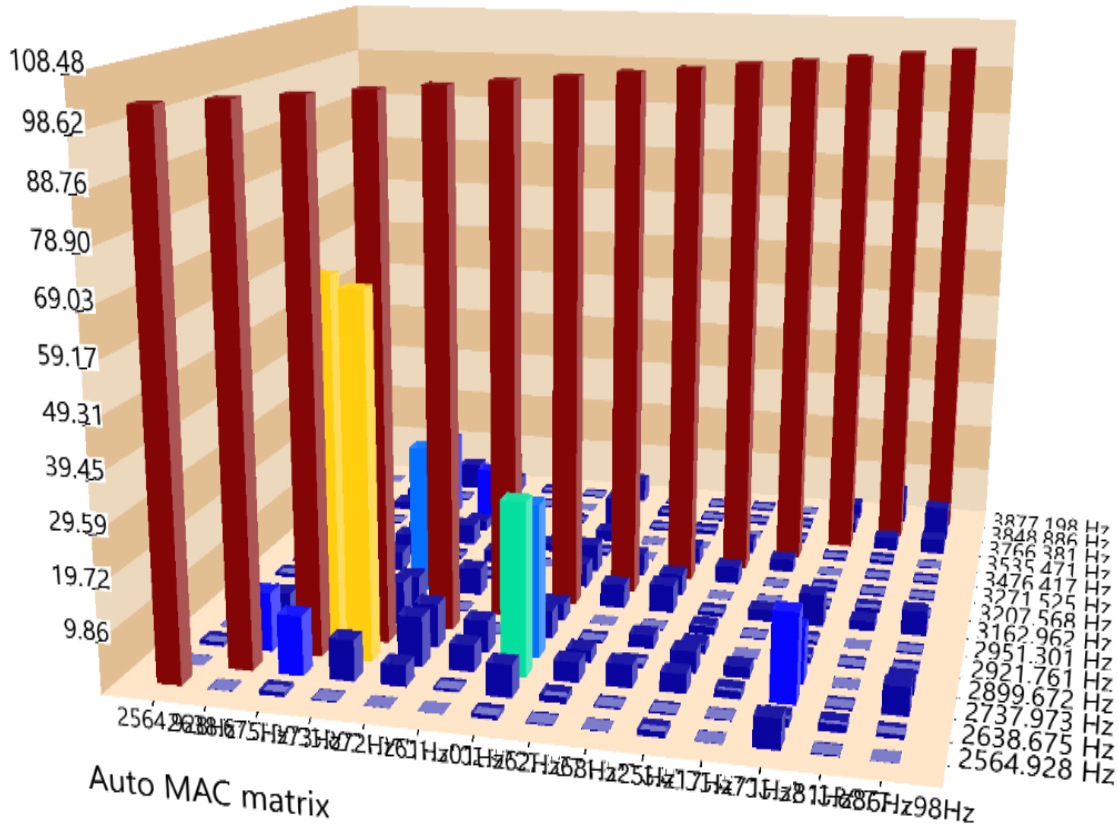

Figure A-34. Display Auto Modal Assurance Criterion (%) of the case with hemispherical with internal pressure of 12.5 kPa within the frequency range from 2940 to 4030 Hz.

Table A-34. Modal Parameter of the case with hemispherical with internal pressure of 12.5 kPa within the frequency range from 2940 to 4030 Hz.

Mode	Frequency (Hz)	Damping (%)
F#1	2564.928	0.52
F#2	2638.675	0.322
F#3	2737.973	1.016
F#4	2899.672	0.536
F#5	2921.761	0.359
F#6	2951.301	0.283
F#7	3162.962	1.206
F#8	3207.568	0.45
F#9	3271.525	0.771
F#10	3476.417	0.632
F#11	3535.471	0.312
F#12	3766.381	0.433
F#13	3848.886	0.375
F#14	3877.198	0.381

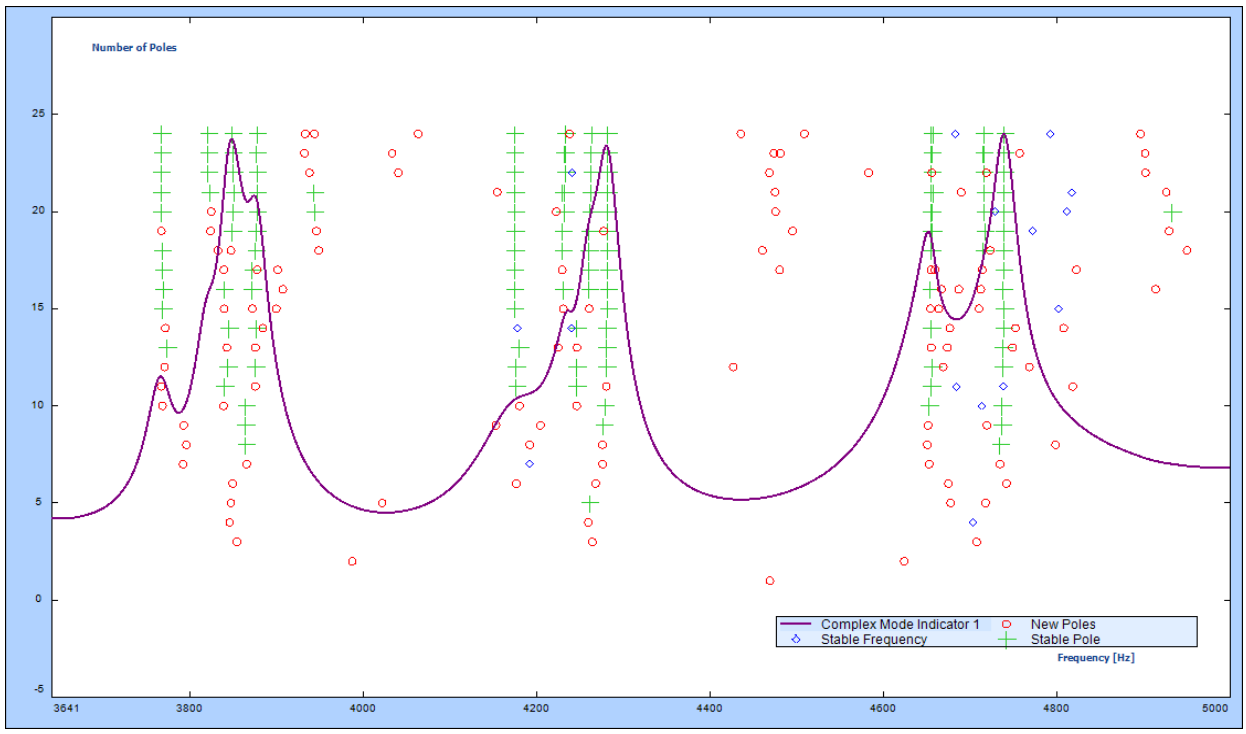

Figure A-35. Stability diagram of the hemispherical head model fully filled with water with internal pressure of 12.5 kPa within the frequency range from 3640 to 5000 Hz.

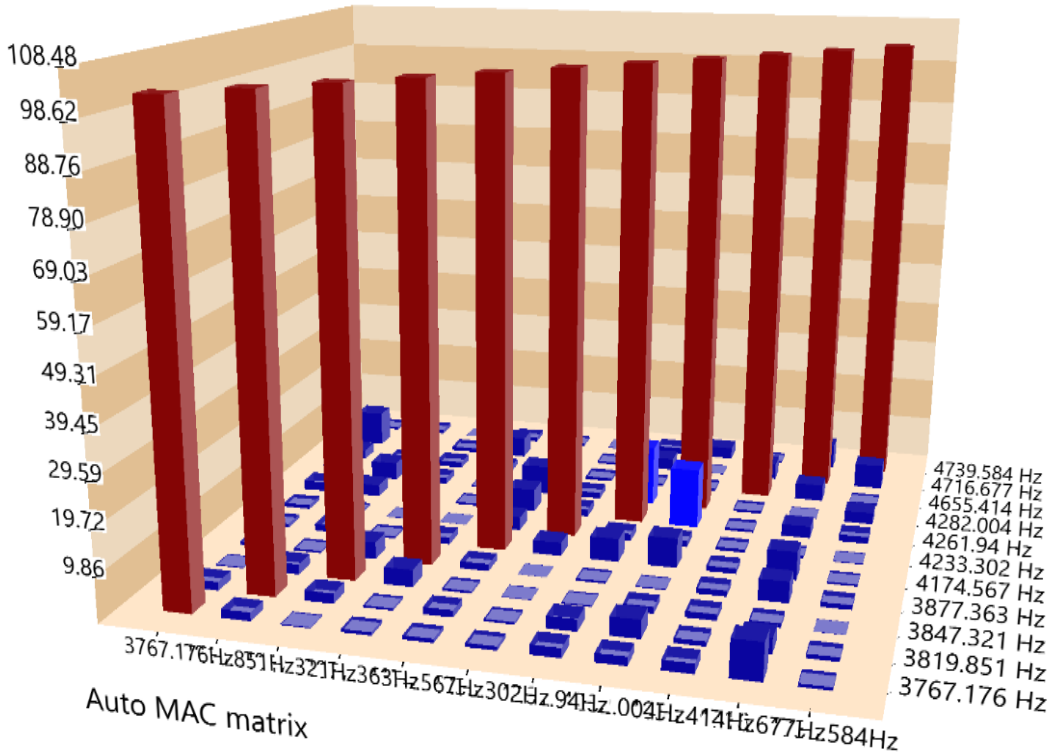

Figure A-36. Display Auto Modal Assurance Criterion (%) of the case with hemispherical with internal pressure of 12.5 kPa within the frequency range from 3640 to 5000 Hz.

Table A-35. Auto MAC Matrix of the extracted modal frequencies for the fully-filled aluminum shell with internal pressure of 12.5 kPa within the frequency range from 3640 to 5000 Hz.

Mode No.	Frequency (Hz)	Mode 1 3767.176 Hz	Mode 2 3819.851 Hz	Mode 3 3847.321 Hz	Mode 4 3877.363 Hz	Mode 5 4174.567 Hz	Mode 6 4233.302 Hz	Mode 7 4261.940 Hz	Mode 8 4282.004 Hz	Mode 9 4655.414 Hz	Mode 10 4716.677 Hz	Mode 11 4739.584 Hz
M 1	3767.176	100	1.851	0.247	0.711	0.869	0.872	2.061	1.902	2.113	7.798	0.665
M 2	3819.851	1.851	100	2.193	0.476	1.505	0.5	2.586	3.919	1.042	3.312	0.919
M 3	3847.321	0.247	2.193	100	3.648	0.521	0.143	0.306	1.467	1.356	0.934	0.065
M 4	3877.363	0.711	0.476	3.648	100	1.538	0.034	0.495	0.244	1.287	4.563	1.044
M 5	4174.567	0.869	1.505	0.521	1.538	100	2.893	5.024	6.394	1.18	6.103	0.457
M 6	4233.302	0.872	0.5	0.143	0.034	2.893	100	1.637	1.35	0.734	0.521	0.189
M 7	4261.94	2.061	2.586	0.306	0.495	5.024	1.637	100	13.07	0.612	2.6	1.507
M 8	4282.004	1.902	3.919	1.467	0.244	6.394	1.35	13.07	100	0.561	0.172	2.537
M 9	4655.414	2.113	1.042	1.356	1.287	1.18	0.734	0.612	0.561	100	3.638	0.489
M 10	4716.677	7.798	3.312	0.934	4.563	6.103	0.521	2.6	0.172	3.638	100	5.381
M 11	4739.584	0.665	0.919	0.065	1.044	0.457	0.189	1.507	2.537	0.489	5.381	100

Table A-36. Modal Parameter of the case with hemispherical with internal pressure of 12.5 kPa within the frequency range from 3640 to 5000 Hz.

Mode	Frequency (Hz)	Damping (%)
F#1	3767.176	0.439
F#2	3819.851	0.408
F#3	3847.321	0.379
F#4	3877.363	0.355
F#5	4174.567	1.083
F#6	4233.302	0.329
F#7	4261.94	0.402
F#8	4282.004	0.371
F#9	4655.414	0.28
F#10	4716.677	2.445
F#11	4739.584	0.351

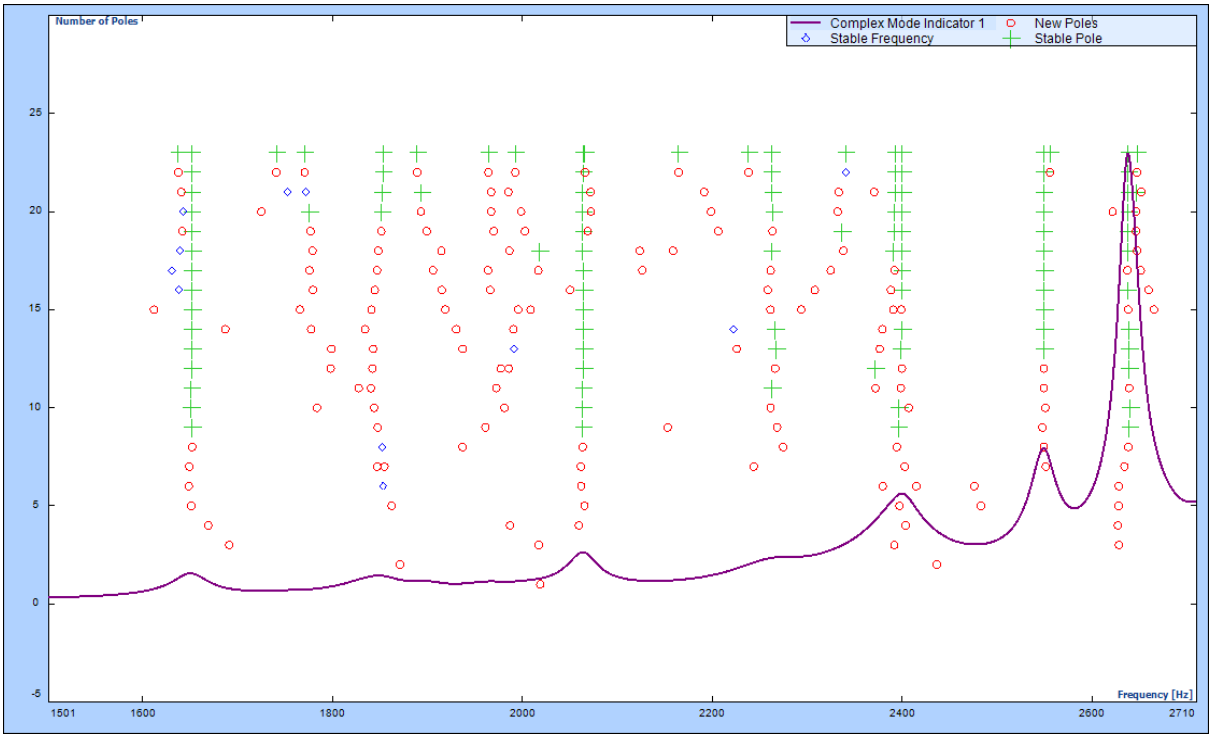

Figure A-37. Stability diagram of the hemispherical head model fully filled with water with internal pressure of 15 kPa within the frequency range from 1500 to 2710 Hz.

Table A-37. Auto MAC Matrix of the extracted modal frequencies for the fully-filled aluminum shell with internal pressure of 15 kPa within the frequency range from 1500 to 2710 Hz.

Mode No.	Frequency (Hz)	Mode 1 1651.752 Hz	Mode 2 1853.287 Hz	Mode 3 2063.967 Hz	Mode 4 2262.57 Hz	Mode 5 2399.109 Hz	Mode 6 2548.868 Hz	Mode 7 2638.263 Hz
M 1	1651.752	100	1.44	0.293	8.888	1.96	0.147	0.086
M 2	1853.287	1.44	100	0.876	0.233	3.293	1.236	0.475
M 3	2063.967	0.293	0.876	100	2.444	0.986	0.171	0.816
M 4	2262.57	8.888	0.233	2.444	100	42.392	0.04	0.167
M 5	2399.109	1.96	3.293	0.986	42.392	100	0.128	0.144
M 6	2548.868	0.147	1.236	0.171	0.04	0.128	100	0.048
M 7	2638.263	0.086	0.475	0.816	0.167	0.144	0.048	100

Table A-38. Modal Parameter of the case with hemispherical with internal pressure of 15 kPa within the frequency range from 1500 to 2710 Hz.

Mode	Frequency (Hz)	Damping (%)
F#1	1651.752	1.154
F#2	1853.287	1.709
F#3	2063.967	0.788
F#4	2262.57	1.841
F#5	2399.109	0.675
F#6	2548.868	0.548
F#7	2638.263	0.344

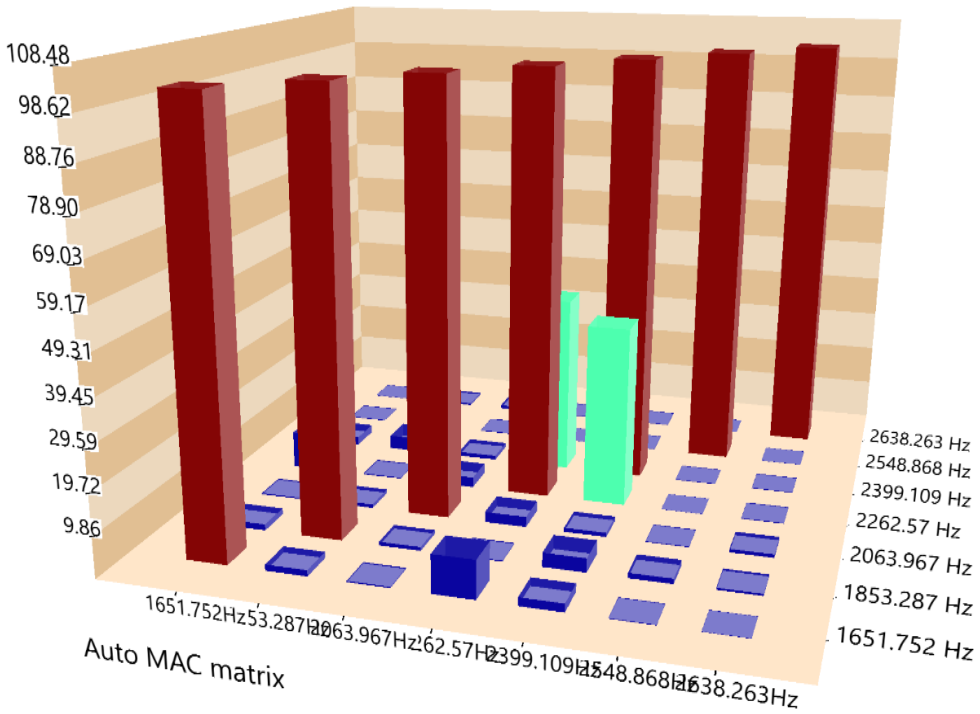

Figure A-38. Display Auto Modal Assurance Criterion (%) of the case with hemispherical with internal pressure of 15 kPa within the frequency range from 1500 to 2710 Hz.

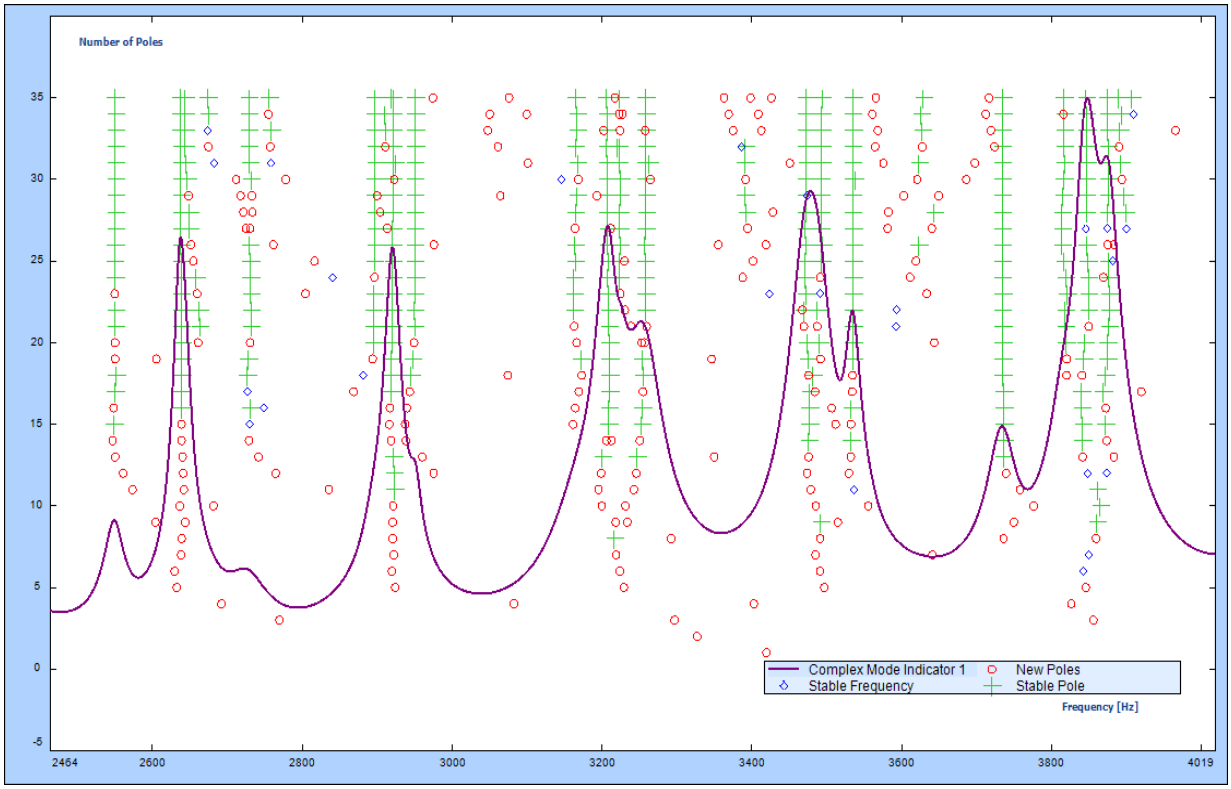

Figure A-39. Stability diagram of the hemispherical head model fully filled with water with internal pressure of 15 kPa within the frequency range from 2940 to 4030 Hz.

Table A-39. Auto MAC Matrix of the extracted modal frequencies for the fully-filled aluminum shell with internal pressure of 15 kPa within the frequency range from 2940 to 4030 Hz.

Mode No.	Frequency (Hz)	M 1 2550.039 Hz	M 2 2637.452 Hz	M3 2728.654 Hz	M 4 2896.657 Hz	M 5 2920.835 Hz	M 6 2950.274 Hz	M 7 3166.399 Hz	M 8 3206.817 Hz	M 9 3224.42 Hz	M 10 3258.011 Hz	M 11 3472.296 Hz	M 12 3493.046 Hz	M 13 3534.698 Hz	M14 3734.284 Hz	M 15 3814.983 Hz	M16 3846.526 Hz	M 17 3875.122 Hz
M 1	2550.039	100	0.682	4.159	8.061	3.357	6.677	4.311	3.168	6.676	1.549	0.026	1.692	0.316	8.323	4.525	0.043	0.509
M 2	2637.452	0.682	100	0.274	2.019	0.035	1.575	1.397	1.454	2.112	0.411	0.059	0.043	0.203	0.261	0.438	0.166	0.029
M 3	2728.654	4.159	0.274	100	10.66	6.34	11.27	7.254	8.802	9.769	12.69	0.054	4.619	0.811	6.602	7.721	0.935	1.769
M 4	2896.657	8.061	2.019	10.66	100	4.762	9.795	6.071	7.773	14.11	9.309	0.675	3.598	0.844	1.995	8.716	2.034	2.25
M 5	2920.835	3.357	0.035	6.34	4.762	100	8.989	6.563	3.95	8.982	2.63	0.338	7.058	0.53	2.538	3.093	0.093	0.46
M 6	2950.274	6.677	1.575	11.27	9.795	8.989	100	6.552	5.669	13.08	8.571	2.046	4.17	1.242	6.326	7.239	1.167	1.966
M 7	3166.399	4.311	1.397	7.254	6.071	6.563	6.552	100	6.508	10.59	8.165	0.443	5.999	1.341	3.99	6.797	3.018	2.252
M 8	3206.817	3.168	1.454	8.802	7.773	3.95	5.669	6.508	100	18.07	4.366	0.407	1.963	0.186	1.552	6.334	2.176	0.54
M 9	3224.42	6.676	2.112	9.769	14.41	8.982	13.08	10.59	18.07	100	3.159	2.334	1.888	0.317	2.929	7.692	1.043	2.079
M 10	3258.011	1.549	0.411	12.62	9.309	2.63	8.571	8.165	4.366	3.159	100	2.783	2.076	0.448	4.904	4.176	1.528	2.796
M 11	3472.296	0.026	0.059	0.054	0.675	0.338	2.046	0.443	0.407	2.334	2.783	100	23.46	0.468	1.016	0.115	0.336	0.113
M 12	3493.046	1.692	0.043	4.619	3.598	7.058	4.17	5.999	1.963	1.888	2.076	23.46	100	3.823	2.227	1.59	0.48	0.565
M 13	3534.698	0.316	0.203	0.811	0.844	0.53	1.242	1.341	0.186	0.317	0.448	0.468	3.823	100	0.586	1.9	1.174	0.068
M 14	3734.284	8.323	0.261	6.602	1.995	2.538	6.326	3.99	1.552	2.929	4.904	1.016	2.227	0.586	100	4.887	0.494	0.511
M 15	3814.983	4.525	0.438	7.721	8.716	3.093	7.239	6.797	6.334	7.692	4.176	0.115	1.59	1.9	4.887	100	0.421	2.616
M 16	3846.526	0.043	0.166	0.935	2.034	0.093	1.167	3.018	2.176	1.043	1.528	0.336	0.48	1.174	0.494	0.421	100	1.963
M 17	3875.122	0.509	0.029	1.769	2.25	0.46	1.966	2.252	0.54	2.079	2.796	0.113	0.565	0.068	0.511	2.616	1.963	100

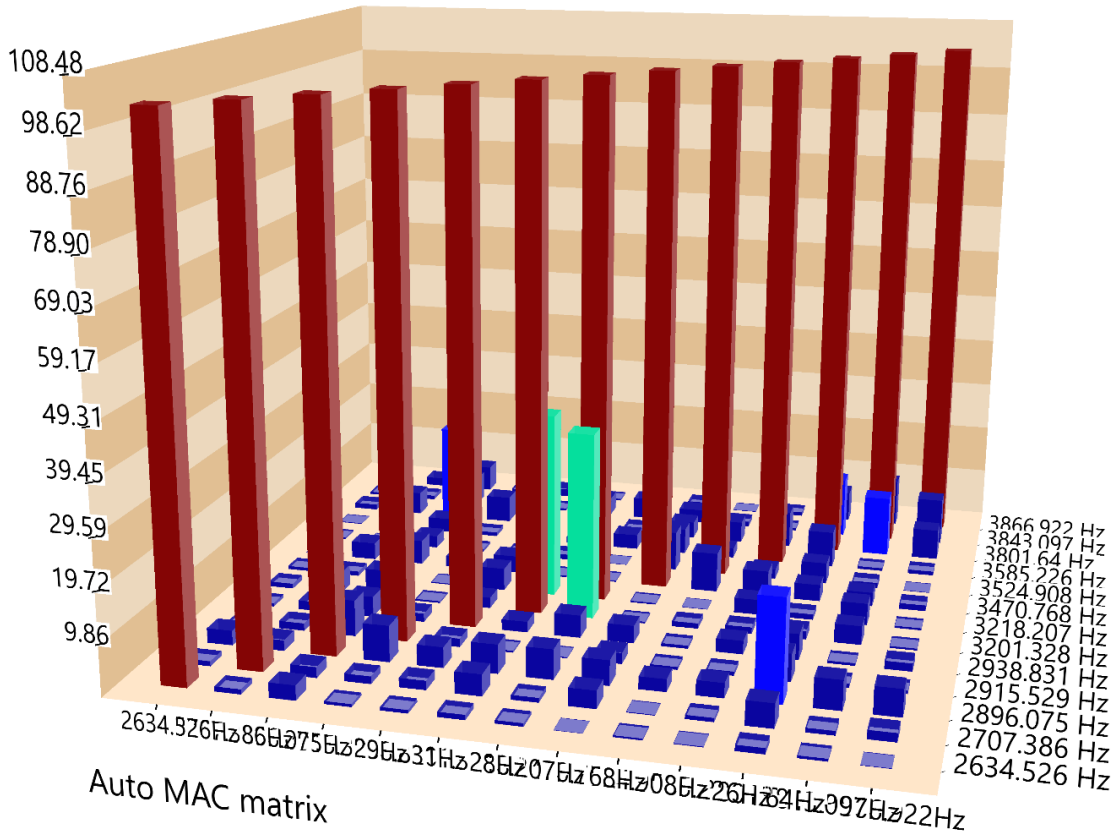

Figure A-40. Display Auto Modal Assurance Criterion (%) of the case with hemispherical with internal pressure of 15 kPa within the frequency range from 2940 to 4030 Hz

Table A-40. Modal Parameter of the case with hemispherical with internal pressure of 15 kPa within the frequency range from 2940 to 4030 Hz.

Mode	Frequency (Hz)	Damping (%)
F#1	2550.039	0.544
F#2	2637.452	0.364
F#3	2728.654	1.021
F#4	2896.657	0.534
F#5	2920.835	0.378
F#6	2950.274	0.292
F#7	3166.399	1.443
F#8	3206.817	0.496
F#9	3224.42	0.474
F#10	3258.011	0.796
F#11	3472.296	0.72
F#12	3493.046	0.587
F#13	3534.698	0.339
F#14	3734.284	0.522
F#15	3814.983	0.592
F#16	3846.526	0.419
F#17	3875.122	0.393

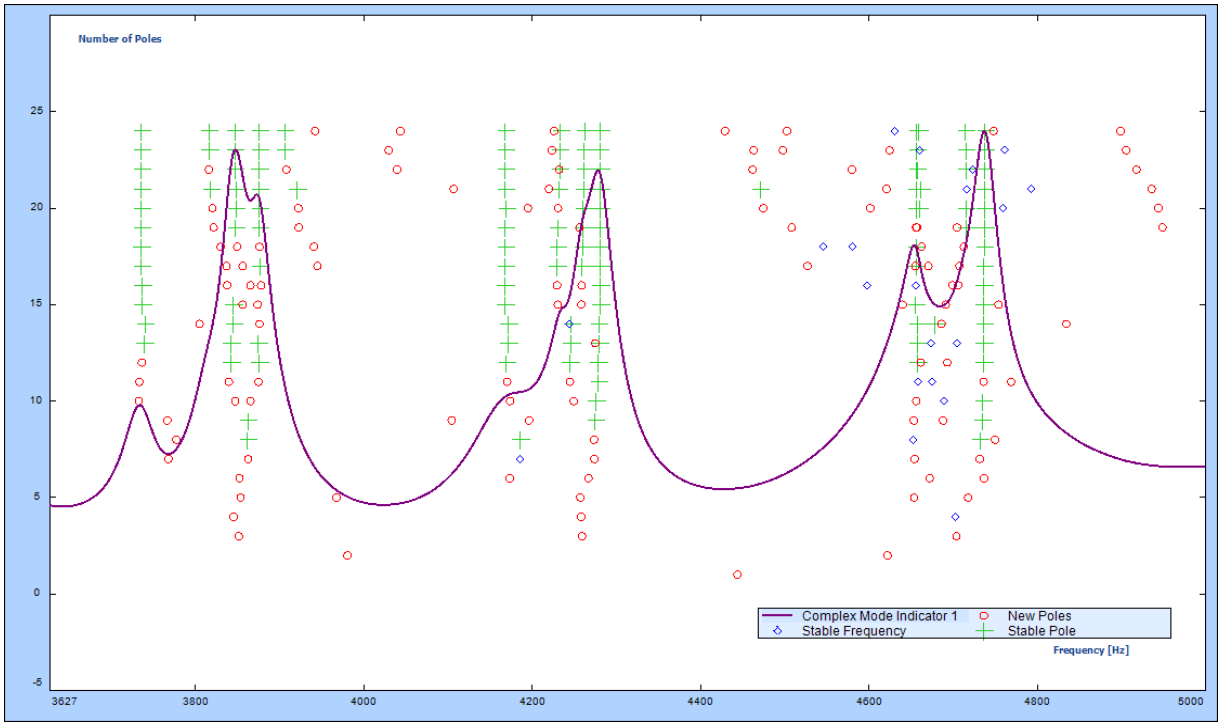

Figure A-41. Stability diagram of the hemispherical head model fully filled with water with internal pressure of 15 kPa within the frequency range from 3640 to 5000 Hz.

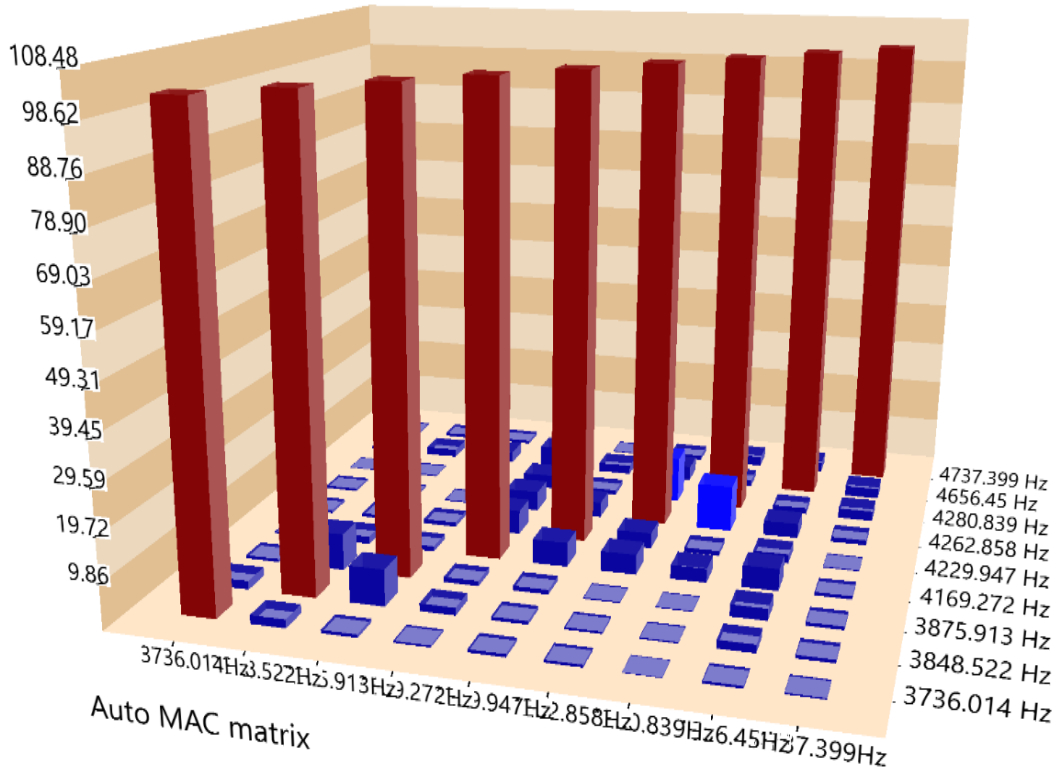

Figure A-42. Display Auto Modal Assurance Criterion (%) of the case with hemispherical with internal pressure of 15 kPa within the frequency range from 3640 to 5000 Hz.

Table A-41. Auto MAC Matrix of the extracted modal frequencies for the fully-filled aluminum shell with internal pressure of 15 kPa within the frequency range from 3640 to 5000 Hz.

Mode No.	Frequency (Hz)	Mode 1 3736.014 Hz	Mode 2 3848.522 Hz	Mode 3 3875.913 Hz	Mode 4 4169.272 Hz	Mode 5 4229.947 Hz	Mode 6 4262.858 Hz	Mode 7 4280.839 Hz	Mode 8 4656.45 Hz	Mode 9 4737.399 Hz
M 1	3736.014	100	1.856	0.699	0.405	0.676	0.566	0.143	0.543	0.317
M 2	3848.522	1.856	100	7.802	1.642	0.755	0.479	0.305	1.775	0.729
M 3	3875.913	0.699	7.802	100	1.109	0.986	0.287	0.223	2.543	0.723
M 4	4169.272	0.405	1.642	1.109	100	5.238	4.321	3.029	4.703	0.721
M 5	4229.947	0.676	0.755	0.986	5.238	100	3.34	1.061	2.01	0.245
M 6	4262.858	0.566	0.479	0.287	4.321	3.34	100	10.086	3.172	1.073
M 7	4280.839	0.143	0.305	0.223	3.029	1.061	10.086	100	1.386	2.19
M 8	4656.45	0.543	1.775	2.543	4.703	2.01	3.172	1.386	100	2.251
M 9	4737.399	0.317	0.729	0.723	0.721	0.245	1.073	2.19	2.251	100

Table A-42. Modal Parameter of the case with hemispherical with internal pressure of 15 kPa within the frequency range from 3640 to 5000 Hz.

Mode	Frequency (Hz)	Damping (%)
F#1	3736.014	0.527
F#2	3848.522	0.432
F#3	3875.913	0.401
F#4	4169.272	1.096
F#5	4229.947	0.434
F#6	4262.858	0.401
F#7	4280.839	0.402
F#8	4656.45	0.29
F#9	4737.399	0.35